PROGRESS IN RESEARCH

April 1, 2018 - March 31, 2019

CYCLOTRON INSTITUTE

Texas A&M University

College Station, Texas

PROGRESS IN RESEARCH

APRIL 1, 2018 - MARCH 31, 2019

Prepared By

The Cyclotron Institute Staff

Texas A&M University

College Station, TX 77843-3366

Phone: (979) 845-1411
Fax: (979) 845-1899

Web: http://cyclotron.tamu.edu

July 2019

TABLE OF CONTENTS

Introduction ..... **xi**
S.J. Yennello, Director

SECTION I: NUCLEAR STRUCTURE, FUNDAMENTAL INTERACTIONS AND ASTROPHYSICS

Superallowed beta decay **I-1**
J.C. Hardy, V.E. Iacob, H.I. Park, N. Nica, M. Bencomo, T. Eronen, V. Horvat, L. Chen, and I.S. Towner

^{34}Ar half-life **I-5**
V.E. Iacob, J.C. Hardy, M. Bencomo, L. Chen, V. Horvat, N. Nica, H.I. Park, B.T. Roeder, and A. Saastamoinen

The ^{33}S(p, γ)^{34}Cl experiment **I-8**
H.I. Park, J.C. Hardy, M Bencomo, W. Tan, K. Macon, and M. Brodeur

Tests of internal-conversion theory **I-9**
J.C. Hardy, N. Nica, V. Horvat, V.E. Iacob, and M.B. Trzhaskovskaya

Precise measurement of α_K and α_T for the 39.8-keV *E*3 transition in ^{103}Rh: Test of internal-conversion theory **I-12**
N. Nica, J.C. Hardy, V.E. Iacob, V. Horvat, H.I. Park, T.A. Werke, K.J. Glennon, C.M. Folden III, V.I. Sabla, J.B. Bryant, and X.K. James

***K* internal conversion of the ^{93m}Nb 30.8-keV gamma ray** **I-15**
V. Horvat, J.C. Hardy, N. Nica, V.E. Iacob, and E.E. Tereshatov

United States Nuclear Structure Data Program (USNDP) and Evaluated Nuclear Structure Data File (ENSDF) at Texas A&M University ENSDF Data Evaluation Center **I-19**
N. Nica and J.C. Hardy

High precision half-life measurement of ^{29}P **I-21**
P.D. Shidling, J.C. Hardy, V.E. Iacob, V. Kolhinen, D. McClain, D. Melconian, N. Morgan, A. Ozmetin, H.I. Park, B.T. Roeder, and B. Schroeder

Improved determination of the gamma branching ratios from the decay of ^{37}K..... I-23
A. Ozmetin, V.E. Iacob, J.C. Hardy, V.S. Kolhinen, D. Melconian, M. Nasser,
H.I. Park, B. Schroeder, and P.D. Shidling

Toward measuring the Fierz parameter in ^{6}He: Cyclotron radio emission spectroscopy modeling with Kassiopeia..... I-25
D. McClain, V. Iacob, V.S. Kolhinen, D. Melconian, M. Nasser, A. Ozmetin,
B. Schroeder, and P.D. Shidling

TRINAT's polarized program with ^{37}K..... I-27
D. Melconian

Study of astrophysically important low-energy resonances in α + ^{22}Ne reaction using ^{6}Li(^{22}Ne,^{26}Mg)*d* alpha transfer with TIARA and MDM spectrometer I-29
S. Ota, G.A. Christian, E.A. Bennett, S. Dede, H. Jayatissa, J. Hooker, C. Hunt,
C. Magana, G. Rogachev, A. Saastamoinen, S. Upadhyayula, W.N. Catford,
S. Hallam, G. Lotay, M. Mouhkaddam, J.A. Tostevin, and R. Wilkinson

Preparation for measurement of the ^{15}O(α,γ)^{19}Ne alpha branching ratio I-33
S. Dede, G. Christian, S. Ota, C.E. Parker, E. Bennett, M. Roosa, D.P. Scriven,
W.N. Catford, and G. Lotay

Precision γ-ray branching-ratio measurements for long-lived fission products of importance to stockpile stewardship..... I-37
K. Kolos, A.M. Hennessy, J.A. Clark, J.C. Hardy, V.E. Iacob, G.E. Miller, E. Norman,
H.I. Park, G. Savard, N.D. Scielzo, A.J. Shaka, M.A. Stoyer, and A.P. Tonchev

Nuclear level densities and gamma-ray strength functions in samarium isotopes..... I-40
F. Naqvi, A. Simon, M. Guttormsen, R. Schwengner, S. Frauendorf, C.S. Reingold,
J.T. Burke, N. Cooper, R.O. Hughes, S. Ota, and A. Saastamoinen

^{35}K experiments..... I-43
R. Chyzh, A. Saastamoinen, B. Roeder, R.E. Tribble, A. Spiridon, A. Kankainen,
E. Pollacco, L. Trache, I. Stefanescu, and G. Lotay

Studying the Hoyle state with β-delayed particle-decays using TexAT I-45
J. Bishop, G.V. Rogachev, E. Aboud, S. Ahn, M. Barbui, A. Bosh, C. Hunt,
J. Hooker, D. Jayatissa, E. Koshchiy, C. Pruitt, E. Pollacco, B. T. Roeder,
A. Saastamoinen, L. Sobotka, S. Upadhyayula, S.T. Marley, and R. Malecek

Study of ^{8}B + ^{40}Ar fusion reaction using TexAT I-48
S. Ahn, G.V. Rogachev, S.M. Lukyanov, J.C. Zamora, E. Aboud, M. Assunão,
M. Barbui, J. Bishop, C. Hunt, V. Guimarães, H. Jayatissa, E. Koshchiy, R. O'Dwyer,
Yu.E. Penionzhkevich, B.T. Roeder, A. Saastamoinen, and S. Upadhyayula

Search for the low-lying T=5 states in ^{48}Ca I-51
S. Upadhyayula, A. Hood, C Deibel, C. Hunt, D. Santiago-Gonzalez, G. Rogachev, J. Blackmon, J. Lighthall, J. Hooker, J. Browne, M. Anastasiou, N. Rijal, S. Bedoor, S. Ahn, W. Ong, and Y. Koshichy

Clustering in ^{10}Be I-55
S. Upadhyayula, G.V. Rogachev, E. Koshchiy, E. Uberseder, V.Z. Goldberg, J. Hooker, H, Jayatissa, C. Hunt, and B.T. Roeder

Resonant elastic scattering of ^{14}O on α particles studied with the TexAT active target..... I-61
M. Barbui, E. Aboud, S. Ahn, J. Bishop, V.Z. Goldberg, J. Hooker, C.H. Hunt, H. Jayatissa, Tz. Kokalova, E. Koshchiy, C. Magana, R. O'Dwyer, S. Pirrie, E. Pollacco, B.T. Roeder, A. Saastamoinen, E. Uberseder, S. Upadhiayula, C. Wheldon, and G.V. Rogachev

T=3/2 isobaric analog states in ^{9}Be I-64
C. Hunt, G.V. Rogachev, V.Z. Goldberg, E. Koshchiy, B.T. Roeder, T. Ahn, J. Hooker, H. Jayatissa, and S. Upadhyayula

Spin physics with STAR at RHIC I-67
C.A. Gagliardi, T. Lin, R.E. Tribble, and the STAR Collaboration

The STAR forward upgrade I-73
C.A. Gagliardi and T. Lin, and the STAR Collaboration

Breakup of ^{9}C and ^{66}Se with SAMURAI in RIKEN I-75
A. Saastamoinen for the NP1412-SAMURAI29R1 and NP1406-SAMURAI24 collaborations

SECTION II: HEAVY ION REACTIONS

Examination of the purification step of the PUREX process with varying HNO_3 concentration....II-1
P.K. Kircher, K.J. Glennon, and C.M. Folden III

Mechanism of indium and thallium extraction into [Hbet][Tf_2N] ionic liquid.....II-4
M.F. Volia, E.E. Tereshatov, M. Boltoeva, and C.M. Folden III

Ternary hydrophobic eutectic mixtures for indium extraction from hydrochloric media II-6
E.E. Tereshatov, J.M. Edgecomb, M. Boltoeva, C.M. Folden III

Introduction of novel hydrophobic eutectics for the liquid-liquid extraction of indium from hydrochloric acid media.....II-9
J.M. Edgecomb, E.E. Tereshatov, M. Boltoeva, and C.M. Folden III

A forensic investigation of the PUREX process to determine Pu separation conditions.....II-12
K.J. Glennon, and C.M. Folden III

Test runs the multi-nucleon transfer reaction detector array for synthesis of heavy elements.....II-15
A. Wakhle, K. Hagel, A.B. McIntosh, M. Barbui, J. Gauthier, A. Jedele, A. Rodriguez Manso, J.B. Natowitz, K. Sekizawa, Z. Tobin, R. Wada, S. Wuenschel, A. Zarrella, and S.J. Yennello

Simulations for proton detection in ^{59}Fe(*d*,*p*)^{60}Fe.....II-18
A.B. McIntosh

Calculation of background reactions for ^{59}Fe(*d*,*p*)^{60}Fe.....II-21
A.B. McIntosh

Proton-proton correlation functions using the upgraded FAUST array.....II-23
L.A. Heilborn, A.B. McIntosh, M.D. Youngs, and S.J. Yennello

High excitation energy resonances in α-conjugate nuclei.....II-26
K. Hagel, J.B. Natowitz, A.B. McIntosh, L. Heilborn, S.J. Yennello, R. Wada, A. Wakhle, A. Jedele, J. Gauthier, M.D. Youngs, Y.-W. Lui, M. Sorensen, A. Hannaman, and Z. Tobin

N/Z equilibration: Mapping isotopic yields in binary projectile breakups.....II-28
A. Hannaman, A.B. McIntosh, A. Jedele, A. Rodriguez Manso, K. Hagel, Z. Kohley, and S.J. Yennello

The nuclear caloric curve: Temperatures of simulated quasiprojectiles.....II-31
M. Sorensen, A.B. McIntosh, Z. Kohley, and S.J. Yennello

Production of super heavy elements using multinucleon transfer reactions.....II-34
Z. Tobin, A. Wakhle, and S.J. Yennello

Study of α-α correlation functions in ^{40}Ar+^{58}Fe at 30 MeV/u.....II-37
A. Abbott, L. Heilborn, A.B. McIntosh, and S.J. Yennello

New results from the fragment yields analysis in ^{124}Sn+^{112,124}Sn at 26*A* MeV reaction.....II-41
J. Gauthier, M. Barbui, X. Cao, K. Hagel, J.B. Natowitz, R. Wada, and S. Wuenschel

Energetic proton emission in intermediate-energy heavy-ion collisions with IQMD.....II-44
S.S. Wang, R. Wada, J.B. Natowitz, K. Hagel, Y.G. Ma, and X.G. Cao

Experimental liquid-gas phase transition signals and reaction dynamics II-46
R. Wada, W. Lin, H. Zheng, X. Liu, M. Huang, K. Hagel, and J.B. Natowitz

Toward understanding relativistic heavy-ion collisions with the STAR detector at RHIC II-49
D.M. Anderson, Y. Liu, S. Mioduszewski, N. Sahoo, and the STAR Collaboration

SECTION III: NUCLEAR THEORY

Description of isoscalar multipole giant resonances within the particle-hole dispersive optical model III-1
M.L. Gorelik, S. Shlomo, B.A. Tulupov, and M.H. Urin

Electric isovector dipole polarizability in ^{40,48}Ca, ^{68}Ni, ^{90}Zr, ^{120}Sn and ^{208}Pb and the second derivative of the symmetry energy coefficient III-2
C. Agodi, G. Giuliani, F. Cappuzzello, A. Bonasera, D. Carbone, M. Cavallaro, A. Foti, R. Linares, and G. Santagati

Isoscalar giant quadrupole resonances in ^{44}Ca, ^{54}Fe, ^{64,68}Zn and ^{56,58,60,68}Ni and the effective mass III-4
G. Bonasera, S. Shlomo, D.H. Youngblood, Y.-W. Lui, Krishichayan, and J. Button

Isovector giant dipole resonances in ^{44}Ca, ^{54}Fe, ^{64,68}Zn and ^{56,58,60,68}Ni and the energy weighted sum rule enhancement factor III-6
G. Bonasera, S. Shlomo, D.H. Youngblood, Y.-W. Lui, Krishichayan, and J. Button

Nuclear astrophysics theory progress III-8
J.W. Holt and Y. Lim

Astrophysical factors of ^{12}C + ^{12}C fusion extracted using Trojan Horse method III-12
A.M. Mukhamedzhanov, D.Y. Pang, and A.S. Kadyrov

Balmer-α emission in proton-hydrogen collisions III-13
O. Erkilic, I.B. Abdurakhmanov, A.S. Kadyrov, and I. Bray, S.K. Avazbaev, and A.M. Mukhamedzhanov

Connection between asymptotic normalization coefficients and resonance widths of mirror states III-14
A.M. Mukhamedzhanov

Extrapolation of scattering data to the negative-energy region: Application to the p-^{16}O system **III-15**
L.D. Blokhintsev, A.S. Kadyrov, A.M. Mukhamedzhanov, and D.A. Savin

Impact of the $^{7}Be(\alpha,\gamma)^{11}C$ Reaction on the Primordial Abundance of ^{7}Li **III-16**
M. Hartos , C.A. Bertulani , Shubhchintak, A.M. Mukhamedzhanov, and S. Hou

Three-body Faddeev equations in two-particle Alt-Grassberger-Sandhas form with distorted-wave-Born-approximation amplitudes as effective potentials **III-17**
A.M. Mukhamedzhanov

Strongly resonating bosons in hot nuclei **III-18**
S. Zhang, A. Bonasera, M. Huang, H. Zheng, D.X. Wang, J.C.Wang, L. Lu,
G. Zhang, Z. Kohley, Y.G. Ma, and S.J. Yennello

Triple α resonances in the decay of hot nuclear systems **III-19**
S. Zhang, A. Bonasera, M. Huang, H. Zheng, D.X. Wang, J.C.Wang, L. Lu,
G. Zhang, Z. Kohley, Y.G. Ma, and S.J. Yennello

Microscopic description of proton-induced spallation reactions with the Constrained Molecular Dynamics (CoMD) Model **III-20**
A. Assimakopoulou, G.A. Souliotis, A. Bonasera, A. Botvina,
N.G. Nicolis, and M. Veselsky

Nuclear probes of an out-of-equilibrium plasma at the highest compression **III-21**
G. Zhang, M. Huang, A. Bonasera, Y.G. Ma, B.F. Sheng, H.W. Wang, W.P. Wang,
J.C. Xu, G.T.Fan, H.J. Fu, H. Xue, H. Zheng, L.X. Liu, S. Zhang, W.J. Li, X.G. Cao,
X.G. Deng, X.Y. Li, Y.C. Liu, Y. Yu, Y. Zhang, C.B. Fu, and X.P. Zhang

Nuclear astrophysics with lasers **III-22**
M. Huang, H.J. Quevedo, G. Zhang, and A. Bonasera

A novel approach to medical radioisotope production using inverse kinematics: A successful production test of the theranostic radionuclide ^{67}Cu **III-23**
G.A. Souliotis, M.R.D. Rodrigues, K. Wang, V. Iacob, N. Nica, B. Roeder,
G. Tabacaru, M. Yu, P. Zanotti-Fregonara, and A. Bonasera

Chiral kinetic approach to chiral magnetic effect in isobaric collisions **III-24**
Y. Sun and C.M. Ko

Light nuclei production as a probe of the QCD phase diagram **III-26**
K.J. Sun, L.W. Chen, C.M. Ko, J. Pu, and Z. Xu

Nuclear matter properties at finite temperatures from effective interactions III-28
Jun Xu, Arianna Carbone, Zhen Zhang, and C.M. Ko

Azimuthal angle dependence of the longitudinal spin polarization in relativistic heavy ion collisions..... III-30
Y. Sun and C.M. Ko

Light nuclei production in Pb+Pb collisions at $\sqrt{s_{NN}}$ = 2.76 TeV..... III-32
L.L. Zhu, H. Zheng, C.M. Ko, and Y. Sun

Spectra and flow of light nuclei in relativistic heavy ion collisions at energies available at the BNL Relativistic Heavy Ion Collider and at the CERN Large Hadron Collider III-34
W. Zhao, L.L. Zhu, H. Zheng, C.M. Ko, and H. Song

Pion production in a transport model based on mean fields from chiral effective theory III-36
Z. Zhang and C.M. Ko

Suppression of light nuclei production in collisions of small systems at the Large Hadron Collider III-38
K.J. Sun, C.M. Ko, and B. Donigus

Probing the topological charge in QCD matter via multiplicity up-down asymmetry..... III-40
Y. Sun and C.M. Ko

Shear viscosity of a hot hadron gas III-42
R.J. Fries and Zhidong Yang

Benchmarking the JETSCAPE 1.0 event generator in p+p collisions III-44
R.J. Fries and JETSCAPE Collaborators

Charm-baryon production in proton-proton collisions..... III-46
Min He and Ralf Rapp

Production of lght anti-/nuclei at thermal freezeout in ultrarelativistic heavy-ion collisions..... III-48
Xinyuan Xu and Ralf Rapp

Extraction of the heavy-quark potential from bottomonium observables in heavy-ion collisions III-49
Xiaojian Du, Shuai Liu, and Ralf Rapp

Dilepton radiation in heavy-ion collisions at small transverse momentum III-51
M. Klusek-Gawenda, R. Rapp, W. Schäfer, and A. Szczurek

Radiative energy loss of heavy quarks in quark-gluon plasma within the T-matrix approach **III-53**
Shuai Y.F. Liu and Ralf Rapp

SECTION IV: SUPERCONDUCTING CYCLOTRON, INSTRUMENTATION AND RIB UPGRADE

K500 operations and development **IV-1**
D.P. May, G.J. Kim, B.T. Roeder, H.L. Clark, and F.P. Abegglen

K150 operations and development **IV-3**
G.J. Kim, B.T. Roeder, F. Abegglen, H.L. Clark, L. Gathings, D.P. May, and H. Peeler

Texas A&M cyclotron radiation effects facility April 1, 2018 – March 31, 2019 ..... **IV-6**
H.L. Clark, J. Brinkley, L. Chen, G. Chubarian, V. Horvat, B. Hyman, H.I. Park, B. Roeder, G. Tabacaru, and J. Thomas

Texas A&M cyclotron K150 radiation effects facility April 1, 2018 – March 31, 2019 ..... **IV-8**
H.L. Clark, B. Hyman, and J. Thomas

Recent progress on the ECR4 ion source **IV-11**
D.P. May, S. Molitor, F.P. Abegglen, H. Peeler, and R. Ohlsen

Light ion guide - a new approach **IV-13**
G. Tabacaru, J. Ärje, D.P. May, A. Saastamoinen, F.P. Abegglen, G.J. Kim, S. Molitor, and B.T. Roeder

Identification of ^{112}In: First re-accelerated radioactive light-ion guide beam **IV-17**
B.T. Roeder, F. Abegglen, J. Arje, G.J. Kim, A. Saastamoinen, and G. Tabacaru

Cyclotron computing **IV-21**
R. Burch, J. Gauthier, and K. Hagel

Data acquisition upgrades at the Cyclotron Institute **IV-22**
K. Hagel, A. Jedele, A.B. McIntosh, R. Burch, and J. Gauthier

Studies of the CB-ECRIS beam background **IV-23**
B.T. Roeder, F. Abegglen, J. Ärje, G.J. Kim, D.P. May, A. Saastamoinen, and G. Tabacaru

MARS status report: Tuning of rare isotope beams of ^{10}C, ^{14}O, ^{42}Ti, ^{29}P, ^{8}B, ^{12}N, ^{9}Li and ^{76}Ge fragmentation IV-25
B.T. Roeder and A. Saastamoinen

Development of electron cyclotron emission imaging optics IV-27
L.E. Henderson, H.L. Clark, C.A. Gagliardi, and D.P. May

Installation and characterization of the AGGIE gas-filled separator IV-29
C.M. Folden III and C.S. Salas

Studies of systematic effects of the AstroBox2 detector in online conditions IV-31
A. Saastamoinen, E. Pollacco, B.T. Roeder, R. Chycz, L. Trache, and R.E. Tribble

Development of TexCAAM: Texas CsI Array for Astrophysical Measurements IV-33
E. Aboud, L. Jeffery, E. Koshchiy, M. Barbui, C. Hunt, G.V. Rogachev,
S. Ahn, and E. Lester

Performance of GEM-Micromegas detector with TexAT IV-35
E. Koshchiy, S. Ahn, J. Bishop, C. Hunt, A. Saastamoinen,
G.V. Rogachev, and E. Pollacco

Toward the development of a next generation fast neutron portal monitor IV-39
E. Aboud, G.V. Rogachev, E. Koshchiy, J. Hooker, S. Ahn, C. Parker,
G. Christian, P. Kuchment, W. Baines, L.G. Sobotka, A. Thomas,
S. Ota, and V. Johnson

Parallel-plate avalanche counter (PPAC) detector as an MDM focal plane detector IV-42
H. Jayatissa, G. Chubaryan, E. Koshchiy, and G.V. Rogachev

Control system for TAMUTRAP IV-43
M. Nasser, V. Iacob, V.S. Kolhinen, D. McClain, D. Melconian, A. Ozmetin,
B. Schroeder, and P.D. Shidling

Making the world's largest Penning trap 2x bigger for beta-delayed proton decay studies IV-45
V.S. Kolhinen, V.E. Iacob, D. McClain, D. Melconian, M. Nasser, A. Ozmetin,
B. Schroeder, and P.D. Shidling

Update on the TAMUTRAP facility IV-47
P.D. Shidling, V.E. Iacob, V. Kolhinen, D. McClain, D. Melconian, N. Morgan,
A. Ozmetin, and B. Schroeder

GEANT4 simulations of the TAMUTRAP facility IV-50
B. Schroeder, V.E. Iacob, V.S. Kolhinen, D. McClain, D. Melconian, M. Nasser,
A. Ozmetin, and P.D. Shidling

Development and prototyping of a new highly-segmented neutron detector IV-52
C.E. Parker, G.A. Christian, D.P. Scriven, E. Aboud, G.V. Rogachev, S. Ahn, and E. Koshchiy

Optimizing the design of a highly-segmented neutron detector with Geant4 ..... IV-55
D.P. Scriven and G. Christian

Progress with the TAMU-ORNL BaF_2 array re-coupling IV-58
J. Gauthier, A.B. McIntosh, and I. Jeanis

Experimental implication of PIGE (Particle Induced Gamma Ray Emission) and standard modifications IV-61
M. McCarthy, E. Salas, A. Rodriguez Manso, J. Gauthier, and S.J. Yennello

Neutron ball background testing IV-64
A. Jedele, K. Hagel, and S.J. Yennello

Comparing the K500 beam pulser and phase shifter: A timing study IV-67
A. Jedele, K. Hagel, and S.J. Yennello

SECTION V: PUBLICATIONS

Papers published V-1

SECTION VI: APPENDIX

Talks presented VI-1

Research personnel and engineering staff VI-11

Students VI-12

Organizational chart VI-13

Graduate degree students VI-14

Institute colloquia and seminars VI-15

Introduction
April 1, 2018 – March 31, 2019

Progress in research and operations at the Texas A&M Cyclotron Institute is summarized in this report for the period April 1, 2018 through March 31, 2019. The format follows that of previous years. Sections I through III contain reports from individual research projects. Operation and technical developments are given in Section IV. Section V lists the publications with Cyclotron Institute authors and outside users and the Appendix gives additional information including talks presented by members of the Institute during the past year. Once again, the full volume of this year's Progress in Research is available only on our web site (http://cyclotron.tamu.edu). *Since most of the contributions presented here are truly reports on progress in research, results and conclusions should not be quoted from the report without the consent of the authors.*

The goal of accelerating radioactive beams by the K500 was achieved recently using beams produced by K150 proton beams impinging on targets in the light-ion guide and then charge-bred by the charge-breeding electron-cyclotron-resonance ion source, CB-ECRIS. In November of 2018, the production of the radioactive ^{112}In (14.4 minute half-life) from a ^{114}Cd target and subsequent charge breeding and re-acceleration with K500 were investigated. Using the CB-ECR ion source the charge bred $^{112}In^{21+}$ ions, along with $^{16}O^{3+}$ which was used as a pilot beam, were accelerated to 14 AMeV from the K500 cyclotron and were then sent to the MARS spectrometer for analysis. The beam switch from $^{16}O^{3+}$ to $^{112}In^{21+}$ was accomplished by shifting the K500 RF frequency by +6.5 kHz. The MARS analysis identified the beam as ^{112}In along with two other contaminants (from the ion source) of similar intensities to the ^{112}In; it was verified that the ^{112}In was indeed produced from the LIG gas cell. Thus this 14 AMeV $^{112}In^{21+}$ became our first accelerated radioactive beam.

The K500 provided an impressive 6,414 hours of beam for both science and radiation effects testing. The K150 cyclotron provided, 3859 hours of beam on target and continues to be used by external users for radiation effects testing with its proton beams. Additionally, efforts to meet the increasing radiation testing demand are underway by developing heavy-ion beams from the K150. Significant effort was devoted to improving the K150 cyclotron vacuum leading to new intensity records for H-minus (24 μA) and heavy-ions such as ^{40}Ar.

As in previous reports, I include here some scientific highlights.

- Explained the large enhancement of Λ production recently observed in proton-proton collisions at the LHC within the statistical hadronization model using a largely augmented set of "missing" charm-baryon resonances (compared to the listings of the particle data group), as predicted by lattice QCD and the relativistic quark model.

- Established tight constraints on the incompressibility coefficient, nucleon effective mass and the enhancement coefficient of the energy weighted sum rule of the isovector giant dipole resonance

by calculating the energies of wide ranges of giant resonances and nuclei with 33 energy density functionals.

- Found a possible new resonance in the middle of the Gamow window for ^{34g,m}Cl(p,γ)^{35}Ar with the AstroBox2 detector through the beta-delayed proton decay of ^{35}K.

- Measured Coulomb dissociation and nuclear breakup of ^{9}C → ^{8}B+p and ^{9}C → ^{7}Be+2p at RIKEN to study the rate of the ^{7}Be+p → ^{8}B+p → ^{9}C reaction chain as a possible bypass of the 3α process in stellar environments. This was the commissioning experiment of the SAMURAI Si-tracker built and instrumented in collaboration with TAMU, WUSTL, and LSU.

- Measured nuclear breakup of ^{66}Se → ^{65}As+p and ^{66}Se → ^{64}Ge+2p at RIKEN to study the destruction of the waiting point nucleus ^{64}Ge in X-ray burst environments.

- Commissioned the TIARA for Texas detector system and measured four transfer reactions of astrophysical interest using the device.

- Measured the n/γ branching ratio for the $E_{c.m.}$ = 705 keV resonance in ^{22}Ne(α,n)^{25}Mg and established partial α width for the four resonances in ^{26}Mg within Gamow window for the ^{22}Ne(α,n) and ^{22}Ne(α,γ) reactions. As a result of these two experiments, the stellar s-process rate for ^{22}Ne(α,n) is reduced by a factor of ~3 for temperatures above 0.3 GK.

- Commissioned the TAMUTRAP facility by measuring the masses of ^{23}Na, ^{85,87}Rb and ^{133}Cs to better than 50 ppb.

- Commissioned TexAT and studied structure of ^{9}C ^{8}B+p resonance elastic scattering. The s-wave p+8B interaction strength was established, providing the location of the 2s1/2 shell in this A=9 T=3/2 nuclear system.

- Populated cluster states in ^{14}O and ^{18}Ne via ^{10}C + α, ^{14}O + α.

- Performed direct measurement of ^{8}B + ^{40}Ar fusion reaction.

- Measured β-delayed charged particle emission targeting the decay of the Hoyle state.

- A strong heavy-quark potential in the quark-gluon plasma has been extracted in a statistical analysis of bottomonium production in heavy-ion collisions at RHIC and the LHC utilizing our previously developed quarkonium transport approach. Substantial remnants of the confining force are found to persist, playing a critical in understanding the strongly coupled properties of the QGP.

- Identified alpha condensate states that could be analogous to Hoyle state in heavier nuclei.

- The redistribution of axial charges in the transverse plane of non-central heavy ion collisions due to produced vorticity field is shown in the chiral kinetic approach to result in an azimuthal angle dependence of the quark and antiquark longitudinal polarization along the beam direction that is similar to that of Lambda hyperons observed in experiments by the STAR Collaboration at the Relativistic Heavy Ion Collider.

- Production of deuteron and helium-3 via the coalescence of nucleons, which includes the effect of their internal structure, is found to provide a natural explanation for the observed suppression of their production in p+p collisions by the ALICE Collaboration at the LHC.

Institute scientists remain active in a number of collaborative research efforts around the world. Major programs include: measurements of beta decays with the TRINAT collaboration at TRIUMF; nuclear structure measurements with TexAT at TRIUMF; continued work with the STAR collaboration at RHIC; fusion studies at MSU; and participation in the SAMURAI collaboration at RIBF in Tokyo, Japan.

I am indebted to Dr. Y.-W. Lui for assembling this report.

S.J. Yennello
July 1, 2019

SECTION I

NUCLEAR STRUCTURE, FUNDAMENTAL INTERACTIONS AND ASTROPHYSICS

Superallowed beta decay

J.C. Hardy, V.E. Iacob, H.I. Park, N. Nica, M. Bencomo, T. Eronen, V. Horvat, L. Chen, and I.S. Towner

Superallowed $0^+ \rightarrow 0^+$ beta decay between T=1 analogue states has been a subject of continuous and often intense study for five decades. The *ft* values of such transitions are nearly independent of nuclear-structure ambiguities and depend uniquely on the vector part of the weak interaction. Their measurement gives us access to clean tests of some of the fundamental precepts of weak-interaction theory, and, over the years, this strong motivation has led to very high precision being achieved both in the experiments and in the theory used to interpret them. We have had a major program at the Cyclotron Institute to study superallowed beta decay.

To obtain the *ft* value for any transition, three quantities must be measured: the half-life $t_{1/2}$ of the parent, the Q_{EC} value for the transition of interest, and the branching ratio R for that transition. Our most recent complete survey of world data on these superallowed decays, published in 2015 [1], provides a critical evaluation of all the experimental data and obtains final *ft* values from the averaged results. Radiative and isospin-symmetry-breaking corrections were then applied in order to derive a final set of "corrected ft values", denoted $\mathcal{F}t$, for 14 transitions known to ~0.1% precision. Fig. 1 shows the results from our 2018 update of the survey, which has now been increased to 15 transitions through inclusion of our new precise measurement of the superallowed transition from ^{26}Si [2]. Excellent consistency among the average $\mathcal{F}t$ values for all 15 transitions – an expected consequence of the conservation of vector current (CVC) – confirms the validity of the correction terms; and our recent measurements focusing on pairs of mirror superallowed transitions with A = 26, 34 and 38 further supports that validity [2-4].

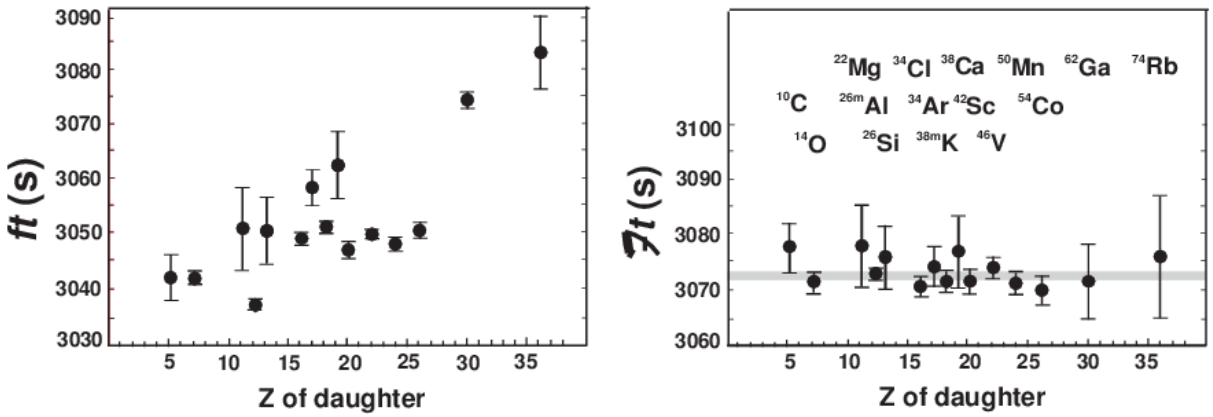

FIG. 1. Results from the 2015 survey [1] updated to 2018: The uncorrected *ft* values for the 15 best known superallowed decays appear on the left; the same results but incorporating the radiative and isospin-symmetry-breaking correction terms are on the right. The grey band in the right panel is the average $\mathcal{F}t$ value and its uncertainty.

The resultant average $\mathcal{F}t$ value, when combined with the muon lifetime, yields the up-down quark-mixing element of the Cabibbo-Kobayashi-Maskawa (CKM) matrix, V_{ud} = 0.97420(21), a result that is consistent with, but more precise than, values we have obtained in previous analyses of

superallowed β decay. The unitarity test on the top row of the matrix becomes $|V_{ud}|^2 + |V_{us}|^2 + |V_{ub}|^2 = 0.99939\ (47)$ if the Particle Data Group recommended value for V_{us} is used. Finally, from the $\mathcal{Ft}$ -value data we also set a limit on the possible existence of a scalar interaction.

Although recent adjustments to the value of V_{us} have driven the top-row sum slightly more than a standard deviation below unity, it can still be viewed as a significant verification of the standard model, and the quoted uncertainty used to provide tight limits on any possible new physics beyond the standard model, such as right-hand currents, extra *Z* bosons or supersymmetric models. In short, superallowed $0^+ \rightarrow 0^+$ beta decay provides a high-profile application of nuclear-physics measurements to the study of fundamental symmetries, a subject of vital interest to both nuclear and particle physicists. Although much has already been achieved in this field by nuclear physicists, improvements are still possible. Reducing the uncertainty on the unitarity sum – and, with it, the scope for new physics – has been the primary goal of our research program.

Our approach follows from the observation [1] that the second largest contributor to the uncertainty in V_{ud} is the theoretical uncertainty in the nuclear-structure-dependent corrections, δ_{NS} and δ_C, used in the derivation of the $\mathcal{Ft}$ values. Though these corrections are only of order 1%, their effect is very significant: The two panels of Fig. 1 show the result of applying the nuclear-structure-dependent corrections, δ_{NS} and δ_C (together with δ'_R, which is nearly independent of *Z*). Obviously they act very well to remove the considerable "scatter" in *ft* values apparent in the panel on the left, replacing it with the consistent set of corrected $\mathcal{Ft}$ values appearing on the right. Since these corrections were determined [5] completely independently of the superallowed decay data, this consistency in $\mathcal{Ft}$ values is already a powerful validation of the calculations, but obviously the remaining uncertainty still influences the final result for V_{ud}.

Even though the 2015 survey [1] included more than 222 individual measurements (and the 2018 update includes over a dozen more) relating now to 15 precisely known *ft* values, it is still possible for well selected experiments to make real improvements in the validation tests of the nuclear-structure-dependent correction terms. At TAMU we have been focusing on adding to the *ft*-value list new superallowed transitions, selected from amongst those with *large* calculated corrections. If the *ft* values measured for cases with large calculated corrections also turn into corrected $\mathcal{Ft}$ values that are consistent with the others, then this must verify the calculations' reliability for the existing cases, which have smaller corrections. We study decays from T_z = -1 parent nuclei, which consistently have higher predicted structure-dependent correction terms than the well-known T_z = 0 cases.

Of particular importance are the four T_z = -1 parent nuclei – ^{26}Si, ^{34}Ar, ^{38}Ca and ^{42}Ti – whose decays are mirrors to well-known superallowed decays from T_z = 0 parents. Specifically, the mirror-decay pairs are $^{26}\text{Si} \rightarrow ^{26m}\text{Al} \rightarrow ^{26}\text{Mg}$, $^{34}\text{Ar} \rightarrow ^{34}\text{Cl} \rightarrow ^{34}\text{S}$, $^{38}\text{Ca} \rightarrow ^{38m}\text{K} \rightarrow ^{38}\text{Ar}$ and $^{42}\text{Ti} \rightarrow ^{42}\text{Sc} \rightarrow ^{42}\text{Ca}$. Their importance stems from our observation that the ratio of mirror *ft* values for such cases is very sensitive to the model used to calculate the small isospin-symmetry-breaking corrections δ_{NS} and δ_C. The details have been described in our report on the first measurement of a mirror pair, with *A* = 38 [3].

What made decay measurements on these T_z = -1 parent nuclei possible was that, after a long period of incremental upgrades to our experimental techniques, we succeeded in pushing our precision in

branching ratio measurements close to ±0.1. This is crucial for the characterization of T_z = -1 parent decays, which – unlike T_Z = 0 decays – exhibit a number of strong Gamow-Teller branches that compete with the superallowed Fermi branch. A first demonstration of our success in this endeavor was our measurement of the superallowed branching ratio for the decay of ^{38}Ca ($t_{1/2}$ = 444 ms) to a precision of ±0.21%, where that precision was actually limited by counting statistics, not systematics [3,4]. Our next precise branching ratio [2] for a T_z = -1 parent nucleus was for ^{26}Si ($t_{1/2}$ = 2.245s), which achieved a precision of ±0.18%, also limited by statistics. To our knowledge, these are the most precise direct branching-ratio measurements ever made for short-lived beta emitters.

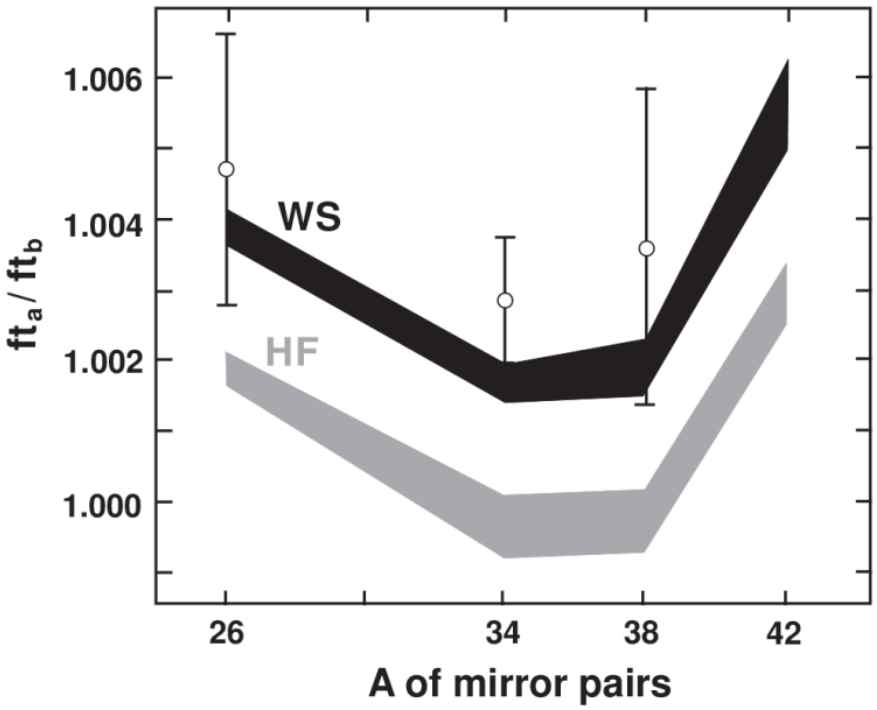

FIG. 2. Mirror-pair ft_a/ft_b values for A = 26, 34, 38 and 42. The black and grey bands connect calculated results that utilize Woods-Saxon (WS) and Hartree-Fock (HF) radial wave functions, respectively. The measured results for A = 26, 34 and 38 appear as open circles with error bars. The A = 34 result is preliminary.

The current status of the mirror-pair measurements is shown in Fig. 2, which also includes our preliminary result for ^{34}Ar. The measured ratios clearly distinguish between the Saxon-Woods-based radial-overlap corrections incorporated in δ_C, and the ones based on Hartree-Fock radial wave functions. All three favor the former over the latter.

We have already completed measurements of the half-life [6] and branching ratio for the superallowed decay of ^{34}Ar. However, the branching-ratio result depends critically on the gamma-branching of the 666-keV level populated by beta decay in the daughter, ^{34}Cl, which decays primarily with a 666-keV γ ray but also weakly with a 519-keV γ ray; the latter is masked in our γ-ray spectrum by the tail of the strong 511-keV annihilation peak. Before publishing our ^{34}Ar results, we have to establish

the relative intensity of these two gamma rays. To do so, we have made a ^{33}S (p, γ) ^{34}Cl measurement at Notre Dame University [7]. The analysis is not complete but a preliminary result was used to arrive at the ratio result shown in Fig. 2.

Finally, for ^{42}Ti decay we have completed a successful measurement of its half-life, as well as a test measurement of its branching ratio. A final branching-ratio measurement will occur in 2019.

With a somewhat different focus, in late 2015 we began a new measurement of the branching ratio for the superallowed decay of ^{10}C. Currently the uncertainty on the branching ratio dominates the uncertainty in the ^{10}C $\mathcal{F}t$ value. However, more interesting than just the precision of the $\mathcal{F}t$ value itself is its relationship to the world average of $\mathcal{F}t$ values for transitions in heavier nuclei, since the ^{10}C transition is the most sensitive to the possible presence of a scalar current. Currently the $\mathcal{F}t$ value for ^{10}C is slightly higher than the world average $\mathcal{F}t$ value, with an error bar that just about touches the world average value's error bar. If a more precise $\mathcal{F}t$ value of ^{10}C were found to deviate with greater statistical significance, it would be a signal for the existence of a scalar current. This work is still in progress.

Note that J.C. Hardy, the Principal Investigator for this research program, officially retired at the end of August 2018. He is nevertheless committed to completing the experiments described in this report, but will undertake no new initiatives.

[1] J.C. Hardy and I.S. Towner, Phys. Rev. C **91**, 025501 (2015).

[2] M. Bencomo, J.C. Hardy, V.E. Iacob, H.I. Park, L. Chen, V. Horvat, B.T. Roeder, A. Saastamoinen, and I.S. Towner, submitted to Phys. Rev. C.

[3] H.I. Park, J.C. Hardy, V.E. Iacob, M. Bencomo, L. Chan, V. Horvat, N. Nica, B.T. Roeder, E. Simmons, R.E. Tribble, and I.S. Towner, Phys. Rev. Lett. **112**, 102502 (2014).

[4] H.I. Park, J.C. Hardy, V.E. Iacob, M. Bencomo, L. Chen, V. Horvat, N. Nica, B.T. Roeder, E. McCleskey, R.E. Tribble, and I.S. Towner, Phys. Rev. C **92**, 015502 (2015).

[5] I.S. Towner and J.C. Hardy, Phys. Rev. C **77**, 025501 (2008).

[6] V.E. Iacob *et al*., *Progress in Research,* Cyclotron Institute, Texas A&M University (2018-2019), p. I-5.

[7] H.I. Park *et al*., *Progress in Research,* Cyclotron Institute, Texas A&M University (2018-2019), p. I-8.

^{34}Ar half-life

V.E. Iacob, J.C. Hardy, M. Bencomo, L. Chen, V. Horvat, N. Nica, H.I Park,
B.T. Roeder, and A. Saastamoinen

We report here a fine-tuned fit of the half-life of ^{34}Ar, based on significant improvements in both data acquisition and fit method since our first measurement of this half-life in 2004 [1]. The experiment itself is described in [2].

The data were acquired in cycles: We turned the beam on, and for 0.7 s implanted ^{34}Ar nuclei in the 76.2 μm-thick mylar tape of our fast tape transport system; then the beam was turned off, and the collected activity was moved rapidly into the center of a 4π proportional counter, which then recorded the emitted positrons for 16.2 s. Cycles were repeated until the desired statistics had been accumulated. The detected events triggered a discriminator, whose signals were passed to two gate generators, which each introduced a different dominant non-updating dead time. The signals from these two gate generators were then passed to two multi-scalers. To allow us to test for the presence of undesired biases in our results, the experiment was subdivided into individual runs, each with a different set of three critical detection parameters: detector bias, discrimination threshold, and dominant dead times.

Each cycle was separately analyzed and accepted only if:

(1) the implantation beam provided more than 5000 ^{34}Ar nuclei;

(2) the ratio of detected positrons to implanted nuclei was at least 95% of the maximum (expected) value; and

(3) a preliminary fit to the decay for that cycle yielded a χ^2 that was below the value corresponding to a probability of less than 10^{-4} for the occurrence of higher values.

The first condition eliminates cycles with anomalously low beam current; the second condition

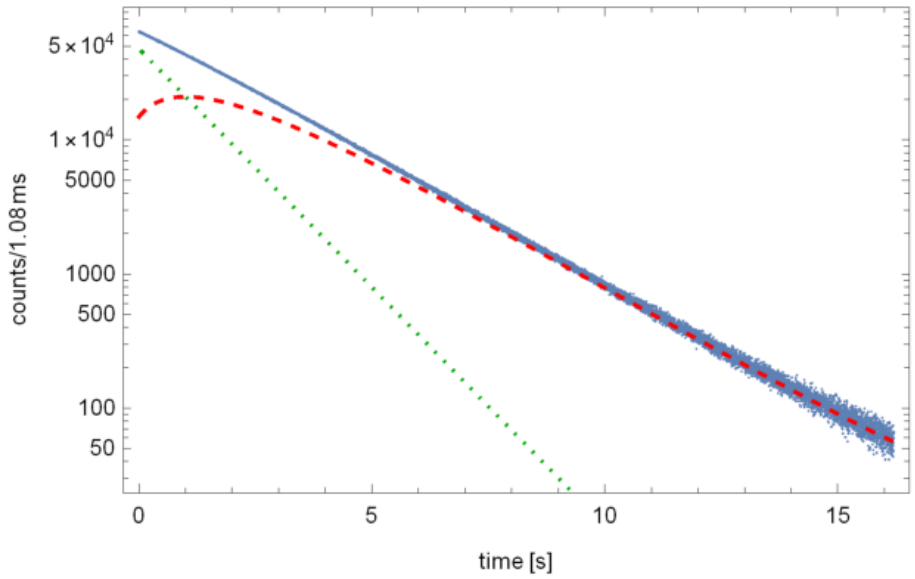

FIG. 1. Total decay spectrum recorded in our measurement. The combined ^{34}Ar and ^{34}Cl decays were recorded in 15,000 channels, each 1.08 ms wide. The total measured spectrum (blue) is shown, along with dotted lines giving the separate contributions calculated for the parent ^{34}Ar (green) and daughter ^{34}Cl (red).

eliminates those with poor positioning of the activity inside the detector; and the third removes any cycles that experienced electrical interference in the detector. The total decay spectrum derived from the cycles that passed these criteria is presented in Fig. 1.

As observed in Fig. 1, the decay of ^{34}Ar is obscured by the decay of its daughter. As the proportional counter cannot disentangle ^{34}Ar decays from ^{34}Cl decays, we use the parent-daughter link dictated by the decay to overcome this difficulty. This is possible because we implant no ^{34}Cl in the collected samples.

The subdivision of the experiment into runs with different experimental parameters, allowed us to test the data for the presence of possible systematic effects from those parameters. Fig. 2 presents the distribution of the fit results as obtained in one of the multichannel scalers (MCS-A): all points represent fit results in a Poisson maximum-likelihood procedure, using the parent-daughter link in the decay.

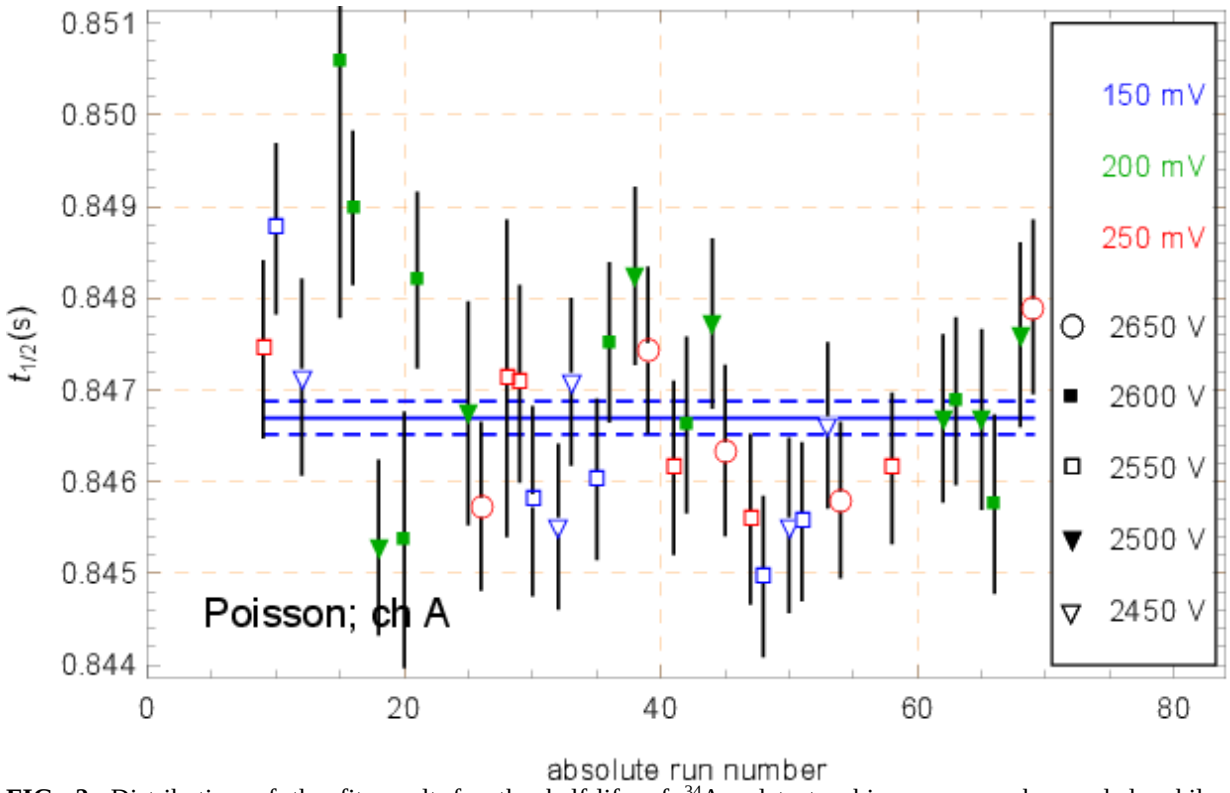

FIG. 2. Distribution of the fit result for the half-life of ^{34}Ar: detector biases are marker coded, while discrimination thresholds are color coded.

The two multichannel scalers collected data from the same detected events but processed them with different imposed dominant dead-times. Thus, a parallel fit of the runs that used different multi-scalar channels offered another check for the consistency of the results and, in particular, the efficacy of our dead-time corrections. No difference between the results associated with different dead-times was observed.

To further check for possibly inconsistent dead-time corrections or for the presence of an unexpected short-lived impurity, we successively removed channels starting from time-zero and repeated

the fit. Fig. 3 presents the fit-stability against front-channel chopping, covering a time interval of three half-lives. No hint of any inconsistency can be identified.

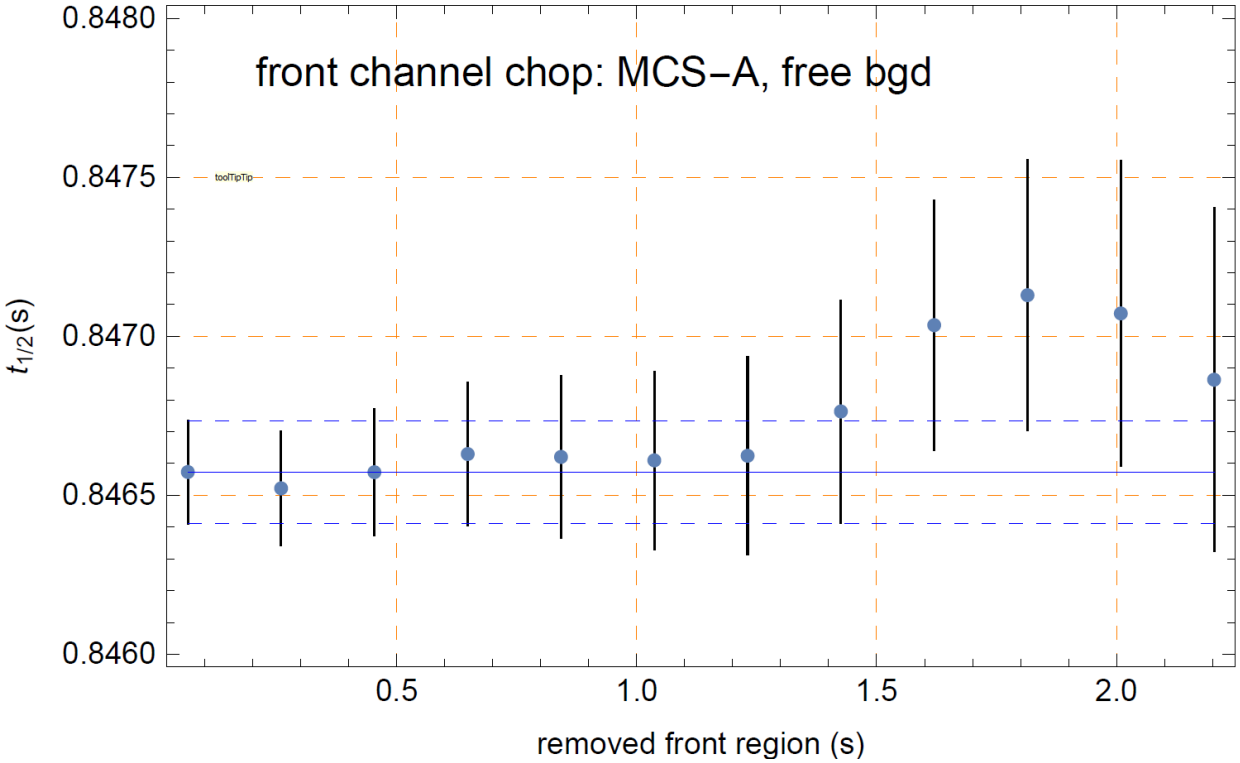

FIG. 3. Fit stability against removal of channels from the front part of the spectrum. This clearly demonstrates the absence of any short-lived contaminants or inconsistent dead-time corrections.

Finally, as mentioned in [2] and [3], the decay of ^{34}Ar is now known to very weakly populate the 32-min isomeric level in ^{34}Cl. This reduces the number of expected daughter decays that are observed during the 16.2 s detect-time, thus modifying the parent-daughter link. A measurement to determine the strength of this "leak" from the parent-daughter link is currently being analyzed [3]. Once this last ingredient is in place, we will complete the full analysis of ^{34}Ar decay.

[1] V.E. Iacob *et al.*, Phys. Rev. C **74**, 055502 (2006).

[2] V.E. Iacob, *et al.*, *Progress in Research*, Cyclotron Institute, Texas A&M University (2015-2016), p. I-14.

[3] H.I. *Park et al.*, *Progress in Research*, Cyclotron Institute, Texas A&M University (2018-2019), p. I-8.

The $^{33}S(p, \gamma)^{34}Cl$ experiment

H.I. Park,[1] J.C. Hardy,[1] M Bencomo,[1] W. Tan,[2] K. Macon,[2] and M. Brodeur[2]
[1]*Cyclotron Institute, Texas A&M University, College Station, Texas 77843*
[2]*Department of Physics, University of Notre Dame, Notre Dame, Indiana 46556*

In the late summer of 2018 we conducted a $^{33}S(p, \gamma)^{34}Cl$ experiment at the University of Notre Dame to investigate the effect that weak γ-ray transitions potentially have on the superallowed β decay of ^{34}Ar, the parent nucleus of ^{34}Cl. Our focus was on a determination of the gamma-branching of the 666-keV level populated in ^{34}Cl. A possible weak 519-keV γ-ray from this level can affect the ^{34}Ar superallowed branching-ratio result, for which we seek 0.1 % precision in order to obtain an *ft* value that can contribute meaningfully to the determination of V_{ud}, the up-down quark-mixing element of the Cabibbo-Kobayashi-Maskawa matrix.

For our two-week measurement we used the Notre Dame Sta. ANA, 5-MV single-ended electrostatic accelerator to produce a proton beam with an energy-spread of less than 1 keV. The accelerated beam was sent through a 90-degree dipole magnet to the 5U solid-target line, where a ^{33}S target was installed at the center of the compact germanium-detector array GEORGINA, which consists of 5 detectors, each with a relative γ-ray efficiency of 100%. The proton beam energy was chosen to be 1072 keV based on resonance-energy scans that determined which one resulted in maximum population of the 666-keV state in ^{34}Cl. During the experiment, the beam current varied between 6.0 and 10.0 μA.

We energy-calibrated the detectors with ^{7}Be, ^{60}Co, ^{137}Cs, ^{133}Ba, and ^{152}Eu sources before and after the $^{33}S(p, \gamma)^{34}Cl$ experiment. These sources provided us with twenty well-known γ-ray peaks covering the energy range from 120 keV to 1400 keV, and therefore our energy calibration for all five Ge detectors could be well established in the region of our interest between 500 keV and 700 keV. The efficiency calibration was done for each individual Ge detector with the ^{60}Co, ^{137}Cs, and ^{152}Eu sources. On the one hand, the ^{60}Co and ^{137}Cs sources have simple decay schemes that permit clean determination of the detectors' efficiencies. The complexity of the decay scheme for ^{152}Eu (to ^{152}Sm by electron capture and to ^{152}Gd via positron emission), on the other hand, led us to use only the 122-keV, 344-keV, 779-keV, and 1112-keV γ-rays and their respective sum peaks at 1234 keV (122+1112) and 1123-keV (344+779) to anchor our efficiency calibration. We have now obtained a well-defined efficiency curve to determine the ratio of the 519-keV to 666-keV γ-ray.

Currently we are developing an analysis program for the very big data set we recorded. It is written in the framework of the ROOT [1]. The results from this measurement will allow us to complete the precise analysis of the superallowed branching ratio for ^{34}Ar.

[1] R. Brun and F. Rademakers, Nucl. Instrum. Methods Phys. Res. **A389**, 81 (1997); http://-root.cern.ch/).

Tests of internal-conversion theory

J.C. Hardy, N. Nica, V. Horvat, V.E. Iacob, and M.B. Trzhaskovskaya[1]
[1]*Petersburg Nuclear Physics Institute, Gatchina RU-188300, Russia*

Except for the very lightest nuclei, where internal conversion is weakest, most nuclear decay schemes depend upon calculated internal conversion coefficients (ICCs). Electromagnetic decay intensities are usually determined from gamma-ray measurements combined with calculated ICCs. Consequently, the reliability of the calculations is a matter of some importance, especially where precise decay-scheme data are required, for example in detector calibration. Until quite recently, although various tables of calculated ICCs were readily available, most ICC measurements were relatively imprecise, being aimed only at determining transition multi-polarities. Rarely were they precise enough to distinguish among different calculations or indeed to establish if any of the calculations reproduced reality. We are rectifying this deficiency.

When we began our program of precise measurements in 2004, the then-current survey of world data [1] included barely twenty ICC values measured to ±2% or better, and eighty more with up to 5% precision. They were divided 45-55 between *K*-shell ICCs (α_K) and total ICCs (α_T), respectively. Based on these data, the authors concluded that all previous tables of ICCs exhibited a 3% systematic bias, but that a table by Band *et al.* [2], which was new at the time, agreed well with the data (within ~1%). This new table was calculated in the framework of the Dirac-Fock method, with the exchange between bound electrons as well as between bound and free electrons treated exactly, an important improvement. Unfortunately, however, the best agreement with the available experimental data was achieved with a version of this calculation in which the final-state electron wave-function was computed in a field that did not include any provision for the atomic vacancy created by the conversion process. Yet the vacancy must be there, since atomic-shell-vacancy lifetimes are known generally to be much longer than the time for a conversion electron to leave the vicinity of the atom. This was an unsatisfactory paradox!

We found ourselves uniquely positioned to potentially resolve the paradox. For our program to measure branching ratios for superallowed β emitters, we had efficiency calibrated an HPGe detector to high precision over a wide range of energies. This would allow us to measure the *K* x rays and γ rays from a converted transition in the same well-calibrated detector, thus affording access to the transition's α_K value with a minimum of systematic uncertainty. For an isolated electromagnetic transition that converts in the atomic *K* shell, the observation of a *K* x ray is a signal that an electron conversion has taken place; whereas a γ ray indicates that no conversion has taken place. If both x rays and γ rays are recorded in a measurement, then the value of α_K is given by

$$\alpha_K \omega_K = \frac{N_K}{N_\gamma} \cdot \frac{\varepsilon_\gamma}{\varepsilon_K}, \qquad (1)$$

where ω_K is the *K*-shell fluorescence yield; N_K and N_γ are the respective peak areas of the *K* x rays and the γ ray; and ε_K and ε_γ are the respective detector photopeak efficiencies.

Not many nuclei feature a single isolated transition, but a number of cases have small enough interference from other converted transitions that the corrections to Eq. (1) are manageable, allowing the α_K value still to be extracted with percent precision. Since we began this program, we have published α_K values for *E*3 transitions in three nuclei, ^{103}Rh [3] ^{111}Cd [4] and ^{134}Cs [5,6], and *M*4 transitions in six nuclei, ^{119}Sn [7,8], ^{125}Te [9], ^{127}Te [10], ^{137}Ba [5,6], ^{193}Ir [11,12] and ^{197}Pt [13]. We are currently completing a measurement on an *M*4 transition, in ^{93}Nb [14].

The results from our completed measurements appear in Fig. 1, which is an updated version of a figure that first appeared in Ref. [15]. In the figure, the results are compared with two theoretical

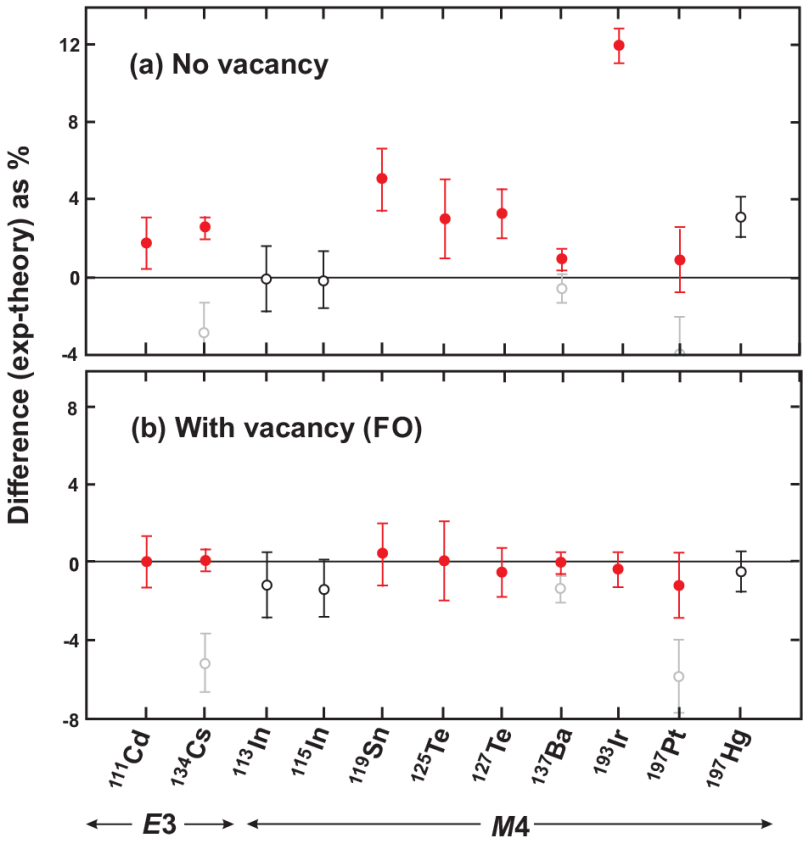

FIG. 1. Percentage differences between the measured and calculated α_K values for the Dirac-Fock calculations with and without provision for the atomic vacancy. Solid (red) circles are our measurements; open circles refer to pre-2002 results, the ones in gray having been replaced. The figure shows all α_K values for high-multiplicity transitions (E3 and above) that are known to ±2% or better.

models, one that ignores the atomic vacancy and one that includes it in the "frozen orbital" (FO) approximation. It is clearly evident that the data are completely inconsistent with the no-vacancy theory and are in remarkable agreement with the vacancy-inclusive theory. This is consistent with the known vacancy lifetimes, and resolves the earlier paradox.

A few of the cases we measured were chosen not because they were particularly sensitive to the vacancy/no-vacancy choice in the calculations, but because previous results disagreed with *both* types of calculation. These discrepancies have been removed as well. Note though that among the twelve

precisely measured α_K values in Fig. 1, there are nine that statistically distinguish between the vacancy and no-vacancy calculations, and they all present a consistent picture that favors inclusion of the atomic vacancy in ICC calculations. All but one of these cases come from our work.

Note that J.C. Hardy, the Principal Investigator for this research program, officially retired at the end of August 2018. He is nevertheless committed to completing the ^{93}Nb measurement mentioned in this report, but will undertake no new initiatives.

[1] S. Raman, C.W. Nestor Jr., A. Ichihara, and M.B. Trzhaskovskaya, Phys. Rev. C**66**, 044312 (2002).

[2] I.M. Band, M.B. Trzhaskovskaya, C.W. Nestor Jr., P. Tikkanen, and S. Raman, At. Data Nucl. Data Tables **81**, 1 (2002).

[3] N. Nica, J.C. Hardy, V.E. Iacob, V. Horvat, H.I. Park, T.A. Werke, K.J. Glennon, C.M. Folden III, V.I. Sabla, J.B. Bryant, and X.K. James, Phys. Rev. C **98**, 054321 (2018); N. Nica *et al*., *Progress in Research*, Cyclotron Institute Texas A&M University (2018-2019) p. I-12.

[4] N. Nica, J.C. Hardy, V.E. Iacob, T.A. Werke, C.M. Folden III, L. Pineda, and M. B. Trzhaskovskaya, Phys. Rev. C**93**, 034305 (2016).

[5] N. Nica, J.C. Hardy, V.E. Iacob, W.E. Rockwell, and M.B. Trzhaskovskaya, Phys. Rev. C**75**, 024308 (2007).

[6] N. Nica, J.C. Hardy, V.E. Iacob, C. Balonek, and M.B. Trzhaskovskaya, Phys. Rev. C**77**, 034306 (2008).

[7] N. Nica, J.C. Hardy, V.E. Iacob, M. Bencomo, V. Horvat, H.I. Park, M. Maguire, S. Miller and M.B. Trzhaskovskaya, Phys. Rev. C**89**, 014303 (2014).

[8] J.C. Hardy, N. Nica, V.E. Iacob, S. Miller, M. Maguire and M.B. Trzhaskovskaya, Appl. Rad and Isot. **87**, 87 (2014).

[9] N. Nica, J.C. Hardy, V.E. Iacob, T.A. Werke, C.M. Folden III, K. Ofodile, and M.B. Trzhaskovskaya, Phys. Rev. C **95**, 064301 (2017).

[10] N. Nica, J.C. Hardy, V.E. Iacob, H.I. Park, K. Brandenburg, and M.B. Trzhaskovskaya, Phys. Rev. C**95**, 034325 (2017); and *Progress in Research*, Cyclotron Institute Texas A&M University (2016-2017) p. I-28.

[11] N. Nica, J.C. Hardy, V.E. Iacob, S. Raman, C.W. Nestor Jr., and M.B. Trzhaskovskaya, Phys. Rev. C**70**, 054305 (2004).

[12] N. Nica, J. C. Hardy, V. E. Iacob, J. R. Montague, and M. B. Trzhaskovskaya, Phys. Rev. C**71**, 054320 (2005).

[13] N. Nica, J.C. Hardy, V.E. Iacob, J. Goodwin, C. Balonek, M. Hernberg, J. Nolan, and M.B. Trzhaskovskaya, Phys. Rev. C**80**, 064314 (2009).

[14] V. Horvat *et al.*, *Progress in Research*, Cyclotron Institute Texas A&M University (2018-2019) p. I-15.

[15] J.C. Hardy, N. Nica, V.E. Iacob, and M.B. Tezhaskovskaya, Appl. Rad. Isot. **134**, 406 (2018).

Precise measurement of α_K and α_T for the 39.8-keV *E*3 transition in ^{103}Rh: Test of internal-conversion theory

N. Nica, J.C. Hardy, V.E. Iacob, V. Horvat, H.I. Park, T.A. Werke, K.J. Glennon, C.M. Folden III, V.I. Sabla, J.B. Bryant, and X.K. James

For more than a decade, we have been testing internal-conversion theory through precise measurements of K-shell internal-conversion coefficients, α_K, for high-multipolarity transitions [1]. Our most recent measurement – the ninth – is of a 39.8-keV *E*3 transition, which de-excites the isomeric first-excited state in ^{103}Rh. Rhodium is the lowest-Z nucleus we have investigated so far.

As illustrated in Fig. 1, the isomeric $7/2^+$ state can be produced both in the β^- decay of ^{103}Ru and in the electron-capture decay of ^{103}Pd. Using sources neutron-activated at the Texas A&M TRIGA reactor, we have studied both decays.

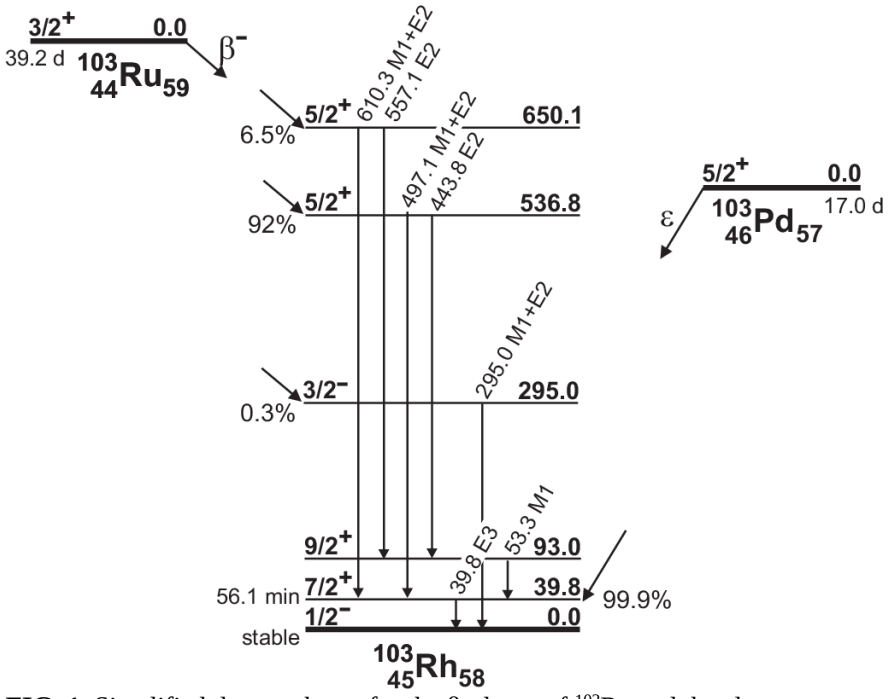

FIG. 1. Simplified decay scheme for the β- decay of ^{103}Ru and the electron-capture decay of ^{103}Pd feeding excited states in their common daughter, ^{103}Rh.

In simple cases with a single transition that can convert in the *K* shell the value of α_K is given by

$$\alpha_K = \frac{N_K}{N_\gamma} \times \frac{\varepsilon_\gamma}{\varepsilon_K} \times \frac{1}{\omega_K}, \qquad (1)$$

where ω_K is the fluorescence yield, N_K and N_γ are the total number of observed *K* x rays and γ rays, respectively; and ε_γ and ε_K are the corresponding photopeak detection efficiencies. If the 39.8-keV level is produced by the ^{103}Ru-decay route, then the decay effectively satisfies the conditions for Eq. (1), with only small corrections needed to account for conversion by the other transitions produced.

The three transitions feeding the 39.8-keV level in the decay of ^{103}Ru also yield a benefit. Because the level is not fed by β decay, the total intensity of the electromagnetic transitions populating the state must equal the total intensity of the transition depopulating it. Thus we can determine the total ICC, α_T, for the 39.8-keV level via the equation,

$$\sum_i (1 + a_{Ti}) \frac{N_{\gamma i}}{\varepsilon_{\gamma i}} = (1 + a_{T39.8}) \frac{N_{\gamma 39.8}}{\varepsilon_{\gamma 39.8}} \qquad (2)$$

where the sum is over all transitions that populate the 39.8-keV level.

The situation might seem to be simpler for the decay of ^{103}Pd since it populates the 39.8 keV state uniquely. There is a complication, however, because electron-capture decay gives rise to *K* x rays in similar numbers to the subsequent internal conversion. From this decay, we can establish a relationship between α_K and α_T as follows:

$$\alpha_K + (1 + \alpha_T) P_{ec,K} = \frac{N_K}{N_\gamma} \times \frac{\varepsilon_\gamma}{\varepsilon_K} \times \frac{1}{\omega_K} \qquad (3)$$

Where $P_{ec,k}$ is the probability per parent decay for electron capture out of the atomic *K* shell.

We recorded sequential ~12-hour decay spectra, later added together for each source. In total, ^{103}Ru decay was recorded for 41 days spread over 3 months; ^{103}Pd decay was recorded for 21 days spread over 2 months. Careful attention was paid to detector efficiency and to corrections for small impurities, attenuation in the sample, fluorescence and the Lorentzian x-ray peak shapes (see [2] for details).

From the combined ^{103}Ru and ^{103}Pd decay data we obtained α_K = 141.1(23) and α_T = 1428(13) for the 39.8-keV transition. In Table 1 these results are compared with Dirac-Fock calculations, with and without the *K*-shell vacancy, and with and without a small contribution from *M*4 into this predominantly *E*3 transition. Our results strongly disagree with the calculations that ignore the vacancy, which is consistent with the conclusion drawn from our series of measurements on high-multipolarity transitions in nuclei with higher *Z*. However, our results disagree with the vacancy-included results as well, albeit by a smaller amount. This latter disagreement disappears entirely if we assume a 0.04% *M*4 admixture (δ=0.02), which is allowed by the upper limit set in the only existing prior study of the mixing ratio [3].

Table I. Comparison of the measured α_K and α_T values for the 39.752(6)-keV *E*3 transition in ^{103}Rh with calculated values based on two different theoretical models, one that ignores the *K*-shell vacancy and one that deals with it in the "frozen orbital" approximation. Shown are the percentage deviations Δ from the experimental values calculated as (experiment-theory)/theory. Calculated values are given, both for a pure *E*3 transition and for an *E*3+*M*4 transition with a mixing ratio of ö=0.02.

Model	**α_K**	**Δ(%)**	**α_T**	**Δ(%)**
Experiment	141.1(23)		1428(13)	
Theory:				
(a) Pure *E*3				
No vacancy	127.5(1)	+10.7(18)	1388(2)	+2.9(9)
Vacancy, FO	135.3(1)	+4.3(17)	1404(1)	+1.7(9)
(b) *E*3+*M*4 δ=0.02				
No vacancy	131.3(1)	+7.5(18)	1410(2)	+1.3(9)
Vacancy, FO	139.4(1)	+1.2(17)	1426(2)	+0.1(9)

Finally, if we take the position that the need for the vacancy to be included in ICC calculations has already been proven by our previous eight measurements, then we can use these calculations to determine the mixing ratio that best fits the data for α_K and α_T. Doing so, we determine the mixing ratio for the 39.8-keV transition to be $\delta = 0.023(5)$. It appears that this is the first transition ever observed with mixed E3 + M4 character and a definitively non-zero mixing ratio.

[1] J.C. Hardy *et al*., Progress in Research, Cyclotron Institute Texas A&M University (2018-2019) p. I-9.

[2] N. Nica, J.C. Hardy, V.E. Iacob, V. Horvat, H.I. Park, T.A. Werke, K.J. Glennon, C.M. Folden III, V.I. Sabla, J.B. Bryant, and X.K. James, Phys. Rev. C **98**, 054321 (2018).

[3] H. Pettersson, S. Antman, and Y. Grunditz, Z. Phys. **233**, 260 (1970); **235**, 485(E) (1970).

K internal conversion of the ^{93m}Nb 30.8-keV gamma ray

V. Horvat, J.C. Hardy, N. Nica, V.E. Iacob, and E.E. Tereshatov

As part of our program to test internal-conversion theory [1], we are studying the M4 transition from the isomeric first-excited state at 30.8 keV in ^{93}Nb. In all previous measurements we have used our well-calibrated HPGe detector but that proved impossible in this case because of the low energy of the Nb *K* x rays (at 16.521 keV - 18.982 keV) , the extreme weakness of the 30.8-keV γ ray, and the fact that random summing of the *K* x rays led to peaks very close to the 30.8-keV γ ray. Instead we used a Si(Li) detector, which is well suited for measurements of the spectra, having better energy resolution and high intrinsic efficiency in the relevant energy range.

Because no other gamma rays are emitted in the decay of ^{93m}Nb, the measurement of the *K* internal conversion coefficient [ICC(*K*)] for the 30.8 keV gamma ray is very straightforward. We rely on the equation

$$\alpha_K = \frac{N_K}{N_\gamma} \cdot \frac{\varepsilon_\gamma}{\varepsilon_K} \cdot \frac{1}{\omega_K}, \qquad (1)$$

where ω_K is the *K*-shell fluorescence yield; N_K and N_γ are the respective peak areas of the *K* x rays and the γ ray; and ε_K and ε_γ are the respective detector photopeak efficiencies. For the Nb fluorescence yield, we use the recommended value of $\omega_K = 0.751(4)$ [2].

To measure ICC(*K*) for the 30.8 keV gamma ray of ^{93}Nb, it is necessary to (a) prepare a source of ^{93m}Nb, (b) use a Si(Li) detector to measure the photon spectrum containing the Nb *K* x rays and the ^{93m}Nb gamma ray, (c) determine the number of events in the corresponding peaks, and (d) determine the relative detection efficiency. Part (a) was described in a previous report [3].

Nb *K* x rays and ^{93m}Nb gamma rays were recorded using a Trump(TM) [4] data acquisition card, the accompanying Maestro(TM) software [5], and a personal computer. Signals from the Si(Li) detector's preamplifier were processed using a TC 249 amplifier [6]. The data acquisition rate was limited to about 50 events per second mainly by the emission rate of the source at hand and by our choosing the appropriate minimum source-to-detector distance taking account of the diameter of the source (19 mm) and the position of the 6 mm diameter Si(Li) crystal inside the detector can and behind a 6.7- mm-diameter Be window. The most serious challenge in the measurement came from the low detection rate of the 30.8-keV ^{93m}Nb γ rays (about 4 events per hour) and the comparably-sized background detection rate in the same vicinity. Consequently, to reduce the statistical uncertainty, the spectrum has to be accumulated over a time period of many months. The spectra are being saved, however, at least once daily.

During the measurements, the Pile-up Rejector (PUR) feature on the TC 249 was turned off. This was done in order to assess relative intensities of the peaks that arise from random summing of Nb *K* x rays. In the present measurements, at a resolution of about 340 eV FWHM, the peak caused by coincident detection of two Nb $K_{\alpha 1}$ x rays (at 2 x 16.615 keV) is clearly separated from the Nb γ-ray peak

at 30.8 keV. This was not the case when we first attempted the measurement with our HPGe detector, which required the two peaks to be unfolded from one another and led to a prohibitively large uncertainty in the extracted area of the 30.9-keV peak. This is what led us to the decision to use a Si(Li) detector instead.

The spectrum shown in Fig. 1 shows a subset of the data collected from the ^{93m}Nb source. The measurement is still in progress at the time this report is being written.

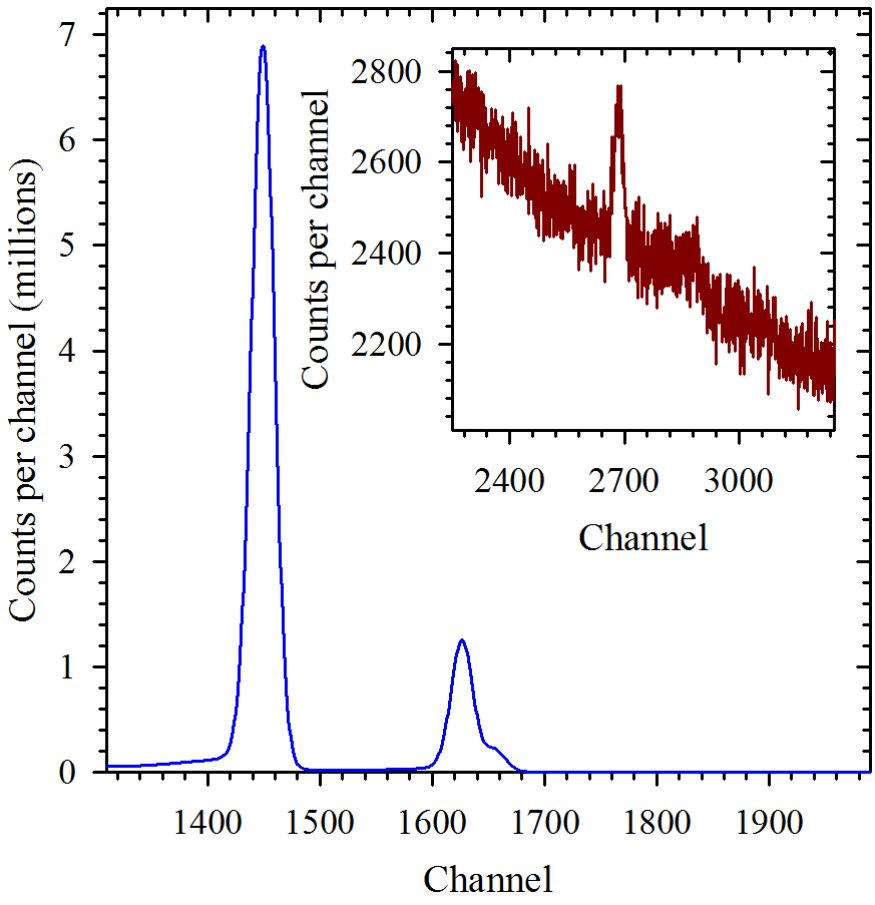

FIG. 1. A subset of the data collected from the ^{93m}Nb source. The blue line shows the spectrum of Nb K x rays, while the brown line in the insert shows a zoomed-in region of the same spectrum around the ^{93m}Nb gamma ray at 30.8 keV, along with the (barely visible) *K* x-ray sum peaks on its high-energy side.

We determined the numbers of events in the peaks of interest using software that we wrote and specifically customized for the present application. The software employs a fitting function that includes Gaussian peaks (integrated over channel limits) with exponential low-energy tails (convolved with the appropriate Gaussian function and integrated over channel limits), peak-specific low-energy-side background modeled as a second-degree polynomial multiplied by the complement of the step function having discontinuity at the centroid of the Gaussian component, all convolved with the appropriate Gaussian function. Here "the appropriate Gaussian function" means "the Gaussian function normalized to

unit area and having standard deviation equal to that of the Gaussian peak component". The overall background (present in the absence of the peaks) is modeled as an eight-order polynomial. Of course, any of the presented features can be limited or turned off, so that only the features that are necessary are used and only to the extent that is necessary. While fitting of the ^{93m}Nb γ-ray peak was straightforward, requiring only a single Gaussian component and a linear overall background, fitting of the *K* x-ray peaks proved to be much more challenging.

Photon energy dependence of the detector's absolute efficiency was established from CYLTRAN [7] Monte-Carlo calculations, which were based on the geometry of the setup (including the detector structure). To verify the results of the calculations, we measured the spectrum of Ag K x rays and the 88-keV γ rays from a ^{109}Cd standard source. A good match between the results of these measurements and the CYLTRAN calculations was obtained after a slight adjustment of the (otherwise not precisely known) geometric input parameters. It should be noted that all we need is the detection efficiency of the 30.8-keV γ rays *relative* to the Nb *K* x rays, which is much less sensitive to the geometric parameters in comparison with the *absolute* efficiency.

A preliminary result that we obtained for the ICC(*K*) of interest (based on less than half of the number of events now collected) is $\alpha_K = 26.2(15)\cdot10^3$. This result is in good agreement with ICC calculations that take account of the atomic vacancy (see Ref. [1]). Already our result agrees with one previous measurement, $\alpha_K = 25.8(15)\cdot10^3$ [8], and convincingly rules out the other, $\alpha_K = 17.0(30)\cdot10^3$ [9]. By the time the measurement is complete, we anticipate reducing our uncertainty by nearly a factor of two.

A considerable effort was made to determine the energy of the ^{93m}Nb gamma ray with competitive precision. We accomplished this by performing additional measurements using a source of ^{241}Am, analyzing selected peaks in the recorded spectrum, and establishing a reliable energy scale for the measured ^{93m}Nb spectrum. A preliminary result obtained with less than half of the events now collected is 30762.2(62) eV, for which the error bar is already better than that reported in the literature [10] by about a factor of 3.

[1] J.C. Hardy *et al*., *Progress in Research*, Cyclotron Institute Texas A&M University (2018-2019) p. I-9.

[2] E. Schönfeld and H. Janßen, Nucl. Instrum. Methods Phys. Res. **A369**, 527 (1996).

[3] E.E. Tereshatov, N. Nica, V. Horvat, J.C. Hardy, and C.M. Folden III, *Progress in Research*, Cyclotron Institute Texas A&M University (2017-2018) p. II-30.

[4] ORTEC, TRUMP, brochure:https://www2.ph.ed.ac.uk/~td/SHlab/Projects/EPR/trumppci.pdf,hard-ware manual: https://wiki.brown.edu/confluence/pages/viewpage.action?pageId= 1164129&-preview=%2F1164129%2F1164165%2FTRUMP+Hardware+Man.pdf

[5] ORTEC/AMETEK, MAESTRO, https://www.ortec-online.com/products/application-software/maes-tro-mca

[6] Oxford Instruments Inc., Nuclear Measurements Group (previously Tennelec / Nucleus Inc.), 601 Oak Ridge Turnpike Oak Ridge, TN 37830. Tel: 423-483-8405.

[7] J.A. Halbleib and T.A. Mehlhorn, Nucl. Sci. Eng. **92**, 338 (1986); J.A. Halbleib, R.P. Kensek, T.A. Mehlhorn, G.D. Valdez, S.M. Seltzer, and M.J. Berger, CYLTRAN 3.0, Sandia National Laboratory (Albuquerque, NM), Report SAND91-1634 (1992).
[8] M. Jurĉeviĉ, A. Ljubiĉiĉ, and D. Rendiĉ, Fizika, **8**, 81 (1976).
[9] J. Morel, J.-P. Perolat, and N. Coursol, C.R. Acad. Sc. Paris, t. **284**, Série B – 223 (1977).
[10] C.M. Baglin, Nucl. Data Sheets **112**, 1163 (2011).

United States Nuclear Structure Data Program (USNDP) and Evaluated Nuclear Structure Data File (ENSDF) at Texas A&M University ENSDF Data Evaluation Center

N. Nica and J.C. Hardy

Nuclear data evaluation fills a century-long chapter of nuclear science. A search in the *Nuclear Science Reference* (NSR) database maintained at the National Nuclear Data Center (https://www.nndc.bnl.gov/nsr/) on the author "M. Curie" produces a paper titled "*The Radioactive Constants as of 1930*" [1]. The introduction to this paper states that "*the need has arisen for the publication of special Tables of the Radioactive Constants*" and continues, "*This responsibility has been assumed by the International Radium Standards Commission chosen in Brussels in 1910 (...)*". Here we have the origin of what today is known as nuclear data evaluation.

Starting with the first generation of nuclear chemists and physicists, when measurements were already producing diverse and sometimes conflicting data, it became evident that assembling and reconciling the data from all across the published literature was a tedious and difficult task. Nevertheless, only after such a systematic analysis could the community arrive at recommended "practical standards," which could then be updated periodically to reflect the continuous improvements in knowledge and technology. Soon nuclear data evaluation became a specialized branch of research in its own right.

After the Second World War most of this activity was taken across the Atlantic and hosted by the United States Nuclear Structure Data Program (USNDP), which maintains the Evaluated Nuclear Structure Data File (ENSDF) database. While mostly undertaken by U.S. national laboratories, it has expanded to a relatively small number of university research labs, which has included the Texas A&M Cyclotron Institute since 2005. For more than a decade, the Texas A&M effort was financed by a contract with Brookhaven National Laboratory, but in 2017 it started to receive direct financing through the DOE Grant DE-FG03-93ER40773, "Cyclotron-based Nuclear Science"; and since May 2017 Texas A&M Cyclotron Institute has been recognized as an independent ENSDF Data Evaluation Center included within the Nuclear Structure and Decay Data international network.

Since 2005 N. Nica has completed and published the following full mass chain evaluations: the superheavy A=252 mass chain [2]; the very data-rich mid-mass chains, A=140 [3], A=141 [4], A=147 [5] and A=148 [6]; the relatively lighter chains, A=97 [7] and A=84 [8], the latter in a large international collaboration. In collaboration with B. Singh and a group of authors from McMaster University, Canada, he also published the A=77 [9], A=37 [10], A=36 [11], and A=34 [12] chains. At the beginning of 2016 another of his big mass chains, A=157, was published in Nuclear Data Sheets [13], followed by A=158 in 2017 [14], and by a new full evaluation of A=140 in 2018 [15]. Evaluation of the A=153 isobars was also completed and submitted to NNDC by Oct 1st, 2018; and a previously completed evaluation of A=160 was resubmitted after a number of pre-review editorial changes had been made.

Also after more than two years in the review process (due to the size of the evaluation and the lack of reviewers in ENSDF) Nica's A=155 evaluation was returned to him from the review process. He is now in the process of finally preparing it for publication. Another evaluation completed some time

ago, that of A=160, is still stuck in the queue waiting to be reviewed. Meanwhile, Nica himself has completed a review of the A=177 mass chain, which was prepared and submitted by another evaluator.

After the crisis created by the lack of ENSDF evaluators over the last decade, in the last couple of years it appears that the crisis has shifted to a lack of ENSDF reviewers. From now on, the most experienced evaluators are going to be required more and more to be involved in the review process, to replace the generation of older evaluators who have now retired.

After Oct 2018, N. Nica started a new full evaluation for the mass chain A=147, covering all publications since Nov 2008. The mass chain consists of the following isobars, in total, 16 nuclei: Xe, Cs, Ba, La, Ce, Pr, Nd, Pm, Sm, Eu, Gd, Tb, Dy, Ho, Er, and Tm. Bibliographical searches found that, since Nov 2008, 242 papers have been published relating to this mass chain, of which 195 are primary references (most important). In all, 96 are experimental. This work is in progress.

[1] M. Curie, A. Debierne, A.S. Eve, H. Geiger, O. Hahn, S.C. Lind, S. Meyer, E. Rutherford, and E. Schweidler, Rev. Mod. Phys. **3**, 427 (1931).
[2] N. Nica, Nucl. Data Sheets **106**, 813 (2005).
[3] N. Nica, Nucl. Data Sheets **108**, 1287 (2007).
[4] N. Nica, Nucl. Data Sheets **122**, 1 (2014).
[5] N. Nica, Nucl. Data Sheets **110**, 749 (2009).
[6] N. Nica, Nucl. Data Sheets **117**, 1 (2014).
[7] N. Nica, Nucl. Data Sheets **111**, 525 (2010).
[8] D. Abriola *et al.*, Nucl. Data Sheets **110**, 2815 (2009).
[9] B. Singh and N. Nica, Nucl. Data Sheets **113**, 1115 (2012).
[10] J. Cameron, J. Chen, B. Singh, and N. Nica, Nucl. Data Sheets **113**, 365 (2012).
[11] N. Nica, J. Cameron, and B. Singh, Nucl. Data Sheets **113**, 1 (2012).
[12] N. Nica and B. Singh, Nucl. Data Sheets **113**, 1563 (2012).
[13] N. Nica, Nucl.Data Sheets **132**, 1 (2016).
[14] N. Nica, Nucl.Data Sheets **142**, 1 (2017).
[15] N. Nica, Nucl.Data Sheets **154**, 1 (2018).

High precision half-life measurement of ^{29}P

P.D. Shidling, J.C. Hardy, V.E. Iacob, V. Kolhinen, D. McClain, D. Melconian, N. Morgan, A. Ozmetin, H.I. Park, B.T. Roeder, and B. Schroeder

Precision measurements of the correlation parameters and *ft* values of β-decaying nuclei continue to improve our understanding of the fundamental symmetries of the weak interaction and allow to test predictions of the standard model. One way to probe the standard model is to determine the precise value of V_{ud}, the up-down element of the Cabbibo-Kobayashi-Maskawa (CKM) matrix, and test whether or not it is unitary as expected. Mixed Fermi and Gamow-Teller transitions between $T = \frac{1}{2}$ mirror nuclei (^{19}Ne, ^{21}Na, ^{29}P, ^{35}Ar, ^{37}K) have also been considered for determining the value of V_{ud} [1]. They are mediated by both the vector and axial-vector component fo the weak interaction. Thus the extraction of V_{ud}, from one fo these transitions requires the measurement of ft value and any one of the angular-correlation coefficients. The decay of ^{29}P is one of the five cases used to determine V_{ud}. The relatively large uncertainty of its contribution is dominated by the precision of ρ, the ratio of Gamow-Teller to Fermi matrix elements, which was obtained from a $\pm 12\%$ measurement of the beta asymmetry parameter, A_β [2]. The ft value [3] is known much better, to $\pm 0.4\%$, with the largest contribution to its uncertainty being the lifetime of the decay. The aim of the present work is to improve the lifetime of ^{29}P so that it no longer dominates the uncertainty in the deduced ft value.

^{29}P was produced via the p (^{30}Si, $2n$) ^{29}P reaction in inverse kinematics at a primary beam energy

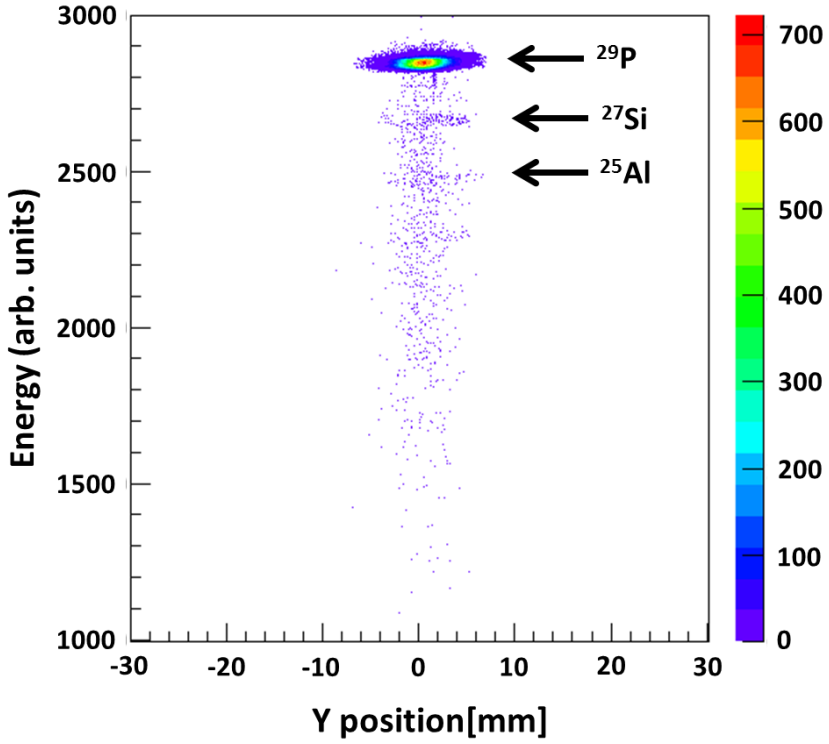

FIG. 1. Two-dimensional plot of energy-loss versus position in the PSSD at the MARS focal plane after the spectrometer had been optimized for ^{29}P production.

of 24 MeV/u. The Momentum Achromatic Recoil Spectrometer (MARS) was used to produce a secondary beam of ^{29}P with a purity of 99.5%. The impurity level of ^{27}Si and ^{25}Al at the exit of MARS were at the 0.1% level. Fig. 1 shows a typical two-dimensional plot of energy-loss vs position as obtained with the position-sensitive silicon detector (PSSD) in the MARS focal plane.

The secondary beam exited the vacuum system through a Kapton foil and then passed through a thick plastic scintillator, a series of Al degraders and eventually implanted in the center of an Al-Mylar tape. The combination of m/q selectivity in MARS and range selectivity in the degrader led to implanted ^{29}P samples that were greater than 99.9% pure. Each source of ^{29}P was prepared by implantation of the ^{29}P into a section of aluminized Mylar tape for 8.4 s. The beam was then turned off and our tape-transport system moved the sample in 180 ms to a well-shielded detector station consisting of a high efficiency 4π proportional gas counter. The decay positrons were then observed for 84 s, which is equal to twenty half-lives of ^{29}P. This cycle was repeated until the desired statistics had been accumulated. The total data set was divided into several runs with different settings of the experimental parameters: bias voltage, discriminator threshold, dominant dead-times. A background measurement was also recorded for which all conditions were the same as for normal data taking except that the tape-move feature was disabled. The analysis is in progress to extract the precise half-life with an associated error budget.

[1] O. Naviliat-Cuncic and N. Severijns, Phys. Rev. Lett. **102**, 142302 (2009).
[2] G.S. Masson and P.A. Quin, Phys. Rev. C **42**, 1110 (1990).
[3] N. Severijns, M. Tandecki, T. Phalet, and I.S. Towner, Phys. Rev. C **78**, 055501 (2008).

Improved determination of the gamma branching ratios from the decay of ^{37}K

A. Ozmetin, V.E. Iacob, J.C. Hardy, V.S. Kolhinen, D. Melconian, M. Nasser, H.I. Park, B. Schroeder, and P.D. Shidling

As part of the TRIUMF Neutral Atom Trap (TRINAT) collaboration, our goal is to search for physics beyond the standard model via precision measurements of the (polarized) angular correlations of the β^+ decay of ^{37}K. In order to achieve the requisite precision in the standard model predictions of the parameter values (<0.1%), it is essential that the *ft* value of ^{37}K be as precise as possible [1-3]. At the moment, the precision of the *ft* value is limited by the uncertainty in the branching ratio to the ground state; Ref. [3] from 1997 had plenty of statistics to see small branches, but the HPGe was not precisely calibrated so the ground state branch was not determined precisely. We will improve this with data we have taken at the Cyclotron Institute using the fast-tape transport system in conjunction with the world's most precisely calibrated HPGe. We are currently in the process of completing the branching ratio analysis.

We have filtered the data to obtain a clean data set (e.g. vetoing bad cycles where the tape does not stop between the HPGe γ detector and the plastic scintillator β detector) and minimized accidental coincidences via the E_γ vs β-γ timing 2D spectrum. We have completed calibrating the HPGe energy using four known prominent peaks at 1184, 1611, 2796 and 3602 keV [3]. In order to optimize the reduction of backgrounds and random coincidences, we iteratively optimized our cuts in both the γ energy and β-γ timing.

Our fits to the areas of the γ photopeaks now account for the random coincidences and background, and include small effects such as incomplete charge collection, as shown in the left panel of Fig. 1. Preliminary comparison to the published work is shown in right panel of the same figure, where

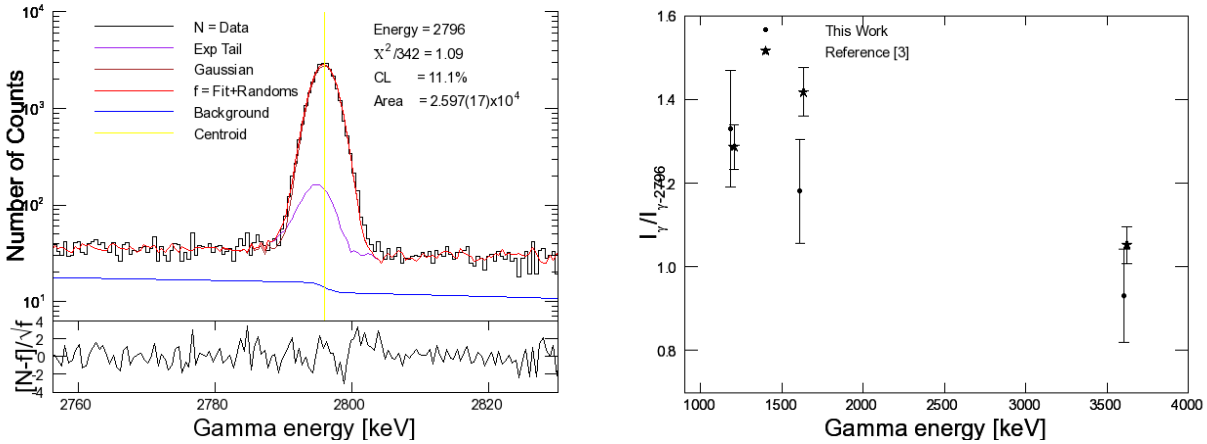

FIG. 1. Example fit to the 2796-keV photopeak from the decay of ^{37}K from a typical run (left). The intensity of 3 other γ rays compared to the dominant 2796-keV branch is plotted on the right, as well as the results from Ref. [3], showing reasonable agreement at this preliminary stage.

our ratio of photopeak areas is compared to the results of Ref. [3]. The comparison is already quite reasonable.

Currently, we are at the stage of making corrections to account for dead times and pile-up as outlined and discussed in detail in Ref. [4]. We expect to arrive at a publishable result before the end of the year.

[1] P.D. Shidling, *et al.*, Phys. Rev. C **90**, 032501(R) (2014).

[2] B. Fenker *et al.*, Phys. Rev. Letts. **120**, 062502 (2018).

[3] E. Hagberg *et al.*, Phys. Rev. C **56**, 135 (1997).

[4] M. Bencomo, Ph.D. Thesis, Texas A&M University (2019); URL: http://oaktrust.library.tamu.edu/-handle/1969.1/174335.

Toward measuring the Fierz parameter in ^{6}He: Cyclotron radio emission spectroscopy modeling with Kassiopeia

D. McClain, V. Iacob, V.S. Kolhinen, D. Melconian, M. Nasser, A. Ozmetin,
B. Schroeder, and P.D. Shidling

An accurate determination of the absolute neutrino mass to < 0.2eV is at the forefront of modern physics, and this demanding measurement has necessarily developed novel and elegant detection techniques. The Cyclotron Radiation Emission Spectroscopy (CRES) technique has been demonstrated by Project-8 [1] – a next-generation tritium end-point experiment – to reach precisions as low as 0.05% in the β energy. The goal of the ^{6}He *b* collaboration is to utilize this technique to measure the energy spectrum of the pure Gamow-Teller β^- decay of ^{6}He. This will allow a very precise measurement of the Fierz interference parameter, *b*, which if non-zero would indicate the existence of tensor components to the weak interaction which is physics beyond the standard model. The ultimate goal is to observe the decay from ^{6}He ions confined in a Penning trap where our projected systematics are at the 10^{-4} level, representing an impact that far exceeds direct searches for tensor interactions at large-scale facilities such as the LHC. As part of this multi-institutional effort, we are simulating ^{6}He and its emitted radiation using the particle tracking package Kassiopeia.

The cyclotron frequency, f, of an electron in a strong uniform magnetic field, *B*, is dependent on the kinetic energy E_k of the electron according to

$$f = \frac{1}{2\pi}\frac{eB}{m_e + E_k/c^2}$$

where e is the electron charge, m_e is the rest mass of the electron, and c is the speed of light in a vacuum. CRES is a form of spectroscopy that turns the energy measurement into one of frequency; as we can measure frequencies very precisely, this is how we obtain such precise energy measurements: the energy resolution $\Delta E/E$ goes like $\Delta f/f$, and the resolution of the frequency is related to the time it is observed $t \sim 1/\Delta f$ [1]. For this reason it is important to observe the cyclotron frequency for ample time.

Kassiopeia is a particle-tracking simulation [2] that focuses on the low energy interactions in complex geometries and electromagnetic fields. Originally created for the Karlsruhe Tritium Neutrino (KATRIN) experiment, the current generation of tritium endpoint experiments, Kassiopeia is required to track particles and compute electromagnetic fields on site. Kassiopeia creates a ROOT file that contains physical quantities such as magnetic field, kinetic energy, time, position, etc. which can be used to show the cyclotron frequency and other qualities of the electron.

A Penning trap simulation in Kassiopeia has been created resembling SHIPTRAP's measurement trap [3]. For the simulation, electrons are currently being generated from the center of the trap reflecting the position and energies of ^{6}He β-decay within the trap. Helium gas will be implemented into the simulation to create special interactions. Future simulations will generate ^{6}He particles directly and allow it to decay and follow the primary particle as well as all of its descendants. From here wave guides will be added to the simulation and measure the cyclotron frequency from the beginning of the simulation until

the electrons reach the waveguide to better interpret the endpoint and output of the simulation for further investigation.

[1] A.A. Esfahani *et al*., J. Phys. G **44**, 054004 (2017).
[2] D. Furse *et al*., New J. Phys. **19**, 053012 (2017).
[3] M.S. Rahaman. Ph.D. Thesis, Heidelberg University 2005; DOI: 10.11588/heidok.00005348.

TRINAT's polarized program with ^{37}K

D. Melconian

As discusssed in last year's report [1], TRINAT recently published the world's most precise measurement of the beta asymmetry parameter in a nucleus: $A_\beta = -0.5707(13)_{\rm syst}(13)_{\rm stat}(5)_{\rm pol}$. This 0.3% measurement was the PhD thesis of TAMU student Ben Fenker. Another student at the University of Manitoba is currently analyzing the same data set, but looking at the beta-energy dependence of the observables. When completed, we will have a measurement (or limit) on beyond the standard model physics parameters $b_{\rm Fierz}$ and second-class currents. These parameters are zero in the standard model, but are predicted to be finite in extensions which include tensor and/or scalar components to the predominantly $V-A$ form of the weak interaction. Our measurement will help search for these small terms or improve limits on their magnitude.

There is a steep learning curve both in the data analysis and in developing the GEANT4 Monte Carlo simulation necessary for this analysis. We have made a preliminary analysis of the observed super-ratio asymmetry as a function of energy, allowing a non-zero $b_{\rm Fierz}$ to be a free parameter of the fit. We include a rough response function for the β telescopes and ave included recoil-order effects. The result, shown in Fig. 1, indicates our statistical uncertainty will be ± 0.04. We hope to complete the analysis by the end of this year.

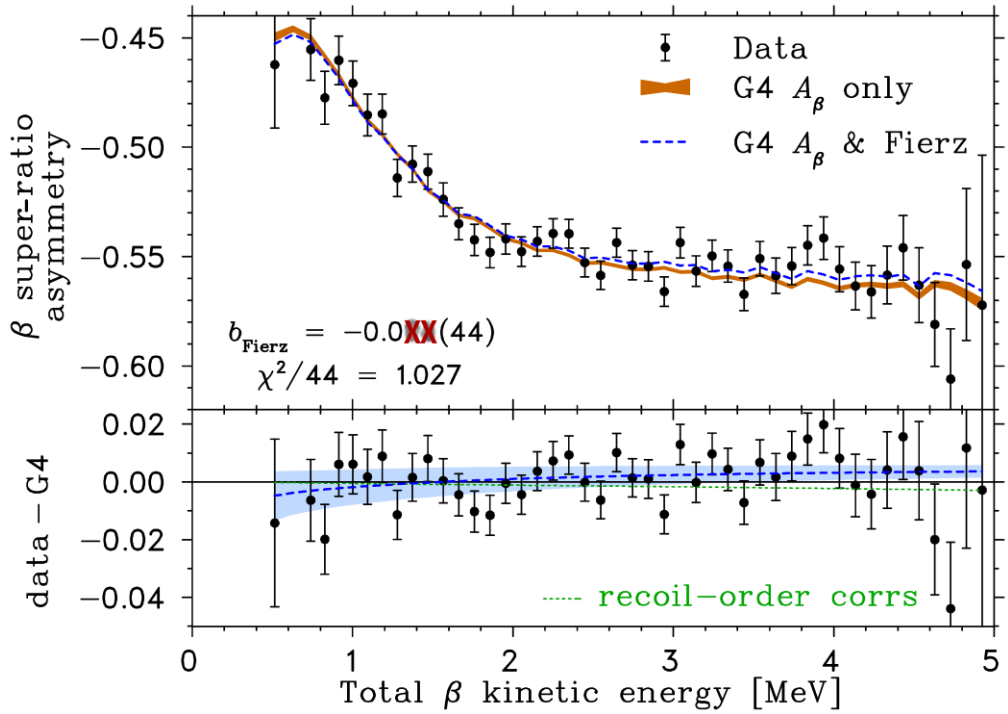

FIG. 1. Asymmetry as a function of energy. This is the same data for the A_β measurement shown in Fig. 3 of Ref. [2], but this time is also fit including a non-zero Fierz parameter. The value has been hidden as this is a very preliminary fit. Nevertheless, the statistical uncertainty of ± 0.044 is a very good estimate as most of the data selection has already been made for the A_β measurement. A detailed analysis and the estimate of systematic uncertainties is

[1] B. Fenker *et al.*, *Progress in Research*, Cyclotron Institute, Texas A&M University (2017-2018), p.I-10.
[2] B. Fenker *et al.*, Phys. Rev. Lett. **120**, 062502 (2018).

Study of astrophysically important low-energy resonances in α + ^{22}Ne reaction using ^{6}Li(^{22}Ne,^{26}Mg)*d* alpha transfer with TIARA and MDM spectrometer

S. Ota, G.A. Christian, E.A. Bennett, S. Dede, H. Jayatissa, J. Hooker, C. Hunt,
C. Magana, G. Rogachev, A. Saastamoinen, S. Upadhyayula, W.N. Catford,[1]
S. Hallam,[1] G. Lotay,[1] M. Mouhkaddam,[1] J.A. Tostevin,[1] R. Wilkinson[1]
[1]*University of Surrey, Guildford GU2 5XH, United Kingdom*

In core He burning and C-shell burning of massive stars (> 8 solar mass), the ^{22}Ne(α,n)^{25}Mg reaction is considered to be a dominant neutron source for the weak s-process during which nuclides in the A=60-90 mass range are produced [1]. The reaction also largely contributes to the neutron production for the main s-process in He-low and intermediate mass asymptotic giant branch (AGB) stars during which nuclides in the A~90-209 are produced [1]. Some attempts to experimentally determine the rate for this reaction at the Gamow window corresponding to the *s* process temperatures (T = 0.2-0.3 GK, equivalent to E_α = 400 – 900 keV, where E_α is energy of α particle in the laboratory system, and E_x=10.9-11.5 MeV, where E_x is excitation energy of ^{26}Mg) have been made through direct (^{22}Ne+^{4}He or α+^{22}Ne) measurements [e.g., 2]. However, they have been hindered by the small cross section due to the Coulomb barrier and the resonance at E_α ~ 830 keV (E_x ~ 11.32 MeV in ^{26}Mg excitation energy) is the lowest resonance identified with this method. Although indirect methods such as ^{26}Mg(α,α')^{26}Mg, ^{22}Ne(^{6}Li,*d*)^{26}Mg, ^{25}Mg(n,γ), ^{26}Mg(γ,γ') reactions [e.g., 3-6] have been used to identify lower-energy resonances, there remain many uncertainties in spin-parity (J^π), partial wave widths of respective decay channels (Γ_γ, Γ_n and Γ_α) of these resonances. Since past studies identified particularly two resonances, E_x=11.32 and 11.17 MeV above neutron separation energy (S_n=11.093 MeV), have the largest contribution to the neutron production during the s-process, unambiguously determining J^π, Γ_γ, Γ_n and Γ_α for these resonances is important.

To determine these resonance parameters, we performed an experiment using the ^{6}Li(^{22}Ne,^{26}Mg)d α-transfer reaction. Because both the α and ^{22}Ne have ground states with $J^\pi=0^+$, the α-transfer reaction preferentially populates natural parity states in ^{26}Mg. This helps us to enable studies of the resonance parameters of astrophysically relevant natural parity states in ^{26}Mg, and J^π of these resonance states can be determined by measuring the angular distribution of deuterons. Furthermore, the inverse kinematics approach enables us to determine Γ_n / Γ_γ by direct measurements of the ratio of produced ^{25}Mg (^{26}Mg*→^{25}Mg$_{g.s.}$ + n) and ^{26}Mg (^{26}Mg*→^{26}Mg$_{g.s.}$ + γ) ions at the resonance states. Determining Γ_n / Γ_γ is important to understand the neutron yield of these resonances. The ^{22}Ne(α,γ)^{26}Mg reaction can be of considerable strength to compete with the ^{22}Ne(α,n)^{25}Mg reaction at E_x=11.32 and 11.17 MeV resonances and therefore could significantly suppress neutron production for the s-process.

The experiment was performed at Cave 3 using a 7 MeV/u ^{22}Ne beam from the K150 cyclotron. ^{6}Li-enriched (99%) lithium flourite (LiF) targets with the thickness of 30 μg/cm^2 on a graphite backing foil (10 μg/cm^2) were prepared so that the effect of the energy loss of the ^{22}Ne beam and deuterons in those materials on the final energy resolution will be negligibly small. The beam bombarded the target at an intensity of about 3 nA for about 10 days. A large Si detector array, TIARA [8] was used for

measuring the energies and angular distribution of light particles (deuterons). The deuteron energies and angles were used to determine excitation energies of ^{26}Mg. TIARA consists of two types of Si detectors, Hyball and Barrel, which cover 145 – 170° and 40-145° in laboratory frame, respectively (see [8]). TIARA was surrounded by four HPGe clover γ-ray detectors, which were used to confirm the populated states of ^{26}Mg. Recoil Mg ions were delivered to the Oxford ionization chamber placed at the back of the MDM spectrometer at 0°with ±2°acceptance [9]. The Oxford chamber consists of four proportional wire counters to determine the trajectories of particles and two MicroMegas detectors to measure the deposited energies in the gas (see details in [10]). The chamber was filled with isobutene gas at 35 torr to stop the Mg ions with the energies of our interests in the region of the second MicroMegas detector. The first and the second MicroMegas detectors thus provide ΔE and E_{res} (residual energy), respectively, and the Mg ions are clearly identified from other elements as shown in [11]. Moreover, ^{26,25}Mg isotopes were identified from each other based on the hit positions on the second wire which is located near the focal plane.

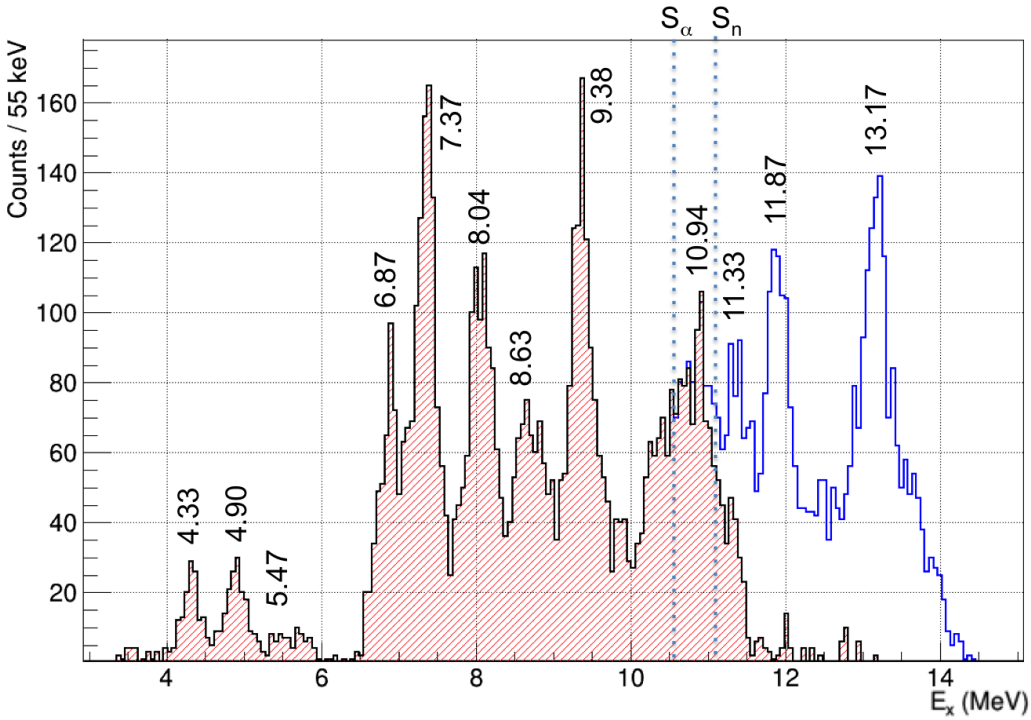

FIG. 1. ^{26}Mg excitation energy spectrum (red shadow: contribution from ^{22}Ne(^{6}Li,d)^{26}Mg, blue: sum of contributions from ^{22}Ne(^{6}Li,d)^{26}Mg and ^{22}Ne(^{6}Li,d+n)^{25}Mg). E_x=11.32 MeV resonance peak is distinct in both spectra.

^{26}Mg excitation spectrum measured with the Hyball is shown in Fig. 1. It is evident that we observe the resonance of our interest (E_x=11.32 MeV) and we concluded the branching ratio of Γ_n / Γ_γ = 1.25±0.28. This result indicates Γ_n / Γ_γ is overestimated in past direct measurements (Γ_n / Γ_γ = 3.8±0.9), which performed the (α,n) and (α,γ) measurements independently. Fig. 2 shows angular distribution of E_x=11.32 MeV resonance and some low-lying excitation states, together with DWBA calculations

assuming various J^{π} for comparison. We can confirm the calculations assuming the known J^{π} agrees with our date well. Although it is not possible to assign definite J^{π} to the E_x=11.32 MeV resonance among possible J^{π} =0+, 1-, 2+, we concluded that $J^{\pi} = 2^+$ is the most probable by comparing spectroscopic factors and resonance strength extracted assuming these J^{π} with results by past measurements, (see [12] for details).

Currently we are making an effort to evaluate effects of our new results on s-process chemical abundances.

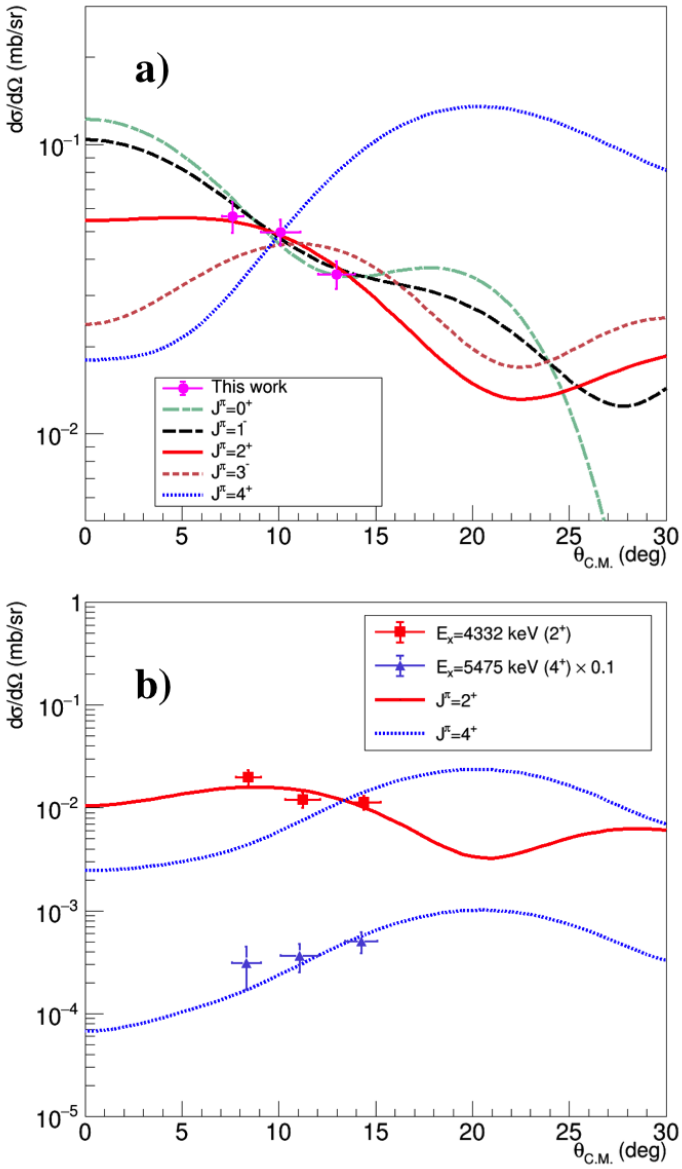

FIG. 2. Angular differential cross sections of a) Ex=11.32 MeV, b) low-lying states where J^{π} are well established from past measurements, together with DWBA calculations.

[1] F. Kappeler, Prog. Part. Nucl. Phys. **43**, 419 (1999).
[2] M. Jaeger *et al.*, Phys. Rev. Let. **87**, 20 (2001).
[3] P. Adsley *et al.*, Phys. Rev. C **96**, 055802 (2017).
[4] U. Giesen *et al.*, Nucl. Phys. **A561**, 95 (1993).
[5] R. Talwar *et al.*, Phys. Rev. C **93**, 055803 (2016).
[6] C. Massimi *et al.*, Phys. Let. B **768**, 1 (2017).
[7] R. Longland *et al.*, Phys. Rev. C **80**, 055803 (2009).
[8] M. Labiche *et al.*, Nucl. Instrum. Methods Phys. Res. **A614**, 439 (2010).
[9] D.M. Pringle *et al.*, Nucl. Instrum. Methods Phys. Res. **A245**, 230 (1986).
[10] A. Spiridon *et al.*, Nucl. Instrum. Methods Phys. Res. **B376**, 364 (2016).
[11] S. Ota *et al.*, *Progress in Research*, Cyclotron Institute, Texas A&M University (2016-2017), p. I - 40.
[12] S. Ota *et al.*, Phys. Rev. Lett. (in preparation).

Preparation for measurement of the $^{15}O(\alpha,\gamma)^{19}Ne$ alpha branching ratio

S. Dede, G. Christian, S. Ota, C.E. Parker, E. Bennett, M. Roosa, D.P. Scriven,
W.N. Catford,[1] and G. Lotay[1]
[1]*University of Surrey, Guildford, Surrey GU2 7XH, United Kingdom*

The $^{15}O(\alpha,\gamma)^{19}Ne$ reaction is one of the two breakout reactions from the hot CNO cycle into the *rp* process, and is crucial to the thermonuclear runaway that causes type I X-ray bursts on accreting neutron stars [1]. As a direct measurement of this reaction is not currently possible, due to the combination of the low reaction cross section and insufficient ^{15}O beam intensities, we will perform an indirect measurement using the $^{21}Ne(p,t)^{19}Ne$ reaction at 40 MeV/nucleon. This reaction selectively populates the state of interest in ^{19}Ne, which is the first state just above the $^{15}O + \alpha$ threshold, at 4.033 MeV, as shown in the level scheme in Fig. 1.

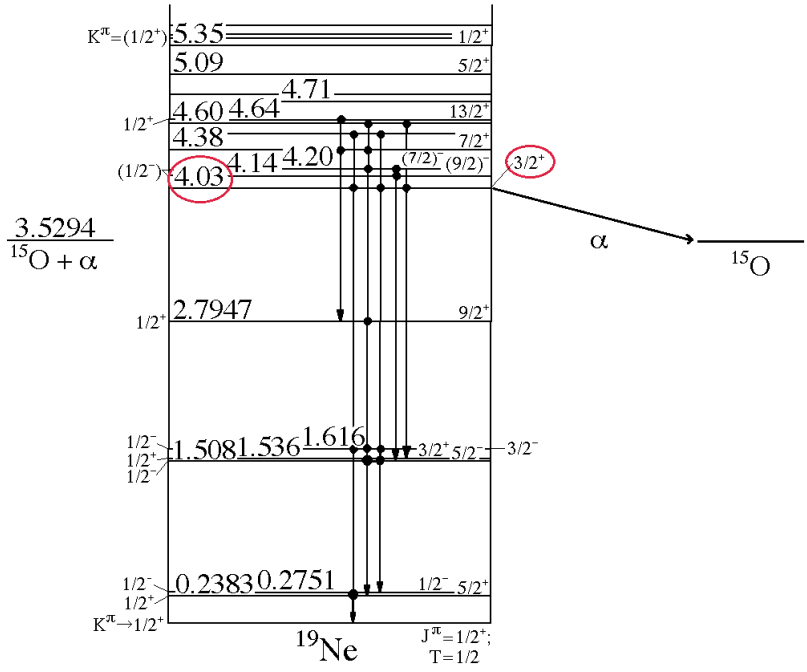

FIG. 1. Level scheme of ^{19}Ne with the state of interest selected.

In order to determine the branching ratio, the resonance partial width of the entrance (Γ_α) and exit (Γ_γ) channels of the reaction are needed. While Γ_γ has previously been measured [2], there is only an upper limit set for the Γ_α [2], which is what we plan to determine with this measurement.

To determine the ideal beam energy and appropriate detectors for this experiment, we used TWOFNR and LISE++, respectively.

Using TWOFNR we simulated the cross section for different beam energies, and compared with the existing data from Fortune et al. [3], shown in Fig. 2. Our calculations are shown in Fig. 3.

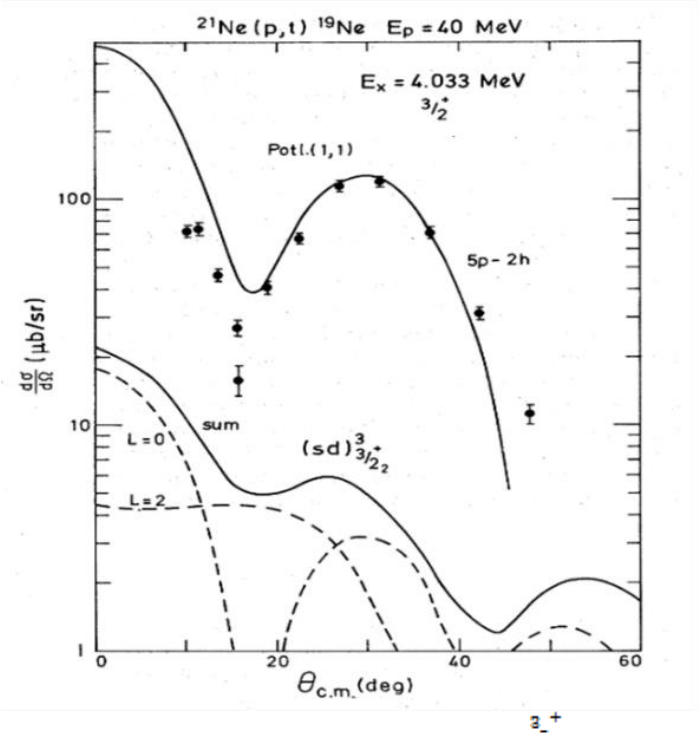

FIG. 2. Experimental angular distribution for the $\frac{3}{2}^+$ state of Ne.

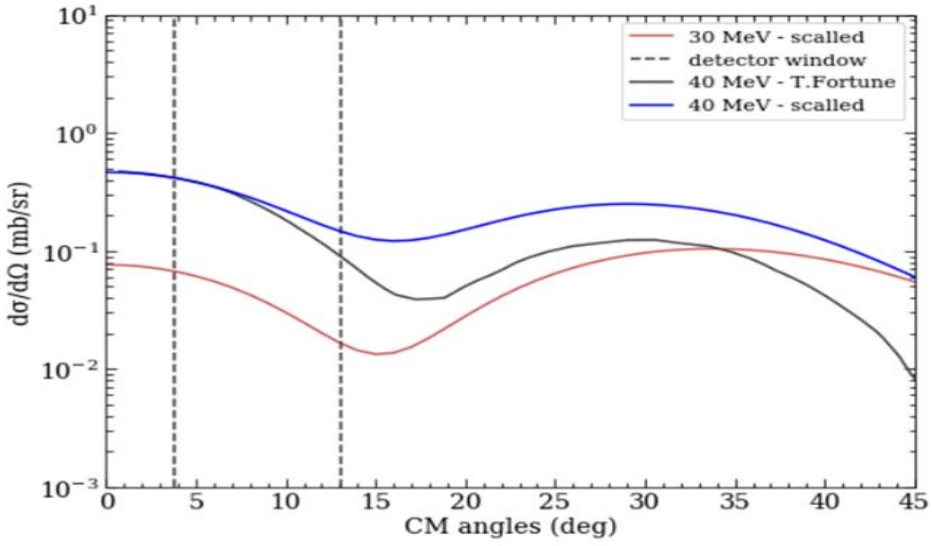

FIG. 3. TWOFNR simulations for a 30 and 40 MeV/nucleon beam scaled to the experimental data from FIG. 2.

From our simulations we conclude that the ideal beam energy for this experiment is 40 MeV/nucleon.

After determining the energy, we use kinematic calculations to calculate the maximum energy that we expect to see from the tritons. Using that energy as an input we determine the number of detectors, as well as the thickness of these detectors, that is needed in order to fully stop the tritons. LISE ++ calculations showed that we will be needing a thin 500μm thick Si detector, followed by three 1500μm thick Si detectors. We will be using the TIARA [3] detector array, which consists of silicon strip detectors designed for transfer reaction studies, to measure the tritons. TIARA is shown schematically in Fig. 4, and the properties of forward-angle Si detectors are listed in Table I.

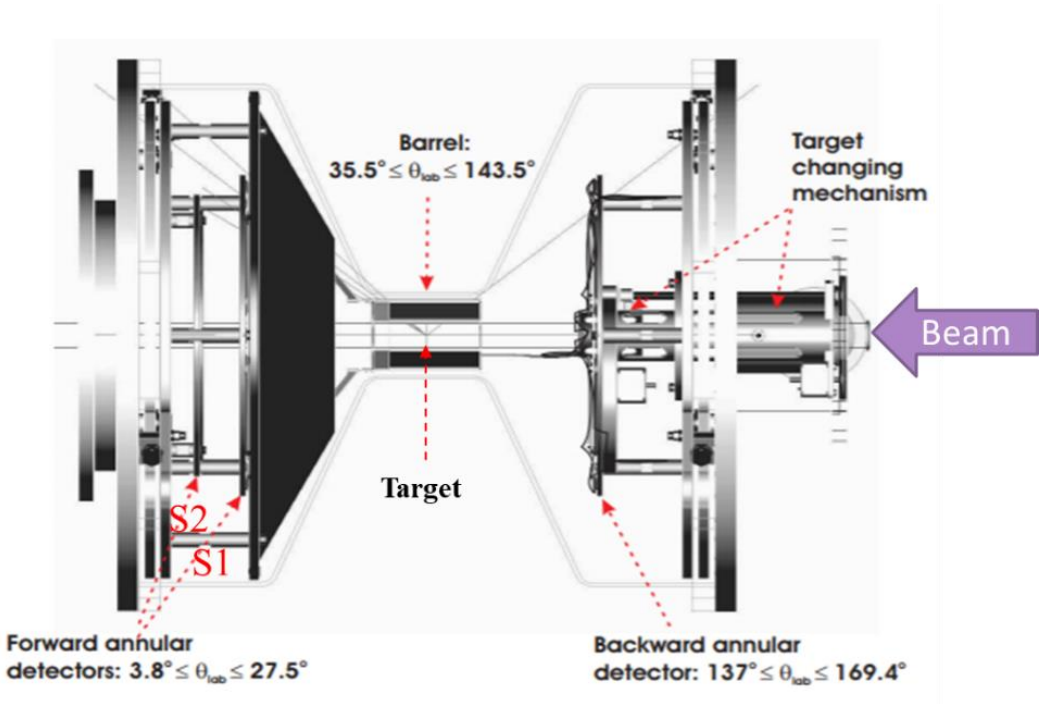

FIG. 4. TIARA chamber setup.

Table I. TIARA forward-angle Si detector properties.

	S1	**S2**
Radius	20.5 mm to 48 mm	11 mm to 35 mm
Position	92 mm	150 mm
Theta	12.6 deg to 27.5 deg	3.8 deg to 13.1 deg
Thickness	500 μm thick	500 μm thick 3 x 1500 μm thick

In addition, the Oxford detector, located at the focal plane of the Multipole-Dipole-Multipole (MDM) Spectrometer, will measure the ^{19}Ne and ^{15}O, which will be used in coincidence with the measured tritons to determine the partial widths.

[1] R.K. Wallace and S.E. Woosley, Astrophys. J. Suppl. Ser. **45,** 389 (1981).
[2] B. Davids *et al.*, Phys. Rev. C **61**, 012801(R) (2003).
[3] H.T. Fortune et al., Phys. Rec. C **18**, 1563 (1978).
[4] W.N. Catford *et al.*, AIP Conference Proceedings **704**, 185 (2004).

Precision γ-ray branching-ratio measurements for long-lived fission products of importance to stockpile stewardship

K. Kolos,[1] A.M. Hennessy,[2] J.A. Clark,[3] J.C. Hardy,[4] V.E. Iacob,[4] G.E. Miller,[2] E. Norman,[5] H.I. Park,[4] G. Savard,[3] N.D. Scielzo,[1] A.J. Shaka,[2] M.A. Stoyer,[1] and A.P. Tonchev[1]

[1]*Lawrence Livermore National Laboratory,*

[2]*University of California at Irvine, Irvine, California*

[3]*Argonne National Laboratory,*

[4]*Texas A&M University, College Station, Texas*

[5]*University of California at Berkeley, Berkeley, California*

We have measured the ^{95}Zr β-decay branching ratios to high (<1%) precision. This serves as a proof-of-principle demonstration that the method we have developed can be used to measure the γ rays and β branching ratios of long-lived fission products. As previously reported [1-2], we collected a high-purity sample of ^{95}Zr (and its decay daughter ^{95}Nb) on a thin (40 μg/cm^2) carbon-foil backing by using a low-energy mass-separated beam of A=95 ions from CARIBU at Argonne National Lab. The subsequent decay measurements were performed at Texas A&M with the HPGe detector for γ-ray measurements and the Livermore 4π gas counter for β counting.

We performed a thorough analysis of the collected data to obtain γ-ray intensities and β branching ratios in the decay of ^{95}Zr and ^{95}Nb. The γ-ray intensity (I_γ) per β decay for a particular transition was determined from the β-γ coincidence detection rate ($R_{\beta\gamma}$) relative to the β particle detection rate from the decay of the isotope of interest (R_β), through the relation

$$I_\gamma = \frac{R_{\beta\gamma}}{R_\beta}\frac{1}{\varepsilon_\gamma}\frac{\varepsilon_\beta}{\varepsilon_{\beta\gamma}}.$$

Here ε_γ is the photopeak efficiency of the HPGe detector for detecting the γ ray of interest. These efficiencies were obtained from the CYLTRAN simulation and are reported in Table I. $\varepsilon_{\beta\gamma}$ is the efficiency for detecting the β particles emitted in coincidence with that γ ray, and ε_β is the efficiency for detecting the β particles from all decay branches of the isotope of interest in the 4π gas counter. The $\varepsilon_\beta/\varepsilon_{\beta\gamma}$ efficiency ratio of the 4π gas proportional counter deviates from unity because the β-particle energy spectra in the ratio are not identical, and a different fraction of low-energy particles are lost to self-absorption in the carbon foil or to the electronic threshold of the counter. We determined the efficiency ratio using simulations of the detector response to the β-decay spectra under consideration.

Table 1. Detector efficiencies for the γ rays in the decay of ^{95}Zr and ^{95}Nb, and the β particle efficiency ratio for the 4π gas counter.

Source	E_{γ_i}	ϵ_{γ_i} (%)	$E_{\beta_{max}}$	$\varepsilon_\beta/\varepsilon_{\beta\gamma}$
^{95}Zr	724.2 keV	0.2977(9)	399.4(18)	0.9987(1)
^{95}Zr	756.7 keV	0.2884(9)	366.9(18)	1.0011(1)
^{95}Nb	765.8 keV	0.2860(9)	159.8(5)	1.0000(1)

Before building the simulation model, we used the measured ratio of β-γ coincidences over γ singles ($R_{\beta\gamma}/R_{\gamma}$) to obtain the efficiency of the 4π gas counter ($\varepsilon_{\beta\gamma}$) for detecting the β particles emitted in coincidence with several detected γ rays. We then adjusted the β-detection threshold setting used in the simulation model to best reproduce those measured 4π gas counter efficiencies. The comparison between the experiment and the simulation of the 4π gas counter detector efficiency for the different β-decay transitions is presented in Fig. 1. The insert shows the χ^2 values obtained from the difference between the measured values and simulated values for a range of thresholds. These results indicate that the detector threshold was 1.1(3) keV. Table I shows the $\varepsilon_{\beta}/\varepsilon_{\beta\gamma}$ efficiency ratios calculated with that threshold.

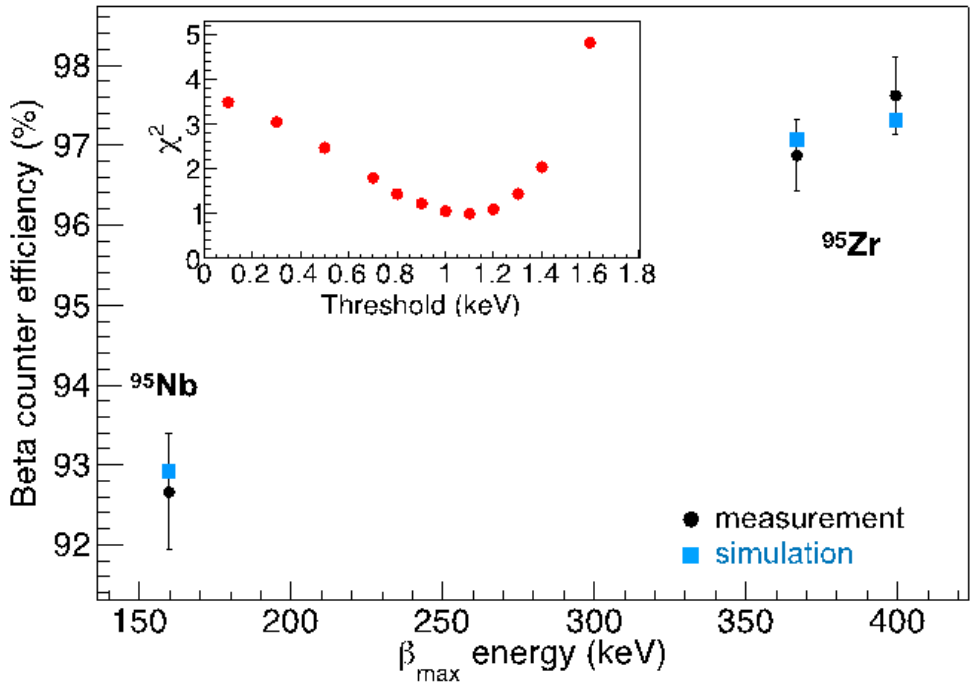

FIG. 1. Comparison of the measured gas counter efficiencies for the highest-intensity transitions in the decays of ^{95}Zr and ^{95}Nb to simulation results obtained with GEANT4 with a 1.1-keV threshold. The insert shows the χ^2 values obtained from the difference between the measured values and simulated values for a range of thresholds. These results indicated the detector threshold was 1.1(3) keV.

We calculated the β-decay branching ratios from the γ-ray intensities after including small contributions from conversion electron emission. The comparison between our results and the evaluated values [3] are presented in Table II. The complete uncertainty budget for γ-ray intensities from the decay of ^{95}Zr and ^{95}Nb is given in Table III. We are currently working on finalizing our results and uncertainties, and writing a manuscript that describes in detail our experimental approach, which will be submitted to the journal Nuclear Instruments and Methods in Physics Research A.

Table II. Preliminary results for the γ-ray intensities and β branching ratios for ^{95}Zr and ^{95}Nb obtained in this experiment in comparison with the evaluated values [3].

Isotope	E_γ	$I_{\gamma_{(\text{this work})}}$	I_γ	$BR_{\beta_{(\text{this work})}}$	BR_β
^{95}Zr	724.2 keV	0.4380(25)	0.4427(22)	0.4387(25)	0.4434(22)
^{95}Zr	756.7 keV	0.5441(28)	0.5438(22)	0.5449(28)	0.5446(22)
Ratio	724.2 keV/756.7 keV	0.805(6)	0.814(4)		
^{95}Nb	765.8 keV	0.9962(94)	0.9981(1)	0.9962(95)	0.9997(1)

Table III. The preliminary uncertainty budget for γ-ray intensities measured in this study.

Source	724.2 keV	756.7 keV	765.8 keV
R_{β_γ}	0.0049	0.0041	0.0078
R_β	0.0008	0.0008	0.0044
ϵ_γ	0.0030	0.0031	0.0031
$\epsilon_\beta/\epsilon_{\beta\gamma}$	0.0001	0.0001	0.0001
Total Uncertainty	0.0058	0.0052	0.0095

[1] K. Kolos *et. al.*, *Progress in Research*, Cyclotron Institute, Texas A&M University (2016-2017), p. I-31.

[2] K. Kolos *et. al.*, *Progress in Research*, Cyclotron Institute, Texas A&M University (2017-2018), p. I-30.

[3] S.K. Basu, G. Mukherjee, and A.A. Sonzogni. Nucl. data sheets for A = 95. Nucl. Data Sheets, **111**, 2555 (2010).

Nuclear level densities and gamma-ray strength functions in samarium isotopes

F. Naqvi,[1] A. Simon,[1] M. Guttormsen,[2] R. Schwengner,[3] S. Frauendorf,[1]
C.S. Reingold,[1] J.T. Burke,[4] N. Cooper,[1] R.O. Hughes,[4] S. Ota,[4] and A. Saastamoinen[5]
[1]*Department of Physics, University of Notre Dame, IN 46556-5670*
[2]*Department of Physics, University of Oslo, N-0316 Oslo, Norway*
[3]*Helmholtz-Zentrum Dresden-Rossendorf, 01328 Dresden, Germany*
[4]*Lawrence Livermore National Laboratory, Livermore, CA 94551*
[5]*Cyclotron Institute, Texas A&M University, College Station, TX 77843*

The spectroscopic properties of excited nuclei provide information on the internal structure of these highly dense, many-body quantum systems. Low-energy excitation regime is treated differently compared to the high- energy quasi-continuum region. In the latter, the quantities such as discrete energy levels are replaced by nuclear level densities (NLD) and transition probabilities are defined as γ-ray strength functions (γSF) which are aver- age reduced radiation or absorption probabilities at any given photon energy E_γ. Both of these observables also form important inputs for Hauser-Feshbach calculations predicting the astrophysical neutron capture rates. Therefore, a comprehensive understanding of NLD and γSF is required for an insight on the astrophysical processes driving the synthesis of nuclei in our universe.

The NLDs are often described by phenomenological analytical formulas built on the first principles of the Fermi gas model. In order to explain the shape of the γSF, phenomena such as giant electric dipole resonances are commonly adopted to fit the enhanced dipole transition probability at energies around 12-17 MeV. A relatively recent observation of the strength enhancement in the energy range below 3-4 MeV shows two features in the γSF: an enhancement at low energies, *upbend*, and a bump around 3-4 MeV corresponding to the scissors mode in deformed nuclei. While the strength of the *upbend* and the scissors mode is a small contribution to the γSF, it has a significant impact on capture and photodissociation reaction rates. TALYS calculations shown in Ref. [1] highlight the profound effect of the observed low-energy strength enhancement on the neutron capture rates. An increase of 3 orders of magnitude in the rates is predicted for Sm iso- topes lying at the neutron drip line provided a similar enhancement exists in that region. Measuring the γSF in nuclei close to the neutron drip line is still a far-fetched goal, however a systematic study of the evolution of low-energy *upbend* in stable members of an isotopic chain is required to have a clear picture of the conclusions made in Ref. [2] and to further extrapolate the properties of the γSF to the less explored neutron-rich regions. In this paper, the systematic study of the evolution of the γSF at low energies was extended to ^{147,149}Sm nuclei which are closer to the $N = 82$ shell.

The experiment was performed at the Cyclotron Institute of Texas A&M University, where two 98(1)% isotopically enriched samarium targets, ^{148}Sm and ^{150}Sm, 0.8 mg/cm^2 and 1.1 mg/cm^2 thick, respectively, were bombarded by a 1.0 nA of 28 MeV proton beam from the K- 150 cyclotron. The reaction products were detected by the Hyperion array [3] that consists of 12 HPGe Clover- type γ-ray detectors combined with ΔE-E STARS telescope for charged particle identification and energy

measurement. The telescope comprised two segmented silicon detectors, 140 μm (ΔE) and 1000 μm (E) thick. Each of the detectors was a disk, 72 mm in diameter, with a 22 mm in diameter opening for the beam in the center. The disk was divided into 24 concentric 1 mm wide rings and into 8 segments in the angular direction. The ΔE-E system was placed 18 mm behind the target, providing an angular coverage for particle detection of 30-58 degrees. The design of the telescope allowed for identification of the light ion charged particle reaction products (protons, deuterons and tritons) and an energy resolution of 130 keV FWHM for detected deuterons. The clover γ-ray detectors were positioned approximately 21 cm from the target at 45, 90, and 135 degrees with respect to the incident beam axis. Using standard γ-ray calibration sources, an energy resolution of 2.6 keV and 3.5 keV FWHM was obtained at 122 keV and 963 keV, respectively. The absolute photopeak efficiency of the Clover array was measured to be 10% at 130 keV [3]. Only the γ rays coincident with a particle were recorded, which provided data required to build the particle-γ matrices for the Oslo method.

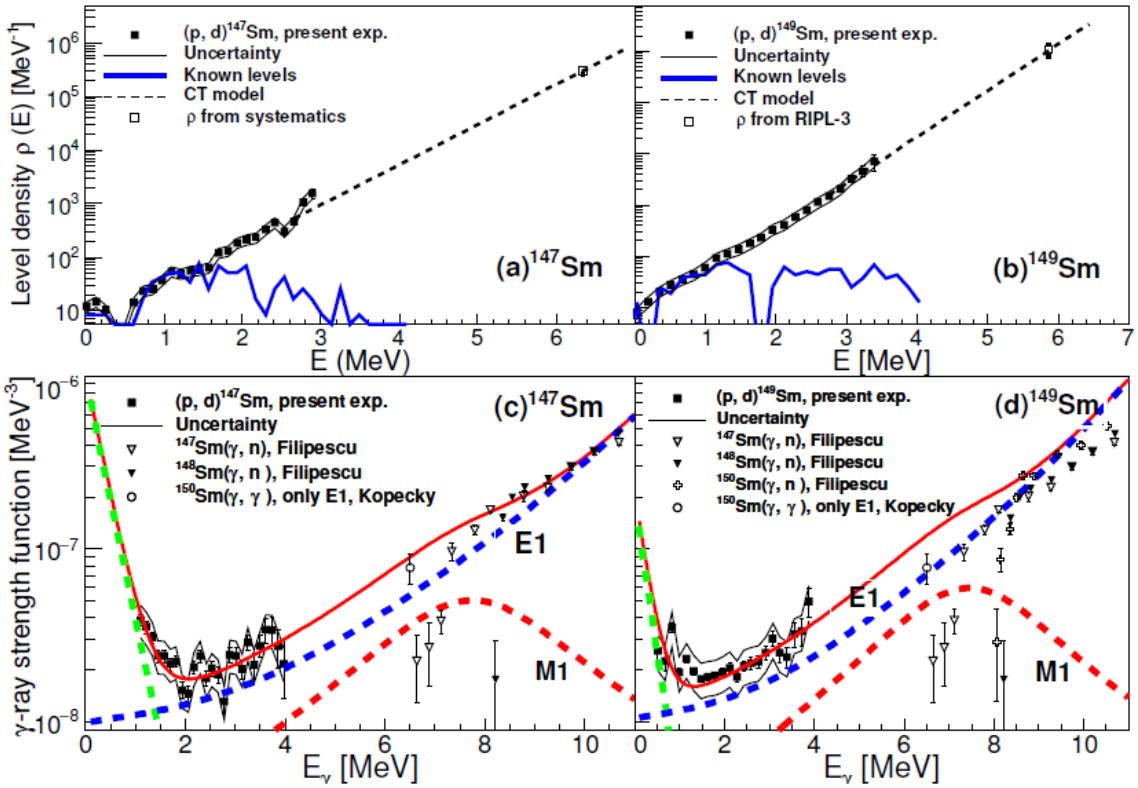

FIG. 1. Level-density functions for ^{147}Sm (a) and ^{149}Sm (b). Experimental data are shown as black squares. The dashed line corresponds to the constant-temperature approximation extrapolating to (S_n) (open squares). The solid line is the known level density in the low-energy discrete region. Experimentally deduced -ray strength functions are shown in (c) and (d). For comparison, the analytical approximations for the E1 strength (blue dashed lines) and M1 strength (red dashed lines) as well as their sums (red solid lines) are shown.

Level densities and γ-ray strength functions were extracted from particle-γ coincidence data for ^{147,149}Sm nuclei using the Oslo method is shown in Fig. 1. As in the previous study of the Sm nuclei, the low-energy upbend in the γSF has been observed at energies below 2 MeV. No structure that could be

attributed to the scissors mode has been observed, which is consistent with the lack of deformation of the studied nuclei. The results of this work are consistent with the previous measurements of the statistical properties of the Sm nuclei [1]. Moreover, the total M1 strength in the γ-ray energy range of 0-5 MeV remains fairly constant across the isotopic chain as it was predicted by Schwengner et al [2]. Shell model calculations for the lowest 60 levels for spin 1/2 - 13/2 were carried out, which reproduce the gross structure of the experimental level densities (exponential increase with excitation energy) and of the γ-ray strength functions (development of a minimum at a transition energy of about MeV caused by the emergence of a scissors resonance with the onset of deformation).

ACKNOWLEDGMENTS

This work was supported by the U.S. Department of Energy No. DE-NA0002914, DE-NA0003780, DEFG02-95ER-40934, DE-NA0003841 and by Lawrence Livermore National Laboratory under Contract No. DE- AC52-07NA27344. R.S. thanks B. A. Brown for his support in using the code NuShellX@MSU and acknowledges the cooperation of the Centers for High-Performance Computing of Technische Universit¨at Dresden and of Helmholtz-Zentrum Dresden-Rossendorf.

[1] A. Simon, M. Guttormsen, A.C. Larsen, C.W. Beau- sang, P. Humby, J.T. Burke, R.J. Casperson, R. O. Hughes, T.J. Ross, J.M. Allmond, R. Chyzh, M. Dag, J. Koglin, E. McCleskey, M. McCleskey, S. Ota, and A. Saastamoinen, Phys. Rev. C **93**, 034303 (2016).

[2] R. Schwengner, S. Frauendorf, and B.A. Brown, Phys. Rev. Lett. **118**, 092502 (2017).

[3] R. Hughes, J. Burke, R. Casperson, S. Ota, S. Fisher, J. Parker, C. Beausang, M. Dag, P. Humby, J. Koglin, E. McCleskey, A. McIntosh, A. Saastamoinen, A. Tamashiro, E. Wilson, and T. Wu, Nucl. Instrum. Methods Phys. Res. **A856**, 47 (2017).

^{35}K experiments

R. Chyzh, A. Saastamoinen, B. Roeder, R.E. Tribble, A. Spiridon, A. Kankainen,[1] E. Pollacco,[2]
L. Trache,[3] I. Stefanescu,[3] and G. Lotay[4]
[1]*University of Jyvaskyla, Finland*
[2]*IRFU, CEA Saclay, Gif-sur-Yvette, France*
[3]*National Institute for Physics and Nuclear Engineering Horia Hulubei, Bucharest, Romania*
[4]*University of Surrey, The United Kingdom*

One the most important questions that nuclear physics is trying to address the origin and abundance of the elements in the universe. Proton-gamma capture reactions, X(p, γ)Y, play an important role in the creation of elements in processes like X-ray bursts or novae explosions [1-3]. The main focus of this work is one of these reactions, ^{34g,m}Cl(p,γ)^{35}Ar. In novae, production of ^{34}S depends on the amount of ^{34}Cl, which β-decays into ^{34}S with a half-life $T_{1/2}$=1.5266 s. Sulfur isotopic ratios can be used for classification of presolar grains, which can be found in the meteorites. One way to destroy ^{34}Cl, is the reaction ^{34g,m}Cl(p,γ)^{35}Ar. The rate of this reaction will eventually determine how much ^{34}Cl will be left for the creation of ^{34}S. To be able to accurately predict the reaction rate of ^{34}Cl(p,γ)^{35}Ar, one needs to know the resonances in ^{35}Ar, including their energy, spin-parity, and proton width. We chose to study this reaction by means of an indirect method where we populate states in ^{35}Ar just above the proton threshold, S_p, and observe them decaying into ^{34}Cl + proton. The detection of low energy protons becomes the major challenge for the experiment. The AstroBoxII was built to address this problem [4,5]. To test our system we had an experiment in March, 2017. A beam of ^{36}Ar at 36 MeV/u was obtained from the K500 cyclotron and impinged on an H_2 cryogenic gas target in the target chamber of MARS [6]. Through the reaction ^{1}H(^{36}Ar,^{35}K)2n we created a secondary beam of ^{35}K and then implanted it into the AstroBoxII. After gain matching the AstroBoxII anode pads, we calibrated two HPGe detectors with ^{137}Cs and ^{152}Eu sources. The estimated production rate for ^{35}K was 2.77 event/nC. An Al degrader (13 mil) on a rotary mechanism was used to control the position for the implantation of ^{35}K in the AstroBoxII. Due to a number of technical issues the beam time was very limited with only about 6 hours of data available. This was sufficient to determine that the system was working as expected.

In July, 2017, we had a second experiment with a ^{35}K secondary beam produced through MARS. After initial calibration of the AstroBoxII by the beam of ^{25}Si we switched to a ^{35}K beam. The production rate for ^{35}K was 2.9 event/nC. Along with the AstroBoxII, we used four HPGe Clover detectors (borrowed from LLNL Hyperion array) that allowed us to measure the coincidences between protons and gamma rays. It was necessary for the setup to be sure that the excited states in ^{35}Ar that were populated by β-decay of ^{35}K are decaying directly to the ground state of ^{34}Cl after emission of a proton. Due to relatively low intensity of the ^{35}K beam to improve our results it was decided to have a third experiment in October, 2017. The setup was identical to the one we had in July, but with more time and higher beam current we significantly improved the statistics for the low energy proton spectrum, which was the main goal of the experiment.

The data analysis for these experiments was done as a part of the Ph.D. thesis of R. Chyzh. The major result is the report of a new proton group at an energy of 441(11) keV that corresponds to the 6348(11) keV level observed in ^{35}Ar. It was assumed that ^{35}Ar was decaying into ^{34}Cl in the ground state. The information available yields a limitation on the spin-parity for the state of $1/2^+$, $3/2^+$, and $5/2^+$. The information about the energy and spin-parity was used to estimate the reaction rate of ^{34}Cl(p,γ)^{35}Ar for this resonance. It was found to be in good agreement with a theoretical calculation provided by JINAWEB [7]. It is worth mentioning that the information on the resonance strength was not directly measured and future experiments are needed to extract full set of physical parameters required for such calculation.

[1] J. Jose and C. Iliadis, Rep. Prog. **74**, 096901 (2011).

[2] J. Jose and M. Hernanz, Eur. Phys. J. A **27**, Supplement 1, 107 (2006).

[3] J. Jose, M. Hernanz, and C. Iliadis Nucl. Phys. **A777**, 550 (2006).

[4] A. Saastamoinen *et al.*, Nucl. Instrum. Methods Phys. Res. **A376**, 357 (2016).

[5] A. Saastamoinen *et al.*, *Progress in Research*, Cyclotron Institute, Texas A&M University (2013 – 2014), p. IV-43; *Progress in Research*, Cyclotron Institute, Texas A&M University (2014-2015), p. IV-33.

[6] R.E. Tribble, R.H. Burch, and C.A. Gagliardi, Nucl. Instrum. Methods Phys. Res. **A285**, 441 (1989).

[7] https://www.jinaweb.org/

Studying the Hoyle state with β-delayed particle-decays using TexAT

J. Bishop,[1] G.V. Rogachev,[1] E. Aboud,[1] S. Ahn,[1] M. Barbui,[1] A. Bosh,[1] C. Hunt,[1] J. Hooker,[1]
D. Jayatissa,[1] E. Koshchiy,[1] C. Pruitt,[2] E. Pollacco,[3] B.T. Roeder,[1] A. Saastamoinen,[1]
L. Sobotka,[2] S. Upadhyayula,[1] S.T. Marley,[4] and R. Malecek[4]
[1]*Cyclotron Institute, Texas A&M University, College Station, Texas*
[2]*Department of Chemistry, Washington University, St. Louis,*
[3]*IRFU, CEA Saclay, Gif-sur-Yvette, France*
[4]*Department of Physics and Astronomy, Louisiana State University, Baton Rouge, Louisiana*

Following the commissioning run for TexAT (a general purpose active-target time projection chamber (TPC)) [1] the possibility to investigate nuclear structure using new techniques became possible. Of particular interest in the overlapping areas of nuclear structure (in terms of α-clustering phenomena) and nuclear astrophysics (via the triple-α process) is the Hoyle state, a 0^+ state in ^{12}C situated above the 3α threshold with an excitation energy of 7.654 MeV. This state has a structure widely understood to correspond to 3 α-particles but the geometrical and physical interpretation of such a conclusion is still yet to be fully understood [2]. The Hoyle state is placed at a sufficient energy in ^{12}C such that it enhances the triple-α reaction rate by 7 orders of magnitude, allowing for the synthesis of ^{12}C and heavier elements, bypassing the A=5, 8 bottleneck in nucleosynthesis [3]. An experiment was performed using TexAT which had two objectives. Firstly, demonstrating the possibility of reconstructing the Hoyle state as it decays in 3 α-particles in TexAT at low pressures. Secondly, perform the most sensitive measurement of the direct 3α breakup branching ratio.

The first of these objectives is important for a subsequent experiment to be performed at Ohio State in 2019 where the ^{12}C(n,n$_2$) reaction rate is to be measured. In certain stellar environments, the inverse of this reaction (de-excitation of the Hoyle state via neutron scattering), can also enhance the triple-α reaction rate by an additional factor of up to 200. By measuring this inverse reaction, models of high density, high temperature stars can accurately reflect this important reaction which can have a dramatic effect on further nucleosynthesis processes.

The second experimental objective is rooted in nuclear structure physics. The 3α structure of the Hoyle state has been suggested as a condensate of α-particles in relative s-orbitals [4]. By virtue of the (pseudo)-bosonic nature of the α-particle, this idea therefore suggests a state of nuclear matter whereby the system transitions from a fermionic to a bosonic system presenting a fantastic chance to probe the properties of the nuclear force by observing this phase transition. Experimental efforts to determine whether such a hypothesis is true have focused on measuring the branching ratio of the Hoyle state whereby, rather than decaying sequentially to the ^{8}Be(g.s) then into a final state of α-particles, the decay occurs directly without any intermediate steps yielding a final state of 3 α-particles. The energy sharing of the α-particles are different with the direct decay corresponding to a more equal sharing of energy whereas with the sequential decay, one of the α-particles always carries roughly half of the decay energy and the other particles share the remainder with a known distribution. Measuring the decay of the Hoyle state and studying this energy partition can therefore provide a sensitive probe of the direct decay and

therefore elucidate on whether this α-condensate picture of the Hoyle state is correct. Recent experimental efforts have so far deduced an upper limit of 0.03% (95% C.L.) [5,6].

States in ^{12}C above the 3α-decay threshold (7.27 MeV) were therefore studied via the decay of ^{12}N. This β^+ decay has a half-life of 11.0 ms therefore must be investigated using the implantation technique rather than 'in-flight'. For this experiment, the Hoyle state is populated by ~1% of ^{12}N decays. The Hoyle state then decays itself (while at rest inside the TPC gas) into 3 α-particles which share 390 keV. This low energy therefore requires experimental care which is facilitated in this experiment by using a low pressure (20 Torr CO_2) fill gas in TexAT which gave the α-particles a long enough range that tracks can be measured. A decay-by-decay measurement can be achieved using the experimental setup shown in Fig. 1. This experiment was performed using the K500 cyclotron in September 2018 where experimental difficulties with TexAT meant only a limited amount of statistics were obtained. The

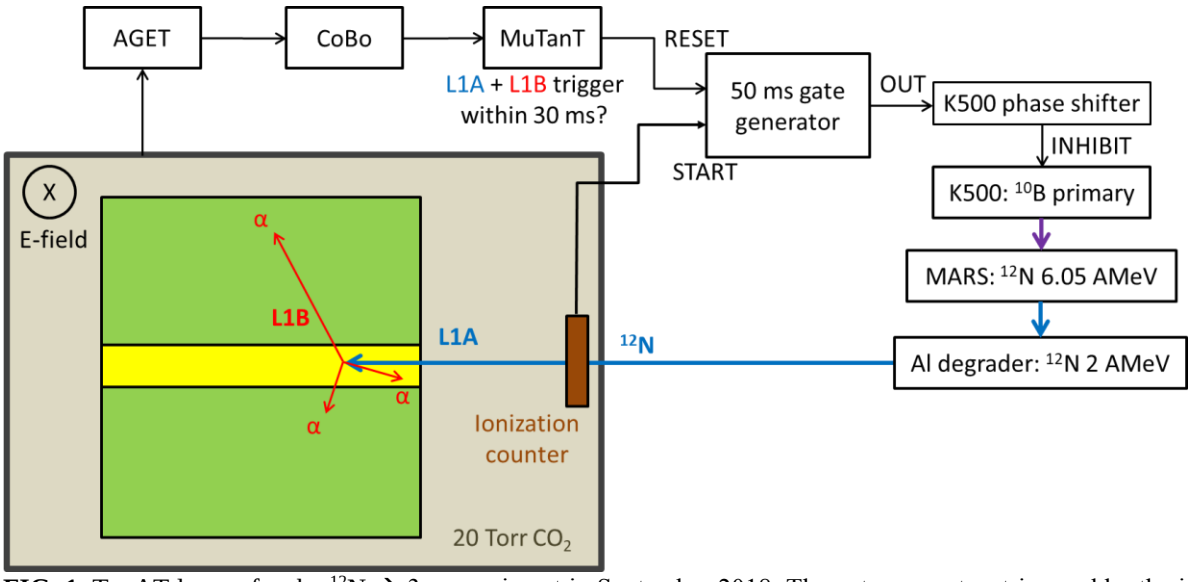

FIG. 1. TexAT layout for the ^{12}N → 3α experiment in September 2018. The gate generator, triggered by the ion counter and reset by the successful measurement of a 3 α-particle decay, feeds into the K500 cyclotron phase shifter. This allows for the beam to be stopped after an implantation has taken place. In the March 2019 experiment the gate generator was replaced by using the CoBo busy signal and half-events were read out (corresponding to L1A trigger but no L1B trigger within 30 ms).

experiment was repeated in March 2019 with 10 days of beam time. The primary beam of ^{10}B then provided a ^{12}N secondary beam via the (^{3}He,n) reaction in the gas-cell on the MARS line. The secondary beam entered the detector at around 2 AMeV with a typical production intensity of 30 pps.

The measured data were split into two different frames using the 2p-mode in the GET electronics system [7,8] with two separate triggers. The first, the L1A trigger, corresponds to the track of the ^{12}N being implanted in the TPC and stopping. From this information, the decay position of the ^{12}N can be determined as well as verification via the energy deposited along its path that the track is a ^{12}N implant rather than a beam contaminant. The second trigger, the L1B, corresponds to the 3 α-particle decay of states in ^{12}C following the β^+ decay of ^{12}N. The TPC allows for 3D tracks of the three α-particles to be reconstructed. By measuring the total energy deposited, the excitation energy can be calculated by E_x =

$E_{measured}$ + Q. Additionally, selecting tracks where the range of the α-particles correspond to that expected from the decay of the Hoyle state (with the maximum α-particle energy being 190 keV), a clean selection on Hoyle decays can be achieved, as seen in Fig. 2 for a subset of the data obtained in September 2018.

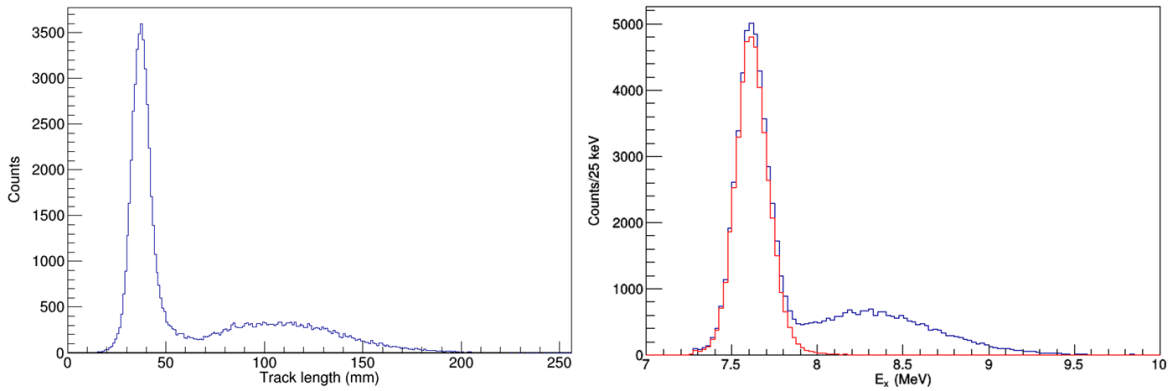

FIG. 2. Left: Length of the longest track from the measured 3 α-decay. The peak around 38 mm corresponds to the expected decay length from the Hoyle state. Right: Excitation function for 3 α-particle events following the decay of ^{12}N. The value is calculated from the total energy deposited in the TPC plus the Q-value of the decay (7.27 MeV). The red line corresponds to selecting events where the longest α-particle track is commensurate with a 190 keV energy corresponding to the decay of the Hoyle state into ^{8}Be(g.s) + α.

The first experimental objective, to demonstrate the ability to reconstruct 3 α-particles in TexAT has been completed and this experiment has allowed the analysis code to be well developed for the ^{12}C(n,n$_2$) experiment as well as a consideration of the necessitudes of further improvements to TexAT. The second experimental objective, to extract a direct decay branching ratio, is still on-going however with an estimated **80,000** Hoyle decays measured in an almost background-free environment, this allows for a sensitivity a factor of 40 lower than the previous experimental results which may be sufficient to measure an absolute value rather than an improved limit [9].

[1] J. Hooker, G.V. Rogachev, E. Koshchiy, S. Ahn, M. Barbui, V.Z. Goldberg, C. Hunt, H. Jayatissa, E. C. Pollacco, B.T. Roeder, A. Saastamoinen, and S. Upadhyayula, *arXiv:1903.01402.*

[2] M. Freer and H.O.U. Fynbo, Prog. Part. Nucl. Phys. **78**, 1 (2014).

[3] E.M. Burbidge, G.R. Burbidge, W.A. Fowler, and F. Hoyle, Rev. Mod. Phys. **29**, 547 (1957).

[4] A. Tohsaki, H. Horiuchi, P. Schuck, and G. Röpke, Phys. Rev. Lett. **87**, 192501 (2001).

[5] R. Smith, Tz. Kokalova, C. Wheldon, J. Bishop, M. Freer, N. Curtis, and D.J. Parker, Phys. Rev. Lett **119**, 132502 (2017).

[6] D. Dell'Aquilla *et al*., Phys. Rev. Lett. **119**, 132501(2017).

[7] E.C. Pollacco *et al*., Nucl. Instrum. Methods Phys. Res. **A887**, 81 (2018).

[8] J. Giovinazzo *et al*., Phys. Rev. Lett. **99**, 102501 (2007).

[9] H. Zheng, A. Bonasera, M. Huang, and S. Zhang, Phys. Lett. B **779**, 460 (2018).

Study of ^{8}B + ^{40}Ar fusion reaction using TexAT

S. Ahn,[1] G.V. Rogachev,[1,2] S.M. Lukyanov,[3] J.C. Zamora,[4] E. Aboud,[1,2] M. Assunão,[5] M. Barbui,[1]
J. Bishop,[1,2] C. Hunt,[1,2] V. Guimarães,[4] H. Jayatissa,[1,2] E. Koshchiy,[1] R. O'Dwyer,[1,2]
Yu.E. Penionzhkevich,[3] B.T. Roeder,[1] A. Saastamoinen,[1] and S. Upadhyayula[1,2]
[1]*Cyclotron Institute, Texas A&M University, College Station, Texas*
[2]*Department of Physics & Astronomy, Texas A&M University, College Station, Texas*
[3]*Flerov Laboratory of Nuclear Reactions, Dubna, Russian Federation*
[4]*Instituto de Fisica, Universidade de São Paulo, Brazil*
[5]*Universidade Federal de São Paulo, Brazil*

The study of fusion reactions induced by light exotic radioactive beams is a powerful tool to understand a variety of interesting and new dynamic effects present in weakly-bound systems. For instance, the low-binding energy and strong cluster configurations in exotic nuclei would produce a decoupling between the valence particle and the core nucleus, which give rise to an increase of the breakup and/or transfer probability in total reaction cross section. However, still it is a question whether fusion in the Coulomb barrier energy region of halo nuclei such as ^{6}He (two-neutron halo nucleus) or ^{8}B (one-proton halo nucleus) is enhanced owing to the extended nuclear-matter distribution, or hindered due to the fact that such nuclei break into two or more fragments. However, the influence of the breakup in the elastic and fusion processes induced by exotic nuclei is not well known and challenging to study in both theory and experiment. Thus, the study of heavy ion fusion has been a subject of renewed interest in our community [1].

The study of ^{8}B fusion reaction on ^{40}Ar has been performed at the Cyclotron Institute of the Texas A\&M University. A primary beam of ^{6}Li was used to create the ^{8}B beam through the two proton pickup reaction (^{3}He,*n*) and a 97% pure ^{8}B beam at energies of 40 MeV and 48 MeV was produced by the recoil separator MARS. This was the first fusion experiment using the recently developed active target, TexAT. The beam was impinged on the ^{40}Ar gas target in the scattering chamber filled with an Ar:CH_4 95:5 (P5) gas mixture at a gas pressure ranging from 150 Torr to 210 Torr. The gas pressure was adjusted for the unreacted ^{8}B beam barely make it to the downstream silicon detector resulting in the fusion product not making any trigger on the silicon detector. Then, the trigger of the silicon detector was used to veto all events of unreacted beam and elastic scattering at small angles, and only fusion-like events could be recorded in data. Fig. 1(a) shows a typical fusion event observed on the Micromegas. As the beam particle loses its kinetic energy in the gas, the beam energy of the fusion reaction is determined by the vertex point where the reaction happened and this provides us the possibility to investigate fusion reactions in a wide range of center-of-mass energies around the Coulomb barrier (V_C = 16.4 MeV). The resulting compound nucleus and the respective fission fragments produce a higher energy loss (in comparison to the unreacted beam) in the gas and stops in only few millimeters of the active area of the Micromegas. Therefore, a large energy loss signal is observed at the edge of the ion range spectra, as seen in Fig. 1(b).

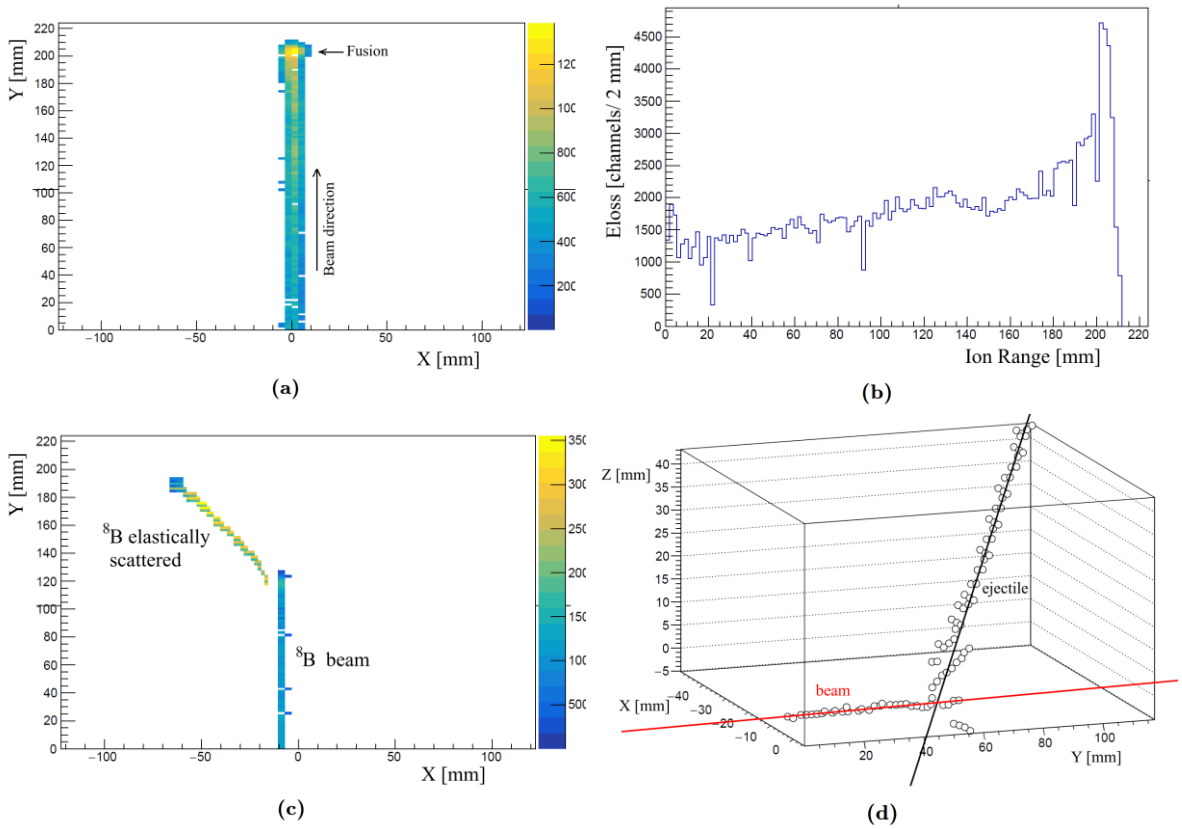

FIG. 1, (a) Fusion event detected on the Micro Megas plane. (b) Ionization ion range of a fusion event. (c) Elastic scattering event. (d) 3 dimensional reconstruction of an elastic scattering event.

In order to fully determine the fusion events from other reaction channels, e.g. elastic scattering (see Fig. 1(c)), it is necessary to have a good method to identify hit patterns. In the present analysis, the RANSAC (random sample consensus) [2] algorithm has been implemented to identify and fit the particle tracks in the 3-dimensional space. The same routine has been successfully used in the analysis of other active target experiments such as AT-TPC and ACTAR. Fig. 1(d) shows a scattering event that was fitted with RANSAC. The next step is to apply the routines to identify all the fusion-fission events measured in the ^{8}B + ^{40}Ar experiment.

Fig. 2 shows a preliminary fusion excitation function from the data taken for two hours of beam time. While the analysis was performed by inspecting event-by-event basis, we are working on developing a tool for the identification of fusion events as mentioned earlier.

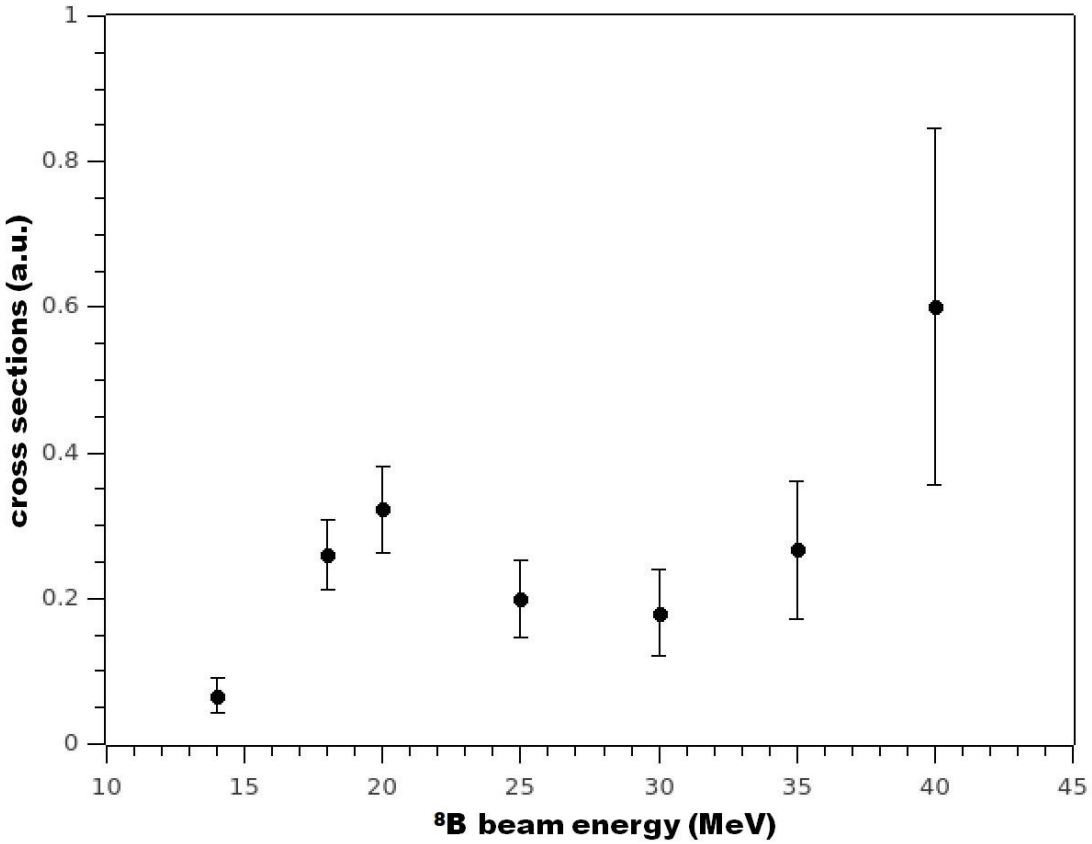

FIG. 2. Preliminary fusion excitation function.

[1] L.F. Canto *et al.*, Phys. Rep. **596**, 1 (2015).

[2] Y. Ayyad *et al.*, Nucl. Instrum. Methods Phys. Res**. A880**, 166 (2018).

Search for the low-lying T=5 states in ^{48}Ca

S. Upadhyayula,[1] A. Hood,[2] C Deibel,[2] C. Hunt,[1] D. Santiago-Gonzalez,[2,3] G. Rogachev,[1] J. Blackmon,[2] J. Lighthall,[2] J. Hooker,[1] J. Browne,[4] M. Anastasiou,[5] N. Rijal,[5] S. Bedoor, S. Ahn,[1,4] W. Ong,[4] and Y. Koshichy[1]

[1]*Cyclotron Institute, Texas A&M University, College Station, Texas*

[2]*Louisiana State University, Baton Rouge, Louisiana*

[3]*Argonne National Laboratory, Argonne, Illinois*

[4]*NSCL, Michigan State University, East Lansing, Michigan*

[5]*Florida State University, Tallahassee, Florida*

Particle-hole excitations near closed shells carry information on single-particle energies and on two-body interactions [1,2]. The particle-hole excitations near the doubly magic nuclei are of special interest. Information on the charge-changing particle-hole excitations (T= 5 negative parity states) in ^{48}Ca is not currently available (Fig. 1). We performed an experiment to establish the level scheme of the low-lying negative parity T=5 states in ^{48}Ca. Excitation functions for the ^{1}H (^{47}K, p) ^{47}K reaction in the c.m. energy range from 1 MeV to 4.5 MeV were measured. The T= 5 states are expected to show up in the p+^{47}K excitation function as narrow resonances.

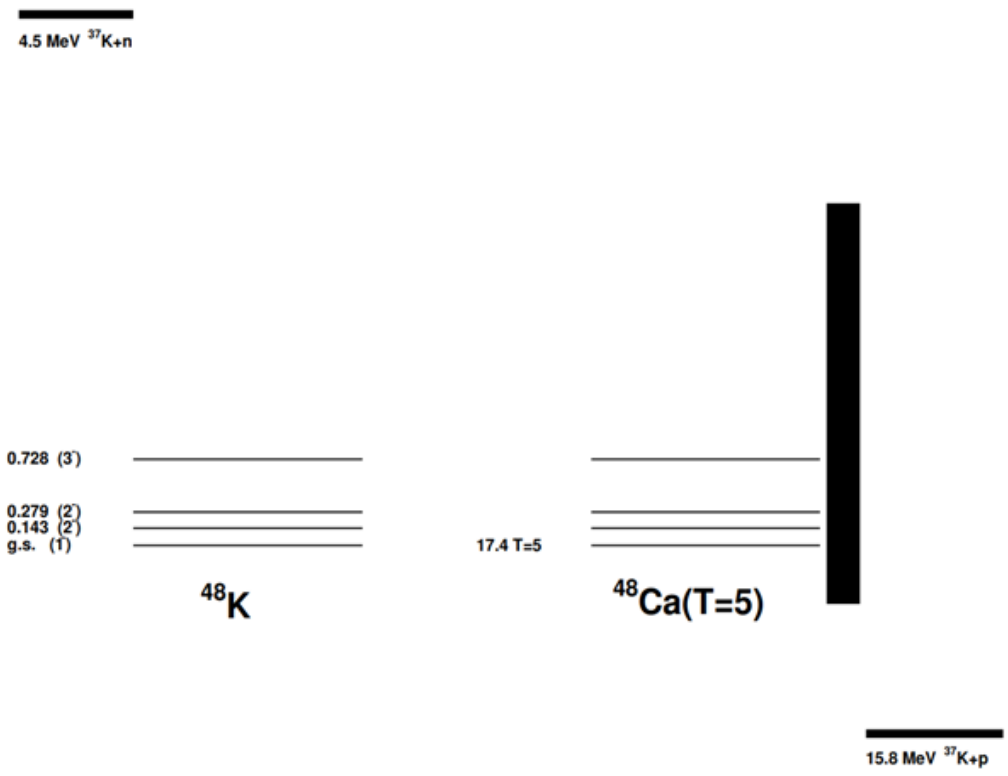

FIG. 1. Level scheme of ^{48}K from [4] and the corresponding (unknown) T=5 isobaric analog states in ^{48}Ca with relevant decay thresholds. Bold vertical line indicates the measured excitation energy range in this experiment.

This experiment was performed at NSCL using the ReA3 beam of ^{47}K at energy of 4.6 MeV/u with an intensity of 10^4 particles per second. The Array for Nuclear Astrophysics and Structure with Exotic Nuclei (ANASEN) [3], set in active target mode, was used for this experiment. Position sensitive silicon barrel and forward annular detector arrays were used along with a cylindrical proportional counter that was installed along the beam axis. Methane gas was used as the active gas volume for the proportional counter wires as well as the target. A 5μm scintillator read out by two PMTs was set up by the entrance of the chamber. There was another thick scintillator that was installed downstream of the beam in the middle of the annular forward detector array. These two scintillators were used together to allow us the measurement of the overall beam normalization as well as to identify any beam contaminants. The gas pressure was set to 95 Torr, allowing the beam ions to make it to the downstream scintillator.

The thick target inverse kinematics technique [4], combined with the active target capabilities of ANASEN detector allows us to measure entire excitation function for ^{47}K+p without changing the energy of the incident beam. The recoil protons were detected by the silicon array, which provided the main trigger for the data acquisition system. These recoil protons were identified using their energy loss in the proportional counter cells (Fig. 2). The position of the hit in the silicon along with the position detected in the proportional counter allows us to reconstruct the reaction vertex location for event identification (Fig. 3).

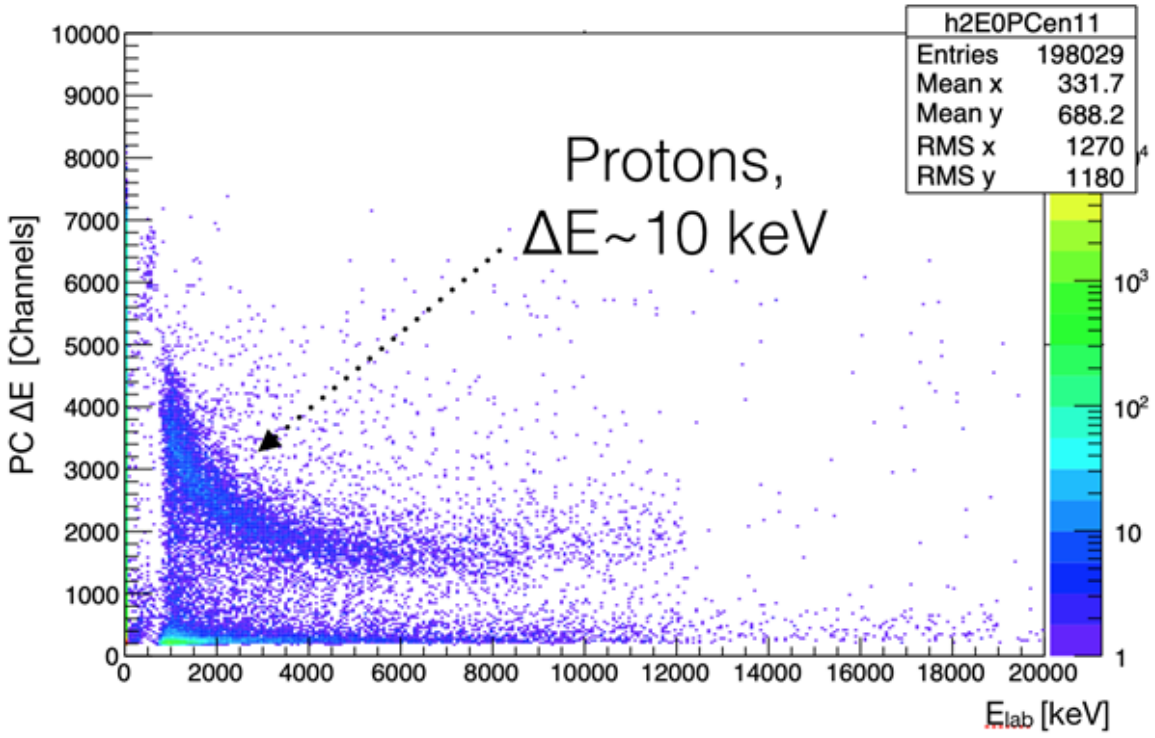

FIG. 2. dE-E plot to identify protons.

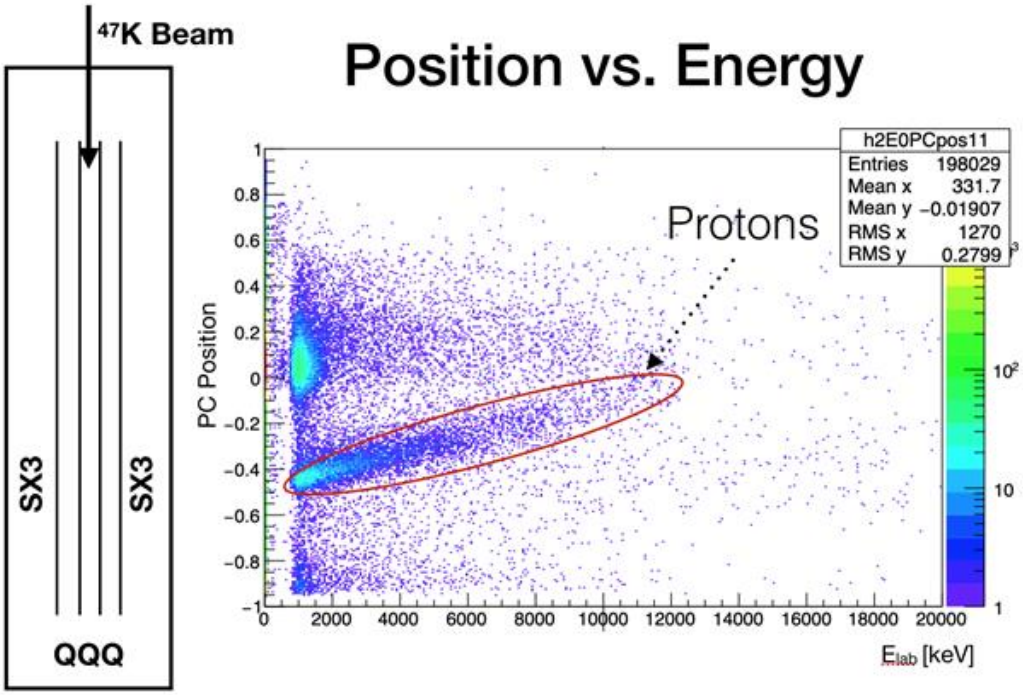

FIG. 3. Uncalibrated position in proportional counter wire.

The main goal of this experiment is to establish the level scheme of the low-lying negative parity T=5 states in ^{48}Ca. These states are expected to show up as relatively narrow resonances between the excitation energy range from 17 MeV to 22 MeV. A preliminary excitation function for ^{47}K+p is shown in Fig. 4 (representing about 10% of the data). There is an indication of narrow states, but the spectrum is

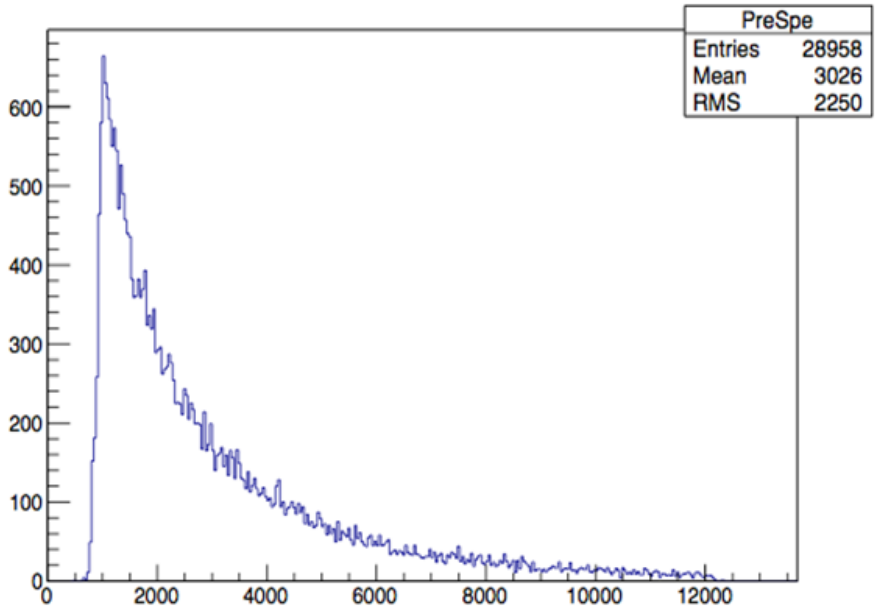

FIG. 4. Preliminary excitation function with about 10% of statistics. We see a peak of interest around 4 MeV.

dominated by Rutherford scattering, as expected. Further analysis is needed to confirm the existence of the isobaric analogue states (with higher statistics) and to extract the excitation function for p+^{47}K elastic scattering. The excitation energies, spin-parities and proton decay widths will be determined using R-Matrix analysis.

[1] T. Otsuka *et al.*, Phys. Rev. Lett. **95**, 232502 (2005).
[2] J. Suhonen, "From Nucleons to Nucleus", Springer-Verlag, ISBN 0172-5998 (2007).
[3] E. Koshchiy *et al.*, Nucl. Instrum. Methods Phys. Res. **A870**, 1 (2017).
[4] K.P. Artemov *et al.*, Sov. J. Nucl. Phys. **52**, 408 (1990).
[5] W. Krolas *et al.*, Phys. Rev. C **84**, 064301 (2011).

Clustering in ^{10}Be

S. Upadhyayula, G.V. Rogachev, E. Koshchiy, E. Uberseder, V.Z. Goldberg, J. Hooker,
H, Jayatissa, C. Hunt, and B.T. Roeder

There is a strong experimental evidence that some states in ^{10}Be exhibit a molecular-like α:2n:α configuration [1,2,3]. Theoretically, these exotic structures can be explored microscopically in the antisymmetrized molecular dynamics (AMD) plus Hartree-Fock approach [4] or in the Molecular Orbital model [5]. Based on these theoretical studies, it appears that the 6.179 MeV 0^+ state in ^{10}Be has a pronounced α:2n:α configuration with an α-α inter-distance of 3.55 fm. This is 1.8 times the corresponding value for the ^{10}Be ground state. The 2^+ resonance at 7.542 MeV in ^{10}Be is believed to be the next member of this rotational band [6]. The state at 10.2 MeV was identified as a 4^+ member [1, 3]. The algebraic model [7] predicts that a 6^+ state at around 13 MeV is the next member of this band. It would be of paramount importance to identify this 6^+ state experimentally and to conclusively establish the α:2n:α rotational band. This would become the most striking and well established case of molecular-like configurations in nuclei and an important step towards a better understanding of clustering phenomena in atomic nuclei.

We performed an experiment to search for the 6^+ state in ^{10}Be at around 13 MeV excitation energy using ^{6}He+α scattering. The Cyclotron Institute Momentum Achromat Recoil Separator (MARS) facility was used to produce a secondary ^{6}He beam at 7.0 MeV/u from the production reaction of ^{7}Li(d,^{3}He). A sketch of the experimental setup is shown in Fig. 1. The modified thick target inverse

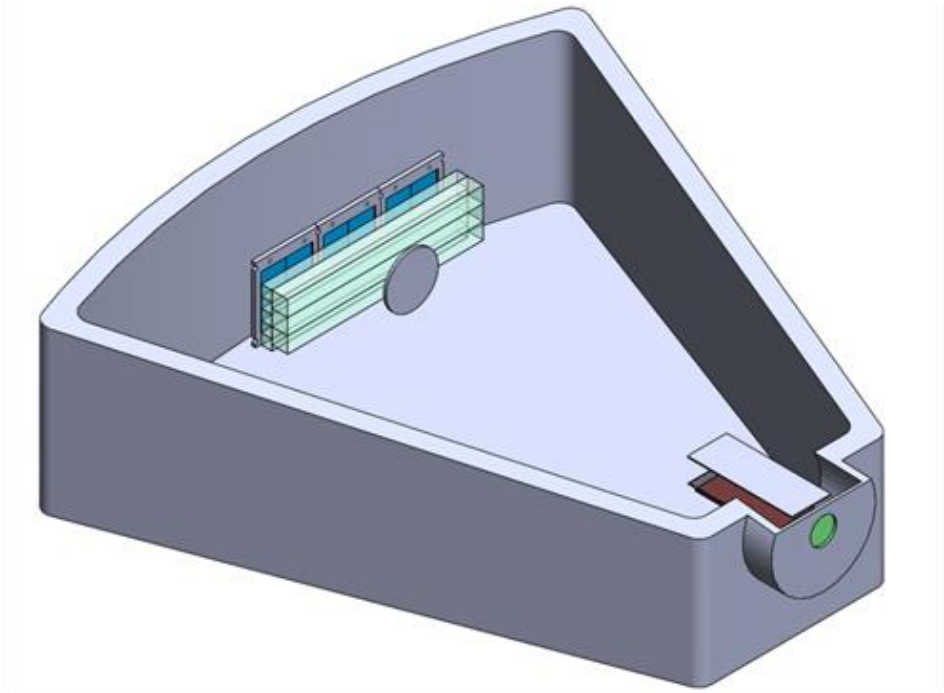

FIG. 1. Sketch of the experimental setup to measure the ^{6}He+α excitation function of ^{10}Be excitation energy.

kinematics approach [8] was used to measure the ^{6}He+α excitation function. Details of the experimental setup can be found in [9]. The energy of the ^{6}He beam was reduced down to 22 MeV by a thick scintillator foil located in front of the scattering chamber filled with a helium+CO_2 96:4 gas mixture at a pressure of 1700 Torr.

We have observed a distinct peak in the α particles energy spectrum that could be a result of the resonance in the ^{6}He+α excitation function which we were looking for. This peak in the α spectrum was verified to be associated with the incoming ^{6}He beam particles and not the other beam contaminants, the dominant of which is tritium. Given the nature of the set up, we expect the highest energy α particles (between 12 and 15 MeV) to correspond to pure elastic scattering. At lower energies, admixtures from α particles due to inelastic scattering and breakup are also possible. Based on the shape of the spectrum compared to Monte Carlo simulations (Fig 3), the experimental yield and angular dependence of the cross section, we can conclude that the α spectrum is dominated by the breakup of ^{6}He into α+2n at energies below 8 MeV.

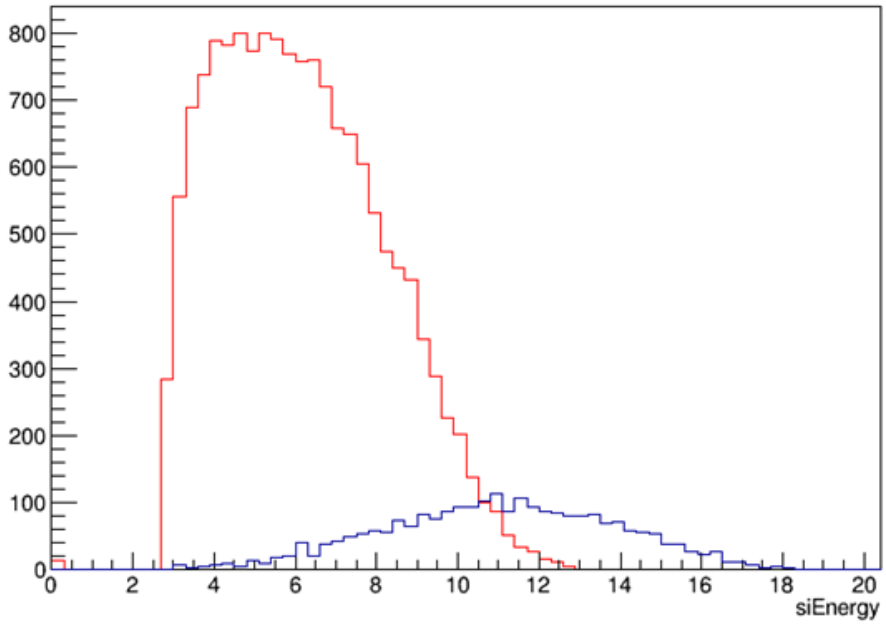

FIG. 2. Monte Carlo simulation of α particles spectrum due to breakup of ^{6}He. The (red) curve at lower energy shows α particles from ^{6}He decay. The (blue) curve at higher energy shows α particles due to elastic scattering.

For analysis purposes, we have divided the three different angles in our set up into regions. The detector at forward angles corresponds to Region 1. The other two angles (170° and 162° in the center of mass frame) correspond to Region 2 and Region 3 respectively. The peak in the α spectrum due to the hypothetical 6^{+} state at 13.5 MeV [10,11,12] would appear in the vicinity of 8 MeV in the lab frame in Region 2 and 6.5 MeV in Region 3 (Fig. 2). We also expect the inelastically scattered α particles to show

a peak around 6 MeV and 4 MeV in the lab frame in Regions 2 and 3 respectively. There is no indication for a resonance-like structure in our spectrum at that energy at any angle that is statistically significant enough to be observed above the breakup contribution. Since we can't conclusively claim the origins of the α particles in the entire spectrum, we were not able to extract a clean excitation function for ^{6}He+α elastic scattering.

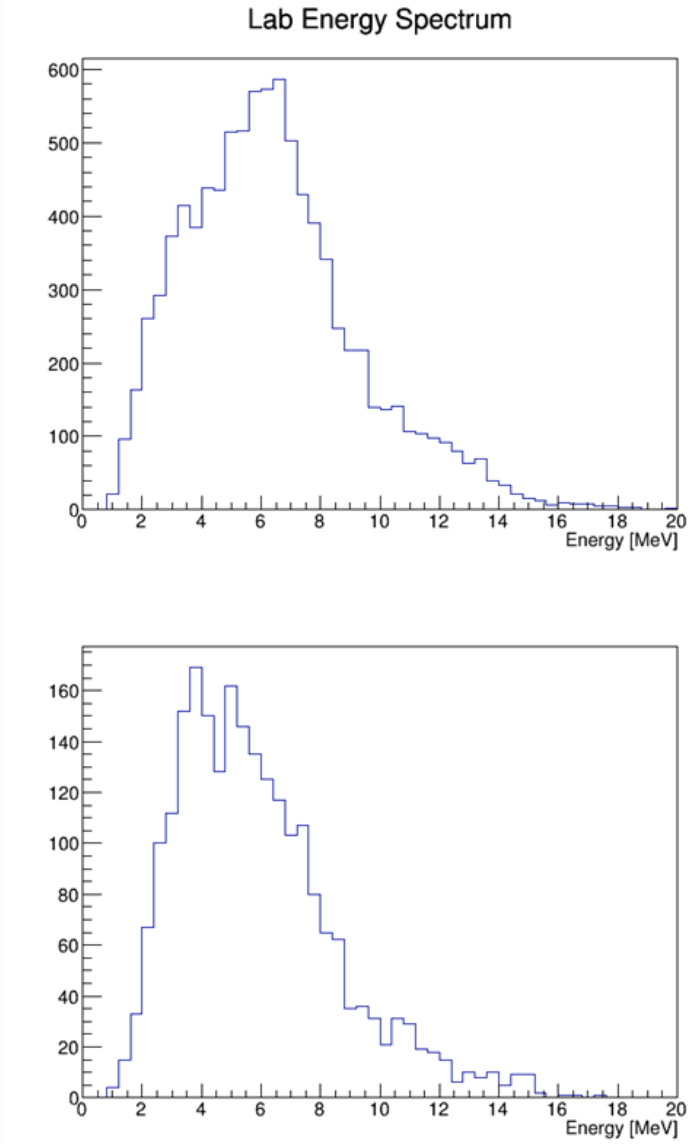

FIG. 3. Spectrum of α particles measured by the off-center Si detectors. The peak at 7 MeV is a result of ^{6}He decay into α + 2n (see text for details).

We performed further GEANT4 simulations to better characterize the experimental spectra. In these simulations, we scaled the reactions (elastic and inelastic scattering) using the cross sections obtained from our R-Matrix analysis. Spectroscopic factors provided by [13] along with parameters

provided by [12] were used. These reactions were further scaled by the absolute normalization from the experiment. The results from the simulations can be seen in Fig. 4. We then subtracted the contribution

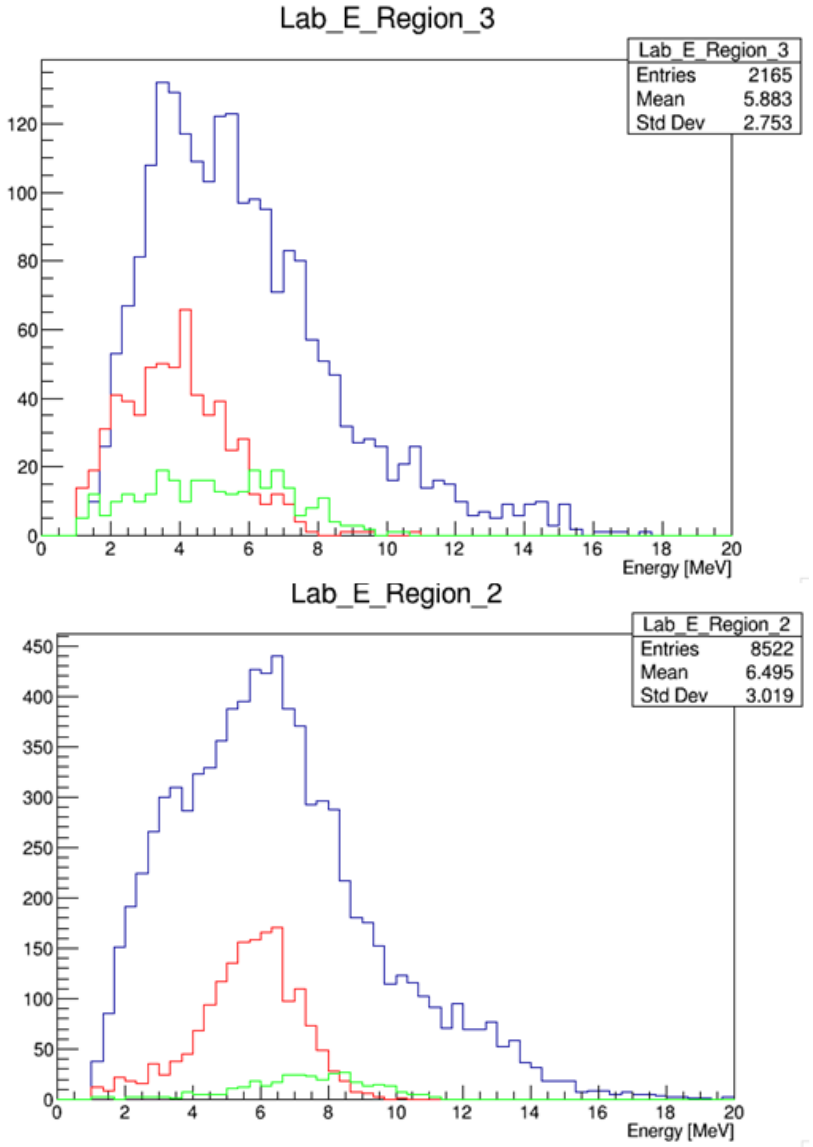

FIG. 4. Blue curve represents our experimental spectrum. Red and green curves represent the simulated inelastic and elastic contributions respectively. Widths resulting from spectroscopic factors (0.1 for elastic and 0.66 for inelastic) provided in [13] were used for the simulations.

from the elastic and inelastic simulations from the experimental spectra to see whether the remaining spectrum is consistent with the breakup process. We also performed a chi-squared hypothesis test to check this (Fig 5). Based on this, we can conclude that the parameters from [12] are **inconsistent** with a 6^+ state at 13.5 MeV. However, if we modify the parameters of the 6^+ state at 13.5 MeV to those from [13] and assume that there is also a breakup that is described by Maxwell-Bolzman distribution then a good description of the observed spectrum can be achieved.

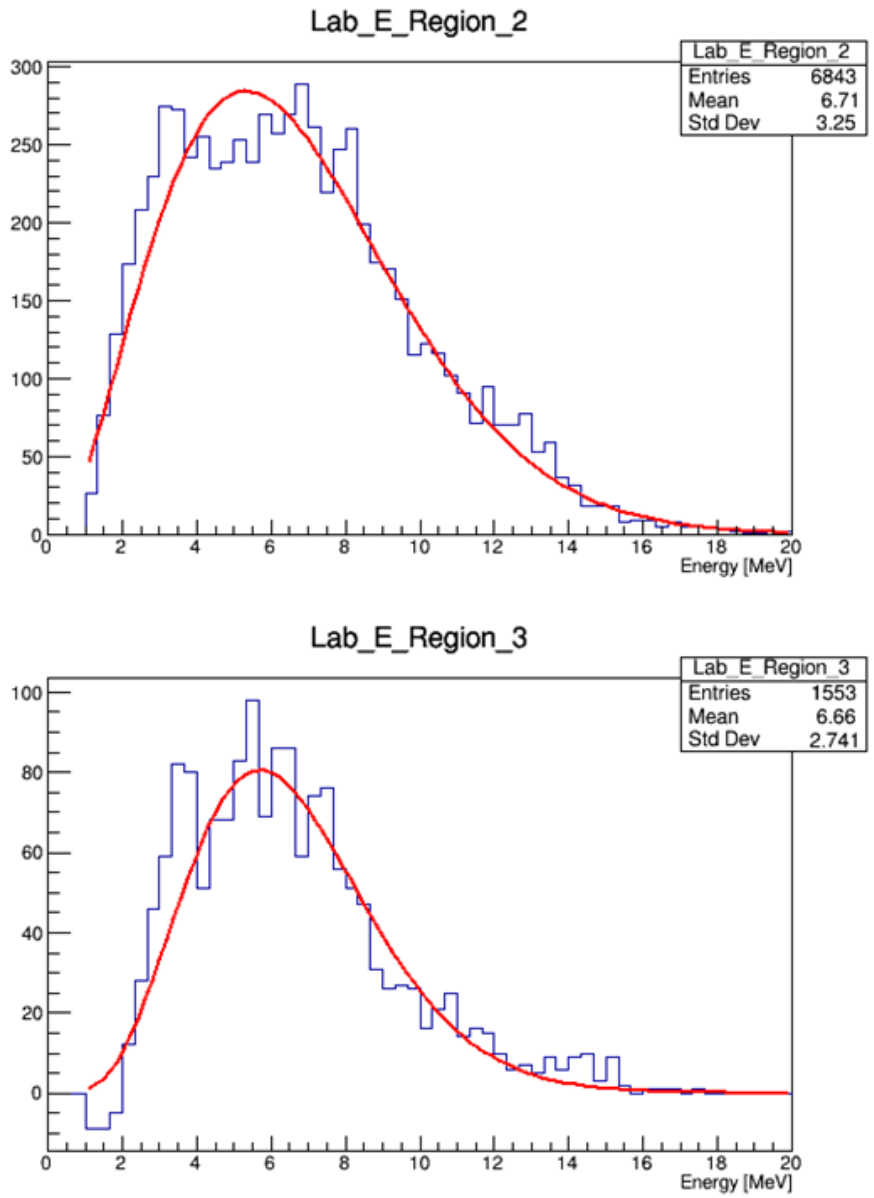

FIG. 5. Blue curve is the resulting spectrum after the simulated elastic and inelastic contributions from Fig. 4 have been subtracted. The red curve is a poisson distribution fit.

In summary, we have performed a search for the lowest 6^+ state in ^{10}Be, which was suggested as the next member of the molecular α:2n:α rotational band [7], in the excitation function for ^{6}He+α. No evidence for strong resonance have been observed in the energy range between 11 and 15 MeV (it was expected at 13 MeV). However, if we assume that the dominant configuration for this state is ^{6}He(2^+)+α, and that the coupling to the ^{6}He(g.s.)+α channel is relatively small, as suggested in [13], than the experimentally observed spectrum can be reproduced as a breakup of ^{6}He plus a resonance at 13.5 MeV in ^{10}Be that decays predominantly to the first excited state of ^{6}He. This experimental information provides important constraints on the theoretical models describing clustering in ^{10}Be and lends support

to predictions made in [13]. It is clear, however, that further experiments are needed to confirm possible existence of this state in ^{10}Be and to further characterize its properties.

[1] M. Freer *et al.*, Phys. Rev. Lett. **96**, 042501 (2006).

[2] M. Milin *et al.*, Phys. At. Nucl. **69**, 1360 (2006).

[3] D. Suzuki *et al.*, Phys. Rev. C **87**, 054301 (2013).

[4] A. Doté, H. Horiuchi, and Y. Kanada-Enýo, Phys. Rev. C **56**, 1844 (1997).

[5] N. Itagaki and S. Okabe, Phys. Rev. C **61**, 044306 (2000).

[6] A.N. Kuchera *et al.*, Phys. Rev. C **88**, 054615 (2011).

[7] R. Wolsky *et al.*, Phys. At. Nucl. **73**, 1405 (2010).

[8] K. Artemov *et al.*, Sov. J. Nucl. Phys. **52** 408 (1990).

[9] S. Upadhyayula *et al.*, *Progress in Research*, Cyclotron Institute, Tesas A&M University (2016-2017), p. I-54.

[10] D. Dell'Aquila *et al.*, Phys. Rev. C **93** 024611 (2016).

[11] E. Koshchiy *et al.*, Nucl. Instrum. Methods Phys. Res. **A870**, 1 (2017).

[12] A.N. Kuchera, Ph.D. Thesis, Florida State University, 2013.

[13] K. Kravvarisb and A. Volya, AIP Conference Proceedings **2038**, 020026 (2018).

Resonant elastic scattering of ^{14}O on α particles studied with the TexAT active target

M. Barbui,[1] E. Aboud,[1] S. Ahn,[1] J. Bishop,[1] V.Z. Goldberg,[1] J. Hooker,[1] C.H. Hunt,[1] H. Jayatissa,[1] Tz. Kokalova,[2] E. Koshchiy,[1] C. Magana,[1] R. O'Dwyer,[1] S. Pirrie,[2] E. Pollacco,[3] B.T. Roeder,[1] A. Saastamoinen,[1] E. Uberseder,[1] S. Upadhiayula,[1] C. Wheldon,[2] and G.V. Rogachev,[1,4]

[1]*Cyclotron Institute, Texas A&M University, College Station, Texas*

[2]*School of Physics and Astronomy, University of Birmingham, Birmingham, United Kingdom*

[3]*IRFU, CEA, Saclay, Gif-Sur-Ivette, France*

[4]*Department of Physics&Astronomy, Texas A&M University, College Station, Texas*

The reaction ^{14}O + alpha was studied at Cyclotron Institute of Texas A&M University as part of the commissioning experiments for the TexAT active target [1]. The ^{14}O beam was produced using Magnetic Achromat Recoil Separator (MARS) with the reaction ^{14}N(p,n)^{14}O. The ^{14}N primary beam with energy of 11 MeV/nucleon was delivered by the K500 Cyclotron. The energy of the ^{14}O beam was 61.8 MeV and the intensity was about 10^4pps.

The data analysis is still in process. The Energy calibration of the TexAT Silicon detectors has been performed using alpha sources. During the run with the beam, some of the signals were saturated. In order to recover the energy of these signals, an average signal of unitary amplitude has been produced by averaging at least 10000 non-saturated waveforms normalized to amplitude one. The real amplitude of the saturated signals has been obtained overlapping the saturated signal with the average signal, normalized to match the tails of the saturated signal. After this procedure ΔE-E plots were produced using the energy deposited in the last few centimeters of the Micromegas as ΔE and the energy deposited in the Silicon detector as E. Fig. 1 shows that the alpha particles can be easily separated from the protons. Alpha particles were identified with a two-dimensional gate around the alpha particle ridge.

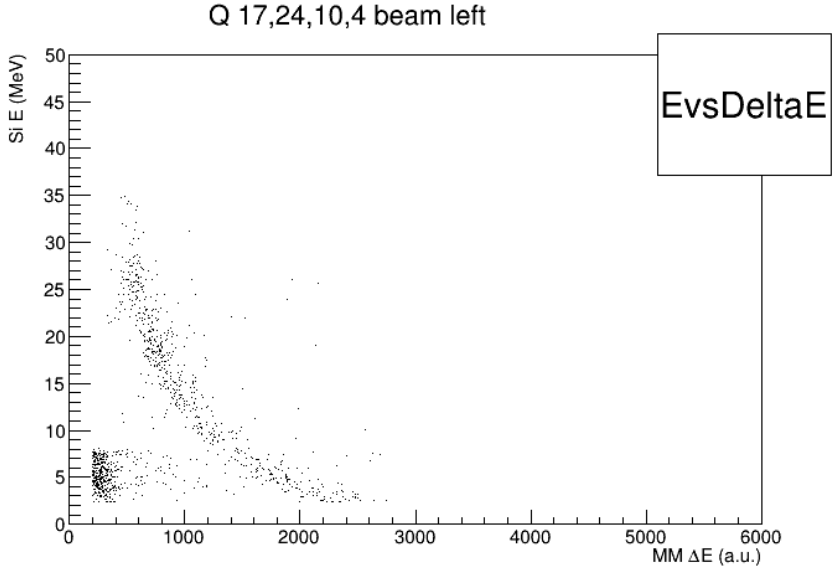

FIG. 1. E vs. ΔE plot.

For each waveform, the timing has been picked up at the 15% of the waveform amplitude as shown in Fig. 2. The tracks of the alpha particles detected in each silicon detector were reconstructed.

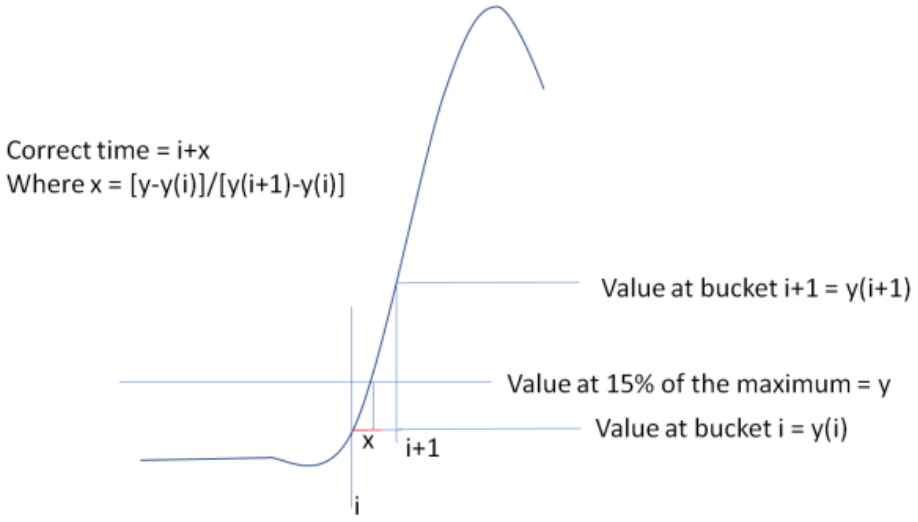

FIG. 2. For each waveform the time is determined at the 15% of the waveform maximum.

The first step of the track reconstruction is done by matching strips and chains in the side regions of the micromegas. This is done for each event using the timing information. For each strip signal, the corresponding chain should have a signal at the same time. After this matching, the Hough transform is used to further clean the tracks from spurious hits produced by random pads firing in coincidence with the track. This procedure is commonly used to optimize the tracking on Time Projection Chambers (see for example Ref. [2]). Event by event, the position of the interaction point in the active target is obtained

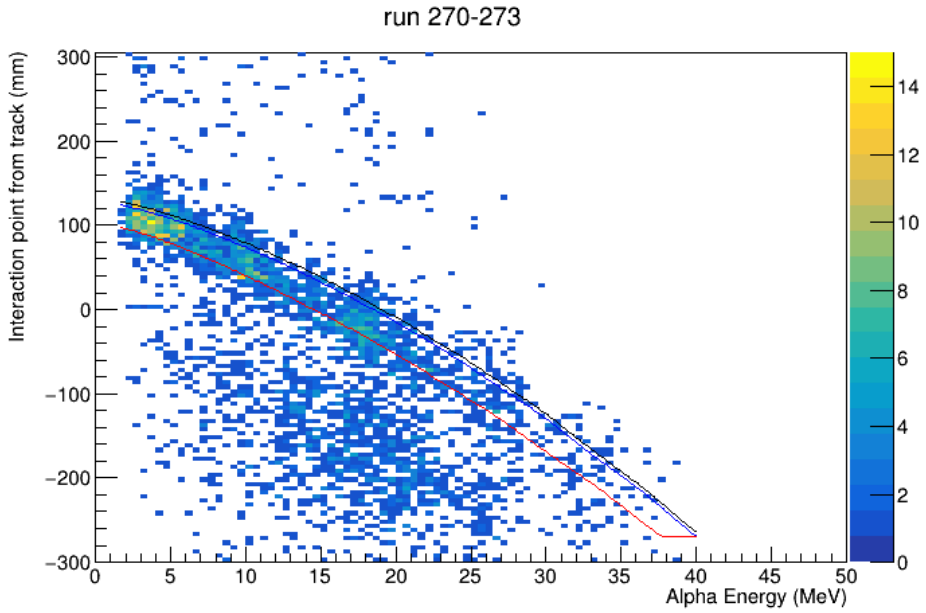

FIG. 3. Interaction point reconstructed from the tracks as a function of the alpha particle energy detected in the silicon detectors. The lines show the interaction point calculated for elastic scattering at 0 degrees (black), 5 degrees (blue), 15 degrees (red).

by intersecting the track corresponding to the detected alpha particle with the track of the beam, if the interaction point is in the region covered by the Micromegas or with the ideal beam line if the interaction point was before the beginning of the Micromegas. Fig. 3 shows the position of the reconstructed interaction point as a function of the alpha particle energy. The interaction point for elastic scattering, calculated from the reaction kinematics at 0, 5 and 15 degrees is also shown in the picture.The events corresponding to elastic scattering of ^{14}O on ^{4}He form a ridge inside the lines from the calculation. Events corresponding to inelastic scattering are located below this region. The determination of the interaction point in the central region requires a different procedure and is still in process.

The elastic scattering events are selected with a 2 dimensional gate around the elastic ridge in Fig. 3. The excitation function of ^{18}Ne at different angles then obtained using these events. Fig. 4 shows as example the excitation function measured at 5 degrees compared with previous data for the same reaction, measured with a thick passive target. The data analysis is still in progress, the full statistics of data needs to be processed and further R-matrix analysis needs to be performed on the measured excitation function.

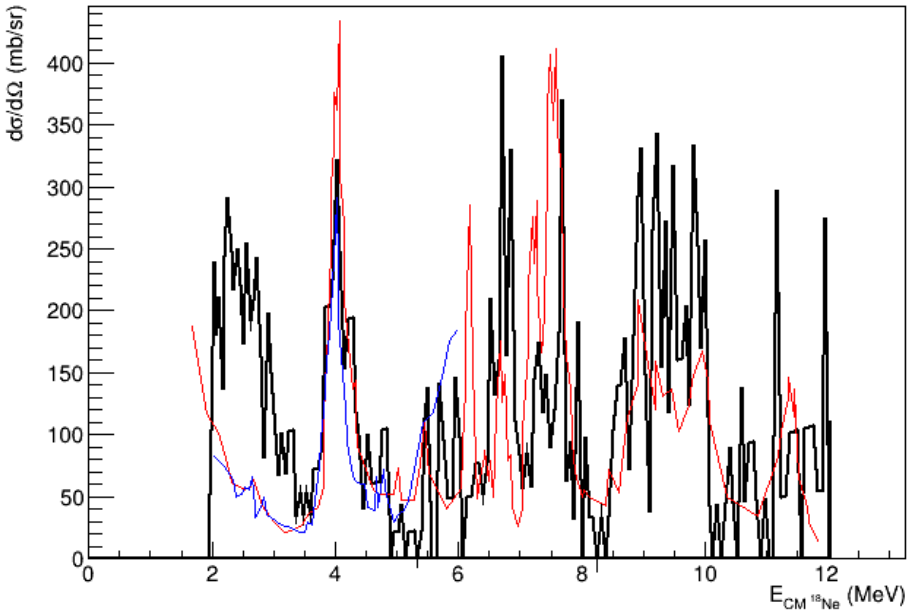

FIG. 4. Preliminary excitation function of ^{18}Ne measured at 4^{o} from the entrance window (black line), compared with the data in Ref.[3] measured with a passive thick target at 4^{o} (blue line) and 0^{o} (red line).

[1] E. Koshchiy *et al.*, *Progress in Research*, Cyclotron Institute, Texas A&M University (2016-2017), p. IV-56.

[2] C. Santamaria *et al.*, Nuclear Instrum. Methods Phys. **A905**, 138 (2018).

[3] C.B. Fu *et al.*, Phys. Rev. C **77**, 064314 (2008).

T=3/2 isobaric analog states in ^{9}Be

C. Hunt, G.V. Rogachev, V.Z. Goldberg, E. Koshchiy, B.T. Roeder, T. Ahn, J. Hooker,
H. Jayatissa, and S. Upadhyayula

Shell evolution with increasing imbalance between protons and neutron is a major question in modern nuclear physics [1,2,3,4]. Experimental information on structure of neutron rich nuclei opens a window into detailed understanding of shell evolution. The study of neutron rich nuclei is currently done with transfer reactions, knock-out reactions and charge exchange experiments. It has been proposed that proton resonance scattering could be used instead by populating isobaric analog states [5]. This would allow for the use of Thick Target Inverse Kinematics and R-Matrix analysis for the study of neutron rich nuclei. However, the higher isospin states in the analogous nuclei tend to be higher energy excited states and at these energies there tend to be many lower isospin states. For complete analysis, the R-Matrix would be used for narrow resonances in the regions of interest while the optical model would be used for the featureless background created by numerous wider T-low states. The A=9, T=3/2 isobaric quartet makes a good test case. ^{9}Li [6] and ^{9}Be have already been studied with transfer reactions and ^{9}C [7] has been studied with resonance scattering. This allows for a comparison of T=3/2 states in ^{9}Be that are above the proton threshold to the analogous states in ^{9}Li and ^{9}C.

In August of 2017 we had the commissioning run of the TexAT [8] active target detector system on the MARS [9] beamline. As part of the commissioning run a 75.5 MeV ^{8}Li beam was produced. TexAT was filled with 470 Torr of iso-butane gas. The goal was to measure the excitation function for ^{8}Li+p to study the T=3/2 states in ^{9}Be. The general view of TexAT detector is shown in Fig 1. In the configuration used for the commissioning run there were fifteen 5x5 cm^{2} Si detectors, segmented into

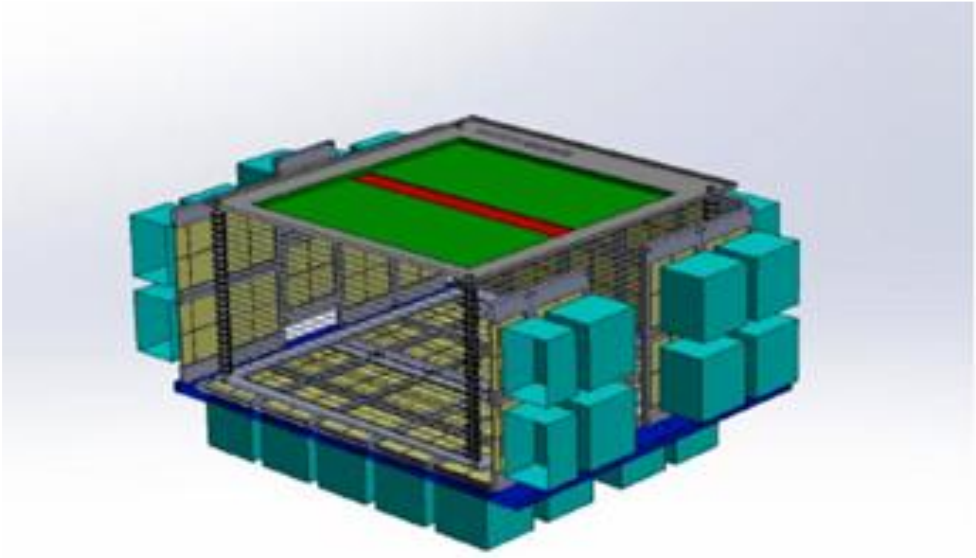

FIG. 1. The general view of TexAT detector.

four quadrants, backed by CsI detectors to measure protons that punch through the 0.7-1 mm thick Si detectors. The forward wall consisted of nine Si detectors and the beam left wall consisted of six detectors. On the top of the chamber was a segmented micromegas plate. The central region was highly segmented with 128 rows of 6 pixels. The side regions were multiplexed, with long strips across the side regions and long chains running the length of the detector. The micromegas, thus, provide particle tracking within the chamber and the Si and CsI detectors measure the energy of the light recoil particles.

TexAT is an active target that allows for the reaction vertex location to be determined. It can be done by tracking of the recoils, but also using information on energy losses along the beam axis. We used the ^{8}Li+p data to explore this second technique, which is particularly useful for the events that correspond to the small scattering angle. Since specific energy losses of the heavy recoil particle (^{8}Li in this case) change suddenly due to scattering a discontinuity in the energy spectrum is expected when plotted against physical location along the beam axis. We normalize energy deposition per micromegas pad to the energy deposited in that pixel by ^{8}Li beam ions that produced no interaction. We then sum up the energy deposited in each row and plot this against the row location and then fit it with a function as in Fig 2. There were some complications involved in using this method. The largest complication comes

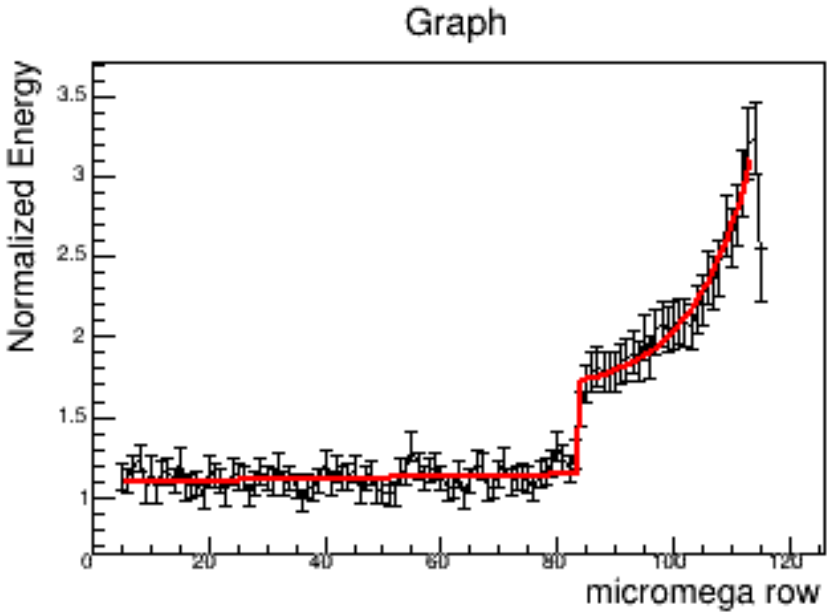

FIG. 2. Plot of Normalized Energy vs micromega row of a single event showing the discontinuity due to a reaction and the fit that calculates the vertex position.

from a threshold in the micromegas that causes not all of the energy deposited to be recorded. This is a problem when the energy is split between two pads in a row. This causes gaps and prevents simple fits to reproduce the correct vertex location. A method was developed to reconstruct the missing energy. First, the energy of the light recoil deposited in the Si-detector is used to determine an approximate reaction vertex location. Second, any points where there is cross over from one column of micromegas to another are set as fixed points. A pair of linear fits are done that are linked through the estimated vertex row and forced through the cross over points identified in the previous step. A normalized Gaussian is placed

along the fit using a standard deviation determined by electron drift to the micromegas plate by GARFIELD [10] simulation. We assume the energy deposited across a row is a Gaussian so the amount of overlap of the Gaussian with any pads that have energy in a row is used to scale for the missing energy in those pads. Fig 3 shows the fitting method and results for a typical event. It was found that less than 10% of good events fail to produce a proper vertex and are easily filtered out using χ^2. Development of this analysis procedure is an important step toward better characterization of experimental data produced by TexAT. Analysis of the TexAT ^{8}Li+p data is still in progress.

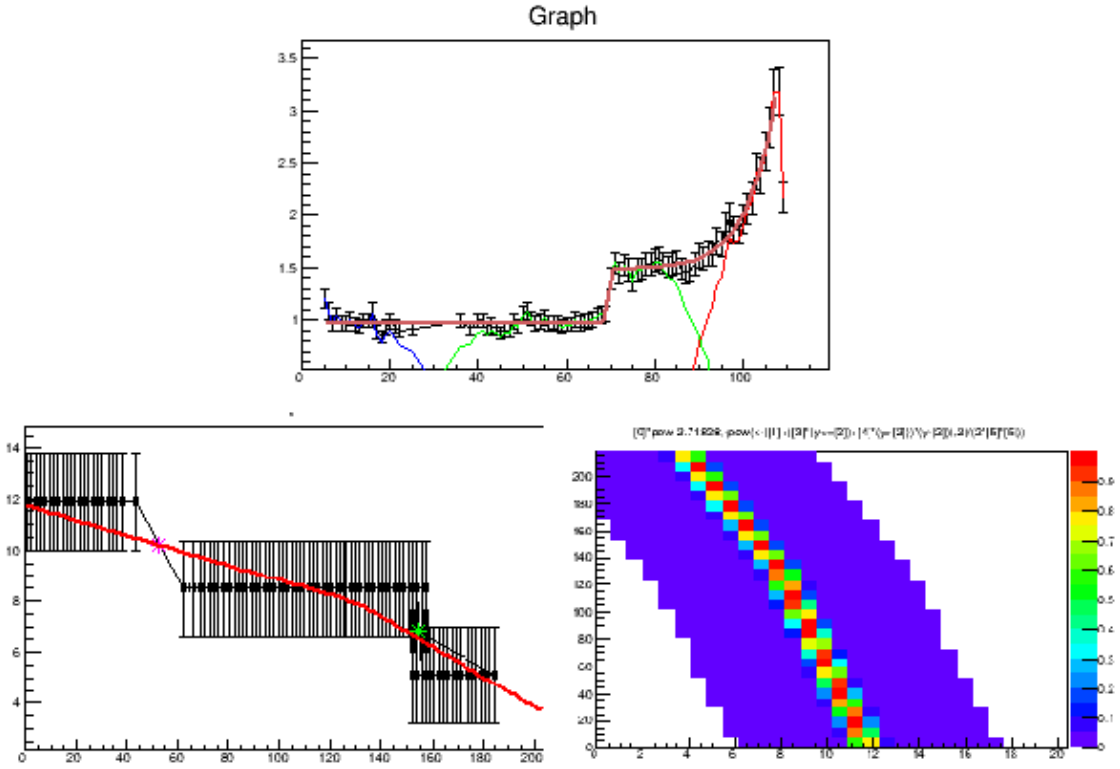

FIG. 3. a) The final reconstructed points and fit on top of the original energy deposited plotted by rows in the micromegas. Note the lower energies on the left side. b) The linear fits over the pads that had energy deposited in them. The stars note the cross over points that were used to constrain the fits. c) The Gaussian with the fit that was used to reconstruct the energy

[1] I. Tanihata *et al.*, J. Phys. G **22**, 157 (1996).

[2] T. Otsuka *et al.*, Phys. Rev. Lett. **87**, 082502 (2001).

[3] T. Otsuka *et al.*, ArXiv:0910.0132 (2009).

[4] N.A. Smirnova *et al.*, ArXiv:1002.1006 (2010).

[5] V.Z. Goldberg, AIP Conference Proceedings **455**, 319 (1998).

[6] A.H. Wuosmaa *et al.*, Phys. Rev. Lett. **94**, 082502 (2005).

[7] G.V. Rogachev *et al.*, Phys. Rev. C **75** 014603 (2007).

[8] E. Koshchiy *et al.*, arXiv:1906.07845 (2019).

[9] R.E. Tribble *et al.*, Nucl. Instrum. Methods Phys. Res. **A285**, 441 (1989).

[10] R.Veenhof. GARFIELD: computer code. (1998).

Spin physics with STAR at RHIC

C.A. Gagliardi, T. Lin, R.E. Tribble, and the STAR Collaboration

Our group continues to play major roles in STAR investigations of both longitudinal and transverse spin phenomena in polarized *pp* collisions at RHIC. A major goal of the RHIC spin program is to determine the gluon polarization in the proton over a wide range of momentum fraction *x*. The longitudinal double-spin asymmetries, A_{LL}, for inclusive jet and di-jet production are ideal tools in this effort because the cross sections are large and dominated by quark-gluon and gluon-gluon scattering processes, both of which have large partonic asymmetries.

As discussed in previous *Progress in Research* issues, our former graduate student, Zilong Chang, performed an analysis of A_{LL} for inclusive jet production in 510 GeV *pp* collisions, using data that STAR collected during 2012. The results will provide new constraints on the gluon polarization in the region $0.015 < x < 0.2$, including the region $x < 0.05$ that isn't sampled by mid-rapidity jet production in 200 GeV collisions. A decision was made to combine the 2012 inclusive jet A_{LL} results with the di-jet A_{LL} measurements that are based on the same data set and were analyzed at University of Kentucky. As of this writing, the paper draft has been approved by the Cold QCD/Spin Physics Working Group and the paper god-parent committee, and is undergoing Collaboration review. Once the Collaboration suggestions have been addressed, it will be submitted to Phys. Rev. D.

Forward rapidity jet production provides an alternative approach to obtain constraints on gluon polarization at low *x*. Our post-doc, Dr. Ting Lin, performed the first measurement of A_{LL} for di-jets with at least one of the jets reconstructed within the pseudorapidity range $0.8 < \eta < 1.8$ for his dissertation. This analysis was complicated by the fact that the tracking efficiency of the STAR Time Projection Chamber falls rapidly when the track pseudorapidity goes beyond $\eta \sim 1.3$. Dr. Lin utilized machine learning techniques to overcome this limitation. His results were published last year [1]. As shown in Fig. 1 right panels, the final results are plotted as a function of the di-jet invariant mass for three different di-jet event topologies: di-jets in which one jet is detected in the east half of the Barrel EMC ($-0.8 < \eta < 0.0$) or in the west half of the Barrel EMC ($0.0 < \eta < 0.8$), while the other is in the Endcap EMC ($0.8 < \eta < 1.8$); and events in which both jets fall into the Endcap EMC. The results are also compared to theoretical model predictions from the DSSV and NNPDF groups, which were generated using the DSSV2014 [2] and NNPDFpol1.1 [3] polarized PDF sets. Both of these global analyses include the data from the STAR 2009 inclusive jet analysis [4].

The momentum fractions, x_1 and x_2, carried by the two interacting partons in the hard scattering, which are probed by these results, are shown in Fig. 1 left panels for the lowest di-jet mass bin. To map with the asymmetry results, the momentum fraction distributions are also separated into the same three event topologies. It is obvious from the distributions that different topologies probe different ranges of the momentum fractions, and as the di-jet goes to higher pseudorapidity, x_2 shifts to lower values and the separation between x_1 and x_2 increases. These results are still limited by the poor statistics especially for both jets going to the higher pseudorapidity region, but with more data from 2012, 2013, and 2015, it will

be an important basis for further analysis at higher pseudorapidity values. Dr. Lin won the 2018 RHIC&AGS Thesis Prize for his dissertation.

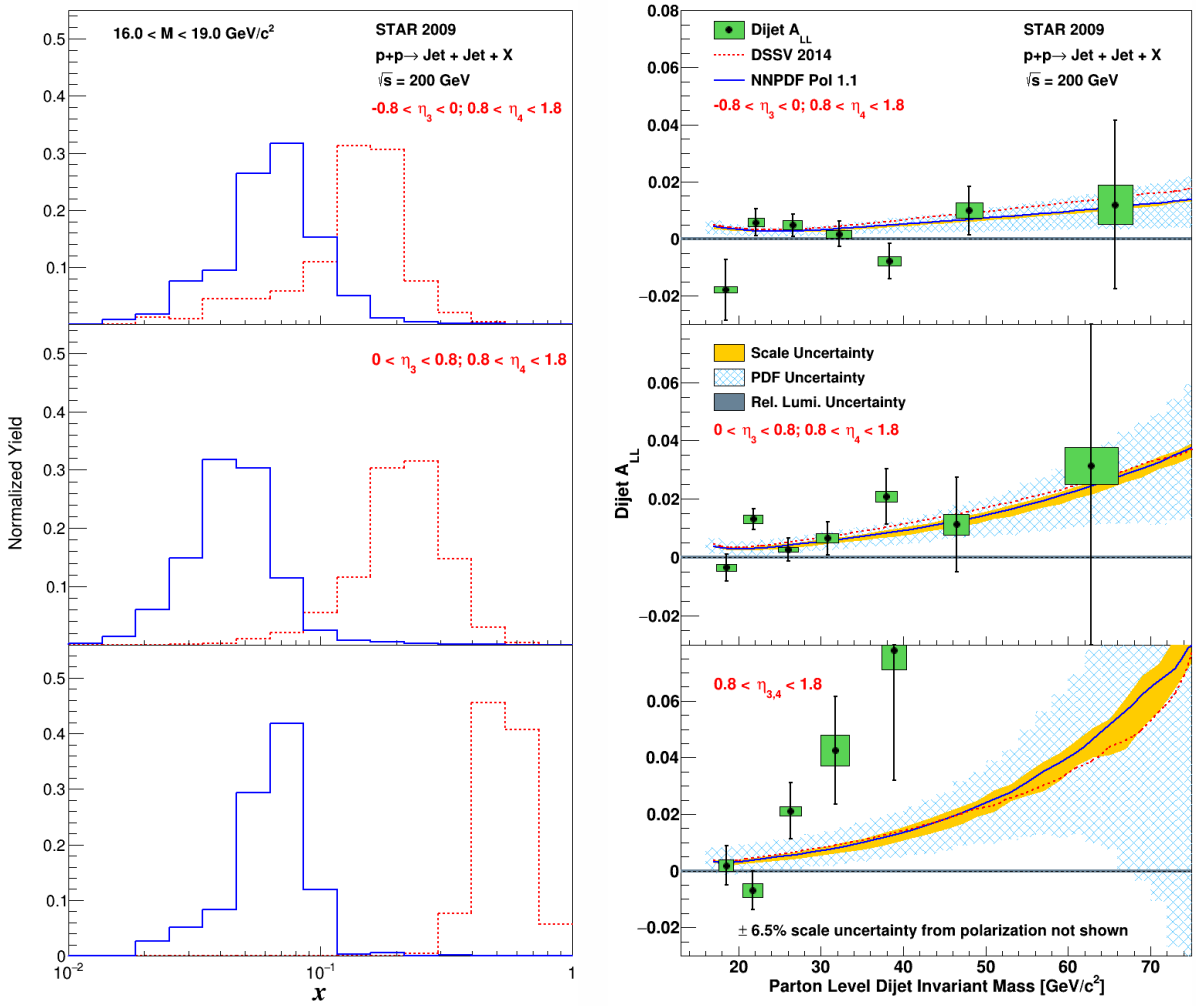

FIG. 1. (Left) The distribution of the parton x_1 and x_2 for di-jets with different jet pseudorapidity. (Right) A_{LL} as function of parton level di-jet invariant mass with different di-jet configurations.

We are also actively investigating transverse spin phenomena at RHIC. Transversity, together with the unpolarized and helicity distributions, are the three leading-twist distributions in the proton. However, much less is known about the transversity distribution because it is chiral odd. The Collins effect convolutes the chiral-odd quark transversity distribution with the chiral-odd Collins fragmentation function, an azimuthal modulation of pion production about the thrust axis of a jet that arises from a transversely polarized quark. It has been observed in semi-inclusive deep-inelastic scattering (SIDIS) by HERMES and COMPASS. The Collins effect is known to be universal in e^+e^- collisions and SIDIS. It has also been argued [5] that the universality of the Collins effect extends to *pp* collisions if the appropriate jet reconstruction algorithm – *e.g.*, the anti-k_T algorithm – is used.

As discussed in last year's *Progress in Research*, in early 2018 we published the first ever observation of the Collins effect in *pp* collisions [6], based on an analysis of 500 GeV data that STAR recorded during 2011. Since then, we have focused on completing and publishing a companion article providing the first-ever investigation of the Collins effect in 200 GeV *pp* collisions, based on data that STAR recorded during 2012. The 200 GeV data from 2012 probe the Collins effect in the region $0.1 < x < 0.3$, which coincides with the peak of the transversity distribution in recent global analyses. When sampling the same x range, the observed asymmetries in the 2012 data are consistent with those we found in [6]. However, the much greater statistics of the 2012 data set bring additional features into focus. For example, Fig. 2 shows that, when the asymmetry is plotted vs. j_T, the momentum of the pion transverse to the jet axis, the peak is observed to shift to higher j_T as the hadron longitudinal momentum fraction within the jet, z, increases. This feature had not been predicted in previous model calculations of the Collins effect. The draft paper describing the 2012 Collins effect analysis and results is nearly ready for the god-parent committee.

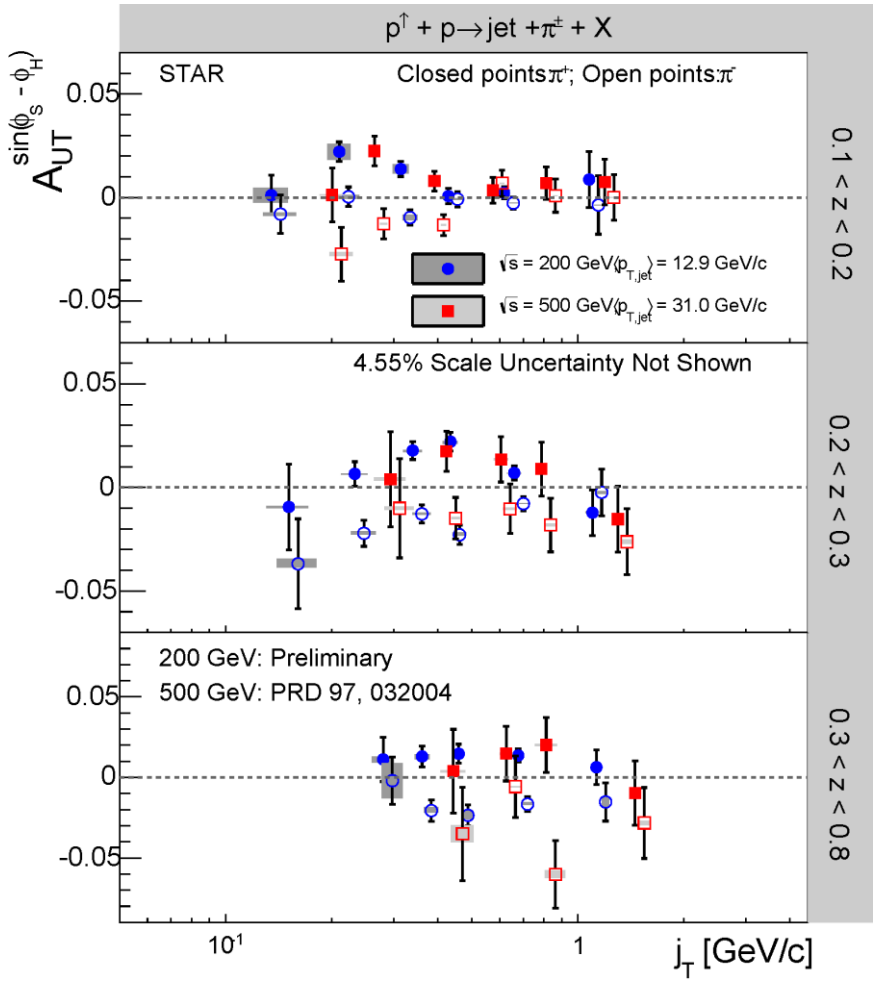

FIG. 2. Collins asymmetry vs j_T, the hadron momentum transverse to the jet thrust axis, for three different ranges of hadron momentum fraction z within the jet. The 500 GeV results in red are from [6]. The 200 GeV results in blue are preliminary.

We are also performing a similar Collins effect analysis based on the much larger 200 GeV data set that STAR recorded during 2015. The high statistics of the 2015 data set will permit the results to be presented as three-dimensional functions of jet p_T, hadron z, and hadron j_T. This fine-grained presentation will provide powerful new constraints for global analyses of the Collins effect, and might elucidate unexpected features, as we've already seen in Fig. 2. On the other hand, the high statistics of the 2015 data set has required us to develop a number of improved analysis procedures in order to minimize the systematic uncertainties.

The STAR Heavy Flavor Tracker was installed during the 2015 RHIC run, significantly increasing the material budget in the middle of STAR compared to the 2011 500 GeV and 2012 200 GeV data sets. So we need a very good understanding of background contributions and the particle identification (PID). Pure samples of protons and pions for PID studies have been obtained using the reconstructed weak decays of the Lambda, anti-Lambda and the short-lived neutral kaon through the $\Lambda \rightarrow p + \pi^-$, $\overline{\Lambda} \rightarrow \bar{p} + \pi^+$ and $K_S \rightarrow \pi^+ + \pi^-$ decay channels. For example, Fig. 3 left panel shows the reconstructed Lambda invariant mass for the momentum range 0.8 - 0.85 GeV/c. A parameter $n_\sigma(\pi)$, which relates the measured energy loss dE/dx (GeV/cm) of the charged particles to the expected value for pions, is used to identify different particles. The $n_\sigma(\pi)$ of the identified pions and protons as functions of the momentum from this PID study are shown in Fig. 3 right panel.

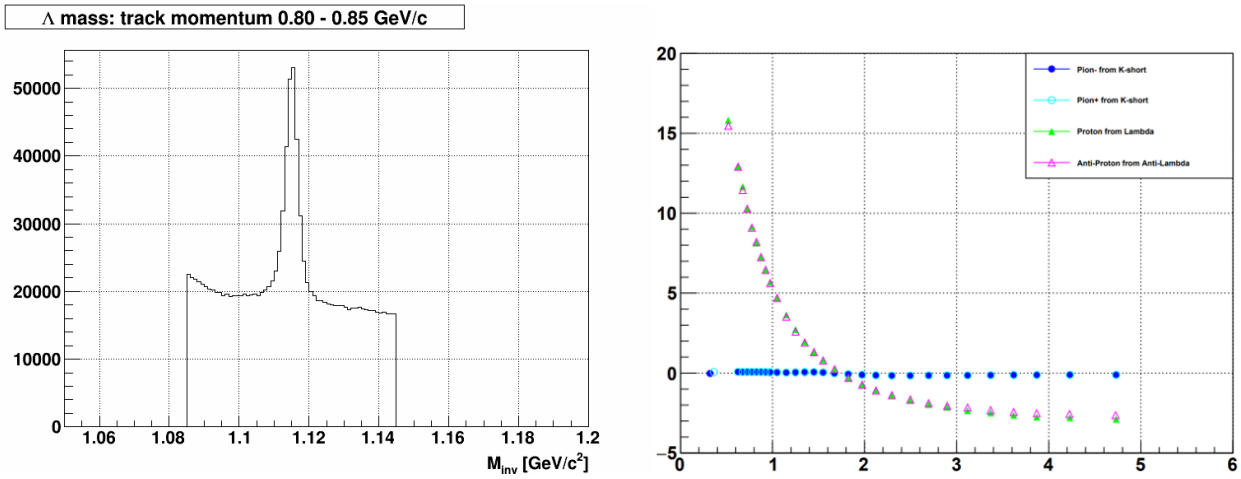

FIG. 3. (Left) Reconstructed Lambda mass for the momentum range 0.8 – 0.85 GeV/c. (Right) $n_\sigma(\pi)$ from the identified pions (from K_S) and protons (from Λ) as functions of the momentum values.

We have also investigated the underlying event contributions to the jets using the off-axis cone method. Generally, the underlying event background is relatively small. However, it can become very large in low-p_T jets at high j_T. In Fig. 4 left panel, the red curve shows the j_T distribution of the tracks inside the jets while the blue one shows the estimated underlying event background, combined with the bottom ratio curve (background over the total yield). Figure 4 shows that the nominal underlying event background can be as large, or larger, than the total signal, which points to a problem estimating the background contribution in the jet periphery. Jets are reconstructed using the anti-k_T algorithm, which is

not a precise circular area, while the background from the off-axis cone method is strictly fixed as a cone with the same radius as the jet. We performed several different studies and finally decided to use a j_T upper limit cut in the analysis in order to minimize the uncertainty in underlying event subtraction. The track j_T range varies with hadron z and jet p_T, so we chose to make the upper j_T limit p_T and z dependent. After some cut optimizations, $j_T < (0.025 + 0.3295 \times z) \times p_T$, was selected. The right panel in Fig. 4 shows the same plots as the left panel but after the implementation of this upper j_T cut. A significant fraction of the background is removed, while this cut has very little impact on the signal yields. We also performed similar studies for a range of jet radii and with the mid-point cone and k_T jet reconstruction algorithms that sample the jet periphery differently from anti-k_T. We have found that the difference between the anti-k_T and k_T algorithm background fractions can be used to estimate the systematic uncertainty for this method.

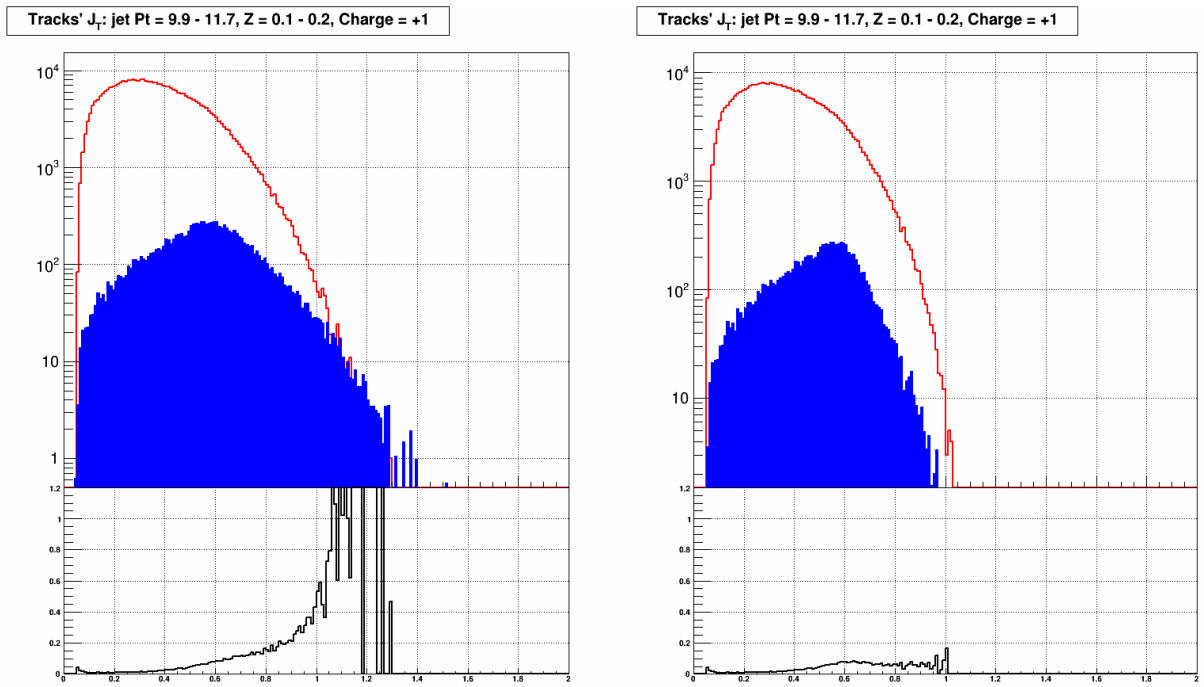

FIG. 4. (Left) The track $\boldsymbol{j_T}$ distributions before the $\boldsymbol{j_T}$ upper limit cut for tracks inside the jets (red curve) and from the off-axis cone method (blue curve). (Right) The track $\boldsymbol{j_T}$ distributions after the $\boldsymbol{j_T}$ upper limit cut for tracks inside the jets (red curve) and from the off-axis cone method (blue curve). The bottom panels are the ratio of the background over the total yield.

Finally, we continue to carry various administrative responsibilities for STAR. Dr. Gagliardi is one of the two conveners of the Cold QCD and Spin Physics Working Group. Dr. Lin is serving as the software coordinator for the EEMC. Dr. Gagliardi served on the god-parent committee for four papers [1,7-9] during the past year. Dr. Lin also served on the god-parent committee for three of them [1,7,8].

[1] J. Adam *et al.* (STAR Collaboration), Phys. Rev. D **98**, 032011 (2018).
[2] D. de Florian, R. Sassot, M. Stratmann, and W. Vogelsang, Phys. Rev. Lett. **113**, 012001 (2014).
[3] E. R. Nocera et al. (NNPDF Collaboration), Nucl. Phys. B **887**, 276 (2014).

[4] L. Adamczyk *et al.* (STAR Collaboration), Phys. Rev. Lett **115**, 092002 (2015).
[5] Z.-B. Kang, X. Liu, F. Ringer, and H. Xing, JHEP **11** (2017) 068.
[6] L. Adamczyk *et al*. (STAR Collaboration), Phys. Rev. D **97**, 032004 (2018).
[7] J. Adam *et al*. (STAR Collaboration), Phys. Rev. D **98**, 091103(R) (2018).
[8] J. Adam *et al*. (STAR Collaboration), Phys. Rev. D **98**, 112009 (2018).
[9] J. Adam *et al*. (STAR Collaboration), Phys. Rev. D **99**, 051102(R) (2019).

The STAR forward upgrade

C.A. Gagliardi and T. Lin, and the STAR Collaboration

STAR has proposed to add a Forward Upgrade during the next few years to enable several critical measurements of proton structure at both high- and low-x. These include explorations of the Collins and Sivers effects in the range $0.3 < x < 0.5$ and gluon polarization down to $x \sim 2 \times 10^{-3}$. Overall, it will enable a suite of measurements in pp and p+A collisions that, when combined with future measurements at the future Electron-Ion Collider, will provide precise tests of the validity – and limits – of factorization and universality. This is essential to separate the effects related to the intrinsic properties of the hadrons under study from interaction-dependent dynamics. For a broad overview of the science of the STAR Forward Upgrade, see the 2016 RHIC Cold QCD Plan [1].

The Forward Upgrade will consist of a Forward Tracking System (FTS), followed by a Forward Calorimeter System (FCS). The FTS will consist of three layers of Si detectors within the STAR magnet, followed by four layers of small thin-gap chambers (sTGCs) in the pole-tip region. The FTS will provide vertex and charge-sign determinations for charged tracks, together with momentum measurements for tracks with $p_T <\sim 2$ GeV/c. The FCS will consist of a pre-shower detector, an electromagnetic calorimeter, and a compact hadronic calorimeter. The FCS will provide triggering, together with neutral particle, charged hadron, and jet measurements.

Our group at Texas A&M has been involved in STAR's planning for the Forward Upgrade since it was first conceived. During this past year, we were among 10 STAR institutions who submitted a consortium development MRI proposal to the NSF to obtain the funds necessary to construct the FCS. The schedule calls for the Forward Upgrade to be completed in time for a planned RHIC 500 GeV pp run in late 2021 or early 2022.

Texas A&M and BNL are jointly responsible for the FCS trigger system. Texas A&M has the responsibility to develop the trigger algorithms, then we will work together with BNL collaborators to implement them. This past year, we developed and simulated the full trigger logic scheme for the FCS, consisting of DEP/ADC boards, which will digitize the analog signals from the Pre-shower, ECal, and HCal and generate logic primitives, followed by DEP/IO boards, which will combine the logic primitives to yield efficient and selective electron, photon, charged hadron, jet, di-electron, and di-jet triggers. DEP/ADC boards are new cost-effective, 32-channel, 12-bit wavelength digitizers operating at 75 MHz (8 times the RHIC bunch-crossing frequency) that also include a powerful FPGA that can perform detailed logic calculations, together with high-speed optical and copper-wire outputs. DEP/IO boards replace the ADC front-ends with 32 high-speed line receivers that feed the identical FPGA and back-end electronics. Both boards have been designed at BNL. Four DEP/ADC boards are now in operation at STAR.

Texas A&M is also responsible for developing calorimeter clustering algorithms. Given the limited momentum resolution of the FTS for energetic charged hadrons, several of the planned Forward Upgrade measurements, including both the planned Collins and Sivers effect measurements, will need to combine track directional information from the FTS with calorimeter cluster energies from the FCS to

infer hadron momenta. This will be our major contribution to the Forward Upgrade during the coming year.

[1] E.-C. Aschenauer *et al*., arXiv:1602.03922.

Breakup of ^{9}C and ^{66}Se with SAMURAI in RIKEN

A. Saastamoinen for the NP1412-SAMURAI29R1 and NP1406-SAMURAI24 collaborations

We have performed the first physics experiments with the SAMURAI Si tracker at the RIBF facility in RIKEN. This Si tracker and related electronics were instrumented in collaboration with TAMU, WUSTL, LSU, and the international partners. The initial commissioning experiment in May/June 2018 was Coulomb dissociation and nuclear breakup of $^{9}C \rightarrow ^{8}B+p$ and $^{9}C \rightarrow ^{7}Be+2p$ at 157 AMeV for studying the rate of $^{8}B+p \rightarrow ^{9}C$ reaction chain as possible bypass of the 3α process in stellar environments [1]. This was followed in March 2019 by nuclear breakup of $^{66}Se \rightarrow ^{65}As+p$ and $^{66}Se \rightarrow ^{64}Ge+2p$ at 270 MeV/u for studying destruction of waiting point nucleus ^{64}Ge in X-ray burst environments [2].

The Si tracker was built to improve the measurement of the relative angle between the breakup products: the resulting heavy ion and proton(s) immediately after the reaction target. The setup is used in combination with the drift chambers and hodoscopes around the SAMURAI magnet. The Si tracker consists of two sets of two 324 μm thick GLAST type Single-Sided Si Strip Detectors (SSD), each with 128 strips that are 684 μm wide. A pair of SSDs is mounted on same PCB so that the strips on opposite side are in 90 angle, forming a tracking coordinate plane. Each of the SSDs is connected into a Dual Gain Charge Sensitive Preamplifier (DGCSP) inside the vacuum chamber. The DGCSP is an application specific integrated circuit (ASIC) designed in RIKEN which are packaged onto preamplifier boards designed and built by ATOMKI. The DGCSP has total dynamic range from about 200 keV to a little under 1 GeV. Two DGCSP chips per preamplifier board can instrument 16 strips, giving 16+16 outputs (high gain and low gain) for each strip. The resulting 4 x 128 x 2 = 1024 data channels are read with HINP16C chips [3]. The total system consists of two motherboards, each with 512 channels. The readout system for the two motherboards was integrated into the RIBFDAQ as its own device and the data synchronized to the data collected from other parts of the setup.

Fig. 1 gives an example of the setup performance for the protons. The left panel of Fig. 1 shows a comparison between proton calibration data run (multiplicity = 1 in each Si layer) and protons from one run of ^{9}C on ^{208}Pb target, with gates placed on incoming ^{9}C beam, a proton detected in the hodoscope after SAMURAI and with Si multiplicity <7 and that the hit strip in Si was more than 4 strips away from the highest energy of the event (the heavy ion). The right panel of Fig 1 shows accumulated proton spectrum with similar conditions from multiple runs of ^{9}C on ^{12}C. The left panel of Fig 2. shows the ^{9}C beam spot in the second tracker layer and the right panel shows the distribution of protons from the right panel of Fig. 1.

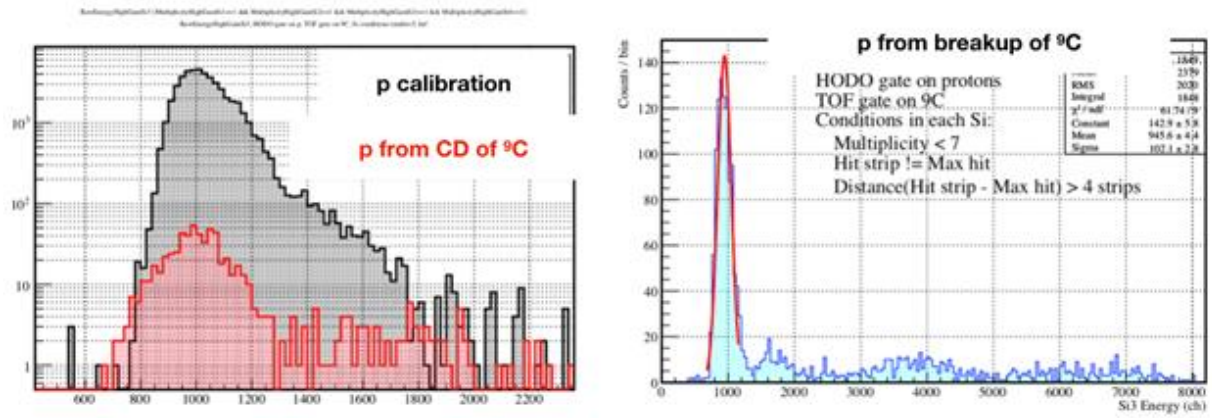

FIG. 1. Left panel: A comparison of energy deposition in one strip from the proton calibration run and one run of Coulomb dissociation of ^{9}C. The calibration data has requirement of multiplicity = 1 in each Si layer whereas the CD data has gates placed on incoming ^{9}C beam, a proton detected in the hodoscope after SAMURAI and with Si multiplicity <7 and that the hit strip in Si was more than 4 strips away from the highest energy of the event (the heavy ion). The right panel shows shows accumulated proton spectrum with similar conditions from multiple runs of ^{9}C on ^{12}C.

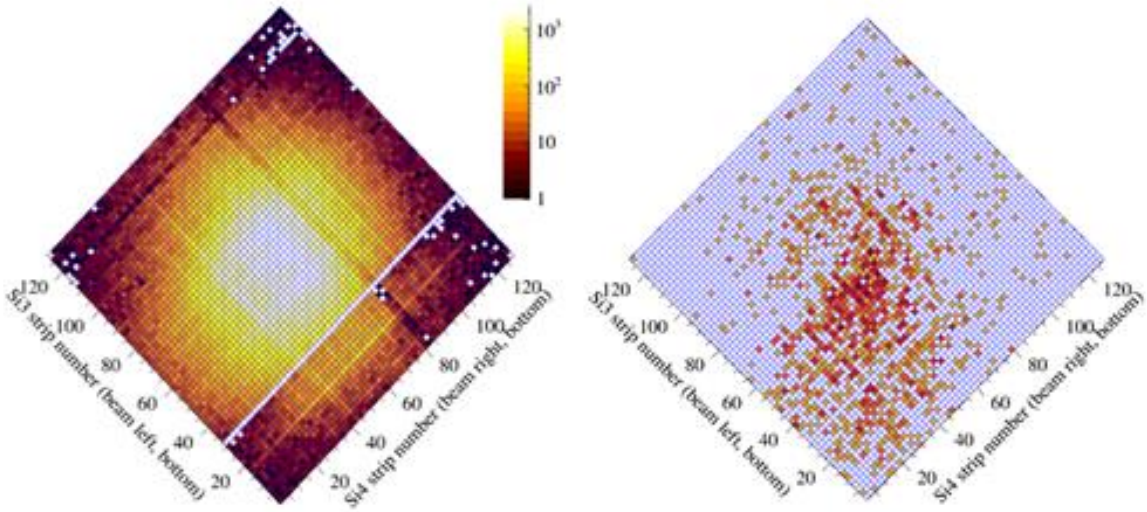

FIG. 2. Left panel: ^{9}C beam spot in the second tracker layer (~60 cm from the target) during nuclear breakup measurement. Right panel: Distribution of protons with same conditions as right panel of Fig. 1. and for the same runs as the left panel.

Data taking for both experiments was successful and the analysis is in progress by the collaboration.

[1] M. Wiescher *et al.*, Astrophys. J. **343**, 352 (1989).

[2] A. Parikh *et al.*, Prog. Part. Nucl. Phys. **69**, 225 (2013).

[3] G.L. Engel *et al.*, Nucl. Instrum. Methods Phys. Res. A**573**, 418 (2007).

SECTION II

HEAVY ION REACTIONS

Examination of the purification step of the PUREX process with varying HNO_3 concentration

P.K. Kircher,[1,2] K.J. Glennon,[1,2] and C.M. Folden III[1,2]
[1]*Cyclotron Institute, Texas A&M University, College Station, TX 77843*
[2]*Department of Chemistry, Texas A&M University, College Station, TX 77843*

Detection and quantification of Pu in proliferated material is of great importance to national security. Pu is created through the irradiation of UO_2 in a nuclear reactor and is later separated from fission products and uranium for further usage. One of the primary ways this is accomplished is through the PUREX process [1,2], which has the main objective of separating and purifying U and Pu from each other and the fission products such as $^{137,134}Cs$, ^{144}Ce, $^{155,154}Eu$, ^{106}Ru, and ^{125}Sb. This separation scheme is a complex process with many conditions that could potentially be varied, which could in turn affect the effectiveness of separation. This change in effectiveness, specifically when comparing the ratio of Pu to other fission products, can give information as to the conditions being used during separation and potentially attribute the proliferated material to a source.

To achieve comparable data, a laboratory mockup of the PUREX process was created based on published data on the Barnwell Nuclear Fuel Plant as there is a large amount of detail known specifically about the concentrations of the aqueous and organic streams used in the extraction processes, including temperature and acid concentration. This fuel reprocessing was constructed in South Carolina but never commercially opened and eventually decommissioned. The fuel that was used for the experiment was obtained from a High Flux Isotope Reactor (HFIR) source. Specifically, studies have been conducted to determine the effect of HNO_3 concentration on extraction yield and decontamination factor in nuclear fuel samples.

The extraction process used in this experiment utilized a sample of irradiated uranium dioxide irradiated in a pseudo-fast neutron spectrum. A working solution containing approximately 0.5% of the fuel pellet activity per 500 μL was created with a HNO_3 concentration of 4 M. This was used in the aqueous phase of the extraction with a total volume of 3 mL with organic phases of 1 mL consisting of n-dodecane. Prior to phase mixing, approximately 100 μg of $NaNO_2$ was added to the aqueous phase containing the HFIR fuel aliquot and both phases were heated to 75 °C using an oil bath to achieve an oxidation state of +4 in Pu necessary for extraction and uniform temperature. After allowing this process to occur for 5 min, the oil bath was turned down to the desired temperature for chemical separation. The phases were then mixed and shaken vigorously for 2 min to ensure thorough mixing for extraction. The phases were then allowed to separate via gravity before being subjected to centrifugation for 1 min at 3000 rpm. The phases were then extracted using a pipette to obtain a 500 μL aliquot of the organic phase and a 1 mL aliquot of the aqueous phase for characterization. One 3 M HNO_3 extraction was conducted at 35 °C for proof of concept and a 1 M, 3 M, 5 M, 7 M, and 9 M HNO_3 series were conducted at 25 °C.

Gamma spectroscopy of the sample was taken of each organic phase and aqueous phase post-extraction using a high-purity germanium (HPGe) detector. All aqueous samples were counted with real times of 1200.00 s. All organic samples were counted with real times between 60000.00 to 90000.00 s to achieve lower error in measurements. A background measurement lasting 87300.00 s was taken and

subtracted out of all measurements. The HFIR working solution was counted with a real time of 14400.00 s. The energy and efficiency calibrations of the instrument was performed using a ^{152}Eu source.

All samples used in alpha spectrometry were taken by using a 20 µL aliquot of the final organic phase and performing a back extraction with 1 mL of 0.03 M HNO_3. Once this mixture had been vortexed for 2 min and centrifuged at 3000 rpm for 1 min, a 20 µL aliquot of the aqueous phase containing the extracted Pu was taken, placed on a planchet, allowed to evaporate, and deposited. These samples were then counted using an alpha spectrometer with count times of a minimum of 43200.00 s. A background of the alpha spectrometer was taken for 129600.00 s and subtracted from results. The HFIR working solution was counted for 259200.00 s. The energy and efficiency calibrations of the instrument were determined using a standard containing ^{148}Gd, ^{239}Pu, ^{241}Am, and ^{244}Cm.

The initial trial of the extraction performed at known conditions (35 °C, 3 M HNO_3, 3:1 aq:org phase ratio) proved to be successful in extracting Pu from the other fission products. Alpha spectrometry indicates that approximately 46% of the Pu was successfully extracted from the aqueous phase. Additionally, gamma spectroscopy showed favorable results with regards to the decontamination factor of the fission products in the final organic phase for this single sample.

The series of trials that varied the concentration of HNO_3 from 1 M to 9 M in 2 M increments indicated that there was no significant change in DF for ^{155}Eu, ^{154}Eu, and ^{241}Am between the varying concentrations except for the 1 M trial, which resulted in a significantly lower Pu extraction at 0.40% compared to an average of 47% extraction. This appears to indicate that the fission products have a generally uniform behavior with regards to varying HNO_3 concentration, with the notable exceptions of ^{137}Cs and ^{106}Ru, which can be observed in Fig. 1. These deviances may potentially be due to experimental

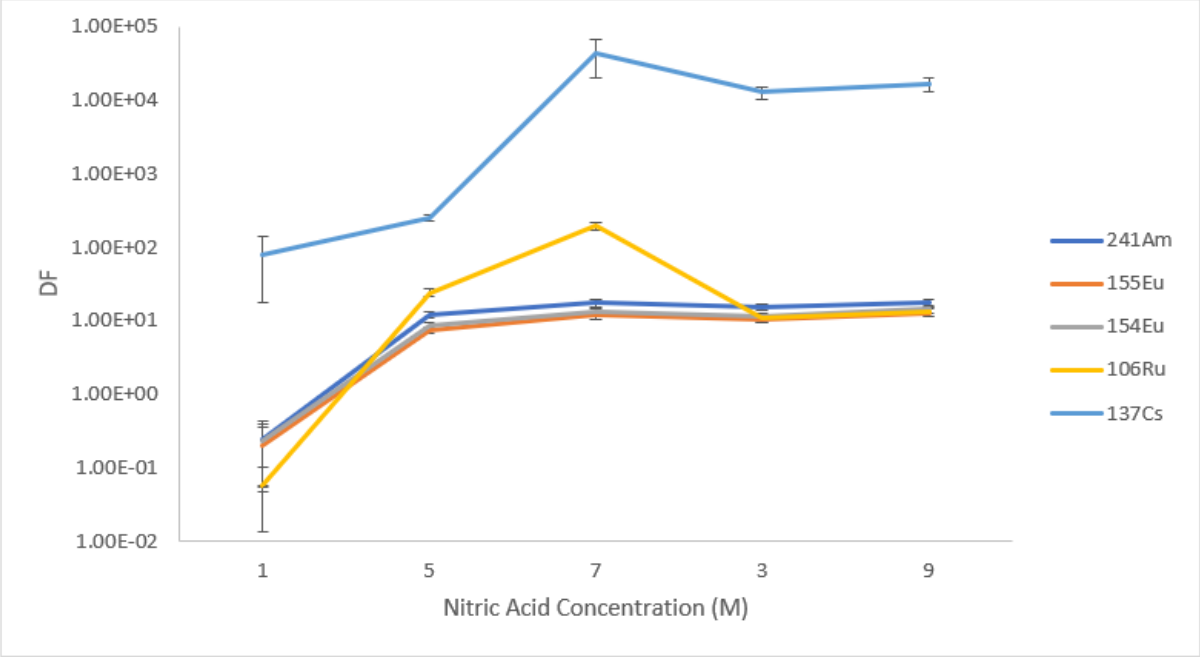

FIG. 1. Decontamination factors of measured fission products performed at 35 °C and varying HNO_3 concentrations.

error as the data was not collected in triplicate to minimize fuel usage, and further studies are being conducted to determine this.

[1] H.A.C. McKay, K.P. Bender, L.L. Burger, and J.D. Navratil, *The PUREX Process*, (CRC Press, Inc. United States, 1990).

[2] M. Benedict, T.H. Pigford, and H.W. Levi, *Nuclear Chemical Engineering*, (McGraw-Hill, New York, 1981).

Mechanism of indium and thallium extraction into [Hbet][Tf_2N] ionic liquid

M.F. Volia,[1, 2] E.E. Tereshatov,[1] M. Boltoeva,[3, 4] and C.M. Folden III[1,5]
[1]*Cyclotron Institute, Texas A&M University, College Station, Texas 77843*
[2]*Department of Nuclear Engineering, Texas A&M University, College Station, Texas 77843*
[3]*Université de Strasbourg, IPHC, Strasbourg, 67037 France*
[4]*CNRS, Strasbourg, 67037 France*
[5]*Department of Chemistry, Texas A&M University, College Station, Texas 77843*

Our research group has been actively studying the liquid-phase chemistry of indium and thallium, the predicted homologs the of superheavy element nihonium (Nh), by using the liquid-liquid extraction technique. This study seeks to establish chemical systems that can potentially be used to investigate the chemical properties of Nh, which still remain largely unknown since this element was first discovered in 2004. Due to its low production rate, Nh chemistry must be studied at a one-atom-at-a-time level. To mimic this condition, the study of the homologs was carried out using radiochemistry techniques, which allow the experiments to be done with ultra-trace In and Tl concentrations. Preliminary results are reported here.

The liquid-liquid extraction technique, also commonly known as solvent extraction, is based on preferential distribution of solutes between two immiscible liquid phases. Our study involves hydrochloric acid as the aqueous phase and an ionic liquid, a type of salt with melting temperature below 100 ^{o}C [1], as the organic phase. Previously, we have reported the preliminary results of In(III) and Tl(I, III) extraction into water-saturated [Hbet][Tf_2N] ionic liquid (IL) [2]. [Hbet][Tf_2N] is a protic and hydrophobic IL composed of a betainium cation and a bistriflimide anion [3]. Betainium is the protonated form of glycine betaine (bet), a zwitterionic compound with a carboxylic acid group in its structure [3]. The structure of this IL is shown in Fig. 1.

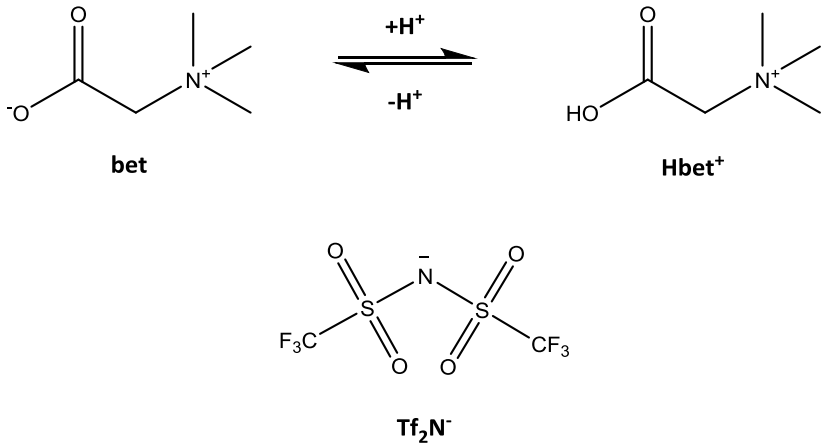

FIG. 1. Chemical structure of [Hbet][Tf_2N] components: zwitterionic betaine and betainium cation (top) and bistriflimide anion (bottom).

The previously reported results showed that the extraction yield of the In(III) and Tl(I, III) was better at lower acid concentrations and it decreased with increasing acidity. Having obtained these data, the mutual solubility between [Hbet][Tf_2N] and the acidic aqueous phase was studied in order to understand the chemical interactions in the system, and these results are reported in Ref. [4]. All this information allowed us to develop mathematical models to explain the extraction mechanisms of In(III) and Tl(I, III) into [Hbet][Tf_2N]. These models are based on the formation of betaine-containing metal complexes as the extracted species. The number of betaine molecules and the structure of the complexes were determined using a slope analysis method. An attempt to estimate the extraction constants of the extracted species and the constants of complexes formed in the aqueous phase was also made. These quantities, combined with the results of the slope analysis as well as the expected chemical behavior of the metals, ultimately led to the following conclusions:

1. In(III) was mostly extracted as $InCl_2^+$ through an ion pair formation mechanism with [Tf_2N^-] anion. The structure of the extracted complex at low acidity and without additional betaine added is most likely [$InCl_2(bet)_4$][Tf_2N]. Meanwhile, in the presence of 15% (w/v) betaine, the extracted complex contains approximately three betaine molecules. Therefore, we considered the possibility that betaine binds with indium as a bidentate ligand when it is present in excess. At higher HCl concentrations, in both systems with and without betaine added, the predominant extracted complex is likely to be $InCl_2$[Tf_2N].
2. Tl(III) was predominantly extracted through ion pair formation with [$Hbet^+$]. The extracted species is most likely $TlCl_4^-$ in the entire range of HCl concentrations studied, with the possibility of betaine molecules incorporated in the extracted complex at low acidity. Unfortunately the number of betaine molecules associated with Tl(III) complex cannot be determined due to insufficient data and the large uncertainty on the slope.
3. Tl(I) was mainly extracted through a cation exchange mechanism with [$Hbet^+$], but we also considered the extraction of [Hbet][$TlCl_2$] complex at high acid concentrations. The extracted species are [$Tl(bet)^+$] at <0.5 M HCl, bare Tl^+ in 0.5 – 5 M HCl region and $TlCl_2^-$ in > 5 M HCl.

The results of this mechanism study would be beneficial should Nh chemistry be studied in the same media. By comparing the extraction behavior of Nh to its lighter homologs, one ideally could infer whether a similar complex is formed and extracted through a particular mechanism, and eventually determine if these elements belong to same group. However, these current data are still preliminary and extensive work is required for a future experimental study of Nh chemistry. Nevertheless, these results provide baseline data that could be useful for that purpose.

[1] A. Berthod *et al.*, J. Chromatogr. A **1559**, 2 (2018). doi:10.1016/j.chroma.2017.09.044.
[2] M.F. Volia *et al.*, *Progress in Research*, Cyclotron Institute, Texas A&M University, (2016-2017), p. II-18; available at https://cyclotron.tamu.edu/progress-reports/2016-2017/.
[3] P. Nockemann *et al.*, J. Phys. Chem. B **110**, 20978 (2006). doi:10.1021/jp0642995.
[4] M.F. Volia *et al.*, J. Mol. Liq. **276**, 296 (2019). doi:10.1016/j.molliq.2018.11.136.

Ternary hydrophobic eutectic mixtures for indium extraction from hydrochloric media

E.E. Tereshatov,[1] J.M. Edgecomb,[1,2] M. Boltoeva,[3] and C.M. Folden III[1,4]
[1]*Cyclotron Institute, Texas A&M University, College Station, TX 77843*
[2]*Department of Natural Sciences, Saint Martin's University, Lacey, WA 98503*
[3]*Université de Strasbourg, CNRS, IPHC, UMR 7178, F-67000 Strasbourg, France*
[4]*Department of Chemistry, Texas A&M University, College Station, TX 77843*

Hydrophobic eutectic mixtures were introduced four years ago [1, 2] and since then there are only three articles to the best of our knowledge devoted to metal extraction by this class of compounds [3-5]. All these articles are based on binary solvent application and there is none on ternary mixtures. The presence of the third compound adds one more degree of freedom in terms of both solubility and viscosity control. Moreover, the third compound can help to convert a solid binary mixture to a liquid ternary one, suitable for liquid-liquid extraction (LLE). The LLE technique is widely applied for recovery of valuable and critical metals. For example, indium is used in liquid crystal displays and this metal supply disruption should not be completely ruled out [6]. In order to maintain hydrophobicity and non-toxicity of the mixtures prepared in our experiments, active pharmaceutical and food grade compounds with low water miscibility have been chosen. Among them there are three that belong to a class of amines, lidocaine [*N*-(2,6-dimethylphenyl)-N^2,N^2-diethylglycinamide; T_m = 68 °C], grape smell (methyl 2-aminobenzoate; T_m = 24 °C) and Proton Sponge® [1,8-bis(dimethylamino)naphthalene; T_m = 48 °C]. These amine-based compounds drive the extraction of indium due to ion pair formation or ion exchange mechanisms [3]. Regardless of the mechanism proposed, the key factor is the mixture solubility. For example, it is known that ibuprofen-menthol binary eutectic (3:7 mass ratio) [7] reveals the highest solubility among other liquid at room-temperature mixtures formed from the same compounds [8]. So, DL-menthol (T_m = 37 °C) can be considered as a dopant to the solid amines mentioned above. Figure 1 shows the phase diagram of one of the ternary mixtures prepared with their corresponding glass transition temperatures (Celsius degrees, green color numbers) and indium distribution ratio values from 0.05 M HCl (red color numbers). The triangle sides represent the corresponding binary mixtures, where light green color indicates regions of liquid at room temperature mixtures (suitable for LLE), blue lines indicate regions of solid and liquid mixtures, and wine color indicates regions of completely solid at room temperature mixtures. The black dots inside the triangle represent the composition of the prepared and analyzed ternary mixtures. Some ternary mixtures are not suitable for LLE because of the simultaneous presence of solid and liquid phases at room temperature and are labeled as "S + L". It can be seen that lidocaine – Proton Sponge binary mixtures do not form systems that are liquids at room temperature, DL-menthol – Proton Sponge has one liquid mixture (7:3 mass ratio), and lidocaine – DL-menthol mixtures are liquid in the range from 6:4 to 2:8 mass ratios. It was found that the presence of at least 20 wt % of the DL-menthol can convert solid binary lidocaine – Proton Sponge mixtures to a liquid ternary one, suitable for LLE, with a glass transition temperature down to –65 °C. The highest distribution ratio measured (~16) indicates that ~94% of indium was successfully extracted into the organic phase. Thus, the ternary mixture concept allows for expansion of compounds applicable for LLE.

Even those that are solid at room temperature and form solid binary mixtures can be used for liquid mixture preparation without implementation of any toxic or flammable conventional solvents. Moreover, careful choice of such compounds can lead to a mixture synthesis with controlled viscosity and extractability of desired analytes.

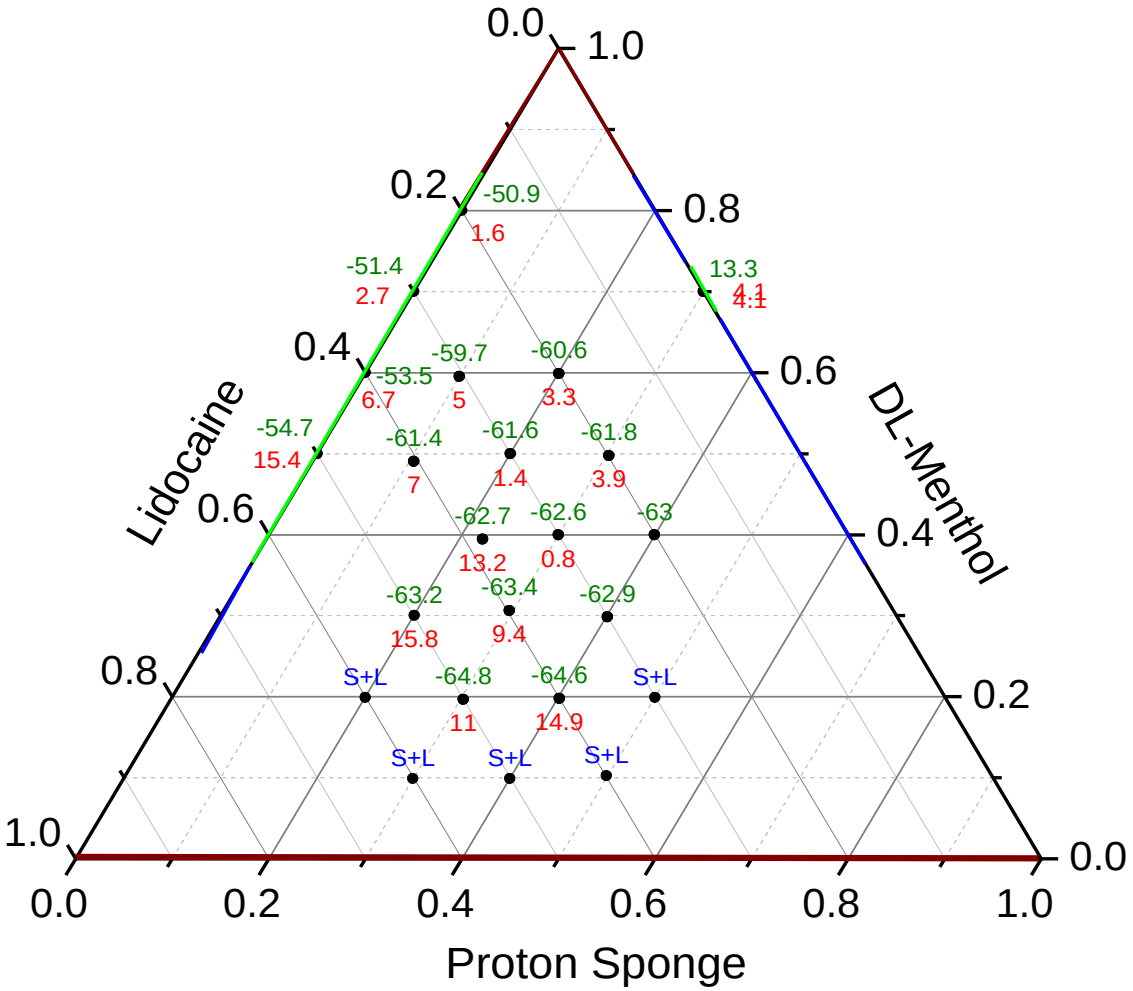

FIG. 1. Ternary phase diagram of lidocaine – Proton Sponge – DL-menthol mixtures (mass ratio): red numbers – indium distribution ratios (0.05 M HCl), green numbers – glass transition temperatures of liquid at room temperature mixtures (°C).

[1] D.J.G.P. van Osch, L.F. Zubeir, A. van den Bruinhorst, M.A.A. Rocha, and M.C. Kroon, Green Chem. **17**, 4518 (2015).

[2] B.D. Ribeiro, C. Florindo, L.C. Iff, M.A.Z. Coelho, and I.M. Marrucho, ACS Sustainable Chem. Eng. **3**, 2469 (2015).

[3] E.E. Tereshatov, M.Y. Boltoeva, and C.M. Folden III, Green Chem. **18**, 4616 (2016).

[4] D.J.G.P. van Osch, D. Parmentier, C.H. Dietz, A. van den Bruinhorst, R. Tuinier, and M.C. Kroon, Chem. Commun. **52**, 11987 (2016).
[5] N. Schaeffer, M.A.R. Martins, C. Neves, S.P. Pinho, and J.A.P. Coutinho, Chem. Commun. **54**, 8104 (2018).
[6] E. McCullough and N.T. Nassar, Miner. Econ. **30**, 257 (2017).
[7] P.W. Stott, A.C. Williams, and B.W. Barry, J. Control. Release, **50**, 297 (1988).
[8] C.S. Yong, Y.K. Oh, S.H. Jung, J.D. Rhee, H.D. Kim, C.K. Kim, and H.G. Choi, Eur. J. Pharm. Sci. **23**, 347 (2004).

Introduction of novel hydrophobic eutectics for the liquid-liquid extraction of indium from hydrochloric acid media

J.M. Edgecomb,[1,2] E.E. Tereshatov,[1] M. Boltoeva,[3] and C.M. Folden III[1,4]
[1]*Cyclotron Institute, Texas A&M University, College Station, TX 77843*
[2]*Department of Natural Sciences, Saint Martin's University, Lacey, WA 98503*
[3]*Université de Strasbourg, CNRS, IPHC, UMR 7178, F-67000 Strasbourg, France*
[4]*Department of Chemistry, Texas A&M University, College Station, TX 77843*

The liquid-liquid extraction (LLE) of indium has become the subject of significant interest over the last several years for two major reasons. First, indium is a homolog of the superheavy element nihonium (Z=113). LLE experiments of indium can be used to more fully describe the chemistry of group 13 elements and therefore assist in the characterization of nihonium in a future online experiment. Second, the global demand for indium has outpaced its supply, with both United States [1] and European [2] agencies including indium as a near critical-metal. Due to low natural abundance, recycling and reprocessing of indium from end-of-life electronics has become an essential step in satisfying industrial demands [3]. LLE of indium can potentially provide useful insight into economically and environmentally sustainable reprocessing methods. The solvents used in this study belong to a class of liquids referred to as hydrophobic eutectics. These are mixtures of compounds that display a large melting point depression, resulting in the formation of room-temperature liquids. We have characterized the physical properties of the studied eutectics and applied them to indium LLE in a systematic fashion, focusing on the charge, speciation, and mechanism of extraction. The results in this report are preliminary and the work is ongoing.

Five compounds [DL-menthol, ibuprofen, lidocaine, methyl anthranilate, and 1,8-bis(dimethylamino)naphthalene (known by its trade name Proton Sponge®) have been used as starting materials for the preparation of the solvents studied. Low toxicity, cost and melting temperature make these compounds ideal candidates to for green solvents. For each binary system, multiple samples with varying mass ratios were prepared in increments of 10%. If the resulting mixture is a homogenous solution, it is studied with a differential scanning calorimeter (DSC) (Fig. 1a). If a melting peak is observed, this composition can be classified as a eutectic. However, only a second-order phase (glass) transition has been observed in the majority of the binary and ternary mixtures. In this case, several models have been adapted to our data that describe the extent of hydrogen bonding and proton exchange in these solvents (Fig. 1b).

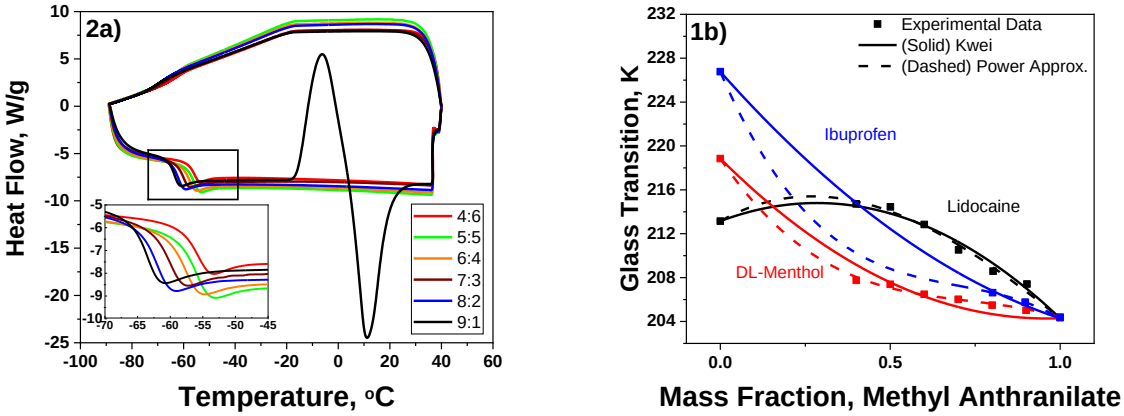

FIG. 1. DSC data for methyl anthranilate (MA)-based binary system. (a) Thermograms of the methyl anthranilate-lidocaine mixture, reported as MA:L (w:w). The glass transition has been magnified. (b) Glass transition temperature as a function of mass composition, fit to both the Kwei [4] and power approximation models [5].

Derived from the Gordon-Taylor relationship for polymer blends, the Kwei model [4] describes the glass transition temperature as a function of composition, where the deviation from linearity is attributed to intramolecular hydrogen bonding. The power series approximation to the Gordon-Taylor model extends this analysis to describe the role of conformational entropy on the glass temperature behavior [5]. These models can be used to describe the type and relative strength of interactions that promote liquid phase behavior in the binary solvents.

Once the selected binary mixtures have been characterized as described above, they have been screened for potential extraction of indium from dilute hydrochloric acid. The extent of extraction is measured using tracer ^{111}In ($t_{1/2}$=2.80 days), a gamma-emitting nuclide. The extraction yield has been quantified as the ratio (D) of activity of indium between the two phases, measured using a NaI scintillation counter. Of the five compounds selected, it has been observed that binary mixtures containing either lidocaine or Proton Sponge® have a high capacity for extraction. The mechanism of extraction can be deduced by loading the aqueous phase with stable indium (Fig. 2). It has been shown [6] that the D-value is related to the change in aqueous indium concentration ($\Delta[In^{Z-}]_{aq}$) by:

$$K_{ip} = D \cdot \frac{z \cdot \Delta[In^{Z-}]_{aq} + \sqrt{\left(z \cdot \Delta[In^{Z-}]_{aq}\right)^2 + 4 \cdot K_{sp}}}{2}$$

where K_{ip} is the constant of extraction and z is the charge of the species. As $\Delta[In^{Z-}]_{aq}$ becomes large, the slope of a plot of D versus $\Delta[In^{Z-}]_{aq}$ approaches -z.

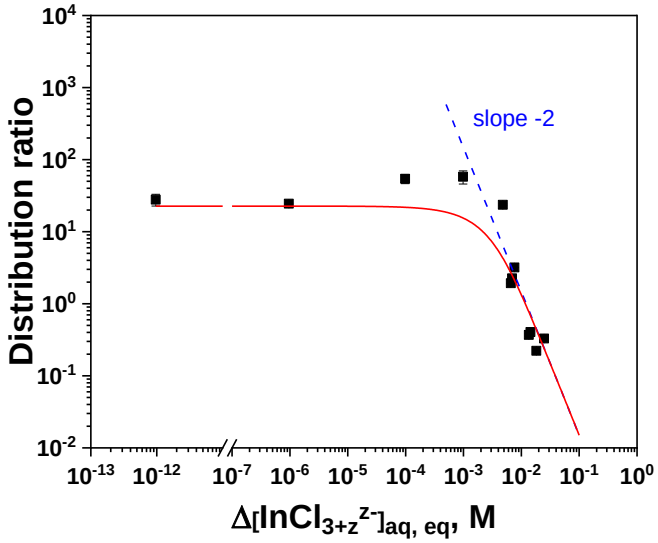

FIG. 2. Loading of stable indium into aqueous phase before extraction into the lidocaine-methyl anthranilate mixture. The slope on the right portion of the curve indicates the charge of the extracted species.

We have developed a systematic approach to studying the mechanism of extraction in these novel solvents and have proposed a set of chemical reactions that describe the extraction of indium and applying these to our eutectic solvents. These findings provide a framework for introducing green alterative solvents for metal extraction and help describe the chemistry of group 13 elements. Moving forward, we hope to finalize the mechanism of extraction and possibly explain the roles of indium complexation, mutual solubility and acidity.

[1] National Minerals Information Center, U.S. Department of Interior, https://www.usgs.gov/centers/nmic.

[2] Report on critical raw materials and the circular economy, European Comission. DOI: 10.2873/331561.

[3] K. Zhang *et al.*, Resour. Conserv. Recycl. **104**, 276 (2015).

[4] T. Kwei, J. Polym. Sci. Polym. Lett. **22**, 307 (1984).

[5] Y. Cui and S. Frank, J. Pharm. Sci. **95**, 701 (2006).

[6] E.E. Tereshatov *et al.*, Green Chem. **18**, 4616 (2016).

A forensic investigation of the PUREX process to determine Pu separation conditions

K.J. Glennon[1,2] and C.M. Folden III[1,2]
[1]*Cyclotron Institute, Texas A&M University, College Station, Texas 77843*
[2]*Department of Chemistry, Texas A&M University, College Station, Texas 77843*

A forensic investigation of the PUREX process is underway to measure the distribution coefficients (D-values) and decontamination factors (DFs) of various fission products throughout the process, and to determine how these values may change under varying conditions. The goal is to learn more about how a sample of unknown Pu was separated by measuring the distribution of the trace fission products remaining in the separated Pu. Several PUREX extractions have been performed to determine the impact of temperature, acidity, and U saturation on the D-values of various fission product elements. All extractions are performed in a contained glovebox, and all extraction yields are assayed via gamma spectrometry. U saturation describes the ratio of U atoms in the aqueous phase to extractant molecules in the organic phase, multiplied by two. This is because a single U atom will chelate with two extractant molecules. Extractions performed at high U saturations have fewer free extractant molecules; therefore, the extraction yield of all metals in solution decreases. Table I shows how the D-values of some fission products change between extractions with low U saturation (0.5%) and high U saturation (50%). These saturations were used because they represent potential U saturation in various streams of a PUREX plant.

Table I. Fission product distribution coefficients (D-values) at two different U saturations.

Radionuclide	0.5% U Saturation		50% U Saturation	
	D-value	Extraction Yield	D-value	Extraction Yield
^{241}Am	$(3.0 \pm 0.2)\times10^{-2}$	(8.1 ± 0.5)%	$(8 \pm 1)\times10^{-3}$	(1.6 ± 0.2)%
^{144}Ce	$(2.1 \pm 0.2)\times10^{-2}$	(6.0 ± 0.5)%	$(3.64 \pm 0.03)\times10^{-3}$	(0.830 ± 0.007)%
^{155}Eu	$(5.0 \pm 0.4)\times10^{-2}$	(13 ± 1)%	$(1.30 \pm 0.07)\times10^{-2}$	(2.9 ± 0.2)%
^{154}Eu	$(4.9 \pm 0.3)\times10^{-2}$	(12.9 ± 0.6)%	$(1.2 \pm 0.1)\times10^{-2}$	(2.7 ± 0.3)%
^{106}Ru	$(5.9 \pm 0.5)\times10^{-2}$	(15 ± 1)%	$(1.7 \pm 0.1)\times10^{-2}$	(3.8 ± 0.2)%
^{137}Cs	$(3.77 \pm 0.08)\times10^{-5}$	(0.0113 ± 0.0003)%	$(1.19 \pm 0.03)\times10^{-5}$	(0.0027 ± 0.0001)%

In the general PUREX process, Pu and U are partitioned from each other by reducing Pu(IV) to Pu(III) to strip it from the organic phase (30% tri-*n*-butyl phosphate in *n*-dodecane), while U remains in the organic phase. Prior to this partition, all extractions performed will have D-values similar to the 50% U saturation columns in Table 1. After the partition, all further Pu purification extractions are performed at low U concentrations, similar to the 0.5% U saturation columns. Therefore, the difference in D-values between these extractions may be used to determine whether a sample of $Pu(NO_3)_4$ received further PUREX separations after the Pu-U partition step. Table II shows how the extracted inter-elemental

fission product ratios change between the two different extraction conditions. The biggest difference between the two extraction conditions can be seen in the Ce inter-elemental ratios.

Table II. Inter-elemental ratios of fission product distribution coefficients (D-values) compared at two different U saturations at 3 M HNO_3. Difference is calculated as (50% – 0.5%)/50%.

Inter-elemental Ratio	0.5% U Saturation	50% U Saturation	Difference
$^{241}Am/^{144}Ce$	1.4 ± 0.1	2.1 ± 0.3	35%
$^{241}Am/^{154}Eu$	0.59 ± 0.06	0.60 ± 0.09	1%
$^{241}Am/^{106}Ru$	0.50 ± 0.06	0.45 ± 0.07	-10%
$^{241}Am/^{137}Cs$	780 ± 60	650 ± 90	-21%
$^{144}Ce/^{154}Eu$	0.43 ± 0.05	0.28 ± 0.02	-52%
$^{144}Ce/^{106}Ru$	0.36 ± 0.04	0.21 ± 0.01	-69%
$^{144}Ce/^{137}Cs$	570 ± 50	305 ± 9	-86%
$^{154}Eu/^{106}Ru$	0.8 ± 0.1	0.76 ± 0.07	-11%
$^{154}Eu/^{137}Cs$	1330 ± 120	1080 ± 70	-22%
$^{106}Ru/^{137}Cs$	1570 ± 140	1400 ± 100	-10%

Fig. 1(a) plots two Ce inter-elemental activity ratios against each other at multiple HNO_3 concentrations to show how distinct the differences between the two extraction conditions can be. Using this preliminary data, it may be possible to distinguish if a sample of $Pu(NO_3)_4$ experienced PUREX extractions after the partition of U or not. Fig. 1(b) plots the $^{154}Eu/^{106}Ru$ activity ratio against nitric acid

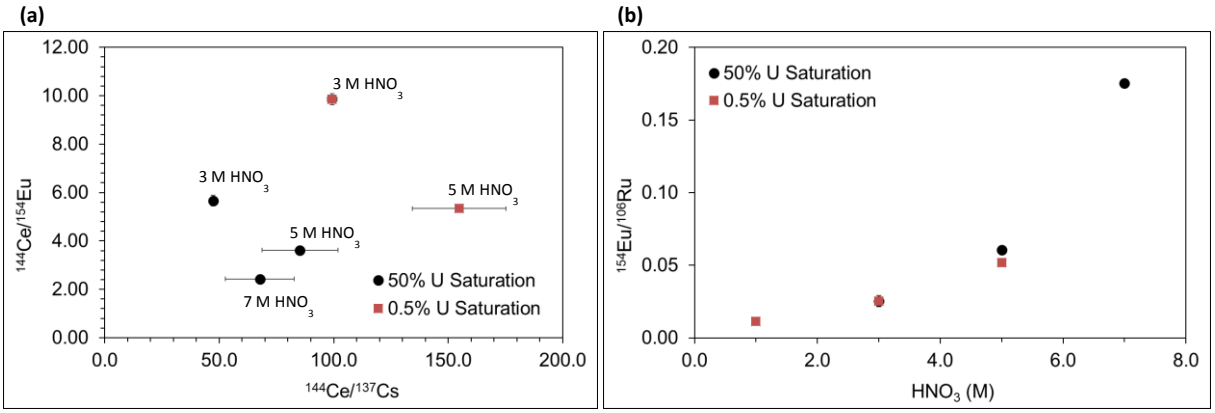

FIG. 1. Examples of how the activity ratio of fission product elements may be used to determine the separation conditions of $Pu(NO_3)_4$. Fig (a) on the left shows separation between PUREX extractions performed at two different U saturations over varying HNO_3 concentrations. Fig (b) on the right shows the possible U saturation independence of one fission product activity ratio.

concentration for the two different U saturations. Preliminary data suggests that the $^{154}Eu/^{106}Ru$ activity ratio may be independent of U saturation. This is useful information that would allow the determination of the HNO_3 concentration used in a PUREX separation regardless of the U saturation of the system.

Further effort is underway to complete the remaining extractions at 1, 3, 5, and 7 M HNO_3 at both 50% and 0.5% U saturation to investigate these effects in more detail.

Test runs the multi-nucleon transfer reaction detector array for synthesis of heavy elements

A. Wakhle, K. Hagel, A.B. McIntosh, M. Barbui, J. Gauthier, A. Jedele, A. Rodriguez Manso, J.B. Natowitz, K. Sekizawa, Z. Tobin, R. Wada, S. Wuenschel, A. Zarrella, and S.J. Yennello

An 'Active Catcher' array was constructed in 2016 [1] to study multi-nucleon transfer reactions forming heavy elements. The array consists of 40 YAP scintillators coupled to Hamamatsu PMTs via Lucite light guides at forward angles, and 8 IC-Si detectors at backward angles. A schematic is shown in Fig. 1. In August 2016, experimental data were taken using this array: a beam of ^{238}U at 7.5 MeV/nucleon was incident on a ^{232}Th target. Digital signal processing was achieved using the Struck SIS3316 250MHz Flash ADC modules, and the results of this experiment have been published [2]. This first 'physics' measurement has shown tantalizing glimpses into the synthesis of elements with Z as high as 116 via correlated pair searches and measurements of alpha energies as high as 12MeV. Clear identification of alpha chains was not possible due to the difficulty of analysis and the relatively uncharted and violent reaction landscape of ^{238}U+^{232}Th.

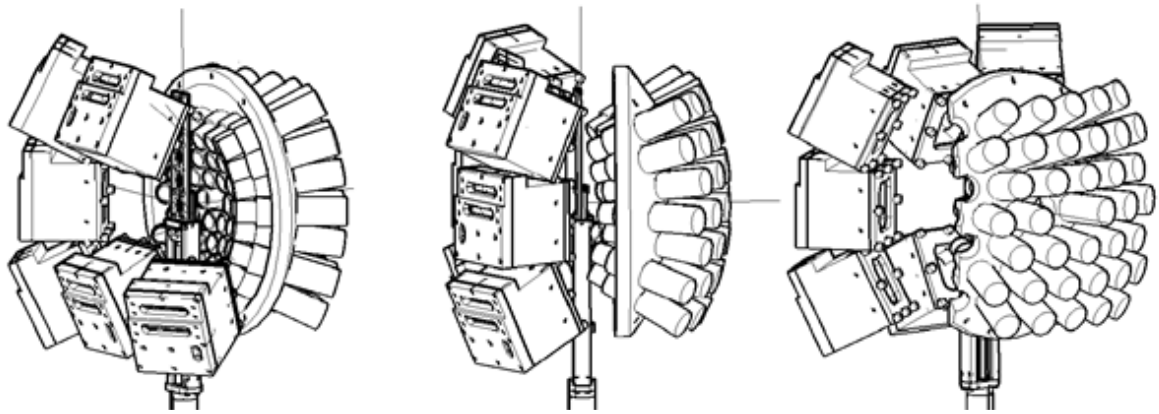

FIG. 1. Schematic of IC-Si and YAP detector array. In the central panel the beam enters from the left.

We have since conducted three experiments to benchmark the AC, progressing towards the grand goal of identifying alpha chains, and establishing parent-daughter relationships. Details of the measurements follow:

1. ^{22}Ne + ^{232}Th

A ^{232}Th target was bombarded with a ^{22}Ne beam at 143 MeV (6.5 MeV/A) to measure the production cross sections of ^{227}Th, ^{226}Ac, ^{225}Ac and ^{224}Ac. These nuclides are long-lived and were implanted in the forward angle YAP+PMT Active Catcher, to determine their activities and cross sections by offline alpha counting in the backward angle Si+IC array. Preliminary cross sections match the measurement of Kumpf and Donets [3], and a more detailed analysis is underway by Zach Tobin.

2. ^{197}Au + ^{208}Pb

This was a stepping stone to the ^{208}Pb+^{208}Pb reaction in the third run. A ^{208}Pb target was bombarded with a ^{197}Au beam at 7 MeV/A to measure the production cross sections of nuclei with 82<Z<92 and 208<A<228. These nuclides decay primarily by alpha emission with alpha energies between 7MeV and 10MeV, and half-lives ranging from ~1s down to a few 100ns.

The beam was pulsed ON for 30ms to build up activity in the nuclides of interest, and the pulsed OFF for 30ms to observe their decay in a low background (beamless) environment. Alpha lines corresponding to decays in the 7MeV to 10MeV range, and mean lives of a few ms were observed. However, we were unable to identify alpha chains and establish parent-daughter relationships due to software of the digital data acquisition system.

3. ^{208}Pb + ^{208}Pb

A ^{208}Pb target was bombarded with a ^{208}Pb beam at 7 MeV/A to measure the production cross sections of nuclei with 82<Z<92 and 208<A<228. Additionally the acquisition system was modified to allow continuous acquisition (i.e. no dead time between detector pulses). This modification fully exploits the capabilities of the SIS3316 250MHz Flash ADC modules. Analysis from this experiment is currently underway.

To complement to experimental work on the AC, a systematic series of TDHF calculations were performed for the ^{238}U+^{232}Th reaction (Fig. 2). Multi-nucleon transfer products were observed in the exit

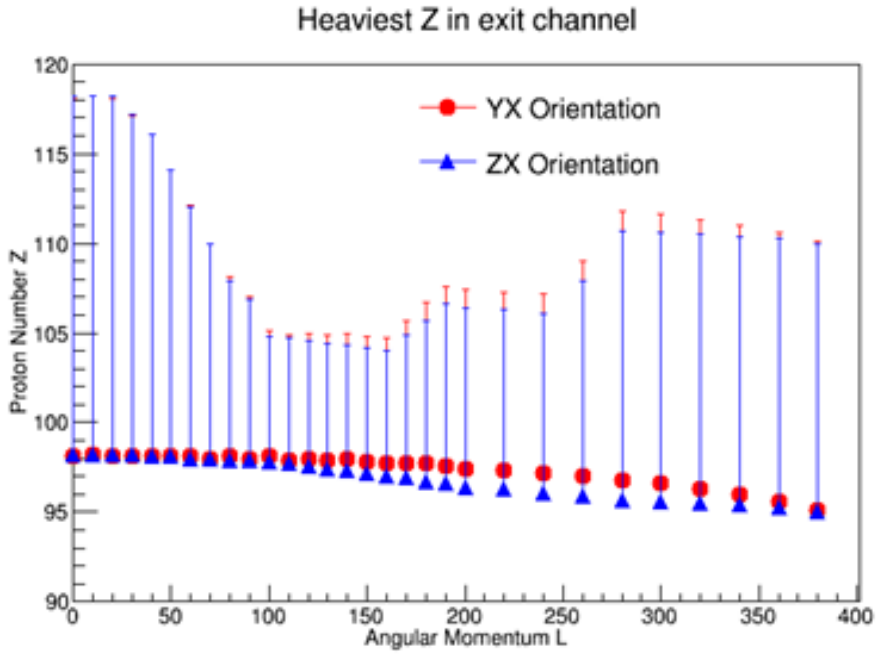

FIG. 2. Results from TDHF calculations of ^{238}U+232Th at 7.5AMeV. Exit channel proton number vs. entrance channel angular momentum. The points correspond to the TDHF prediction for proton number of the larger of two fragments in the exit channel. The bars correspond to mass widths as predicted by TDRPA (calculations by K. Sekizawa). Limits correspond to approximately 0.1microbarn cross section. Results are shown for two orientations of the entrance channel nuclei. Other cases lead to less exotic products.

channel, and TDHF suggests that elements with Z>100 can be produced in this reaction. TDRPA calculations, performed by our collaborator K. Sekizawa, suggest that the Z distribution of these fragments extends up to Z=118 with a cross section of 0.1 microbarns.

We have purchased two sCVD diamond detectors from Cividec, and Micron, and two preamplifiers on loan from each company. These will be tested with an alpha source, and protons from the K-150 to benchmark sCVD diamonds as a potential forward angle implantation detector.

[1] S. Wuenschel *et al.*, *Progress in Research*, Cyclotron Institute, Texas A&M University (2015-2016), p. II-21.
[2] S. Wuenschel *et al.*, Phys. Rev. C **97**, 064602 (2018).
[3] H. Kumpf and E.D. Donets, Soviet Phys. Jetp, **17**, 3 (1963).

Simulations for proton detection in ^{59}Fe(d,p)^{60}Fe

A.B. McIntosh

This report describes simulations done in preparation for an experiment to measure the gamma ray strength function of ^{60}Fe. Iron-60 is of interest in s-process nucleosynthesis since this is a branch point, and therefore impacts the abundances of heavier elements. Iron-60 has been observed in the gamma spectrum nearby in our galaxy [1]. Iron-60 has been measured in sea floor sediments across the globe, and on the surface of the moon [2,3]. Iron-60 has also been observed in cosmic rays [4]. These findings all imply that ^{60}Fe was produced in the relatively recent past and distributed in our region of the galaxy, and by studying it we may learn about s-process nucleosynthesis.

Measurement of the gamma ray strength function in reactions of ^{57}Fe(d,p)^{58}Fe and ^{59}Fe(d,p)^{60}Fe will be made at TAMU. To measure the excitation energy, we will measure the energy and angle of the recoil proton at backward angles in the lab frame using an annular silicon detector (S3 from Micron Semiconductor). Consideration of background reactions is assessed in another 2019 TAMU annual report [5].

The excitation energy resolution is determined by several factors: the energy resolution of the silicon detector, the angular resolution of the silicon detector, the finite width of the beam-spot on target, the depth of the reaction point in the target, the energy loss of the proton in the target, and the energy loss of the proton in the dead layer of the silicon detector. To assess the impact of these factors, a simple simulation was developed. The radioactive beam is considered to impinge on the target with a Gaussian distribution with a width of 5mm (FWHM). The reaction point in the target is chosen uniformly within the thickness of the target (1000ug/cm2). The excitation energy of the ^{60}Fe is chosen at specific discrete values selected by the user (7.0MeV and 9.5MeV). The energy of the recoil proton is determined by conservation of energy (including Q value, which is a significant contribution). The angle of the proton is selected in the CM frame on a distribution described by TWOFNR calculations (a DWBA (Distorted Wave Born Approximation) code) for angular momenta of 1, 2, 3 and 4 hbar. A cos(theta) weighting is applied, which dominates the angular yield distribution. The proton loses an appropriate amount of energy as it exits the previously chosen fraction of the target at the appropriate angle in the lab frame. The proton loses energy in the dead layer of the silicon detector (8000 Angstroms, with random fluctuations of 800 Angstroms). The proton then loses its remaining energy in the silicon detector in a specific ring segment. The S3 silicon detector contains 24 ring segments between 22mm and 70mm radius, and is positioned 2 cm upstream of the target. The sector side must face the target since the ring side has a much thicker dead-layer. The energy is smeared by sampling a Gaussian with width 50 keV. The center of the ring is used as the measured angle relative to the ideal target location (this is the best the experimenter would be able to do). This "measured" angle and smeared energy is used to back correct for energy loss in the dead silicon (this time neglecting the unknown fluctuations) and for energy loss in the target (assuming the reaction occurred at the center of the target in all three dimensions). This corrected energy and angle are used to calculate the excitation energy of the ^{60}Fe.

Fig. 1 (left) shows the correlation between the true energy and angle of the proton in the lab frame for E* = 7.0 MeV and E* = 9.5 MeV. The lowest energy (around 500 keV) protons are at 180 degrees. The neutron separation energy for 60Fe is at E* = 8.8 MeV. States above this are not strictly necessary for the analysis but are helpful as a check of the measurement, as the gamma decay branch decreases as the neutron decay branch turns on. The right panel of Fig. 1 shows the same energy-angle correlation after considering the finite acceptance of the detector and all the factors noted above. The distribution is cut out except within 120-150 degrees. The proton energy is diminished and broadened. Some very low energy protons that would otherwise strike the detector are stopped before they reach the active part of the silicon.

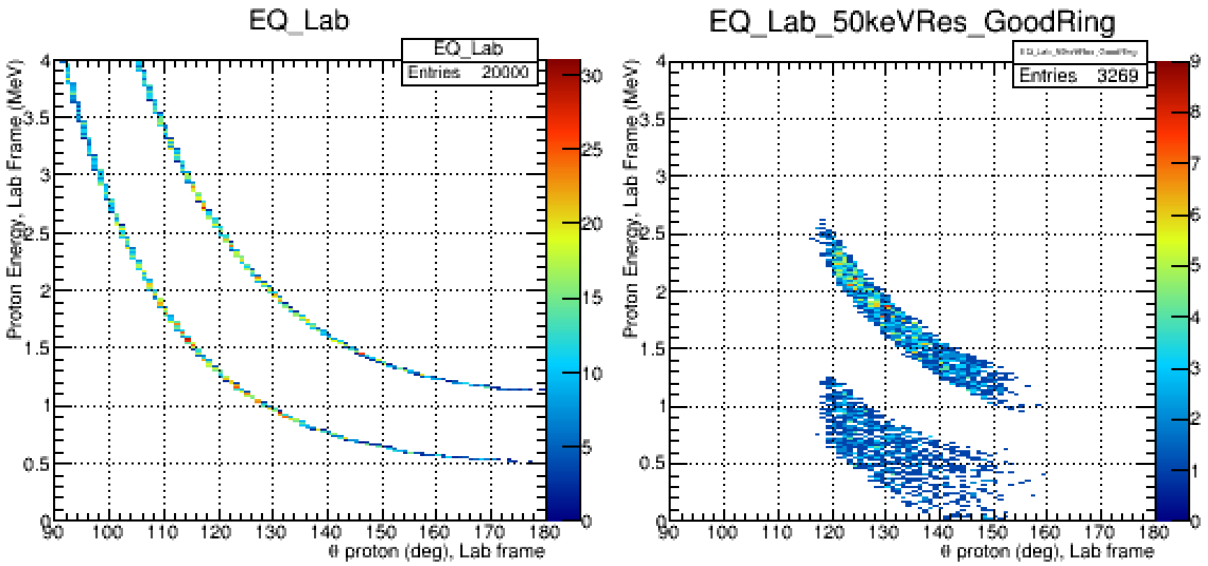

FIG. 1. Energy-angle correlation of the proton from ^{59}Fe(d,p)^{60}Fe @ 7.5 MeV/u for "perfect" detectors (left) and "reasonable" detectors (right).

Using the values "measured" in Figure 2 (left) to calculate the excitation energy resolution gives around 270 keV (σ) at E* = 7.0 MeV and between 350 and 450 keV at E* = 9.5 MeV (the width depends on the ring, with worse resolution for larger angles). Since we are not looking for discrete states, but only need to select on a region of excitation energy in the analysis (the Forward Analysis Method), this resolution expected is acceptable.

We now consider the rate of good measured events, summarized in Table I. Assuming a beam intensity of 1E5 pps, a cross section of 27.8 mb (obtained from the TWOFNR calculations mentioned above), and a target thickness of 1000 ug/cm2, one expects a reaction rate of 0.2 reactions per second. The silicon efficiency is about 17% due entirely to the geometrical coverage. Assuming an efficiency for measuring gamma rays of 25%, we expect on the order of 5000 good measured reactions per week.

Table 1. Predicted reaction rate for ^{59}Fe(*d*,*p*)^{60}Fe @ 7.5 MeV/u.

N=Iσt		
Intensity	1.00E+05	particles/sec
Cross section	27.8	mb
	2.78E-26	cm2
Thickness	1000	ug/cm2
Thickness	0.001	g/cm2
molar mass	16	g/mol for CD2
Thickness	0.0000625	molCD2/cm2
NA	6.02E+23	moleculesCD2/mol
Thickness	3.76E+19	moleculesCD2/cm2
Thickness	7.53E+19	Dnuclei/cm2
Reaction Rate	2.09E-01	reactions/sec
silicon eff	17%	
BaF2 efficiency	25%	
Residue Efficiency	100%	
Detected Reaction Rate	0.008891	reactions/sec
Detected Reaction Rate	32.01	reactions/hour
Detected Reaction Rate	224.05	reactions/day
Detected Reaction Rate	5377.15	reactions/week

[1] R. Diehl. Rep. Prog. Phys. **76**, 026301 (2013).

[2] A. Wallner *et al.*, Nature **532**, 69 (2016).

[3] L. Fimiani *et al.*, Phys. Rev. Lett. **116**, 151104 (2016).

[4] W.R. Binns *et al.*, Science **352**, 677 (2016).

[5] A.B. McIntosh, *Progress in Research*, Cyclotron Institute, Texas A&M University (2018-2019),p. II-21

Calculation of background reactions for ^{59}Fe(d,p)^{60}Fe

A.B. McIntosh

Another 2019 TAMU Annual Report discusses the excitation energy resolution and reaction rate for the reaction of ^{59}Fe(d,p)^{60}Fe @ 7.5 MeV/u which is of astrophysical and geological interest as well as of nuclear interest. This report discusses the main anticipated sources of background in this reaction, and proposes a means to deal with them.

The radioactive ion beam developed with MARS at TAMU contains some heavy and light species. Of the heavy species, 79% is the desired ^{59}Fe, 13% is ^{57}Co, and 7% is ^{59}Co. If the iron can be distinguished from cobalt, the lighter species will be trivial.

The target is to be CD2 with purity greater than 95%. Fusion evaporation reactions on carbon, deuterium, and protons must be considered.

PACE4 (packaged with LISE++) calculations indicate that for fusion of ^{59}Fe on ^{1}H and ^{2}H produce negligible charged products backward of 120 degrees. The excitation energy is low enough that particles are rarely ejected with sufficient velocity to overcome the boost of the compound nucleus. The yield of such rare particles is expected to be a factor of 70 below the yield of the desired protons from (d,p).

Fusion of ^{59}Fe on ^{12}C creates compound nuclei with high enough excitation energy that charged particles can be evaporated with enough velocity to overcome the velocity boost of the compound nucleus and strike the silicon detector backward of the target. These cannot be discriminated from protons from the (d,p) reaction by only the energy and angle of the light charged particle. The velocity of the residue, however, does provide a means to discriminate. From momentum conservation, the compound nucleus in ^{59}Fe + ^{12}C fusion is significantly slower than the (d,p) residues. Fig. 1 shows the separation. The angle of the proton in the lab frame is plotted against the time of flight of the heavy residue across a 1 m flight path. The color shows the yield of protons produced in carbon fusion reactions. The red cross-hatched region shows the kinematically allowed range for ^{59}Fe(d,p)^{60}Fe reactions. These regions are well separated requiring no better than 1 ns time resolution.

The cobalt beam contaminants can undergo (d,p) reactions that are kinematically indistinguishable from the iron. Energy loss measurement of the beam particles event by event appears to be a possible way forward. Energy loss was calculated for an 20 mm thick ionization chamber with 30 Torr of isobutate and a total of 1.5 um mylar windows. Iron @ 7.5 MeV/u loses 5.42 MeV total in the mylar and 6.49 MeV in the gas. Cobalt @ 7.5 MeV/u loses 5.75 MeV total in the mylar and 6.78 MeV in the gas. The difference in energy loss in the gas of 390 keV is a difference of 6.1%. Thus an energy loss detector that is radiation hard to the 1E5 particle/sec level with an energy resolution sufficient to resolve peaks separated by 6.1% will allow event-by-event identification of beam contaminants.

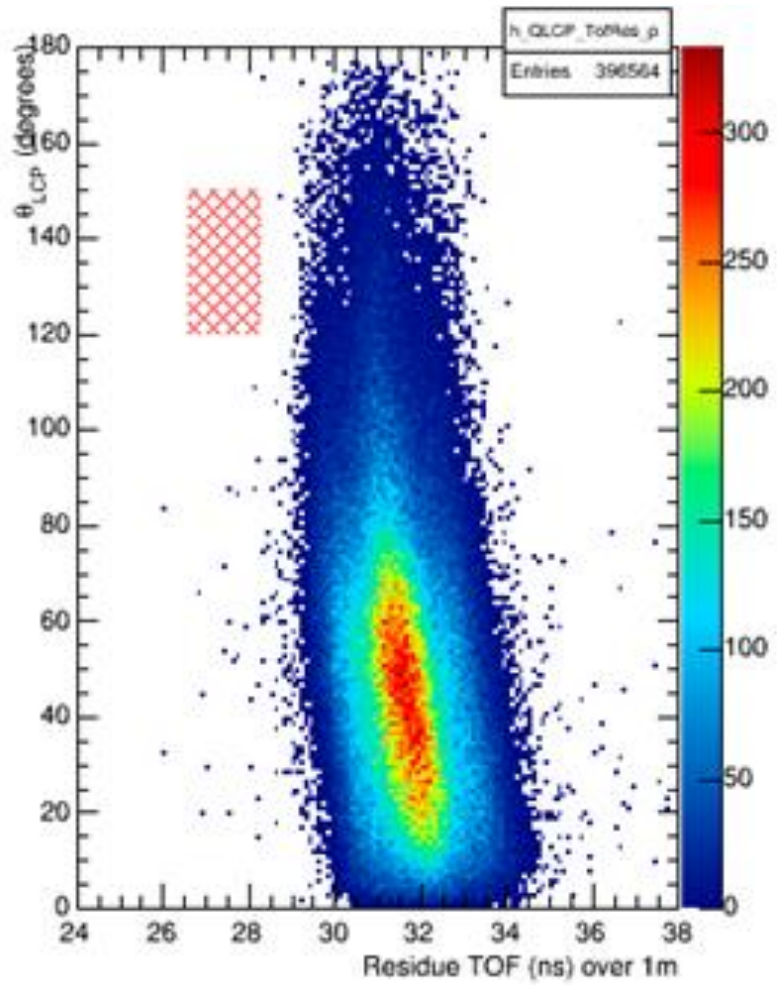

FIG. 1. GEMINI calculation for ^{59}Fe + ^{12}C fusion evaporation at 7.5 MeV/u. The angle of evaporated protons is shown as a function of the flight time of the heavy residue on a 1 m flight path. The red cross-hatched region indicates the region of interest for proton angle and residue time of flight for ^{59}Fe(d,p)^{60}Fe reactions.

Proton-proton correlation functions using the upgraded FAUST array

L.A. Heilborn, A.B. McIntosh, M.D. Youngs, and S.J. Yennello

Proton-proton correlation functions have been predicted to be sensitive to the asymmetry energy in the nuclear equation of state using transport simulations [1]. As detailed in previous annual reports [2-4], position-sensitive Dual-Axis Dual-Lateral (DADL) Si detectors [5] were implemented as the dE detectors in the Forward Array Using Silicon Technology (FAUST) [6]. This setup was used to collect light-charged particle (LCP) data in four heavy-ion reactions: ^{40}Ca+^{58}Ni at 40 MeV/nucleon, ^{40}Ar+^{58}Fe at 40 and 30 MeV/nucleon, ^{40}Ar+^{70}Zn at 30 MeV/nucleon to extract proton-proton correlation functions and compare to Boltzmann-Uehling-Uhlenbeck transport simulations (pBUU).

Proton-proton correlation functions were extracted from experimentally measured proton pairs chosen to have been emitted early in the collision (momentum of the proton pair>250 MeV/c) and from central collisions (event transverse momentum>180 MeV/c). Both of the cuts are necessary in order to draw out the proton-proton interaction peak at 20 MeV/c. The proton-proton correlation functions are shown in Fig. 1. The resolution and efficiency at low q_{Rel} of FAUST achieved in this experiment is

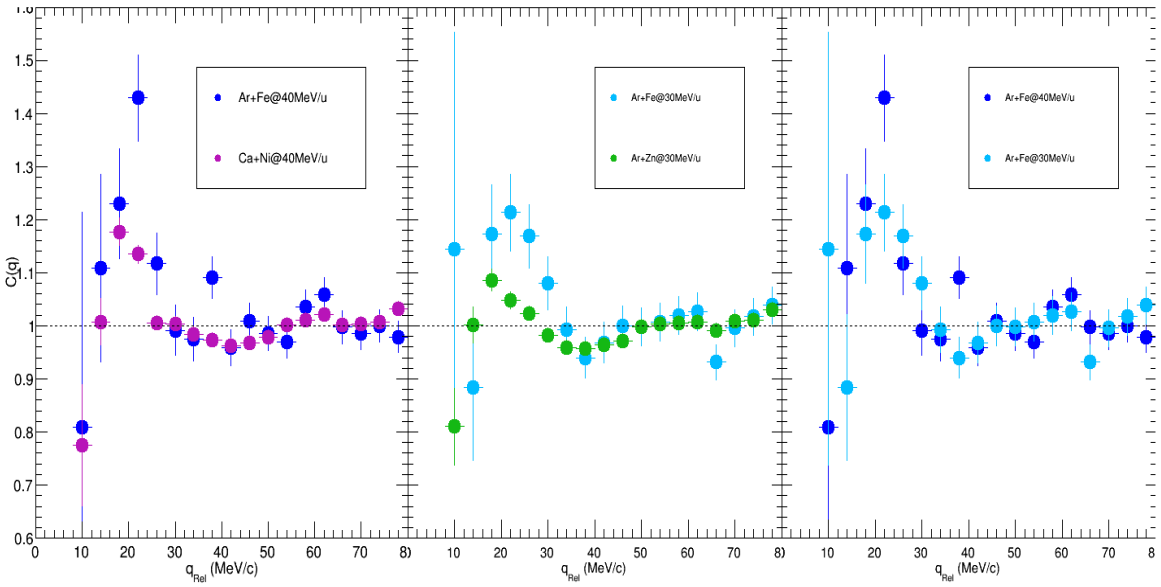

FIG. 1. Experimental proton-proton correlation functions extracted from, from left to right: the 30 MeV/nucleon systems (Ar+Zn green, Ar+Fe cyan), 40 MeV/nucleon systems (Ca+Ni purple, Ar+Fe blue), and the Ar+Fe systems at 40 MeV/nucleon (blue) and 30 MeV/nucleon (cyan). Figure from [7].

sufficient to extract light charged particle correlation functions, particularly proton-proton correlation functions, which was the goal of this undertaking. Other light-charged particle correlation functions are shown in [7]. The four systems included in this analysis have sufficient data to consider the ordering of the strength of the proton-proton correlation functions when varying system (asymmetry and size) and beam energy. The four systems were compared in three sets: Varying the system at 40 MeV/nucleon,

varying the system at an energy of 30 MeV/nucleon, and changing the beam energy for the same system. In the 40 MeV/nucleon case, the more neutron-rich system has a stronger correlation function, while in the 30 MeV/nucleon case, the less neutron-rich system has a stronger correlation function, which may be because it has fewer overall nucleons. The correlation functions extracted for the same system at two different beam energies are within error bars.

Correlation functions were also extracted from pBUU, using three different parametrizations of the asymmetry energy by varying the value of γ. The correlation functions from pBUU showed no dependence on the asymmetry energy (varied by varying γ) at low impact parameter selected for early emitted (last collision before 100 fm/c) protons. All three parametrizations are shown in Fig. 2 for the Ar+Zn at 30 MeV/nucleon reactions. The different parametrizations for the other three systems were also indistinguishable. The results from the transport simulations were therefore inconclusive when compared to the experimental correlation functions.

In order to extract this information, the angular resolution of the FAUST array was enhanced

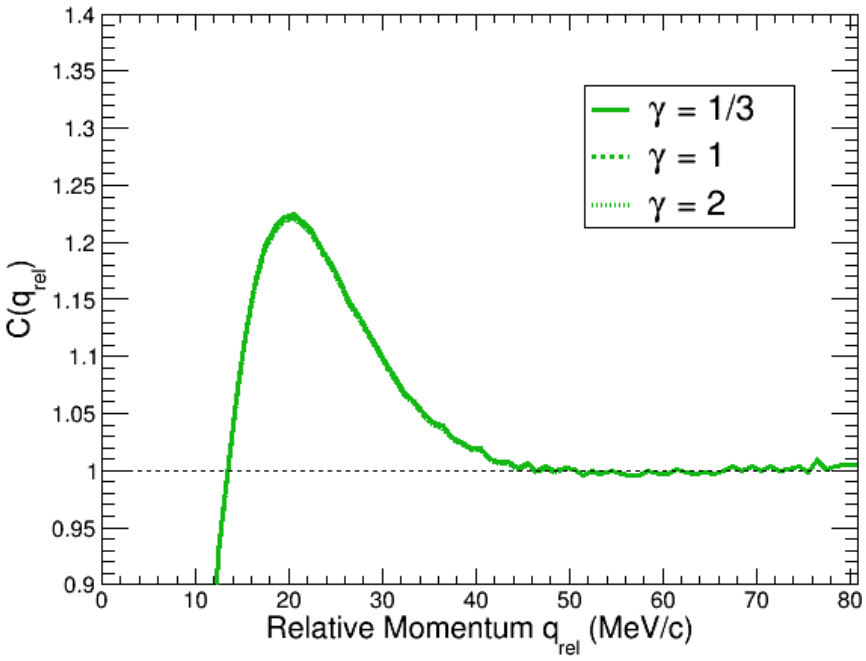

FIG. 2. Proton-proton correlation functions extracted from pBUU simulations using three different parametrizations of the asymmetry energy, denoted by γ. These three parametrizations result in indistinguishable proton-proton correlation functions for this system, Ar+Zn at 30 MeV/nucleon.

significantly by using a new style of position-sensitive DADL silicon detectors in every Si-CsI telescope. The new position-sensitive configuration along with the infrastructure established in this project for running in this mode was used for the first time in this campaign. The slotted mask, designed for use with the FAUST, has appropriately sized slits to verify the position calibration. The upgraded configuration has already been used in a subsequent experiment.

[1] L.W. Chen, V. Greco, C.M. Ko, and B.A. Li, Phys Rev. Lett. **90**, 162701 (2003).
[2] L. Heilborn, *et al., Progress in Research*, Cyclotron Institute, Texas A&M University (2014-2015), p. IV-54-57.
[3] L. Heilborn, *et al., Progress in Research,* Cyclotron Institute, Texas A&M University (2015-2016) p. IV-61-64.
[4] L. Heilborn, *et al., Progress in Research,* Cyclotron Institute, Texas A&M University (2016-2017) p. IV-37-39.
[5] S. Soisson, *et al.*, Nucl. Instr. and Meth. A **613**, 240 (2010).
[6] F. Gimeno-Nogues, *et al.*, Nuclear Instrum. Methods Phys. Res. **A399**, 94 (1997).
[7] L. Heilborn, Ph.D. Thesis, Texas A&M University, 2018.

High excitation energy resonances in α-conjugate nuclei

K. Hagel, J.B. Natowitz, A.B. McIntosh, L. Heilborn, S.J. Yennello, R. Wada, A. Wakhle, A. Jedele, J. Gauthier, M.D. Youngs, Y.-W. Lui, M. Sorensen, A. Hannaman, and Z. Tobin

We reported on an investigation where we performed an "*Examination of evidence for resonances at high excitation energy in the 7α disassembly of ^{28}Si*" [1]. In this work, we studied excitation energy distributions of the breakup of ^{28}Si and observed several high energy peaks in the 7α decay as shown by the red points in Fig. 1. Some of the observed peaks were in the region of excitation energies predicted by constrained self-consistent Skyrme–Hartree–Fock model calculations [2]. In that

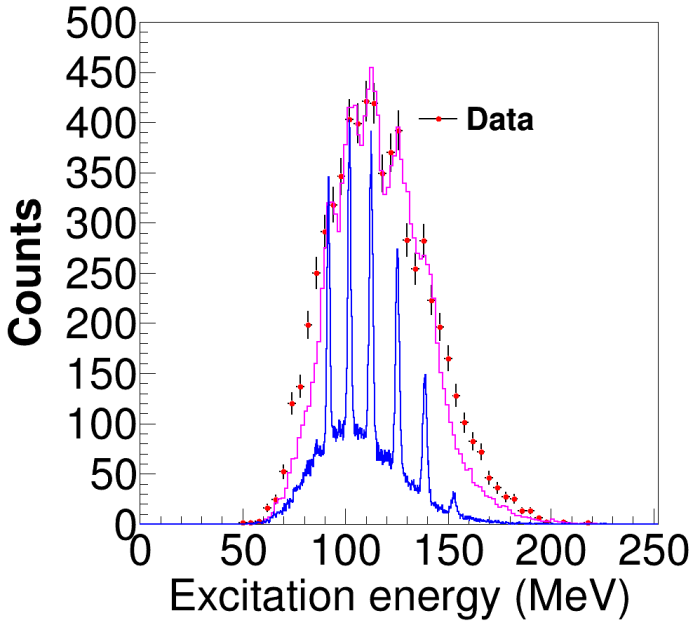

FIG. 1. Excitation energy distribution of the 7α breakup of ^{28}Si.

work, the excitation energy was calculated as a function of the quadrupole moment and a toroidal isomer was consider located if a minimum in the distribution was observed [2]. Since some of the peaks in the experiment were in the range of those predicted for toroidal configurations, namely about 143MeV for ^{28}Si, we decided to pursue this interesting subject in more depth.

The experiment was performed using the NIMROD [3] multi-detector array. The angular resolution of the detectors in NIMROD is completely determined by the area of the respective detector leading to angular uncertainty in the reconstruction of any excitation energy. Any possible resonances, therefore, will be smeared.

The pink curve in Fig. 1 represents a background distribution which is constructed by using mixed 7α events from the experimental data. Narrow peaks representing possible resonances are added to this background distribution. The entire curve is then filtered by the experimental acceptance of NIMROD in particular taking into account the finite angular resolution given by the size of the respective

detector elements. We can observe in the distribution that the smearing of these narrow peaks leads to peaks of similar widths to what is observed in the experiment.

In order to confirm that these high energy peaks are truly resonances, we propose to repeat the experiment using a position sensitive detector array. The FAUST [4] array at the Cyclotron Institute has been outfitted with position sensitive DADL detectors. Any narrow peaks which show up as wide peaks in the pink curve in Fig. 1 would be significantly narrower with the 1mm position resolution that the DADL detectors provide. This is shown by the blue curve in Fig. 1 where the same mixed event background distribution with narrow resonances added are filtered by the FAUST acceptance using a DADL position resolution of 1mm. We observe that the peaks are significantly sharper.

While the initial experiment focused on ^{28}Si, we anticipate using a number of alpha conjugate projectiles that include, but are not limited to, ^{28}Si, ^{32}S, ^{36}Ar and ^{40}Ca in the experiments to extend this study. We also anticipate doing a beam energy scan in order to further characterize the observed peaks.

The experiment is in the planning stages and we anticipate executing the experiment in the coming year.

[1] X.G. Cao, E.J. Kim, K. Schmidt, K. Hagel, M. Barbui, J. Gauthier, S. Wuenschel, G. Giuliani, M.R.D. Rodriguez, S. Kowalski, H. Zheng, M. Huang, A. Bonasera, R. Wada, N. Blando, G.Q. Zhang, C. Y. Wong, A. Staszczak, Z.X. Ren, Y.K. Wang, S.Q. Zhang, J. Meng, and J.B. Natowitz, Phys. Rev. C **99**, 014606 (2019).

[2] Andrzej Statszczak and Cheuk-Yin Wong, Phys. Lett. B **738**, 401 (2014).

[3] S. Wuenschel, K. Hagel, R. Wada, J.B. Natowitz, S.J. Yennello, Z. Kohley, C. Bottosso, L.W. May, W.B. Smith, D.V. Shetty, B.C. Stein, and S.N. Soisson, Nucl. Instrum. Methods Phys. Res. **A604**, 578 (2009).

[4] F. Gimeno-Nogues, D.J. Rowland, E. Ramakrishnan, S. Ferro, S. Vasal, R.A. Gutierrez, R. Olsen, Y.-W. Lui, R. Laforest, H. Johnston, and S. J. Yennello, Nucl. Instrum. Methods Phys. Res. **A399**, 470 (1997).

N/Z equilibration: Mapping isotopic yields in binary projectile breakups

A. Hannaman, A.B. McIntosh, A. Jedele, A. Rodriguez Manso, K. Hagel, Z. Kohley, and S.J. Yennello

N/Z equilibration in dynamically deformed atomic nuclei formed from heavy ion collisions has been studied to gain new insights into the nuclear equation of state [1,2]. A low-density neck formed between the projectile and target produces a region of neutron-richness due to the density dependence of the asymmetry energy. The evolution of this dynamic system leads to N/Z equilibration between the neutron-rich and neutron-poor regions of the PLF* depicted in Fig 1; these two regions can develop into the "heavy fragment" and "light fragment" in the exit channel.

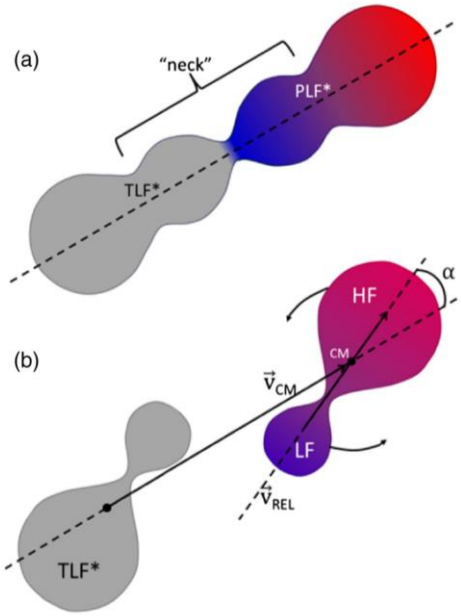

FIG. 1. Illustration from [3] depicting dynamical projectile and target interaction and decay. (a) Deformed PLF* and TLF* during the interaction. (b) At a later time, the PLF* will break after rotating relative to the TLF* (measured by the angle α) forming the heavy fragment (HF) and light fragment (LF). The blue region denotes neutron richness while the red region denotes neutron deficiency.

The rotation angle $\alpha = \mathrm{acos}[\vec{v}_{CM} \cdot \vec{v}_{REL}/(\| \vec{v}_{CM} \| \| \vec{v}_{REL} \|)]$ of the PLF* prior to binary breakup into the HF and LF is used as a measure for probing the equilibration time [3,4]. The velocity vectors used in the calculation of α are the two-fragment center-of-mass velocity $\vec{v}_{CM} = (m_{HF}\vec{v}_{HF} + m_{LF}\vec{v}_{LF})/(m_{LF} + m_{HF})$ and the relative velocity between the HF and LF $\vec{v}_{REL} = \vec{v}_{HF} - \vec{v}_{LF}$. In this work, the isotopic yields of the light fragment are mapped against α to seek a more sensitive probe for equilibration and to discover the contributions and behaviors of each isotope during this process. In this

study, a 35 MeV/u beam of ^{70}Zn accelerated by the K500 Cyclotron at Texas A&M University was impinged on a thin ^{70}Zn target and reaction products were measured in NIMROD (Neutron Ion Multidetector for Reaction Oriented Dynamics) [5, 6].

Prior studies show stronger signatures of equilibration when the HF is significantly larger than the LF, therefore the requirement that $Z_{HF} \geq 12$ is used for this analysis [7]. The average composition <N-Z/A> of the LF as a function of α shows characteristic first order kinetics, with neutron richness decreasing as the PLF* undergoes greater rotation prior to breakup [Fig. 2]. The deviation from exponential behavior at α values less than ~15° results from the inability to measure the HF and LF in the same detector as well as the confined phase space that this aligned breakup orientation occupies. Equilibration resulting from the dynamical process depicted in Fig. 1 is observed in the α range of 0° to 90°, with statistical decay dominating past an α of 90° [2].

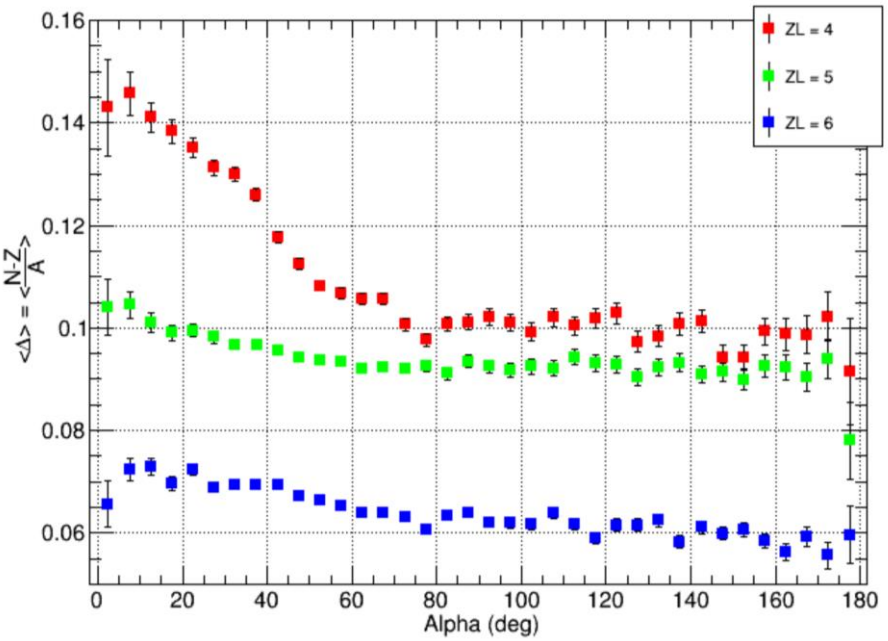

FIG. 2. The average composition <N-Z/A> of the LF for Z = (4,5,6) as a function of the α angle for events allowing all values of Z_{HF} above 12. Error bars are statistical.

When these LF composition curves are decomposed into their constituent isotopic fractional yields, some interesting features become apparent [Fig. 3]. Generally, the most neutron rich and neutron poor isotopes have the largest relative change in fractional yield made apparent by the logarithmic scale; however, these changes contribute little to the average composition due to their low yield. The strong rare isotope sensitivity in this analytical framework reflects the enhanced sensitivity of rare isotope yields across varying compositions of colliding systems [8]. Additionally, while most isotopes exhibit exponential behavior that asymptotically levels off akin to the average composition equilibration curves in Fig. 2, the more abundant N = Z + 1 isotopes decline across the entire α range and are better fit linearly. Further analysis and interpretation of isotopic yields is ongoing.

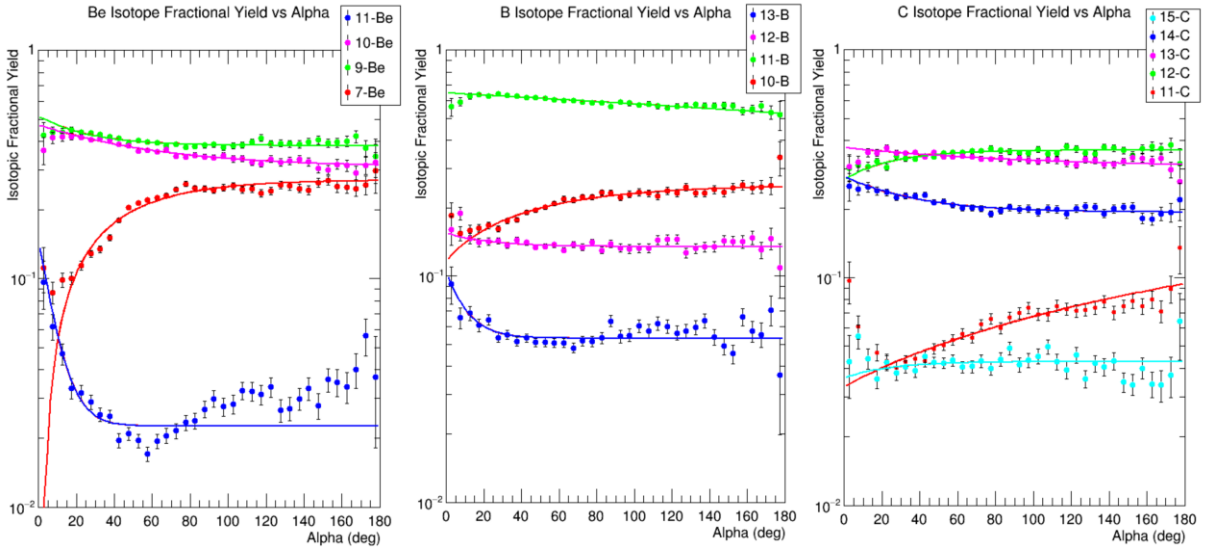

FIG. 3. The average composition <N-Z/A> of the LF for Z = 4,5,6 on log scale plotted as a function of the α angle for events allowing all values of Z_{HF} above 12 (exponential fit parameters exclude data points below 15° α and serve to guide the eye).

[1] S. Hudan *et al.*, Phys. Rev. C **86**, 021603(R) (2012).

[2] A. Rodriguez Manso *et al.*, Phys. Rev. C **95**, 044604 (2017).

[3] A. Jedele *et al.*, Phys. Rev. Lett. **118**, 062501 (2017).

[4] K. Brown *et al.*, Phys. Rev. C **87**, 061601 (2013).

[5] S. Wuenschel *et al.*, Nucl. Instrum. Methods Phys. Res. **A604**, 578 (2009).

[6] Z. Kohley *et al.*, Phys. Rev. C **82**, 064601 (2010).

[7] A.B. McIntosh *et al.*, Phys. Rev. C **81**, 034603 (2010).

[8] E. Ramakrishnan *et al.*, Phys. Rev. C **57**, 1803 (1998).

The nuclear caloric curve: Temperatures of simulated quasiprojectiles

M. Sorensen, A.B. McIntosh, Z. Kohley, and S.J. Yennello

The equation of state describes the emergent physical properties of matter. Experimental data is needed to help constrain the equation of state for nuclear matter. These constraints can help determine between a "ays-stiff" and a "ays-soft" equation of state, which has important astrophysical implications. For example, the proton-neutron makeup of neutron stars, and thus the cooling of neutron stars by the direct Urca process[1]. How temperature and the asymmetry of the nuclear matter interact has important implications for the strength of the asymmetry term.

The physical experimental data was taken on NIMROD (Neutron Ion Multidetector for Reaction Oriented Dynamics) [2]. The experiment ran a number of systems, ^{70}Zn+^{70}Zn , ^{64}Ni+^{64}Ni, and ^{64}Zn+^{64}Zn at 35 MeV/u [3]. The charged particles produced in these reactions were detected, along with the neutron multiplicity.

These runs proved to be a rich data set, which was analyzed to determine temperatures of the reconstructed quasiprojectiles(QP) [4]. As seen in Fig. 1, the temperatures increase as expected with excitation energy per nucleon. However, when the Quasi-projectile's asymmetry was used to further separate the data, a clear trend was observed. As the asymmetry of the quasi projectile increased the temperature as a function of excitation energy is shifted to lower temperature. This trend proved to be robust for multiple temperature probes using both momentum quadrupole fluctuations (kinetic) and the Albergo chemical thermometer. This phenomenon is consistent with the thermal Thomas-Fermi model.

The purpose of this research is to use antisymmetrized molecular dynamics (AMD) [5] coupled

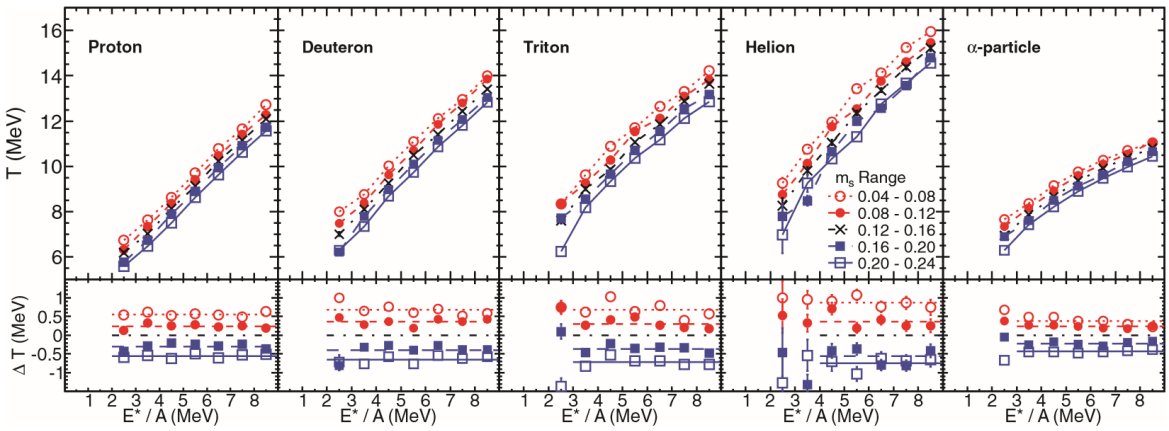

FIG. 1. Temperatures calculated as a function of excitation energy per nucleon. The different asymmetry values of the quasiprojectile(QP) are shown with different colors and marking according to the legends. The temperatures were determined by momentum quadrupole method. The temperature probes used are indicated on the top left of each curve. Taken from reference[4].

to GEMINI afterburner [6,7] to reproduce the trends seen with the experimental data. Once this is achieved, the effects of the imperfect nature of NIMROD can be removed, to see if the trend is preserved. Additionally, further alterations to the assumptions made in the model could be used to explore how the

asymmetry interacts with this affect. The focus of this analysis was on the ^{70}Zn+^{70}Zn system, as it was the data set with the most statistics. 10000 AMD-DS events where run by Z. Kohley to a time of 300fm/c, afterwards Gemini was used to deexcite the nuclides, with each AMD event used as a starting point for Gemini 20 times[3]. These events where then subjected to the same event selection cuts used to select the experimental data. First, these events were run through the NIMROD filter, in order to mimic the detector effects. The first gate was that the parallel velocity of the particle detected must be within a certain range of the projectile like fragment (PLF) (the largest fragment detected). This is done to remove particles that are more likely to have been emitted from the excited target like fragment (too little parallel velocity), and fast pre-equilirium particles (too much parallel velocity). The velocity conditions depend on the Z of the particle detected. For hydrogen particles the ratio range was from 35% to 165% of the PLF parallel velocity. Helium particles range was from 40% to 160% and for all other charged particles the range was 55% to 145%. Those particles that pass this condition where then combined with the neutrons detected from the neutron ball to reconstruct the quasi projectile. The event was only used for further analysis if the quasi projectile had a mass number between 48 and 52. The QP velocity could then be calculated from the momentum and masses of the particles emitted from it.

As seen in Fig. 2, the projectile appears aligned with the direction of the beam as expected for a

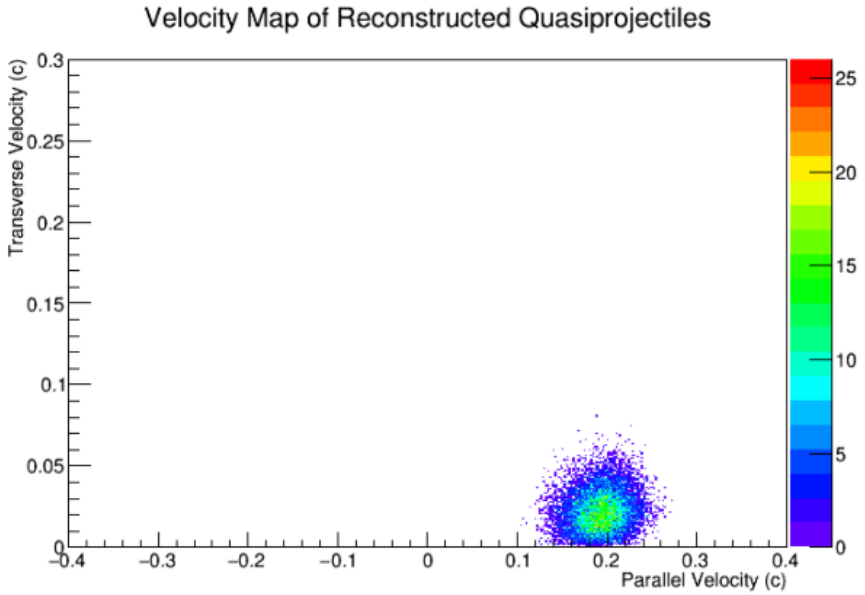

FIG. 2. The velocity map for the reconstructed QP. The velocity map for the reconstructed QP. The velocity in the transverse direction is plotted on y axis, it is an absolute value as it is taken from the vector addition of the velocity in the x direction and the y direction. The parallel velocity is plotted on the x axis. All the velocities are in unit c. This is plot is with the velocity cut and mass cut.

heavy fragment produced by the projectile. This fact suggests that the cuts give a reasonable reconstruction of the quasi projectile.

Once this was done the momentum quadrupole moment (Q) was calculated in the quasi projectile frame in order to gate on the sphericity of the particle emission.

$$Q = \frac{\Sigma p_{Z,i}{}^2}{\frac{1}{2}\Sigma p_{T,i}{}^2} \quad (1)$$

Where $p_{Z,i}{}^2$ is the momentum parallel to the beam in the QP frame of reference and $p_{T,i}{}^2$ is the momentum in the transverse direction.

In Fig. 3, a comparison between the sphericities of the simulated and the physical events is made. As shown in the figure on the right the sphericity cut is between log10(Q) values of -.3 and .3. These constraints gate on roughly spherical decompositions. Gating on the spherical events selects for thermally equilibrated QPs.

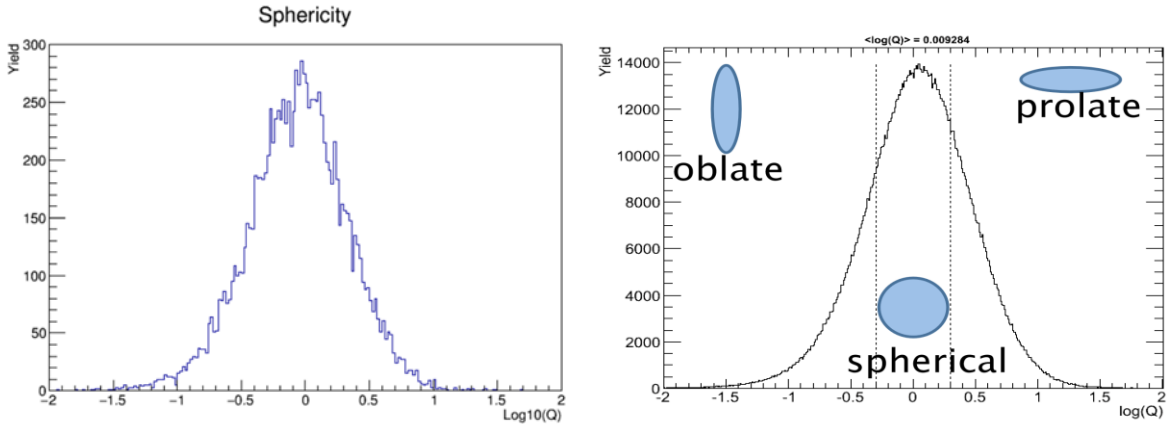

FIG. 3. On the left: the log of the momentum quadrupole for the events that pass both the nimrod filter, the velocity cut, and the mass cut is plotted for the simulated events. On the right: The analogous plot using the physical data, taken from reference[8]. While the statistics are lower than for the experimental data, the general shape is preserved. There is a however a slight tendency for more oblate momentum quadrupole moments than in the experiment data.

With the basic cuts and QP reconstruction now working the next step is to correctly reconstruct the excitation energy of the QP. Afterwards temperatures will be extracted from the momentum quadruple fluctuation method and slope method. Further statistics may also be necessary, especially for probes that use rarer particles.

[1] D.G. Yakovlev and C. Pethick, Ann. Rev. Astron. Astrophys. **42**, 169 (2004).

[2] S. Wuenschel *et al.*, Nucl. Instrum. Methods Phys. Res. **A604**, 578 (2009).

[3] Z. Kohley, Ph.D. thesis, Texas A&M University, 2010.

[4] A.B. McIntosh *et al.*, Phys. Rev. C **87**, 034617 (2013).

[5] A. Ono and H. Horiuchi, Prog. Part. Nucl. Phys. **53**, 501 (2004).

[6] R.J. Charity, Phys. Rev. C **82**, 014610 (2010).

[7] D. Mancusi, R.J. Charity, and J. Cugnon, Phys. Rev. C **82**, 044610 (2010).

[8] A.B. McIntosh (private communication).

Production of super heavy elements using multinucleon transfer reactions

Z. Tobin, A. Wakhle, and S.J. Yennello

A problem of significant interest in nuclear science has been the production and chemical characterization of super-heavy elements (SHEs) [1]. The most commonly used (and thus far successful) technique for SHE synthesis is to fuse a light projectile with a heavy target (such as a Ca projectile on a Cf or Cm target) [1-4]. Fusion reactions lead to the formation of a highly excited compound nucleus (CN). De-excitation of this CN can result in fission or the production of heavy isotopes. Additionally, fusion reactions typically produce nuclei that are neutron deficient relative to the line of beta stability, thus producing SHEs that are more likely to undergo β^+ decay. With these limitations in mind, multinucleon transfer has been examined as an alternative reaction mechanism for SHE production, especially to synthesize longer-lived, neutron rich isotopes [5-8].

We would like to continue the investigation on multinucleon transfer to see if it is a viable mechanism for SHE synthesis. Reactions using ^{22}Ne on ^{232}Th, ^{197}Au on ^{208}Pb, and ^{208}Pb on ^{208}Pb have been conducted by Aditya Wakhle using an Yttrium Aluminum Perovskite (YAP) active catcher (AC) detector array and ionization chamber-Si detectors in the same setup used in Ref. [8]. With this detector setup, the purpose is to measure the energies of alphas and establish alpha decay chains for the identification of decaying heavy isotopes. To aid with isotope identification, we can extract decay curves from the alphas identified in both the YAP ACs (Fig. 1) and the IC-Sis (Fig. 2).

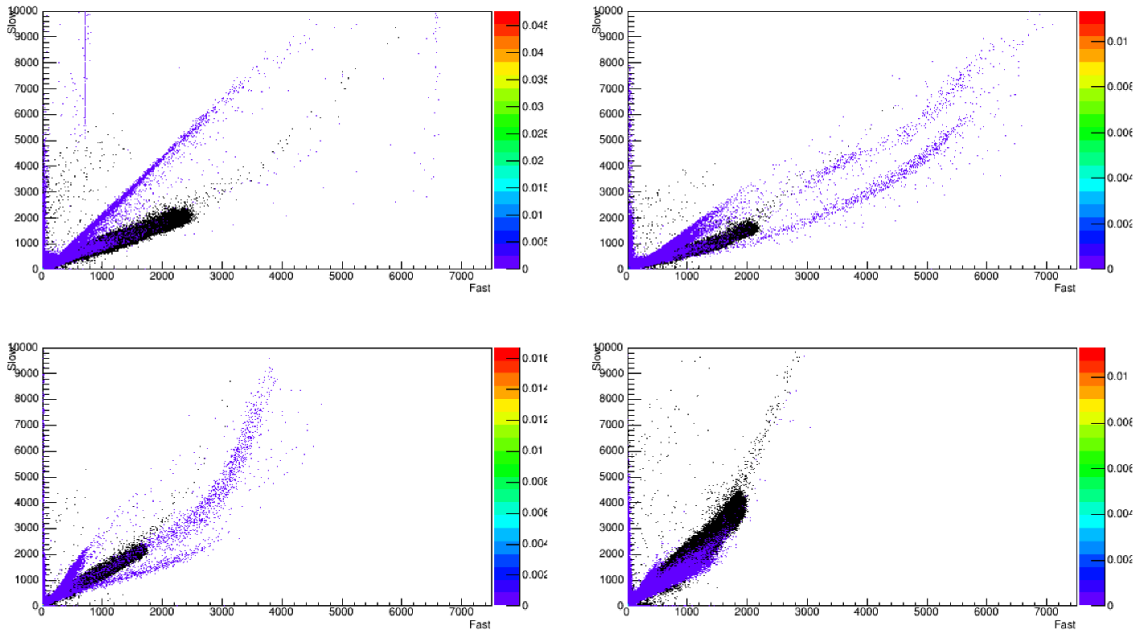

FIG. 1. Pulse shape discrimination plots for the YAP AC array. Shown are representative plots for each of the 4 rings (from top-left to bottom-right: ACs 1, 13, 30, and 39). The data shown was taken from the Au + Pb run. Here, the data collected from beam is plotted over the data from the calibration source. Note that the slow is plotted as a function of the fast.

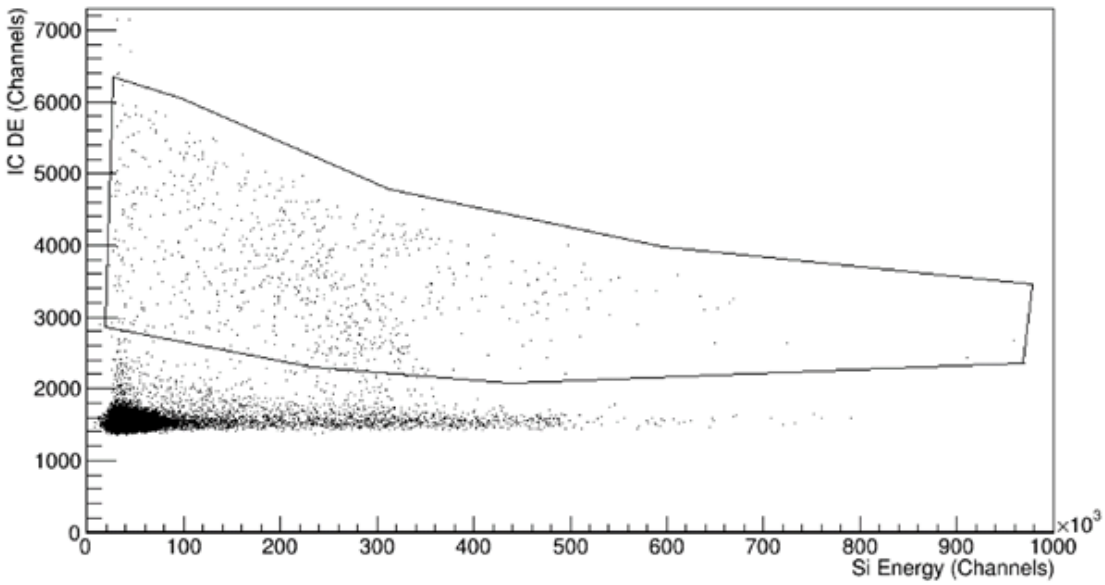

FIG. 2. An example of an DE_E plot for one of the IC-Sis. Here, the IC DE is plotted as a function of the Si energy. In the figure, a gate is drawn around the alpha branch. Below this branch are protons. The Au+Pb run data was used for this plot.

To begin the data analysis, the gain-matching and energy calibrations of the YAP ACs were examined. The gain-matching for the YAP ACs were updated. The detectors had been calibrated and gain-matched in earlier runs, but it was necessary to check if any drifting had occurred or if there were any issues with the calibration curve. As a result of the non-linearity of the energy calibration for the YAP scintillators, some higher energy (>12 MeV) particles were not accurately displayed in the PSDs.

Particle identification for the alphas was done by examining the pulse-shape discrimination plots (PSDs) of the YAP ACs and the ΔE-E plots for IC-Si plots. In order to identify the α particles in PSD plots, an a α particles band from a ^{228}Th calibration source was overlaid on the PSDs collected from beam (Fig. 1). In Fig. 2, the α particles are shown within the gate. Below this branch, lighter charged particles, such as protons, are present.

The next short-term goal of this project is to extract decay curves. To do this, we will examine data collected using a beam pulser and offline counting. In the pulsed beam mode, the beam was turned on and off throughout the run, with 30 ms beam-on and 30 ms beam off. From the pulser, we can measure the half-lives of short-lived heavy isotopes within a 30 ms beam-off window. This has already been examined for the IC-Si plots. Preliminary analysis for this was done by looking at different time windows (e.g. 0 to 2.5 ms, 0 to 5 ms, 0 to 15 ms, and 0 to 30 ms) during the beam-off period at certain energy ranges. Further refinements to this procedure are currently being examined. We will next perform this procedure on the AC detector array. For longer lived nuclei, offline counting after beam will need to be examined. From this, we can use the energies of the emitted alphas and the half-lives to identify the heavy isotopes.

[1] J.H. Hamilton *et al.*, Annu. Rev. Nucl. Part. Sci. **63**, 383 (2013).
[2] Y.T. Oganessian *et al.*, Phys. Rev. Lett. **83**, 3154 (1999).
[3] Y.T. Oganessian *et al.*, Phys. Rev. C **74** (2006).
[4] E.K. Hulet *et al.*, Phys. Rev. Lett. **39**, 385 (1977).
[5] V.I. Zagrebaev and W. Greiner, Phys. Rev. C **83** (2011).
[6] H. Kumpf and E.D. Donets, J. Exptl. Theoret. Phys. **44**, 798 (1963).
[7] V.I. Zagrebaev and W. Greiner, Phys. Rev. C **87** (2013).
[8] S. Wuenschel *et al.*, Phys. Rev. C **97** (2018).

Study of α-α correlation functions in ^{40}Ar+^{58}Fe at 30 MeV/u

A. Abbott, L. Heilborn, A.B. McIntosh, and S.J. Yennello

Correlation functions have the potential to give interesting information about the resonant states of a fragment produced in a heavy ion reaction as the shape and size will allow one to understand the lifetime and energy state of the fragment [1]. Large correlation at a specific relative momentum would indicate a strong interaction between α particles at a specific energy which would refer to a distinct state of ^{8}Be, as shown in Fig. 1. In order to calculate correlation functions experimentally, the ratio of the

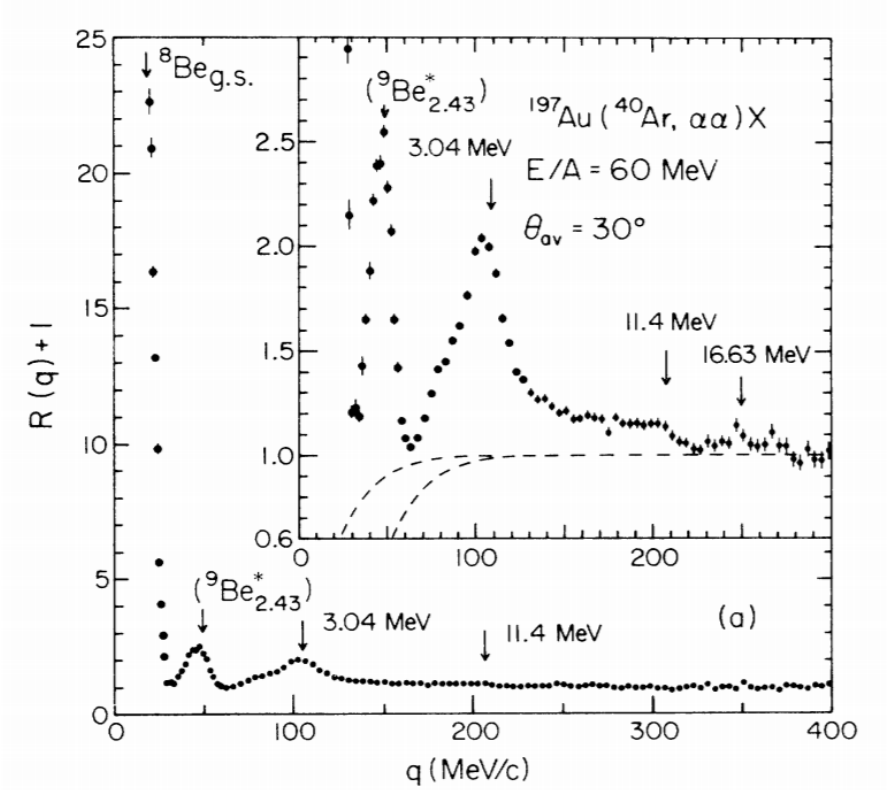

FIG. 1. Reprinted from Ref. [2]. Alpha-alpha correlation function from ^{40}Ar +^{197}Au. Illustrates the correlation between two alphas from different resonant states produced in the reaction. Shows correlation as a function of relative momentum in MeV/c.

yields

of correlated and uncorrelated particles' relative momenta are used (see Eq. 1)

$$1 + R(q) = N\left(\frac{Y(q)}{ucorr\,Y(q)}\right) \tag{1}$$

and is plotted as a function of the relative momentum, an example of which is listed as Fig. 1 and was reprinted from Ref. [2]. Particles from the same event are considered correlated while the uncorrelated yield is calculated through the use of a technique called "event mixing" where the relative momentum is calculated between two α particles detected in separate events [1-3]. $Y(q)$ and $ucorr\ Y(q)$ are the yields of the correlated and uncorrelated relative momenta and N is a normalization constant that requires $R(q)$=0 at large relative momenta because particles are expected to have little to no interaction when separated largely in space [1-4].

Fig.1 gives information about the fragments produced in the reaction that decay into alpha particles. The plot is dominated by the large peak around 25 MeV/c shows the emitting source of the two alphas to be the ground state of ^{8}Be. The decay of the 3.04 MeV and 11.4 MeV excited states of ^{8}Be can also be seen despite having very short lifetimes. Even an excited state of ^{9}Be can be determined to have emitted alphas in this system. The energy uncertainty, or width, for the peaks gives indications for the lifetime of those states as defined by Heisenberg uncertainty principle.

The experiment was performed using the Forward Array Using Silicon Technology (FAUST), which was used to detect particles emitted from the excited projectile-like fragments (PLF*) produced from the collision between the beam and target [1]. Due to the requirement of precise position detection for the calculation of correlation functions, the telescopes utilized dual-axis duo-lateral (DADL) Si detectors with a CsI(Tl) crystal coupled to a photodiode. This allowed for the determination of the angle at which the particle left the target and for the measurement of the particle energy. The current short term goal is to construct an alpha-alpha correlation function using the known energies and angles of the alpha particles emitted from the decay of excited projectile-like fragments produced by ^{40}Ar+^{58}Fe at 30 MeV/u. Using these values, the velocity vectors for the alpha particles are determined and used to calculate their relative momentum both for particles from the same event, and particles from different events. Calculating the uncorrelated relative momenta involves filling an array with 200 alpha particles and randomly selecting pairs. In order for the pair of particles to be used, they must pass certain restrictions including occurring in different events, having not been paired before, and having not hit the same detector. Once pairs have been made, the array is cleared and filled with the next 200 particles. The relative momentum is calculated according to Eq. 2

$$P_{rel} = \mu(v_1 - v_2) \tag{2}$$

where v_1 and v_2 are the velocity vectors of the alpha particles in m/s and μ is the reduced mass.

The relative momentum yields for both are shown below and labeled Fig. 2 and Fig. 3 respectively. The ratio of these two plots gives the correlation function plot shown below as Fig. 4, where the dominant 20 MeV/c peak referring to the ground state of ^{8}Be can be observed. The idea of this project is to generate correlation functions for many light charged particles in order to obtain information about the specific system. More work is being done to normalize the plot in Fig. 4 at high relative momenta, to investigate possible restrictions to be added to the event mixing process and to produce an alpha-alpha correlation function for the system at a different energy so that excited states can be observed.

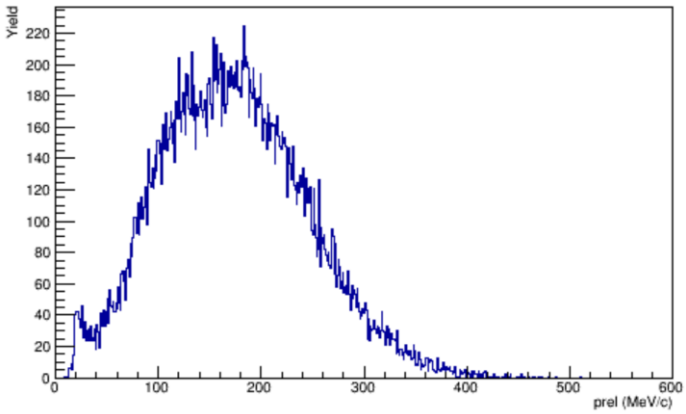

FIG. 2. Alpha-alpha correlated relative momentum. Shows the yield as a function of the relative momentum in MeV/c.

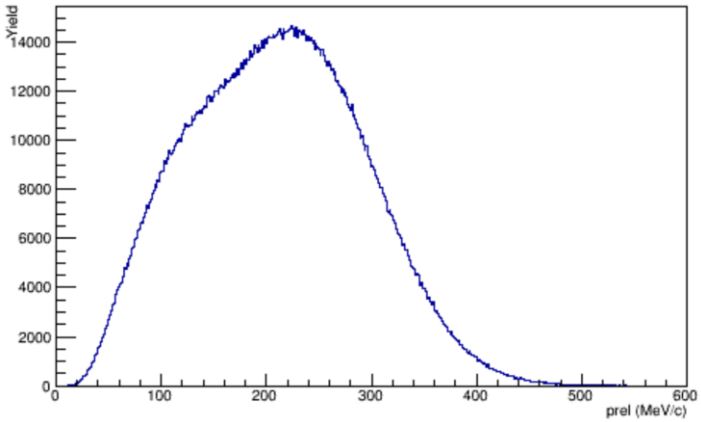

FIG. 3. Alpha-alpha uncorrelated relative momentum. Illustrates the yield of the calculated relative momentum between two alpha particles from separate events as a function of the relative momentum in MeV/c.

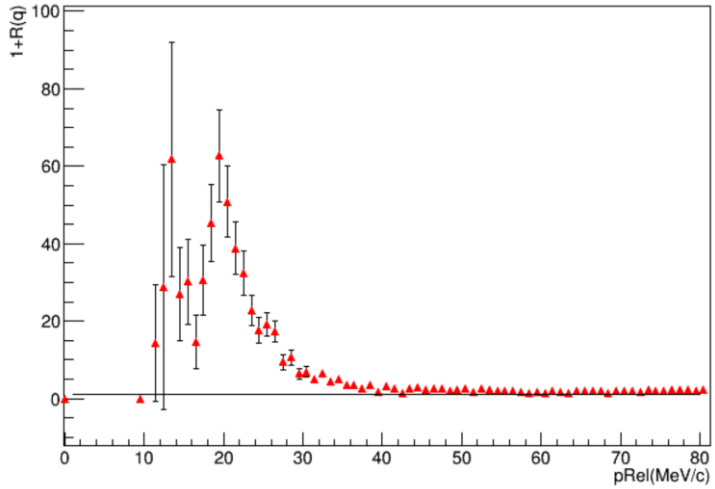

FIG. 2. Low relative momentum alpha-alpha correlation function. The strong peak at 20 MeV/c indicates the ^{8}Be ground state. The solid black line placed at 1+R(q) = 1 corresponds to no correlation.

[1] L. Heilborn, Ph.D. Thesis, Texas A&M University, 2018.
[2] J. Pochodzalla *et al.*, Phys. Rev. C **35**, 1695 (1987).
[3] G. Verde *et al.*, Eur. Phys. J. A **30**, 81 (2006).
[4] L. Heilborn *et al.*, *Progress in Research*, Cyclotron Institute, Texas A&M University (2011-2012), p. II_36.

New results from the fragment yields analysis in ^{124}Sn+^{112,124}Sn at 26*A* MeV reaction

J. Gauthier, M. Barbui, X. Cao, K. Hagel, J.B. Natowitz, R. Wada, and S. Wuenschel

Ref. [1] describes the analysis we are currently working on. The main purpose is to use a nucleation time moderated statistical equilibrium model that has previously been used to reproduce ternary neutron induced fission isotopic yields [2] to characterize the neck emission in Sn+Sn collisions at 26*A* MeV obtained with the NIMDOR detector array [3]. The model description, experimental procedure and selection can be found in detail in Ref. [1]. Most of the parameters previously derived from the model were in a realistic range for the mid-rapidity source. Several exceptions included time and critical cluster size values that were too high. During the last year we worked on achieving a better fit by improving the normalization and the minimization algorithm. We also tried different sets of initial parameters in order to locate other minima. The fit results for both reactions are presented in Fig. 1 and

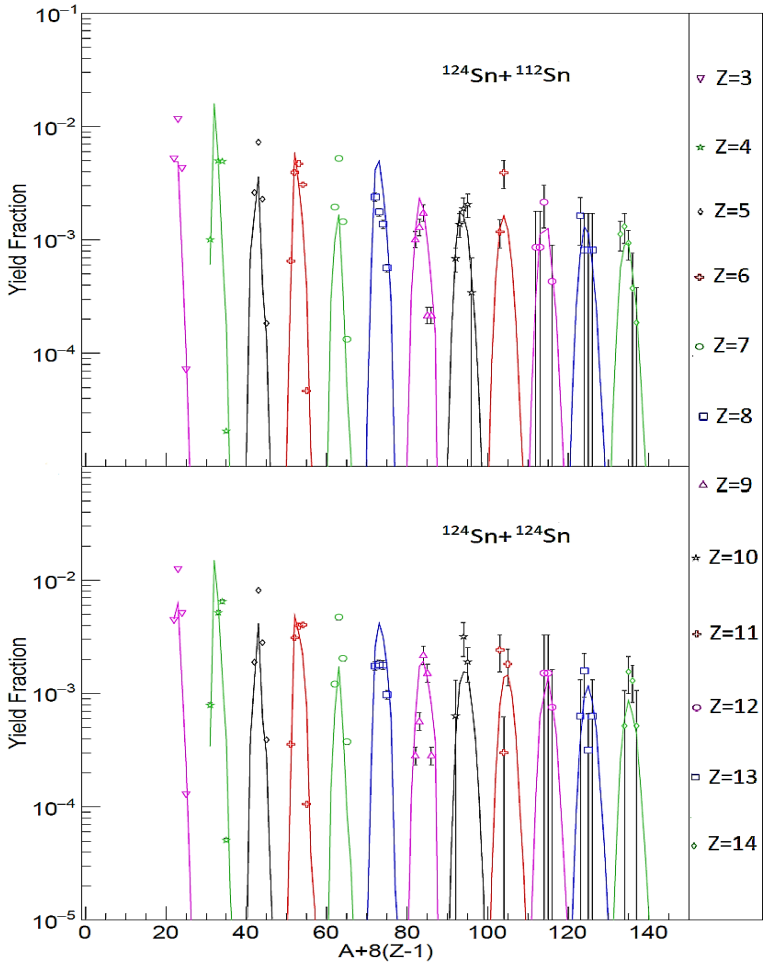

FIG. 1. Corrected yield as a function of N/Z for each isotope and both reactions inside the relative angle selection window.

Table I. The previous parameters and the ones from the induced fission (Ref. [2]) are also shown in Table I.

Table I. Previous and new fit parameter comparison. The neutron induced ^{241}Pu fission parameters are also shown.

System	^{112}Sn target		^{124}Sn target		^{241}Pu
Fit version	**old**	**new**	**old**	**new**	
Temperature (MeV)	**2.76**	**2.52**	**2.72**	**2.43**	**1.4**
Density (10-4 fm-3)	**18.67**	**194**	**16.38**	**150**	**4**
Time (fm/c)	**6000**	**600**	**7300**	**950**	**6400**
Ac	**15.8**	**6.3**	**16.1**	**6.2**	**5.4**
Proton ratio (system)	**0.47 (0.42)**	**0.47 (0.42)**	**0.44 (0.40)**	**0.46 (0.40)**	**0.34 (0.39)**
Fit Metric (M^2)	***1.11***	***0.72***	***1.07***	***0.75***	***1.18***

Previous and new fit parameter comparison. The neutron induced ^{241}Pu fission parameters are also shown.

$$M^2 = \sum_j \left\{ ln\left[Y_{TF}^{exp}(Z_j, A_j)\right] - ln\left[Y_{TF}(Z_j, A_j)\right] \right\}^2 / n \qquad (1)$$

Another point is the experimental temperature calculation. In the previous report we showed that the temperature estimated using the Albergo calculation with light particles [4] was very similar to the fit parameter (2.7 MeV). The problem is that the source overlap for light particles is significant causing a significant fraction of the yield in in the mid-rapidity source in the fit to be contributions from other sources. To obtain a better estimate we can use IMF isotopic ratios to calculate the Albergo temperature [5]. Since we have good statistics for ^{11,12}C isotopes, we used these in combination with several other IMFs to calculate an average temperature for our selection window.

Table II shows the ratios we used and the results we obtained. We see that the average temperature value is around 3.5 MeV, which is 40% higher than the new fit value and 30% higher than the light particle Albergo calculation but is still in a realistic range. The improvements described in this report make us confident that we can now publish the results.

Table II. IMF albergo temperature calculation results.

	$T_{^{112}Sn}$ (MeV)	$T_{^{124}Sn}$ (MeV)
$^{6,7}Li/^{11,12}C$	3.57	3.42
$^{7,8}Li/^{11,12}C$	4.26	3.98
$^{8,9}Li/^{11,12}C$	2.19	2.2
$^{9,10}Be/^{11,12}C$	3.96	3.8
$^{11,12}B/^{11,12}C$	3.94	3.68
$^{12,13}B/^{11,12}C$	2.72	2.82
$^{12,13}C/^{11,12}C$	3.76	3.46
$^{13,14}C/^{11,12}C$	3.94	4.06
$^{15,16}N/^{11,12}C$	3.98	4.05
$^{16,17}O/^{11,12}C$	3.62	3.58
$^{17,18}O/^{11,12}C$	3.55	3.4
mean	**3.59**	**3.49**

[1] J. Gauthier *et al.*, *Progress in Research*, Cyclotron Institute, Texas A&M University (2016-2017), p. II-3.

[2] S. Wuenschel *et al.*, Physical Review C **90**, 011601, (2014).

[3] S. Wuenschel *et al.*, Nucl. Instrum. Methods Phys. Res. **A604**, 578 (2009).

[4] S. Albergo *et al.*, Il Nuovo Cimento, **89** A, N. 1 (1985).

[5] M.B. Tsang *et al.*, Phys. Rev. Lett. **78**, 3836 (1997).

Energetic proton emission in intermediate-energy heavy-ion collisions with IQMD

S.S. Wang, R. Wada, J.B. Natowitz, K. Hagel, Y.G. Ma, and X.G. Cao

The energetic protons emitted from intermediate-energy heavy-ion collisions are studied under the framework of the isospin-dependent quantum molecular dynamics model (IQMD model) [1-2], which is modified to take into account the Fermi motion in the process of nucleon-nucleon collision and 3N collision. Simulated energetic proton spectra are compared with those in the reactions of ^{40}Ar+^{51}V at 44 *A* MeV from ref. [3] and ^{40}Ar+^{40}Ca at 92 and 137 *A* MeV from ref. [4]. Wave packet width dependence and nucleon-nucleon cross section dependence on the energetic protons are also investigated.

In the IQMD modeling, the width of the Gaussian wave packet is traditionally set to different values for different reaction systems, to obtain the best stability of the initial nuclei. Fig.1 shows the results of the wave packet width dependence of energetic proton energy spectra of ^{40}Ar +^{51}V at 44 *A* MeV at different angles, together with free nucleon-nucleon cross section (free NNCS), screened nucleon-nucleon cross section (screened NNCS) [5] and Li-Machleidt nucleon-nucleon cross section (LM NNCS) [6] from left to right panel. The energetic proton yield decreases as the width parameter

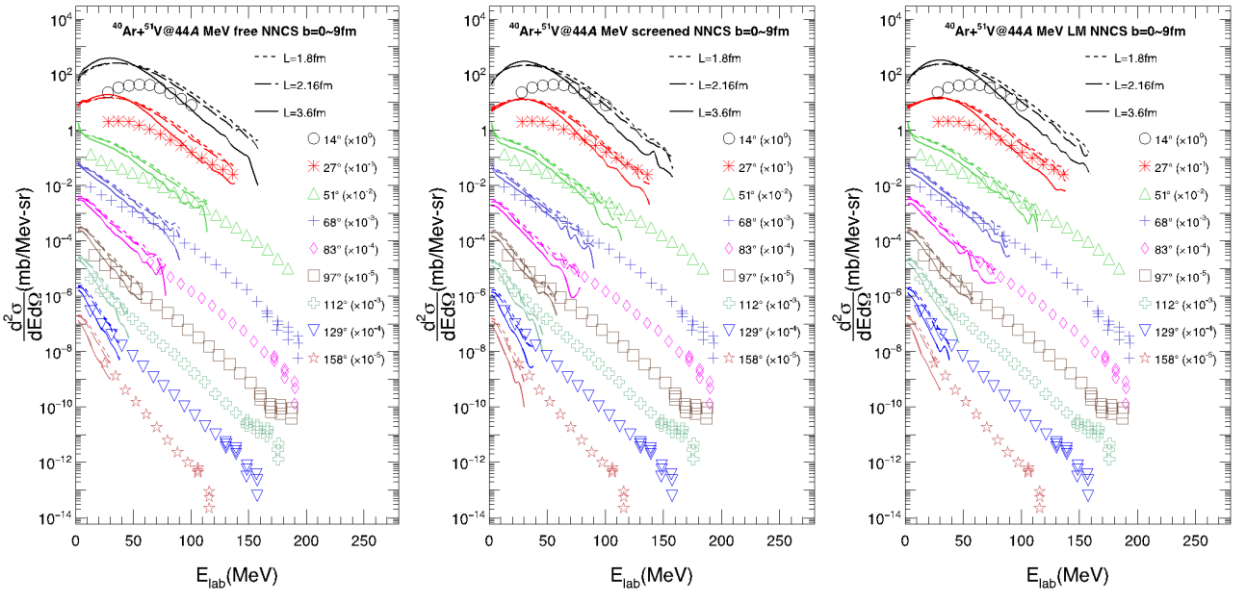

FIG. 1. The wave packet width dependence of proton energy spectra at different angles for ^{40}Ar+^{51}V at 44 A MeV, together with the free NN cross section (left), screened cross section (middle) and L-M in-medium NN cross section (right). Markers represent measured proton spectra. The calculated data are showed by lines.

increases, and decreases as the NN cross section decreases from the free NN to the screened cross section. In other words, the choice of the width parameter depends on the choice of the NN cross section used in the calculation. The calculated data is in a good agreement with the experimental proton spectra when wave packet width is equal to 2.16fm for the screened NNCS.

Low energy proton yields are significantly over-predicted, because of the instability of the initial nuclei. In order to suppress the nucleon emission from the un-stabilized initial nuclei, the Fermi motion is

decreased and the Fermi boost is incorporated in the collision process, in a similar way to that in [7] (results are still in preliminary and not shown here).

The model has been applied to the experimental spectra at ^{40}Ar+^{40}Ca at 92, 137 A MeV and the results are shown in Fig.2. We found that none of the parameter sets, the widths and the NN cross sections, can reproduce the experimental spectra in their slopes and amplitudes, similar to the conclusion in Ref. [8]. We are currently working on the incorporation of the reduced Fermi motion, Fermi boost in the two body collision term and a 3 body collision term [8]. The study is underway.

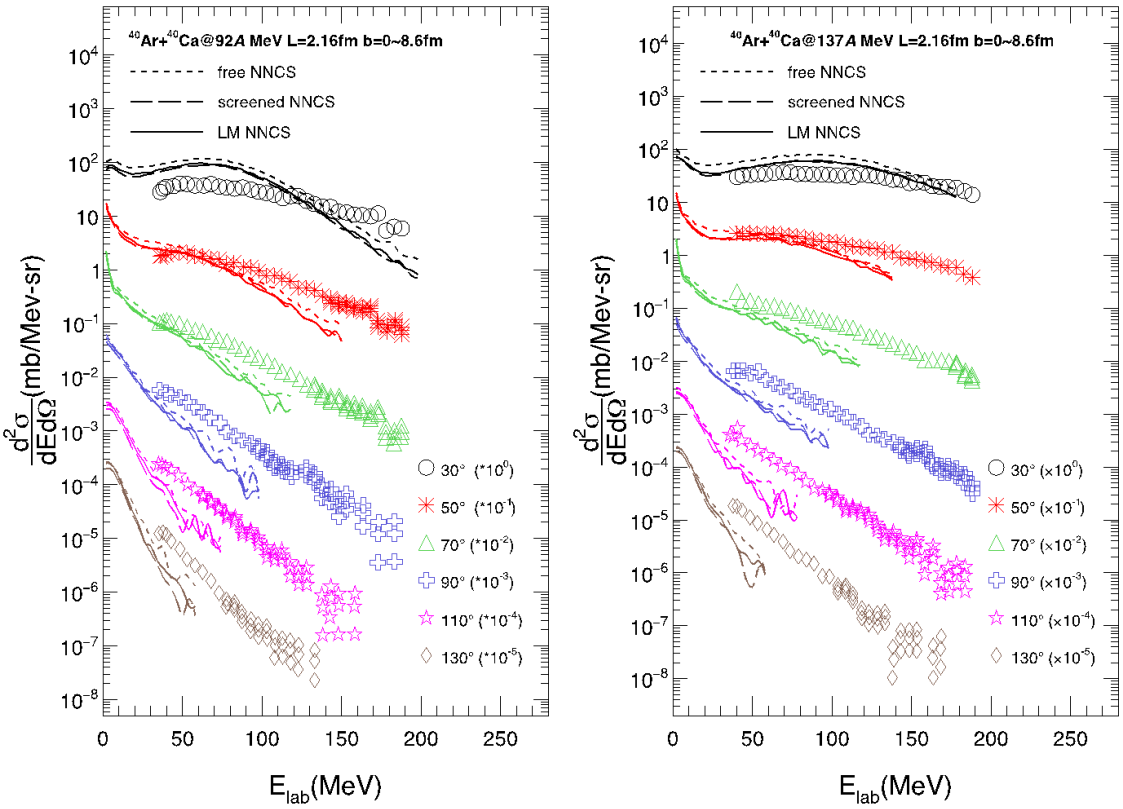

FIG. 2. The simulated results at higher incident energies.

[1] Lie-wen Chen *et al.*, Phys. Rev. C **58**, 2283 (1998).

[2] Lie-Wen Chen *et al.*, Phys. Lett. B **459**, 21 (1999).

[3] R.Coniglione *et al.*, Phys. Lett. B **471**, 339 (2000).

[4] H. Kruse *et al.*, Phys. Rev. C **31**, 1770 (1985).

[5] D.D. S. Coupland *et al.*, Phys. Rev. C **84**, 054603 (2011).

[6] G.Q. Li and R. Machleidt, Phys. Rev. C **49**, 566 (1994); Phys. Rev. C **48**, 1702 (1993).

[7] W. Lin *et al.*, Phys. Rev. C **94**, 064609 (2016).

[8] R. Wada, Phys. Rev. C **96**, 031601(R) (2017).

Experimental liquid-gas phase transition signals and reaction dynamics

R. Wada, W. Lin, H. Zheng, X. Liu, M. Huang, K. Hagel, and J.B. Natowitz

The experimental liquid-gas phase transition signals are examined for quasi-projectiles (QP) reconstructed from the reactions of ^{40}Ar+^{27}Al, ^{48}Ti, ^{58}Ni at 47 MeV/nucleon, using different measures for the nuclear liquid-gas phase transition. The experimental data were taken, using NIMROD and details can be found in Ref.[1,2]. The data are revisited, using a new thermometer described below.

A quasi-projectile (QP) is reconstructed for a given reaction using a moving source (MS) fit with three sources, a QP, intermediate-velocity (IV) and target-like sources in a similar way as described in Refs.[1,2]. In this analysis, the three fixed source velocities of the IV source are used to study different contributions of the mid-rapidity particles to the QP source. For these different three sources, the light charged particle energy spectra are reasonably well fitted. Using these extracted MS parameters, the excitation energy of the QP source is evaluated in a similar fashion described in Ref.[1,2]. All events of different centrality classes are analyzed.

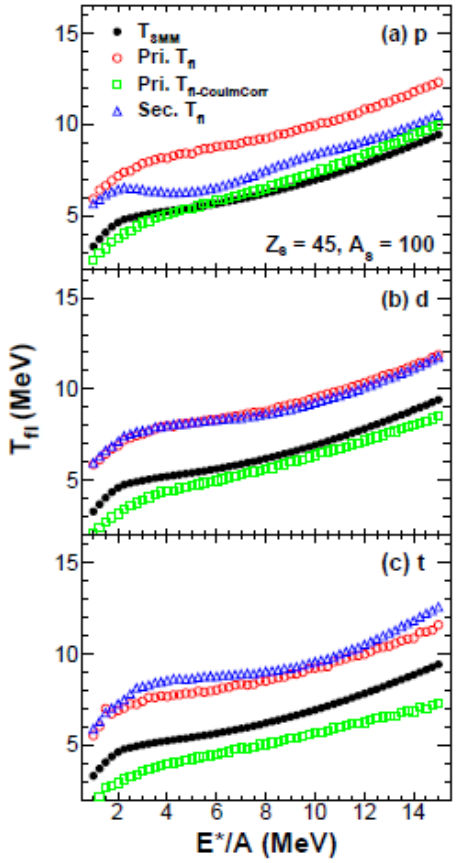

FIG. 1. Quadrupole momentum fluctuation temperatures (T_{fl}) of SMM with A = 100 and Z = 45 for (a) protons, (b) deuterons and (c) tritons. T_{SMM} is the average temperature calculated from the SMM input value. Open circles represent the extracted T_{fl} values from the primary particles and triangles are for those after the secondary decays. Squares represent the Coulomb corrected T_{fl} values of the primary particles.

A new thermometer is proposed from a SMM event study. In Fig.1, the input value of the SMM temperature, T_{SMM}, is compared with the calculated quadrupole fluctuation temperature, T_{fl}, for protons, deuterons and tritons, with and without an fterburner. Only Z=1 particles are examined because of their minimum Coulomb effect. From this study, we concluded that the deuteron fluctuation temperature gives the most reliable temperature both in primary and secondary stages. Therefore in the following, the deuteron thermometer is used.

The quadrupole thermometer uses the average fluctuation values of the quadrupole moment in a given event set and therefore cannot be used on an event by event basis in principle. In Fig.2(a) and (b), the extracted T_{fl} values and their standard deviation (SD) are plotted as a function of the excitation

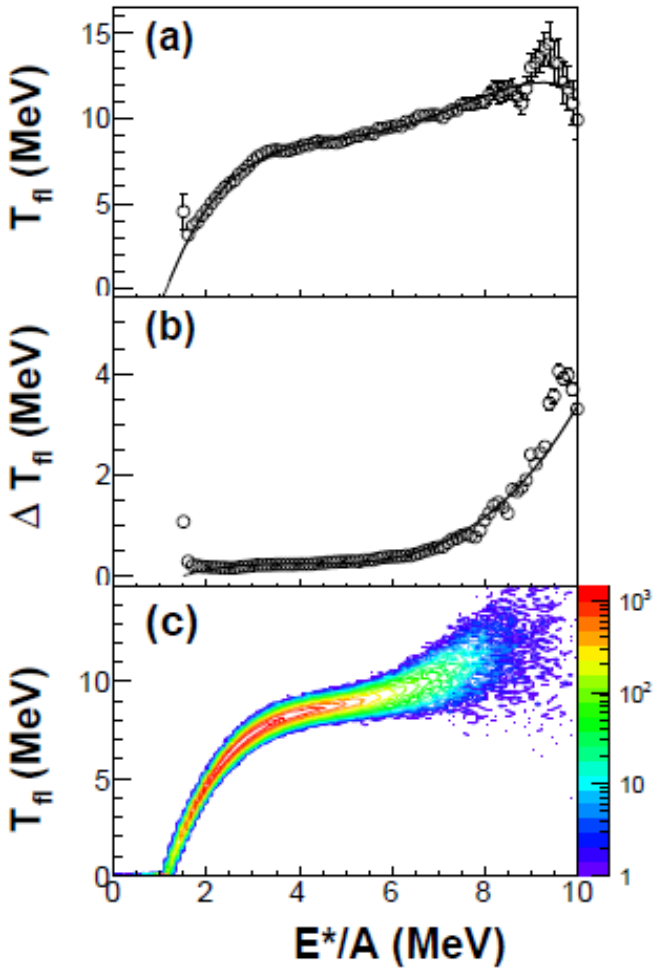

FIG. 2. Experimental deuteron quadrupole momentum fluctuation temperature, T_{fl} in (a) and the standard deviation values ΔT_{fl} in (b), as a function of E*/A for inclusive data of ^{4}0Ar + ^{48}Ti at 47 MeV/nucleon with the QP selection of $V^{NN}{}_{s}$ = 4:0 cm/ns. Curves in (a) and (b) are from a polynomial fit. (c) Calculated T_{fl} vs E*/A distribution using the fit parameters in (a) and (b) on the event-by-event basis. Z axis is the yield given by a logarithmic scale.

energy, E*/A, for a given event set. As one can see, the SD values are rather small for E*/A<8 MeV. These values are fit by polynomial functions as shown by the solid curves in the figure. Using these polynomial parameters, a T_{fl} value is generated randomly using a Gaussian distribution for each extracted E*/A in event-by-event basis and used as the temperature for QP. A result is shown in (c). As one can see in Fig.2(c), the extracted caloric curve shows a plateau at E*/A ~ 4 MeV with T_{fl}~9 MeV, which is a strong indication of the first phase transition at this temperature. After a Coulomb correction (~ 0.7 MeV), we extracted the phase transition temperature of 8.3 +/- 0.4 MeV. This same feature is observed for ^{27}Al and ^{58}Ni target runs and different source velocity event sets in each reaction system.

In this work, other measured values are examined and all show a peak or pleateu at similar temperature values. Therefore we conclude that in a system size of A~ 40, a liquid-gas phase transition indeed occurs at the temperature of ~8.3 MeV. The results has been published in Ref.[3].

[1] Y.G. Ma, J.B. Natowitz, R. Wada, K. Hagel, J. Wang, T. Keutgen, Z. Majka, M. Murray, L. Qin, P. Smith *et al.*, Phys. Rev. C **71**, 054606 (2005).

[2] Y.G. Ma, R. Wada, K. Hagel, J. Wang, T. Keutgen, Z. Majka, M. Murray, L. Qin, P. Smith, J.B. Natowitz *et al.*, Phys. Rev. C **69**, 031604(R), (2004).

[3] R. Wada, W. Lin, P. Ren, H. Zheng, X.Liu, M. Huang, K. Yang, and K. Hagel, Phys. Rev. C **99**, 024616 (2019).

Toward understanding relativistic heavy-ion collisions with the STAR detector at RHIC

D.M. Anderson, Y. Liu, S. Mioduszewski, N. Sahoo, and the STAR Collaboration

This project is a study of high-energy heavy-ion collisions at the Relativistic Heavy Ion Collider (RHIC). The focus of the study is on two probes of the dense, partonic matter created in these collisions: 1) direct-photon-triggered jets (and their correlations) and 2) heavy-quarkonium production and suppression.

1 Investigating Energy Loss through Photon-Triggered Jet Measurements

The hard production of a direct photon back-to-back with a jet (γ-jet) is a probe of the parton energy loss in heavy-ion collisions [1]. In the "γ-jet" coincidence measurement, the measured energy of the trigger particle (the photon) serves as a calibrated baseline for the total energy of the jet particles on the recoil side (i.e. opposite in azimuth) of the trigger. The mean-free path of the γ in the medium is large enough so that its momentum is preserved, regardless of the position of the initial scattering vertex. Thus it does not suffer from the geometric biases, i.e. the non-uniform spatial sampling of hadron triggers due to energy loss in the medium, of e.g. π^0 triggers. Because of the difference in path length traversed, on average, between a direct-γ and a π^0 trigger, comparisons of γ-jet to hadron(π^0)-jet measurements can provide insight into the path-length dependence of the energy loss.

As the dominant background to direct photons are π^0 (decaying to two photons), the Barrel Shower Maximum Detector (BSMD) has provided the capability of distinguishing direct photons from neutral pions via the transverse shower shape. Our group has used this method in the measurement of direct photon+hadron correlations [2]. The γ-hadron correlation studies can be extended to studies of γ-triggered jet reconstruction measurements (as has been done at the LHC [3, 4]). The away-side jet will then be reconstructed in coincidence with triggers selected as direct photon candidates or (for $p_T<20$ GeV using the shower shape with the BSMD) identified π^0 triggers. The advantage of this should be the ability to reach lower energy fragments in the jet to study jet-shape modification and possible redistribution of energy.

The Run-14 photon-triggered data set in Au+Au collisions has been fully analyzed for charged jets recoiling from a high-energy neutral (π^0 or γ) trigger. We have chosen to concentrate initially on charged-particle jets, for simplicity, recoiling from the trigger particle. Charged-jet reconstruction is performed using the anti-k_T algorithm from the Fastjet package [5]. In this analysis, charged particles with transverse momentum between $0.2 < p_T < 15$ GeV/c are included as constituents. A fiducial cut in jet pseudorapidity, $|\eta_{jet}| < 1-R_{jet}$, where R_{jet} is the jet resolution parameter associated with the radial size of the jet.

Fig. 1 shows the charged recoil-jet spectra for a sample of π^0, using cuts on the transverse-shower profile as measured by the BSMD, for two different ranges of transverse energy (E_T) of the trigger. In this figure, the jet yields are corrected for the background energy density (ρ) but have not been corrected for instrumental effects. The low panel clearly shows the growing signal of "true" jets over combinatorial jets, as estimated by a mixed-event technique [6].

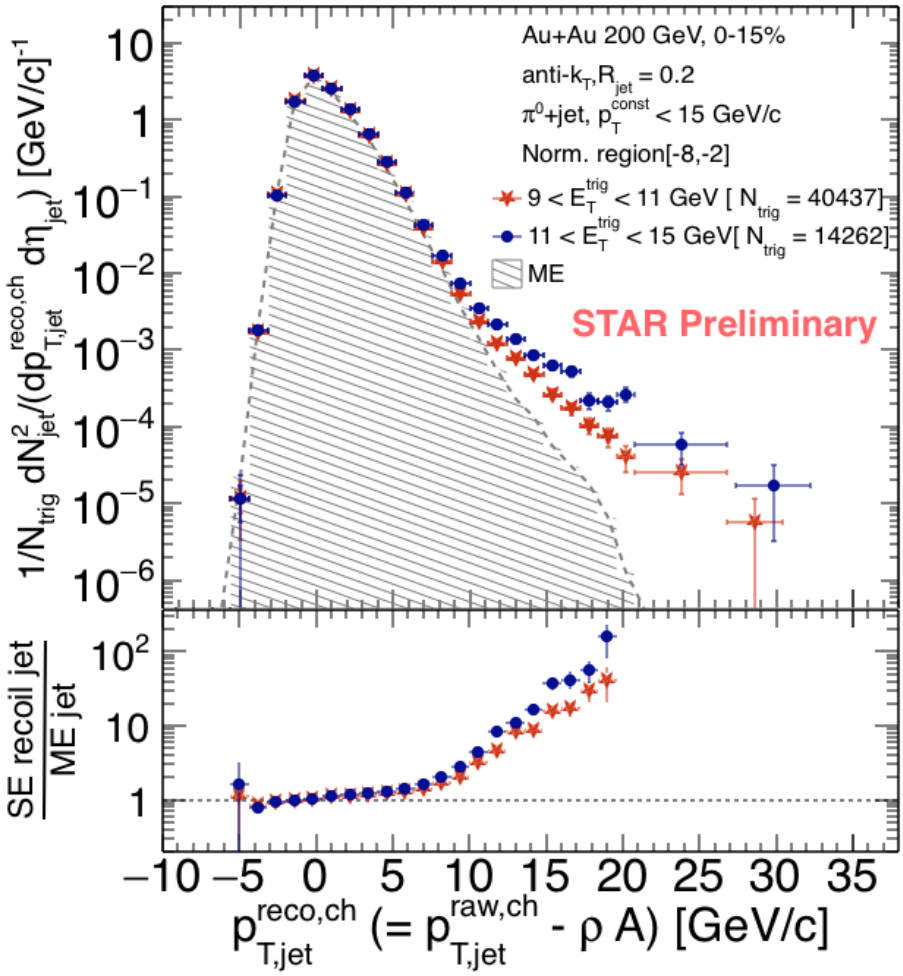

FIG. 1. Reconstructed charged-jet transverse-momentum spectrum (corrected for the background energy density ρ) recoiling from π^0 triggers with different cuts on transverse energy (E_T), using the high-statistics Run-14 Au+Au data set. The hatched histogram shows the estimated combinatorial jets from mixed events (ME). The bottom panel shows the ratio of the measured spectrum in real events to the spectrum from mixed events. The signal (yields greater than 1) increases for increasing trigger E_T.

Fig. 2 shows our STAR preliminary result of the fully corrected charged recoil-jet spectra for π^0 and direct-γ triggers (presented at the Hard Probes Conference, 2018).

As a baseline measurement, we have also analyzed Run-9 p+p collisions. Fig. 3 shows the result of the fully corrected charged-jet spectrum on the recoil side of a π^0 trigger with E_T=9-11 GeV, in p+p collisions, compared to the same from PYTHIA [7]. This shows that PYTHIA describes the p+p data for semi-inclusive recoil jets well.

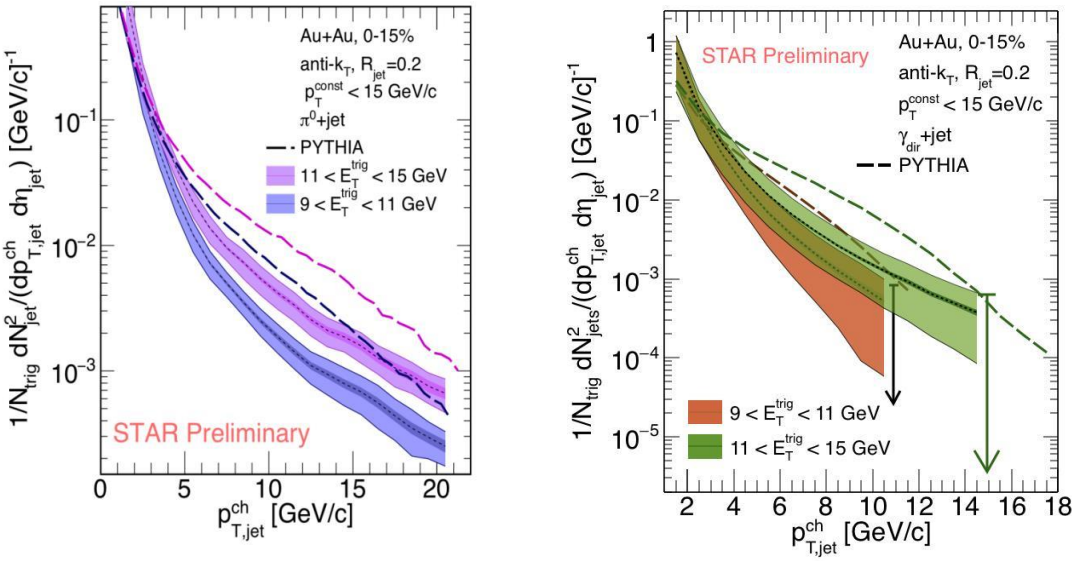

FIG. 2. (Left Panel) Fully corrected charged-jet spectra on the recoil of π^0 triggers with E_T=9-11 GeV (blue) and E_T=11-15 GeV (pink) compared to their respective PYTHIA [7] baselines (dashed lines, also in blue and pink). (Right panel) Fully corrected charged-jet spectra on the recoil of direct-γ triggers with E_T=9-11 GeV (brown) and E_T=11-15 GeV (green) compared to their respective PYTHIA baselines (dashed lines, also in brown and green).

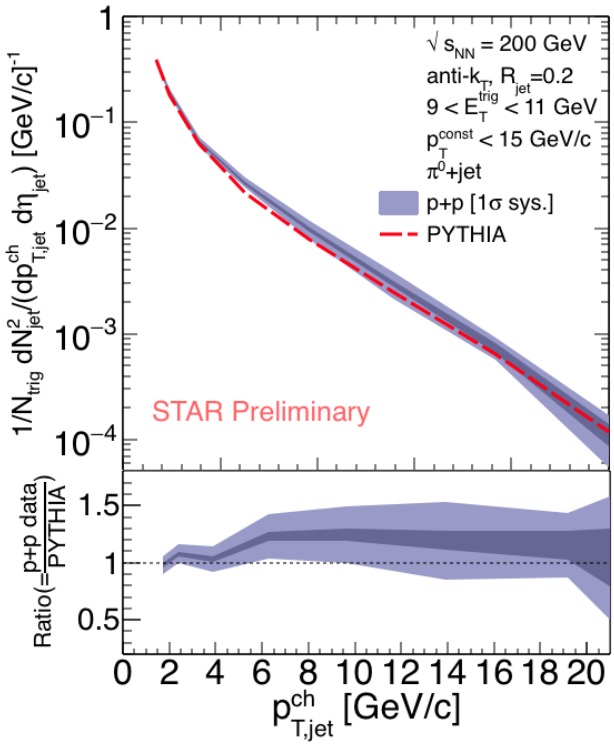

FIG. 3. (Upper Panel) Fully corrected charged-jet spectrum measured in Run-9 p+p collisions on the recoil of π^0 triggers with E_T=9-11 GeV, compared to the same spectrum reconstructed in PYTHIA events. (Lower Panel) The ratio of the measurement to PYTHIA. The inner (darker) band represents the statistical uncertainties, and the outer (lighter) band represents the systematic uncertainties.

2 Unraveling Cold Nuclear Matter Effects in J/Ψ Suppression

The J/ψ has long been considered one of the most promising direct probes of deconfinement. According to theoretical predictions in 1986 [8], the produced $c\bar{c}$ pair will not be able to form a J/ψ bound state in the QGP, if a sufficiently high temperature is reached where the screening radius is smaller than the binding radius of the J/ψ resonant state. The "Debye" screening radius is the distance at which the color charges of two quarks are screened from one another, so that the confinement force is not able to hold the quarks together. A suppression in the yield of J/ψ was first observed in Pb+Pb collisions by the NA50 experiment at the CERN SPS (see, for example, [9]).

At RHIC, the predicted suppression of J/ψ due to screening in the QGP is much larger than the suppression observed at SPS due to the higher initial density of the produced medium [10]. The RHIC measurements, however, show a level of suppression similar to NA50 at mid-rapidity [11], which is significantly smaller than expectations due to color screening effects alone. This can be understood in a scenario where charmonium is regenerated due to the large initial production of charm + anti-charm quarks at $\sqrt{s_{NN}}$= 200 GeV, in conjunction with their possible thermalization in the created medium [12]. If charm quarks (partially) thermalize in RHIC collisions, then the coalescence of $c\bar{c}$ could lead to a smaller than expected suppression [13].

With counteracting effects, it is a challenge to disentangle the suppression from the regeneration. Further complicating this task is that the J/ψ-particle yields that are measured are not all primordial; some ~40% are feed-down from χ_c (approximately 30%) and ψ′ (approximately 10%) decays. Since the survival rate of different charmonium states may be different, due to the different sizes, it is important to know these feed-down fractions precisely. In addition, there are cold nuclear matter effects [14], including modification of the parton distribution functions ("shadowing") and partonic multiple scattering, that also lead to suppression of heavy quarkonium and need to be disentangled from QGP suppression. In order to quantify effects of deconfinement, cold nuclear matter effects (via p+A collisions) must be measured and disentangled.

Our goal is to have a measurement of charmonium production in p+Au collisions as a function of "centrality" or "event activity". Quite some effort has gone into the centrality determination for this data set. We based the centrality determination on an event multiplicity of the number of good primary tracks, for which we calculated corrections for the luminosity and vertex dependence.

Thus far, we have extracted J/Ψ yields, as a function of p_T. Fig. 4 shows the mass distribution of muon pairs (unlike-sign in black and like-sign in blue) obtained as a function of p_T. We have started working on the "centrality"-dependent yields.

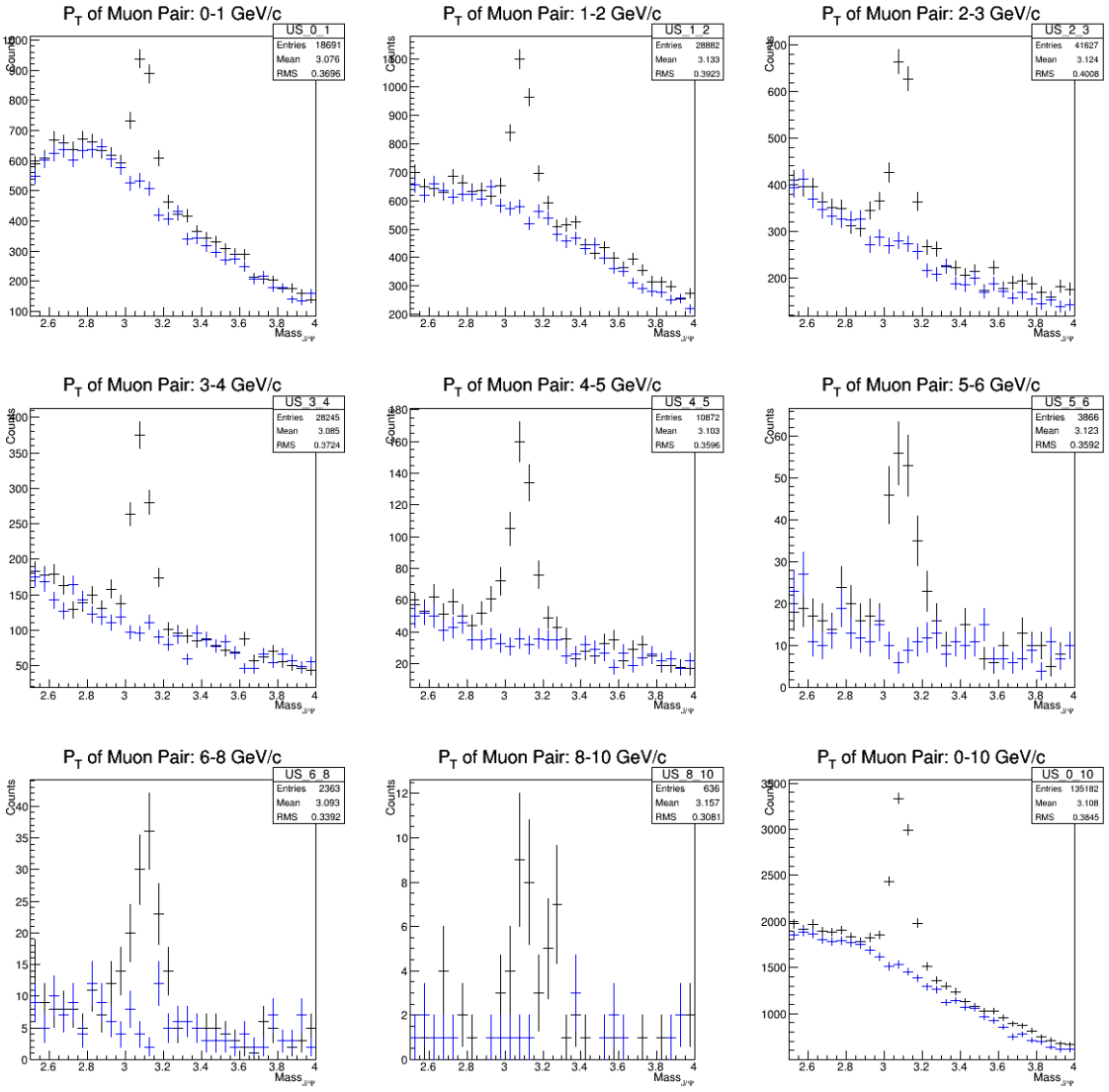

FIG. 4. Mass distributions for muon pairs: unlike-sign pairs in black and like-sign pairs (background) in blue, with each panel showing a different range of pair p_T.

For the efficiency corrections, we have been analyzing "embedding" data (simulated particles embedded into real data). In particular, we have analyzed J/ψ particles embedded into the Run-15 p+Au data set and are currently calculating the centrality-dependent corrections. The fully corrected centrality-dependent J/ψ yields are expected to be finalized within the following year.

[1] X.N. Wang, Z. Huang, and I. Sarcevic, Phys. Rev. Lett. **77**, 231 (1996).

[2] L. Adamczyk *et al.* (STAR Collaboration), Phys. Lett. B **760**, 689 (2016).

[3] S. Chatrchyan *et al.* [CMS Collaboration], Phys. Lett. B **718**, 773 (2013).

[4] [ATLAS Collaboration], ATLAS-CONF-2012-121.

[5] M. Cacciari, G. Salam, and G. Soyez, JHEP **0804** 063 (2008), http://fastjet.fr.
[6] L. Adamczyk *et al.* (STAR Collaboration), Phys. Rev. C **96**, 024905 (2017).
[7] T. Sjöstrand, S. Mrenna, and P. Skands, Comput. Phys. Commun. **178**, 852 (2008).
[8] T. Matsui and H. Satz, Phys. Lett. B **178**, 416 (1986).
[9] M.C. Abreu *et al.* (NA50 Collaboration), Eur. Phys. J. C **39**, 335 (2005).
[10] L. Grandchamp, R. Rapp, and G. E. Brown, Phys. Rev. Lett. **92**, 212301 (2004); A. Capella and E. G. Ferreiro, Eur. Phys. J. C **42**, 419 (2005).
[11] A. Adare *et al.* (PHENIX Collaboration), Phys. Rev. Lett. **98**, 232301 (2007).
[12] P. Braun-Munzinger and J. Stachel, Phys. Lett. B **490**, 196 (2000).
[13] L. Grandchamp and R. Rapp, Phys. Lett. B **523**, 60 (2001).
[14] R. Vogt, Phys. Rev. C **71**, 054902 (2005).

SECTION III

NUCLEAR THEORY

Description of isoscalar multipole giant resonances within the particle-hole dispersive optical model

M.L. Gorelik,[1] S. Shlomo, B.A. Tulupov,[2] and M.H. Urin[3]
[1]*Moscow Economic School, Moscow, Russia;*
[2]*Institute for Nuclear Research, RAS, Moscow, Russia;*
[3]*National Research Nuclear University "MEPhI" (Moscow Engineering Physics Institute), Moscow, Russia*

A continuing interest in experimental and theoretical studies of the isoscalar multipole giant resonances (ISMPGRs), in particular, the compression modes of nuclear excitations, is explained by the possibility of determining the nuclear-matter incompressibility coefficient. In this work, we present a description of the mentioned giant resonances in closed shell medium-heavy nuclei. Calculations performed within the particle-hole dispersive optical model (PHDOM) [1], provide the description of properties of each GR, including the energy-averaged strength function, double and one-body projected transition densities and partial probabilities of direct one-nucleon decay. All the model parameters (related to a mean field and Landau-Migdal particle-hole interaction) are taken from independent data. Only the parameters related to the imaginary part of the energy-averaged particle-hole self-energy term, responsible for the spreading effect, are adjusted to describe within the model the total width of the considered giant resonance. An example of the application of the above-described approach for the isoscalar giant monopole resonance in ^{208}Pb is given in Refs. [2]. In the present work, we extend such a description for ISMPGRs with multipolarity $L \leq 3$. Overtones of the isoscalar monopole and quadrupole giant resonances are also considered. Calculation results obtained for Zr, Sn and Pb are compared with the available experimental data. In particular, the unique data on the direct one-nucleon decay of the isoscalar dipole giant resonance [3] are considered. Possibilities to use the one-body projected transition density for describing inelastic α-scattering accompanied by excitation of isoscalar giant multipole resonances are also discussed.

This work was partially supported by the Russian Foundation for Basic Research (grant No. 19-02-0060).

[1] M.H. Urin, Phys. Rev. C **87**, 044330 (2013).
[2] M.L. Gorelik, S. Shlomo, B.A. Tulupov, and M.H. Urin , Nucl. Phys. **A955**, 116 (2016); Nucl. Phys. **A970**, 353 (2018).
[3] M. Hunyadi *et al*., Phys. Rev. C **75**, 014606 (2007).

Electric isovector dipole polarizability in ^{40,48}Ca, ^{68}Ni, ^{90}Zr, ^{120}Sn and ^{208}Pb and the second derivative of the symmetry energy coefficient

E. Hunt, G. Bonasera, and S. Shlomo

We carried out fully self-consistent Hartree-Fock (HF)-based random phase approximation (RPA) calculations of the centroid energies for the isovector dipole resonance for ^{40,48}Ca, ^{68}Ni, ^{90}Zr, ^{120}Sn, and ^{208}Pb and extracted the electric dipole polarizability, α_D. The calculations were done using 33 different Skyrme-type effective nucleon-nucleon interaction commonly adopted in the literature. The interactions considered cover a wide range of nuclear matter properties.

The Pearson Linear Correlation Coefficient, P, is calculated between α_D and each nuclear matter (NM) property. In figure 1 we show the electric isovector dipole polarizability as a function of the second derivative of the symmetry energy at saturation density, Q_{SYM}. We obtained a weak correlation between the calculated values of α_D and Q_{SYM} for the ^{48}Ca isotope, a medium correlation for ^{40}Ca, ^{90}Zr and ^{120}Sn, while a strong correlation is found for ^{68}Ni and ^{208}Pb. We also extracted the value of α_D from the experimental data for the isovector dipole centroid energy, shown by the dashed lines in Fig. 1. We found that interactions associated with a value of Q_{SYM} = 300-500MeV reproduce most of the data.

These results, together with the results of a similar analysis done for a wide mass range of spherical nuclei from which we extracted constraints on the values of the incompressibility coefficient of nuclear matter, effective mass and the enhancement coefficient of the energy weighted sum rule of the IVGDR [1], may be used in a fit to determine the next generation nuclear energy density functional with improved predictive power for properties of nuclei and nuclear matter.

[1] G. Bonasera, M. R. Anders, and S. Shlomo, Phys. Rev. C **98**, 054316 (2018).

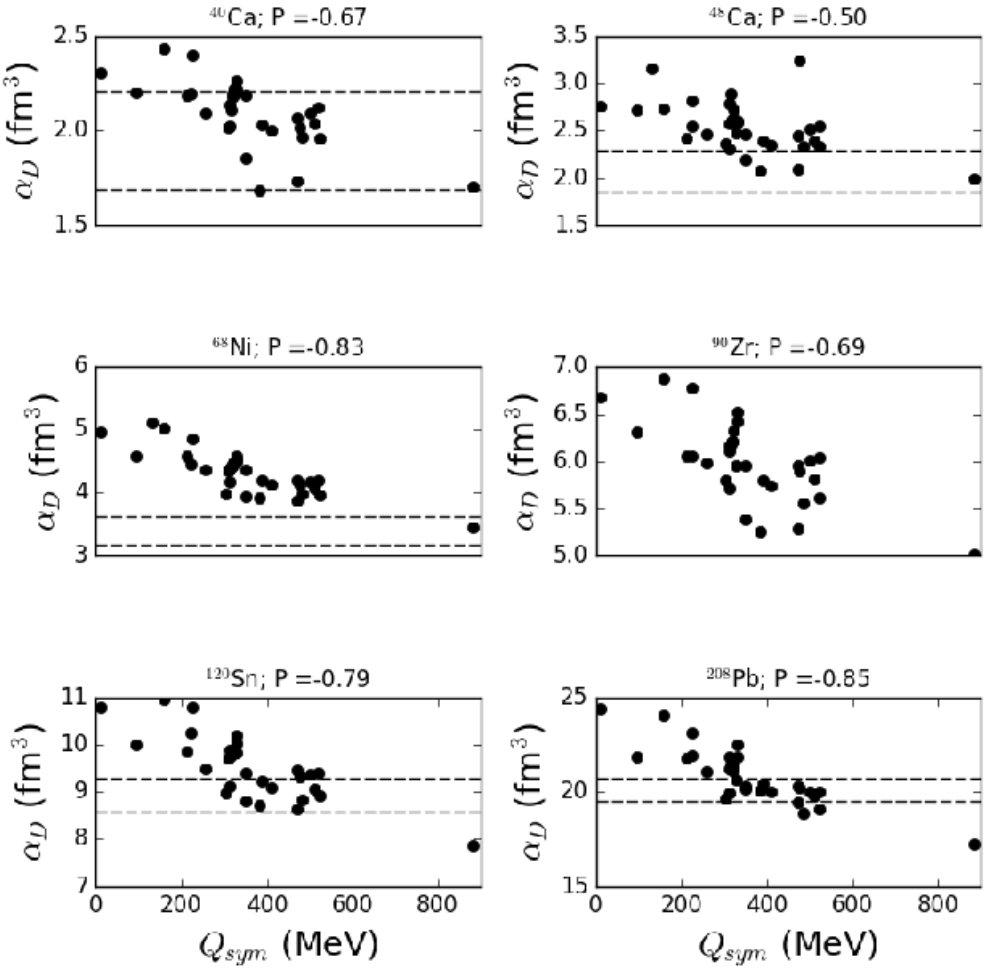

FIG. 1. Calculated electric dipole polarizability (full circle), for the different interactions, as a function of the second derivative of the symmetry energy coefficient. Each nucleus has its own panel and the experimental uncertainties are contained by the dashed lines. The Pearson linear correlations, P, are given for each nucleus.

Isoscalar giant quadrupole resonances in ^{44}Ca, ^{54}Fe, ^{64,68}Zn and ^{56,58,60,68}Ni and the effective mass

G. Bonasera, S. Shlomo, D.H. Youngblood, Y.-W. Lui, Krishichayan, and J. Button

We carried out fully self-consistent Hartree-Fock (HF)-based random phase approximation (RPA) calculations of the centroid energies, E_{CEN}, for the isoscalar resonances up to L=3 multipolarity for the isotopes of ^{44}Ca, ^{54}Fe, ^{64,68}Zn and ^{56,58,60,68}Ni [1]. The calculations were done using 33 different Skyrme-type effective nucleon-nucleon interaction commonly adopted in the literature. The interactions considered are associated with a wide range of nuclear matter properties. For the single particle orbits of the open shell nuclei we used the occupation number approximation to perform the calculations. We also calculated the Pearson Linear Correlation Coefficient, C, between the centroid energies of each giant resonance and every nuclear matter (NM) property.

In Fig. 1 we plot the calculated centroid energies E_{CEN} (shown as circles) of the isoscalar giant quadrupole resonance as a function of the effective mass, m*/m. Experimental data is available for all the nuclei considered and is marked by the dashed lines. We find a strong correlation between the values of E_{CEN} and m*/m (C~ -0.93). As shown in the figure, we obtained the best agreement between the calculated and measured centroid energies for interactions with a value of effective mass in the range m*/m = 0.6-0.8 in the case of ^{44}Ca and ^{54}Fe, whereas for all the other nuclei a slightly higher effective mass is in better agreement with the data. We note that some interactions, associated with a value of the effective mass as high as m*/m=1, reproduced the E_{CEN} of ^{56,58,60}Ni and ^{64}Zn. These fluctuations in the value of the effective mass was also found in our other study regarding the region of A = 90 -100 [2] and remains an unsolved issue.

[1] G. Bonasera *et al*., in preparation.
[2] G. Bonasera *et al*., Nucl. Phys. A (submitted).

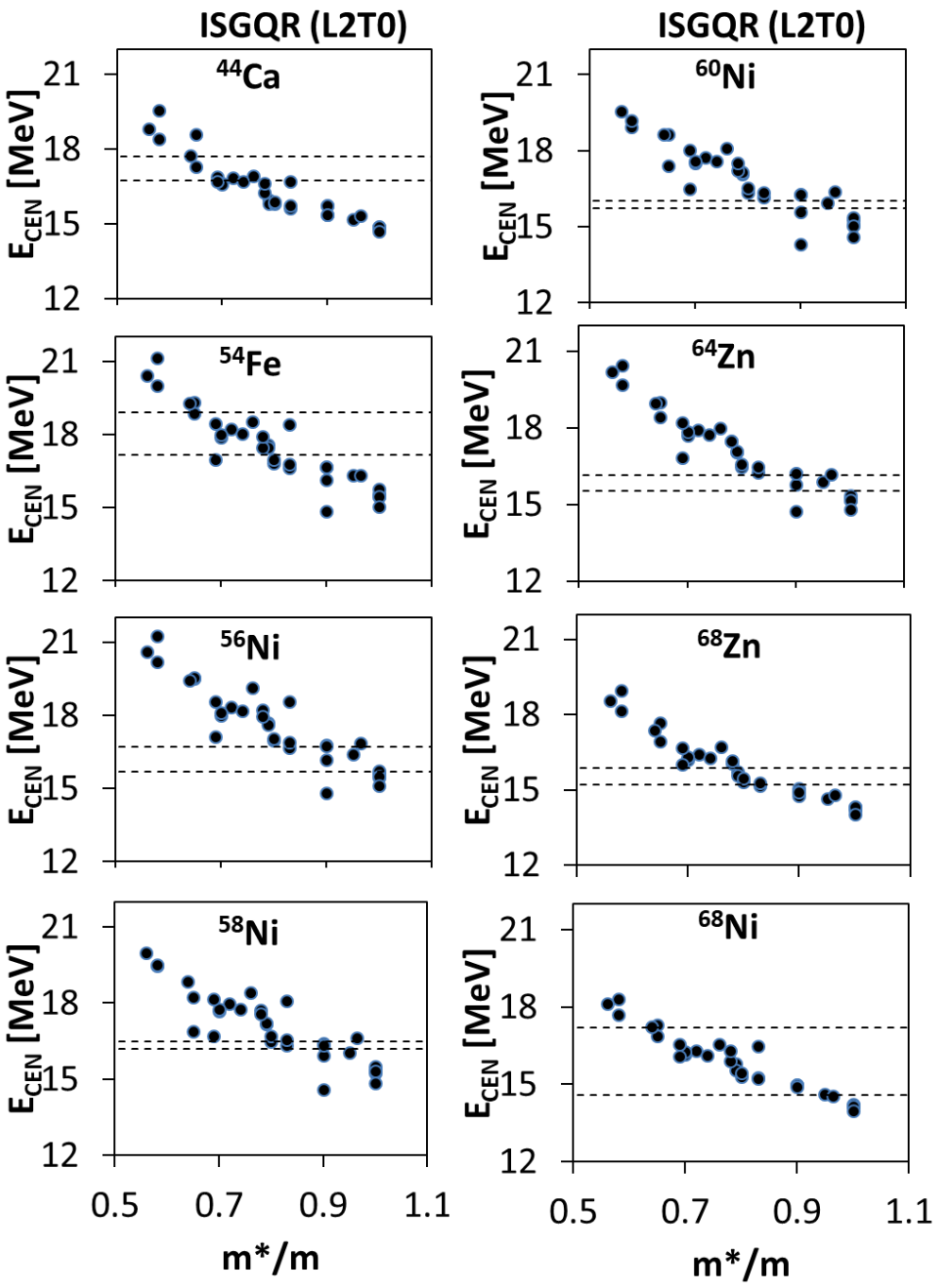

FIG. 1. Calculated centroid energies E_{CEN} in MeV (full circle) of the Isoscalar Giant Quadrupole Resonance, for the different interactions, as a function the effective mass. Each nucleus has its own panel and the experimental uncertainties are contained by the dashed lines. We find strong correlation between this NM property and the calculated E_{CEN} with a Pearson Correlation C ~-0.93 for all isotopes considered.

Isovector giant dipole resonances in ^{44}Ca, ^{54}Fe, ^{64,68}Zn and ^{56,58,60,68}Ni and the energy weighted sum rule enhancement factor

G. Bonasera, S. Shlomo, D.H. Youngblood, Y.-W. Lui, Krishichayan, and J. Button

We carried out fully self-consistent Hartree-Fock (HF)-based random phase approximation (RPA) calculations of the centroid energies for the isovector resonances up to L=3 multipolarity for the isotopes of ^{44}Ca, ^{54}Fe, ^{64,68}Zn and ^{56,58,60,68}Ni [1]. The calculations were done using 33 different Skyrme-type effective nucleon-nucleon interaction commonly adopted in the literature. The interactions considered are associated with a wide range of nuclear matter properties. For the single particle orbits of the open shell nuclei we used the occupation number approximation to perform the calculations.

The Pearson Linear Correlation coefficient, C, is calculated between the centroid energies, E_{CEN}, of each giant resonance and every nuclear matter (NM) property. We then compare our theoretical calculation to the available experimental data and in the cases where we have high correlation we can set limiting values on the NM properties. Here we report on a strong correlation between the centroid energies of the Isovector Giant Dipole Resonances and the energy weighted sum rule enhancement factor κ. In Fig. 1 we show the centroid energies of the isovector giant dipole resonance as a function of κ. We obtained a strong Pearson linear correlation coefficient, for all shown nuclei, between the calculated values of E_{CEN} and κ with C~0.80. From the comparison with the experimental data, we find that for ^{44}Ca, ^{56,60}Ni and ^{64}Zn the interactions associated with a higher value of κ are closest to reproducing the data. Conversely, for ^{54}Fe and ^{68}Zn interactions associated with a smaller value of κ reproduce the data, while for ^{58,68}Ni the intermediate region of κ = 0.25-0.7 reproduces the data. Overall, we find that the region of κ = 0.25-0.7 is the best at reproducing most of the data.

These results confirm a similar analysis done for a wide mass range of spherical nuclei [2] and can be used as part of a set constrains on NM properties to determine the next generation nuclear energy density functional with improved predictive power for properties of nuclei and nuclear matter.

[1] G. Bonasera *et al*., in preparation.
[2] G. Bonasera, M.R. Anders, and S. Shlomo, Phys. Rev. C **98**, 054316 (2018).

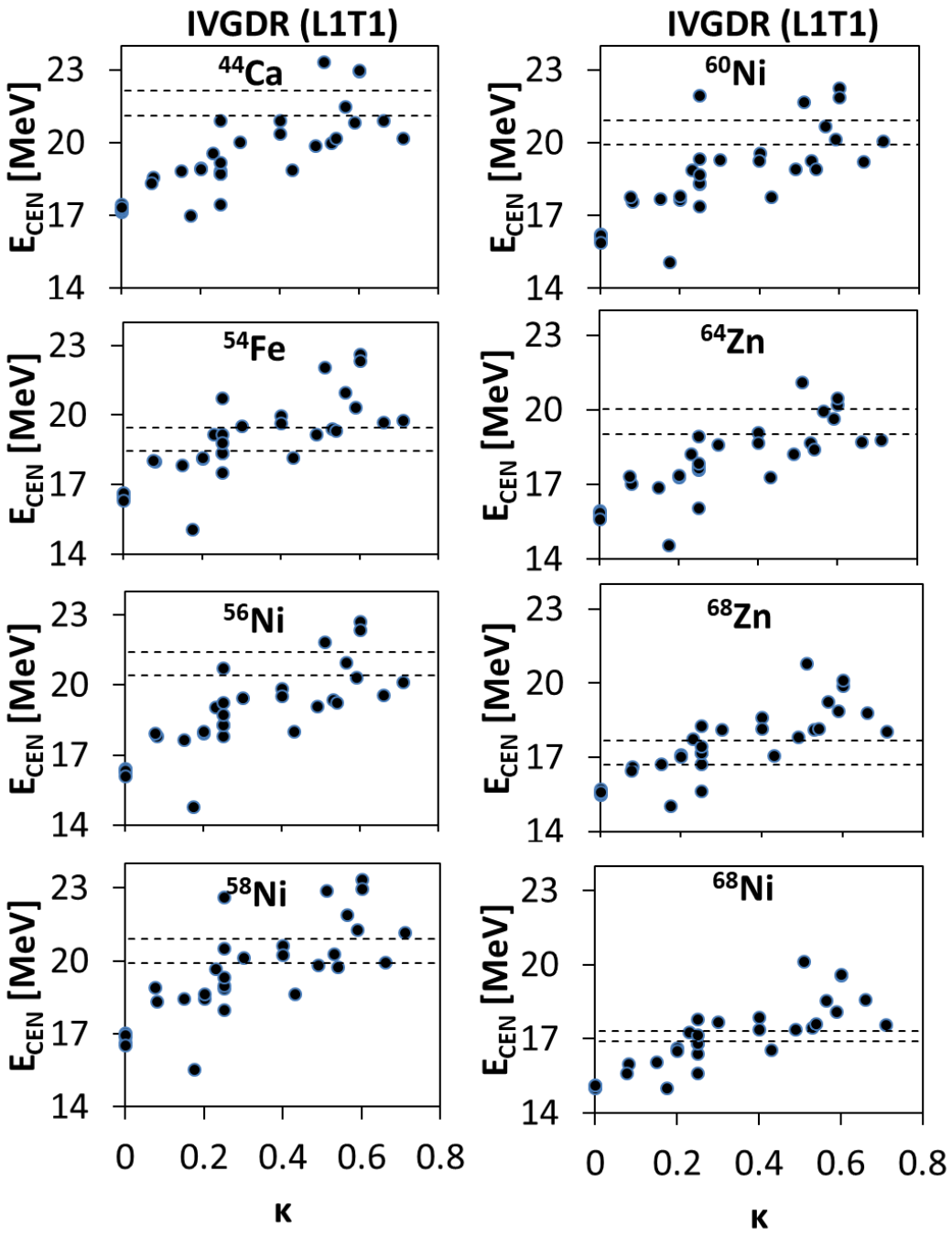

FIG. 1. Calculated centroid energies E_{CEN} in MeV (full circle) of the Isovector Giant Dipole Resonance, for the different interactions, as a function of the isovector dipole enhancement factor κ. Each nucleus has its own panel and the experimental uncertainties are contained by the dashed lines. We find strong correlation between this NM property and the calculated E_{CEN} with a Pearson Linear Correlation C ~0.80 for all considered nuclei.

Nuclear astrophysics theory progress

J.W. Holt and Y. Lim

Nuclear forces up to fifth order in the chiral expansion

The equation of state of neutron-rich matter from sub- to supra-nuclear densities directly influences neutron star structure and evolution, the dynamics of core-collapse supernovae, r-process nucleosynthesis, as well as features of gravitational waves produced during the late inspiral and post-merger phases of binary neutron star coalescence. The major challenge is to model the free energy $F(n, T, Y_p)$ of baryonic matter over approximately eight orders of magnitude in density ($n \sim 10^8 - 10^{15}$g/cm^3), temperatures up to $T \sim 5 \times 10^{11}\, K$, and proton fractions $Y_p \leq 0.6$. Under this range of conditions (well below the chiral symmetry breaking scale of $\Lambda_\chi \approx 1$ GeV) chiral effective field theory [Wei79, Epe09, Mac11] is expected to provide a suitable framework for the description of strongly interacting matter. In the previous year we have extended [Sam18] the modeling of the nuclear equation of state to include contributions from nucleon-nucleon interactions up to next-to-next-to-next-to-next-to-leading order (N4LO) in the chiral expansion with several values of the momentum-space cutoff $\Lambda = 450, 500, 550$ MeV. The parameters of the leading three-body force were refitted in each case to the triton binding energy and lifetime. The new set of chiral potentials leads to reduced uncertainties in the nuclear equation of state at and below normal nuclear densities $n < 0.16$ fm^{-3}, and saturation in symmetric nuclear matter is qualitatively reproduced at the correct binding energy and density.

Correlations among the nuclear symmetry energy, slope parameter, and curvature

The nuclear isospin-asymmetry energy, which characterizes the energy cost of converting protons into neutrons in an interacting many-body system, is an important organizing concept linking the properties of atomic nuclei to the structure and dynamics of neutron stars. In particular the isospin-asymmetry energy governs the proton fraction of dense matter in beta equilibrium, the thickness of neutron star crusts, and the typical radii of neutron stars. Modeling the isospin-asymmetry energy at several times normal nuclear densities is theoretically and experimentally challenging but crucial for linking upcoming neutron star observations to fundamental properties of the nuclear equation of state. Recently [Hol18] we have investigated correlations among the nuclear symmetry energy (J), its slope parameter (L), and curvature (K_{sym}) that parameterize the density dependence of the isospin-asymmetry energy S_2:

$$S_2(n) = J + L\left(\frac{n-n_0}{3n_0}\right) + \frac{1}{2}K_{sym}\left(\frac{n-n_0}{3n_0}\right)^2 + \cdots,$$

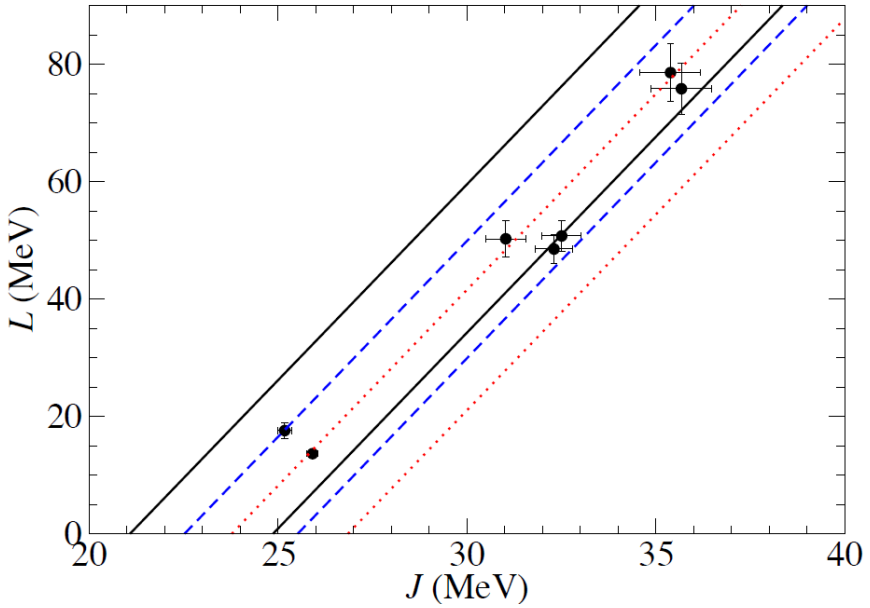

FIG. 1. Correlation [5] between $\boldsymbol{L}$ and $\boldsymbol{J}$ from explicit chiral effective field theory calculations (dots) and from a general Fermi liquid theory analysis (lines).

where n_0 is the saturation density of symmetric nuclear matter. In particular, starting from a Fermi liquid theory description of nuclear matter based on chiral two- and three-body forces, we found a relatively strong linear correlation between L and J, and between K_{sym} and J. In addition, certain features of the correlations, such as their slopes, were found to be insensitive to detailed properties of the nuclear force. In Fig. 1 we show the L vs. J correlation obtained from Fermi liquid theory (lines) as well as from explicit calculations from chiral two- and three-nucleon forces. These correlations were then employed in a new Bayesian framework [Lim18a] for deriving neutron star radius and tidal deformability probability distributions.

Neutron star moments of inertia constrained by nuclear theory and experiment

Neutron star observations are a promising tool to infer the properties of nuclear matter at several times normal nuclear densities. Radio timing observations of the relativistic double pulsar system PSR J0737-3039 are expected to produce in the next several years an estimate of the more rapidly rotating pulsar's moment of inertia. Recently, we have made theoretical predictions [Lim18b] for the mass and radius dependence of neutron star moments of inertia from a Bayesian analysis of the nuclear equation of state constrained by nuclear theory and experiment [Lim18a]. We have found that for pulsar J0737-3039A with mass $M = 1.338 M_{\odot}$, the moment of inertia lies in the range $0.98 \times 10^{45}\,\mathrm{g\,cm^2} < I_{1.338} < 1.48 \times 10^{45}\,\mathrm{g\,cm^2}$ at the 95% credibility level. In Fig. 2 we show the strong correlation between the moment of inertia of PSR J0737-3039A and its radius R, demonstrating that a precise measurement of $I_{1.338}$ will enable robust predictions for its radius complementary to other astronomical observations, such

as tidal deformabilities from gravitational wave detectors and direct radius measurements from the NICER X-ray telescope.

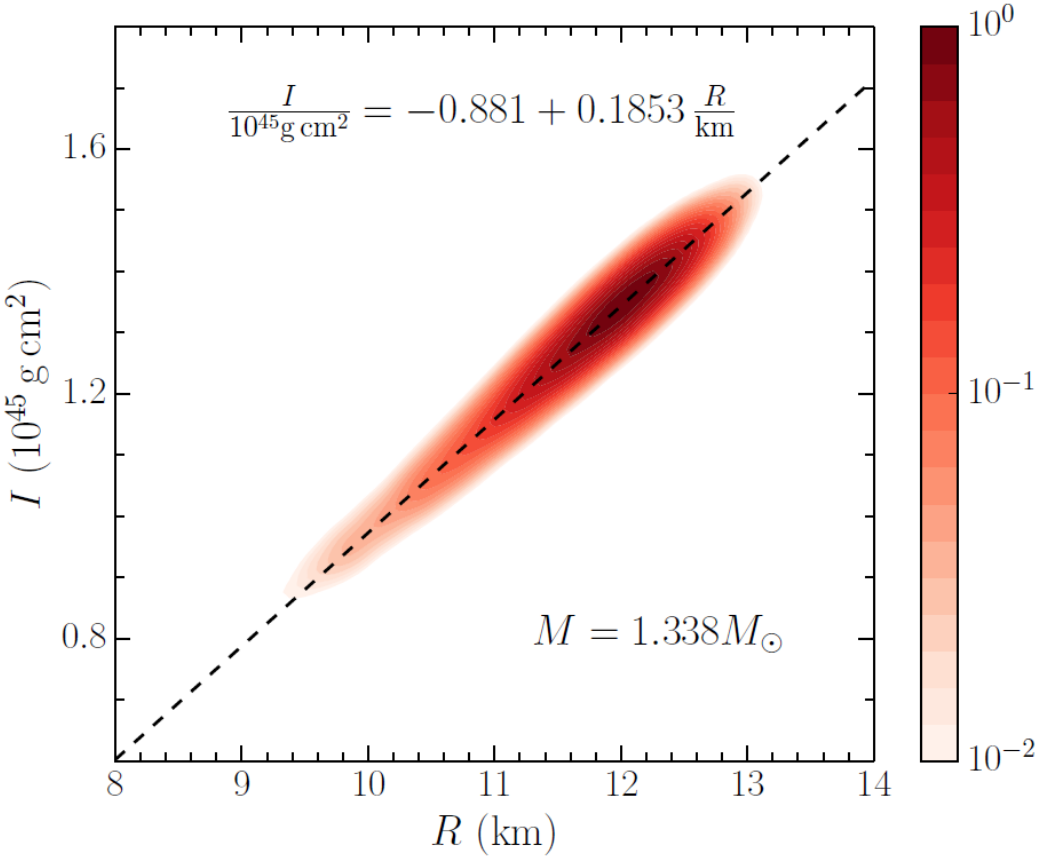

FIG. 2. Correlation between the moment of inertia of a $\boldsymbol{M = 1.338 M_\odot}$ neutron star and its radius predicted from a Bayesian analysis of the nuclear equation of state.

We have also studied the fraction of the neutron star moment of inertia residing in the crust, which sets the ratio of the superfluid angular momentum to the total angular momentum in the neutron star. This angular momentum reservoir must be sufficiently large in order to support the observed glitch activity of the Vela pulsar [Cor88]. From our theoretical modeling we find that the crustal fraction of the moment of inertia is in the range 1-6% for typical neutron star masses, which is insufficient to explain glitches in the Vela pulsar under the scenario of strong neutron entrainment [Cha12, And12]. Additional theoretical modeling, such as the inclusion of pairing [Wat17] in the band theory calculations of neutron entrainment, may be needed to resolve the observed discrepancy.

[1] S. Weinberg, Physica A **96**, 327 (1979).
[2] E. Epelbaum, H.-W. Hammer, and U.-G. Meissner, Rev. Mod. Phys. **81**, 1773 (2009).
[3] R. Machleidt and D.R. Entem, Phys. Rep. **503**, 1 (2011).

[4] F. Sammarruca, L.E. Marcucci, L. Coraggio, J.W. Holt, N. Itaco, and R. Machleidt, arXiv: 1807.06640.
[5] J.W. Holt and Y. Lim, Phys. Lett. B **784**, 77 (2018).
[6] Y. Lim and J.W. Holt, Phys. Rev. Lett. **121**, 062701 (2018).
[7] Y. Lim, J.W. Holt, and R.J. Stahulak, arXiv:1810.10992.
[8] J.M. Cordes, G.S. Downs, and J. Krause-Polstorff, Astrophys. J. **330**, 847 (1988).
[9] N. Chamel, Phys. Rev. C **85**, 035801 (2012).
[10] N. Andersson, K. Glampedakis, W.C.G. Ho, and C.M. Espinoza, Phys. Rev. Lett. **109**, 241103 (2012).
[11] G. Watanabe and C.J. Pethick, Phys. Rev. Lett. **119**, 062701 (2017).

Astrophysical factors of $^{12}C + ^{12}C$ fusion extracted using Trojan Horse method

A.M. Mukhamedzhanov, D.Y. Pang, and A.S. Kadyrov

Carbon-carbon burning plays an important role in many stellar environments. Recently, Tumino *et al.* [1] reported a sharp rise of the astrophysical S factor for carbon-carbon fusion determined using the indirect Trojan Horse method. We demonstrate that the rise at low energies seen in the aforementioned work is an artefact of using an invalid plane-wave approximation that neglects the Coulomb interactions. Our analysis shows that such a rise disappears if the Coulomb (or Coulomb-nuclear) interactions in the initial and final states are included.

The paper has been submitted to Phys. Rev. C.

[1] A. Tumino *et al.*, Nature **557**, 687 (2018).

Balmer-α emission in proton-hydrogen collisions

O. Erkilic, I.B. Abdurakhmanov, A.S. Kadyrov, and I. Bray, S.K. Avazbaev, and A.M. Mukhamedzhanov

The semiclassical two-centre convergent close-coupling approach is applied to study Balmer-α emission in proton-hydrogen scattering at the incident proton energies from 10 keV to 1 MeV. The approach uses wave-packet pseudostates for the discretization of the continuous spectrum of the target and projectile, constructed from the Coulomb wave function, the eigenstate of the hydrogen atom Hamiltonian. The Balmer- α cross section is calculated from the excitation cross sections into the final states with principal quantum number n = 3. The obtained results are in good agreement with the recent theoretical calculations, but significantly lower than the experimental measurements at high energies. Surprisingly, the cross section for excitation of the n = 3 shell as a whole and the individual cross section for excitation of the 3p state display very good agreement with the available experimental measurements. A polarisation fraction of the Balmer- α emission is also calculated. Significant disagreement with experimental measurements and between various theoretical calculations is observed.

Connection between asymptotic normalization coefficients and resonance widths of mirror states

A.M. Mukhamedzhanov

Asymptotic normalization coefficients (ANCs) are fundamental nuclear constants playing important role in nuclear reactions, nuclear structure and nuclear astrophysics. In this paper a connection between ANCs and resonance widths of the mirror states is established. Using Pinkston-Satchler equation the ratio for resonance widths and ANCs of mirror nuclei is obtained in terms of the Wronskians from the radial overlap functions and regular solutions of the two-body Schr¨odinger equation with the short-range interaction excluded. This ratio allows one to use microscopic overlap functions for mirror nuclei in the internal region, where they are the most accurate, to correctly predict the ratio of the resonance widths and ANCs for mirror nuclei, which determine the amplitudes of the tails of the overlap functions. If the microscopic overlap functions are not available one can express the Wronskians for the resonances and mirror bound states in terms of the corresponding mirror two-body potential-model wave functions. A further simplification of the Wronskians ratio leads to the equation for the ratio of the resonance widths and mirror ANCs, which is expressed in terms of the ratio of the two-body Coulomb scattering wave functions at the resonance energy and at the binding energy [1]. Calculations of the ratios of resonance widths and mirror ANCs for different nuclei are presented. From this ratio one can determine the resonance width if the mirror ANC is known and vice versa. Comparisons with available experimental ratios are done.

The paper has been published in Phys. Rev. C **99**, 024311 (2019).

[1] N.K. Timofeyuk, R.C. Johnson, and A.M. Mukhamedzhanov, Phys. Rev. Lett. **91**, 232501 (2003).

Extrapolation of scattering data to the negative-energy region: Application to the p-^{16}O system

L.D. Blokhintsev, A.S. Kadyrov, A.M. Mukhamedzhanov, and D.A. Savin

The problem of analytic continuation of the scattering data to the negative-energy region to obtain information on asymptotic normalization coefficients (ANCs) of bound states is discussed. It is shown that a recently suggested method [1] is not strictly correct in the mathematical sense since it is not an analytic continuation of a partial-wave scattering amplitude to the region of negative energies. However, it can be used for practical purposes for sufficiently large charges and masses of colliding particles. Both the D-method and the standard method of continuing of the effective range function are applied to the p-^{16}O system, which is of interest for nuclear astrophysics. The ANCs for the ground 5/2+ and excited 1/2+ states of ^{17}F are determined.

The paper has been published in Phys. Rev. C **98**, 064610 (2018).

[1] O.L. Ramírez Suárez and J.-M. Sparenberg, Phys. Rev. C **96**, 034601 (2017).

Impact of the $^{7}Be(\alpha,\gamma)^{11}C$ Reaction on the Primordial Abundance of ^{7}Li

M. Hartos , C.A. Bertulani , Shubhchintak, A.M. Mukhamedzhanov, and S. Hou

We calculate the radiative capture cross section for $^{7}Be(\alpha,\gamma)^{11}C$ and its reaction rate of relevance for the Big Bang nucleosynthesis (BBN). The impact of this reaction on the primordial ^{7}Li abundance is revised including narrow and broad resonances in the pertinent energy region. Our calculations show that it is unlikely that very low energy resonances in ^{11}C of relevance for the BBN would emerge within a two-body potential model. Based on our results and a comparison with previous theoretical and experimental analyses, we conclude that the impact of this reaction on the so-called "cosmological lithium puzzle" is completely irrelevant.

The paper has been published in Astrophys. J. **862**, 62 (2018).

Three-body Faddeev equations in two-particle Alt-Grassberger-Sandhas form with distorted-wave-Born-approximation amplitudes as effective potentials

A.M. Mukhamedzhanov

A(d,p)B reactions on heavier nuclei are peripheral at sub-Coulomb energies and can be peripheral even at energies above the Coulomb barrier due to the presence of the distorted waves in the initial and final channels. Usually, to analyze such reactions the distorted-wave Born approximation (DWBA) is used. The DWBA amplitude for peripheral reactions is parametrized in terms of the asymptotic normalization coefficient (ANC) of the bound state B = (nA). However, in the DWBA, the coupling of the different channels is not taken into account explicitly. The three-body Faddeev equations written as the two-particle Alt-Grassberger-Sandhas (AGS) equations are very suitable for the analysis of the A(d,p)B reactions because they take into account explicitly the coupling of the different channels. It is well known that the overall normalization of the DWBA amplitude or even of the more advanced continuum-discretized coupled channels (CDCC) amplitude for peripheral reactions (both sub-Coulomb and above the Coulomb barrier) is determined by the ANC. However, it is not apparent that it is the case for the AGS solution due to the coupling of the (d,p) channel to other channels. In this paper, it is proved that the sub-Coulomb *A(d,p)B* reaction amplitude, which is a solution of the two-body AGS equations, is peripheral and is parametrized in terms of the ANC of the bound state B = (nA) if the corresponding DWBA amplitude is peripheral. Both nonlocal separable and local nuclear interaction potentials between the constituent particles are considered. To prove the peripheral character of the AGS amplitude for the sub-Coulomb A(d,p)B reactions the effective potentials are expressed in terms of the corresponding sub-Coulomb DWBA amplitudes of the different channels. The analysis of the *A(d,p)B* reactions above the Coulomb barrier requires the inclusion of the optical potentials. Hence, to analyze such reactions, the AGS equations are generalized by including the optical nuclear potentials in the same manner as it is done in the DWBA. The obtained AGS equations contain the DWBA effective potentials with distorted waves generated by the sum of the nuclear optical and the channel Coulomb potentials. It is shown that if the DWBA amplitude is peripheral than this is also the case for the AGS amplitude, which is also parametrized in terms of the ANC of the bound state B = (nA). The inclusion of the coupling of the different channels in the AGS formalism allows one to improve, compared to the DWBA and CDCC methods, the treatment of peripheral (d,p) reactions at sub-Coulomb energies and at energies above the Coulomb barrier.

The paper has been published in Phys. Rev. C **98**, 044626 (2018).

Strongly resonating bosons in hot nuclei

S. Zhang,[1] A. Bonasera,[2, 3] M. Huang,[1] H. Zheng,[4] D.X. Wang,[1] J.C.Wang,[1] L. Lu,[1] G. Zhang,[5, 6] Z. Kohley,[2, 7] Y.G. Ma,[5, 6, 8] and S.J. Yennello[2, 7]

[1]*College of Physics and Electronics information, Inner Mongolia University for Nationalities, Tongliao, 028000, China*

[2]*Cyclotron Institute, Texas A&M University, College Station, TX 77843, USA*

[3]*Laboratori Nazionali del Sud, INFN, via Santa Sofia, 62, 95123 Catania, Italy*

[4]*School of Physics and Information Technology, Shaanxi Normal University, Xian 710119, China.*

[5]*Key Laboratory of Nuclear Physics and Ion-beam Application (MOE), Institute of Modern Physics, Fudan University, Shanghai, 200433, China.*

[6]*Shanghai Institute Applied Physics, Chinese Academy of Sciences, Shanghai, 201800, China.*

[7]*Chemistry Department, Texas A&M University, College Station, Texas 77843, USA*

[8]*University of the Chinese Academy of Sciences, Beijing, 100080, China*

When two heavy ions near the Fermi energy collide, a warm and low-density region can form in which fragments appear. This region is mainly dominated by proton (p) and alpha (α) particles. In such an environment, the alphas interact with each other, and especially through strong resonances, form complex systems such as ^{8}Be and ^{12}C. Our experiments show that in the reactions $^{70(64)}$Zn(^{64}Ni)+$^{70(64)}$Zn(^{64}Ni) at E/A=35 MeV/nucleon levels of ^{8}Be appear around relative energies Eij=0.092 MeV, 3.03 MeV as well as above 10 MeV and 100 MeV [1]. We propose a different method to derive the correlation function based on the relative transverse energy distribution to minimize the experimental uncertainties. For the 3α systems, multi resonance processes give rise to excited levels of ^{12}C. In particular, the Hoyle state at 7.654 MeV excitation energy shows a decay component through the ground state of ^{8}Be and also components where two different α couples are at relative energies consistent with the ground state of ^{8}Be at the same time [1].

[1] S. Zhang *et al.*, Phys. Rev. C **99**, 044605 (2019).

Triple α resonances in the decay of hot nuclear systems

S. Zhang,[1] A. Bonasera,[2, 3] M. Huang,[1] H. Zheng,[4] D.X. Wang,[1] J.C.Wang,[1] L. Lu,[1] G. Zhang,[5, 6] Z. Kohley,[2, 7] Y.G. Ma,[5, 6, 8] and S.J. Yennello[2, 7]

[1]*College of Physics and Electronics information, Inner Mongolia University for Nationalities, Tongliao, 028000, China*

[2]*Cyclotron Institute, Texas A&M University, College Station, TX 77843, USA*

[3]*Laboratori Nazionali del Sud, INFN, via Santa Sofia, 62, 95123 Catania, Italy*

[4]*School of Physics and Information Technology, Shaanxi Normal University, Xian 710119, China.*

[5]*Key Laboratory of Nuclear Physics and Ion-beam Application (MOE), Institute of Modern Physics, Fudan University, Shanghai, 200433, China.*

[6]*Shanghai Institute Applied Physics, Chinese Academy of Sciences, Shanghai, 201800, China.*

[7]*Chemistry Department, Texas A&M University, College Station, Texas 77843, USA*

[8]*University of the Chinese Academy of Sciences, Beijing, 100080, China*

The Efimov (Thomas) trimers in excited ^{12}C nuclei, for which no observation exists yet, are discussed by means of analyzing the experimental data of $^{70(64)}$Zn(^{64}Ni)+$^{70(64)}$Zn(^{64}Ni) at E/A=35 MeV/nucleon. In heavy ion collisions, the αs interact with each other and can form complex systems such as ^{8}Be and ^{12}C. For the 3α systems, multi resonance processes give rise to excited levels of ^{12}C. The interaction between any two of the 3α particles provides events with one, two or three ^{8}Be. Their interfering levels are clearly seen in the minimum relative energy distributions. Events of three couple α relative energies consistent with the ground state of ^{8}Be are observed with the decrease of the instrumental error at the reconstructed 7.458 MeV excitation energy of ^{12}C, which was suggested as the Efimov (Thomas) state [1].

[1] S.Zhang *et al.*, Chinese Phys. C (in press).

Microscopic description of proton-induced spallation reactions with the Constrained Molecular Dynamics (CoMD) Model

A. Assimakopoulou,[1] G.A. Souliotis,[1] A. Bonasera,[2,3] A. Botvina,[4,5] N.G. Nicolis,[6] and M. Veselsky[7]

[1]*Laboratory of Physical Chemistry, Department of Chemistry, National and Kapodistrian University of Athens, Athens 15771, Greece*

[2]*Cyclotron Institute, Texas A & M University, College Station, Texas, USA*

[3]*Laboratori Nazionali del Sud, INFN, Catania, Italy*

[4]*Frankfurt Institute for Advanced Studies, Goethe University, D-60438 Frankfurt am Main, Germany*

[5]*Institute for Nuclear Research, Russian Academy of Sciences, RU-117312 Moscow, Russia*

[6]*Department of Physics, The University of Ioannina, Ioannina 45110, Greece*

[7]*Institute of Physics, Slovak Academy of Sciences, Bratislava 84511, Slovakia*

We studied the complete dynamics of the proton-induced spallation process with the microscopic framework of the Constrained Molecular Dynamics (CoMD) Model. We performed calculations of proton-induced spallation reactions on ^{181}Ta, ^{208}Pb, and ^{238}U targets with the CoMD model and compared the results with a standard two-step approach based on an intranuclear cascade model (INC) followed by a statistical deexcitation model. The calculations were also compared with recent experimental data from the literature. Our calculations showed agreement with some aspects of the experimental data and suggest further improvements in the models. We point out that this CoMD study represents the first complete dynamical description of spallation reactions with a microscopic N-body approach and may lead to advancements in the physics-based modelling of the spallation process.

Nuclear probes of an out-of-equilibrium plasma at the highest compression

G. Zhang,[1,2] M. Huang,[3] A. Bonasera,[4,5] Y.G. Ma,[2,6,9] B.F. Sheng,[10] H.W. Wang,[1,2] W.P. Wang,[7] J.C. Xu,[7] G.T.Fan,[1,2] H.J. Fu,[2] H. Xue,[2] H. Zheng,[10] L.X. Liu,[1,2] S. Zhang,[3] W.J. Li,[2] X.G. Cao,[1,2] X.G. Deng,[2] X.Y. Li,[2] Y.C. Liu,[2] Y. Yu,[7] Y. Zhang,[2] C.B. Fu,[11] and X.P. Zhang[11]

[1]*Shanghai Advanced Research Institute, Chinese Academy of Sciences, Shanghai 201210, China.*

[2]*Shanghai Institute Applied Physics, Chinese Academy of Sciences, Shanghai 201800, China.*

[3]*College of Physics and Electronics information, Inner Mongolia University for Nationalities, Tongliao, 028000, China.*

[4]*Cyclotron Institute, Texas A&M University, College Station, Texas 77843, USA.*

[5]*Laboratori Nazionali del Sud, INFN, via Santa So_a, 62, 95123 Catania, Italy.*

[6]*Key Laboratory of Nuclear Physics and Ion-beam Application (MOE), Institute of Modern Physics, Fudan University, Shanghai 200433,China*

[7]*State Key Laboratory of High Field Laser Physics, Shanghai Institute of Optics and Fine Mechanics,Chinese Academy of Sciences,Shanghai 201800, China.*

[8]*Department of Physics, Shanghai Normal University, Shanghai 200234, China*

[9]*University of the Chinese Academy of Sciences, Beijing 100080, China.*

[10]*School of Physics and Information Technology, Shaanxi Normal University Xi'an 710119, China.*

[11]*School of Physics and Astronomy, Shanghai Jiao Tong University, Shanghai 200240, China*

We report the highest compression reached in laboratory plasmas using eight laser beams, $E_{laser}\approx 12$ kJ, $\tau_{laser}=2$ ns in third harmonic on a CD2 target at the ShenGuang-II Upgrade (SGII-Up) facility in Shanghai, China [1]. We estimate the deuterium density $\rho_D=2.0 \pm 0.9$ kg/cm3, and the average kinetic energy of the plasma ions less than 1 keV. The highest reached areal density $\Lambda\rho_D=4.8 \pm 1.5$ g/cm2 was obtained from the measured ratio of the sequential ternary fusion reactions (dd→t+p and t+d→α+n) and the two body reaction fusions (dd→^{3}He+n). At such high densities, sequential ternary and also quaternary nuclear reactions become important as well (i.e. n(14.1 MeV) + ^{12}C → n'+^{12}C*etc.) resulting in a shift of the neutron (and proton) kinetic energies from their birth values. The Down Scatter Ratio (DSR-quaternary nuclear reactions) method, i.e. the ratio of the 10-12MeV neutrons divided by the total number of 14.1MeV neutrons produced, confirms the high densities reported above. The estimated lifetime of the highly compressed plasma is 52 ±9 ps, much smaller than the lasers pulse duration.

[1] G. Zhang *et al.*, Phys. Lett. A (in press), https://doi.org/10.1016/j.physleta.2019.04.048

Nuclear astrophysics with lasers

M. Huang, H.J. Quevedo, G. Zhang, and A. Bonasera

A systematic program of investigations of nuclear reactions in laser-produced plasmas is addressed. Such reactions provide an important diagnostic tool for probing the dynamics and thermodynamics in the plasma and understanding laser ion acceleration and neutron production mechanisms. The goal will be to reach the level of understanding that allows the measurement of fundamental nuclear cross sections at low and high densities. The quantitative measurement of fusion probabilities in hot and dense plasmas will contribute significantly to our understanding of stellar composition and evolution and will provide important information for development of fusion energy production and applications such as medical isotope production and compact neutron source development. All of these are some of the main goals of the European Extreme Light Infrastructure (ELI) and similar projects in China and other countries [1].

[1] M. Huang *et al.*, Nucl. Phys. News International (NUPECC) (in press).

A novel approach to medical radioisotope production using inverse kinematics: A successful production test of the theranostic radionuclide ^{67}Cu

G.A. Souliotis,[1] M.R.D. Rodrigues,[2,5] K. Wang,[2] V. Iacob,[2] N. Nica,[2] B. Roeder,[2] G. Tabacaru,[2] M. Yu,[3] P. Zanotti-Fregonara,[3] and A. Bonasera[2,4]

[1]*Laboratory of Physical Chemistry, Department of Chemistry, National and Kapodistrian University of Athens, Athens 15771, Greece*

[2]*Cyclotron Institute, Texas A & M University, College Station, Texas 77048, USA*

[3]*Houston Methodist Research Institute, Houston, Texas , 77030, USA*

[4]*Laboratori Nazionali del Sud, INFN, Catania 95123, Italy*

[5]Instituto *de F´ısica, Universidade de S˜ao Paulo, S˜ao Paulo 05508-090, Brazil*

A novel method for the production of important medical radioisotopes has been developed. The approach is based on performing the nuclear reaction in inverse kinematics, namely sending a heavy-ion beam of appropriate energy on a light target (e.g. H, d, He) and collecting the isotope of interest [1]. In this work, as a proof-of-concept, we studied the production of the theranostic radionuclide ^{67}Cu ($T_{1/2}$=62 h) via the reaction of a ^{70}Zn beam at 15 MeV/nucleon with a hydrogen gas target. The ^{67}Cu radionuclide, alongside other coproduced isotopes, was collected after the gas target on an Al catcher foil and their radioactivity was measured by offline γ-ray analysis. After 36 h from the end of the irradiation, apart from the product of interest ^{67}Cu, the main radioimpurity coming from the ^{70}Zn+p reaction was ^{69m}Zn ($T_{1/2}$=13.8 h) that can be reduced by further radio-cooling. Moreover, along with the radionuclide of interest produced in inverse kinematics, the production of additional radioisotopes is possible by making use of the forward-focused neutrons from the reaction and letting them interact with a secondary target. A preliminary successful test of this concept was realized in the present study. The main requirement to obtain activities appropriate for preclinical studies is the development of high-intensity heavy-ion primary beams.

[1] G.A. Souliotis *et al.*, Appl. Radiat. Isot. **149**, 89 (2019); https://doi.org/10.1016/j.apradiso.-2019.04.019

Chiral kinetic approach to chiral magnetic effect in isobaric collisions

Y. Sun and C.M. Ko

Based on the chiral kinetic approach using quarks and antiquarks from a multiphase transport model [1] as initial conditions, we have studied the chiral magnetic effect, i.e., the magnetic field induced separation of charged particles in the transverse plane, in non-central isobaric collisions of Zr+Zr and Ru+Ru, which have the same atomic number but different proton numbers [2]. For the observable $\gamma^{OS} - \gamma^{SS}$ related to the difference between the correlations of particles of opposite charges and of same charges, we find a difference between the two collision systems if the magnetic field has a long lifetime of 0.6 fm/*c* and the observable is evaluated using the initial reaction plane as shown in Fig.1. This signal of the chiral magnetic effect becomes smaller and comparable to the background contributions from elliptic flow if the event plane determined from particle emission angles is used. For the other observable given by the $R(\Delta S)$ correlator related to the distribution of average charge separation in a collision, it depends less on whether the reaction or event plane is used in the analysis as shown in Fig. 1, making it a plausible observable for identifying the chiral magnetic effect from its difference in the two isobaric collision systems.

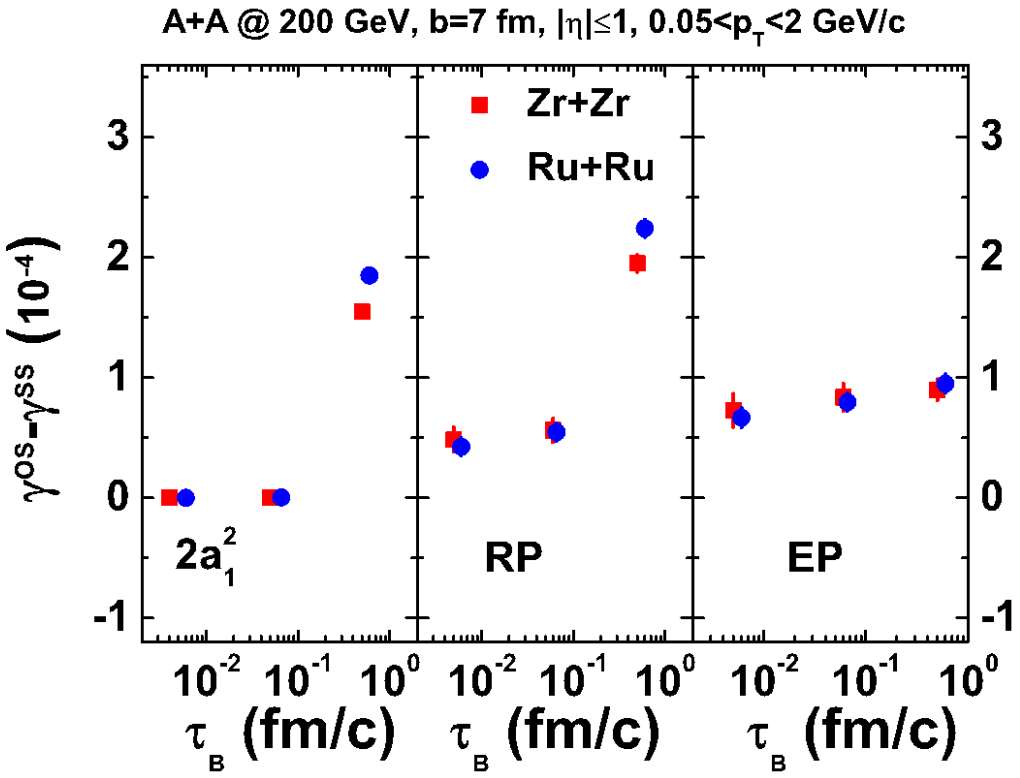

FIG. 1. Magnetic field lifetime dependence of the $\boldsymbol{\gamma^{OS} - \gamma^{SS}}$ correlator and of mid-pseudorapidity ($\boldsymbol{|\eta| \leq 1}$) light quarks in Ru+Ru and Zr+Zr collisions at $\boldsymbol{\sqrt{s_{NN}} = 200}$ GeV and impact parameter b = 7 fm for transverse momenta in the range $\boldsymbol{0.05 \leq p_T \leq 2}$ GeV/*c* and using different calculation methods. The error bars denote the statistical errors due to the finite number of events used in the study.

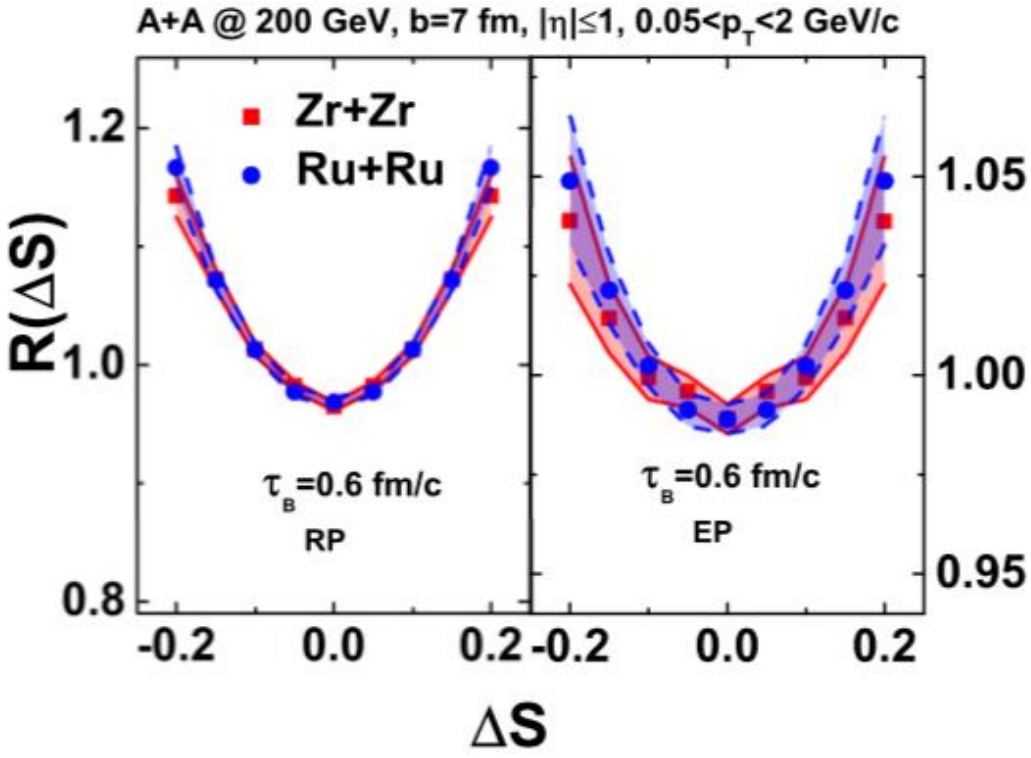

FIG. 2. Same as Fig. 1 for ΔS dependence of the $R(\Delta S)$ correlator.

[1] Z.-W. Lin, C.M. Ko, B.-A. Li, B. Zhang, and S. Pal, Phys. Rev. C **72**, 064901 (2005).
[2] Y. Sun and C.M. Ko, Phys. Rev. C **98**, 014911 (2018).

Light nuclei production as a probe of the QCD phase diagram

K.J. Sun,[1] L.W. Chen,[1] C.M. Ko, J. Pu,[1] and Z. Xu[2,3]

[1]*School of Physics and Astronomy and Shanghai Key Laboratory for Particle Physics and Cosmology, Shanghai Jiao Tong University, Shanghai 200240, China*

[2]*Brookhaven National Laboratory, Upton, NY 11973, USA*

[3]*School of Physics & Key Laboratory of Particle Physics and Particle Irradiation (MOE), Shandong University, Jinan, Shandong 250100, China*

We have proposed in Ref.[1] a double-peak structure in the collision energy dependence of the baryon density fluctuation in heavy-ion collisions as a probe to the structure of the QCD phase diagram, with the lower energy one due to the spinodal instability associated with a first-order quark-hadron phase transition and the higher energy one induced by the second-order phase transition at the critical end point (CEP). This double-peak structure seems to be supported by the collision energy dependence of the relative neutron density fluctuation $\Delta\rho_n$ at kinetic freeze-out that we have extracted from analyzing the measured yields of *p*, d and 3H in central heavy-ion collisions at AGS and SPS [2] energies within the coalescence model. In particular, we have found $\Delta\rho_n$ to display a clear peak at $\sqrt{s_{NN}} = 8.8$ GeV and also a possible strong enhancement at $\sqrt{s_{NN}} = 4.86$ GeV as shown in Fig. 1, suggesting that the CEP could have been reached or closely approached in central Pb+Pb collisions at $\sqrt{s_{NN}} = 8.8$ GeV and the first-order phase transition could have occurred in central Au+Au collisions at $\sqrt{s_{NN}} = 4.86$ GeV. Our results thus provide a complementary evidence for the occurrence of a first-order phase transition and a critical

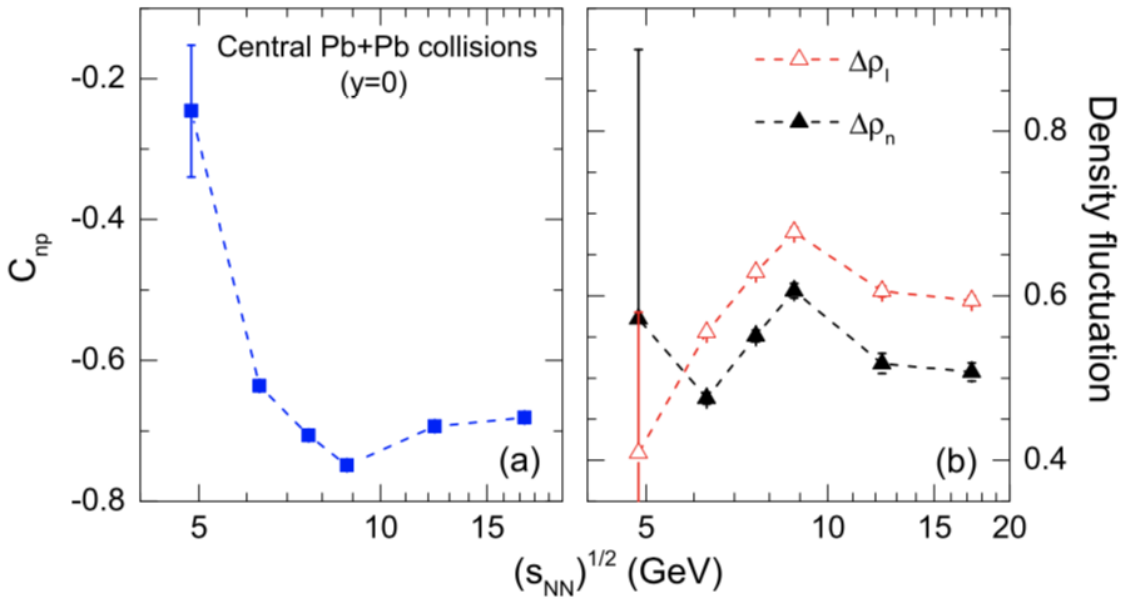

FIG. 1. Collision energy dependence of the neutron and proton density correlation C_{np} (panel (a)) and the neutron and isospin density fluctuations $\Delta\boldsymbol{\rho_n}$ and $\Delta\boldsymbol{\rho_I}$ (panel (b)) in central Pb+Pb collisions at SPS energies and Au+Au collisions at AGS energies.

endpoint in the QCD phase diagram to those that have been suggested in the literatures.

[1] K.J. Sun, L.W. Chen, C.M. Ko, J. Pu, and Z. Xu, Phys. Lett. B **781**, 499 (2018).
[2] K.J. Sun, L.W. Chen, C.M. Ko, and Z. Xu, Phys. Lett. B **774**, 103 (2017).

Nuclear matter properties at finite temperatures from effective interactions

Jun Xu,[1] Arianna Carbone,[2] Zhen Zhang,[3] and C.M. Ko

[1]*Shanghai Institute of Applied Physics, Chinese Academy of Sciences, Shanghai 201800, China*

[2]*European Centre for Theoretical Studies in Nuclear Physics and Related Areas (ECT*) and Fondazione Bruno Kessler, Strada delle Tabarelle 286, I-38123 Villazzano (TN), Italy*

[3]*Sino-French Institute of Nuclear Engineering and Technology, Sun Yat-Sen University, Zhuhai 519082, China*

To study if the commonly used nucleon-nucleon effective interactions, which are usually constructed from fitting the properties of cold nuclear matter and of finite nuclei, can properly describe nuclear matter at finite temperatures, we have used the improved isospin- and momentum-dependent interaction ImMDI-GF [1,2] and the recently constructed Skyrme interaction Skχm* [3] to evaluate the nucleon occupation probabilities, the equations of state, and the mean-field potentials in symmetric nuclear matter and pure neutron matter at finite temperatures using the Hartree-Fock approach [4]. These results have been compared with those from the microscopic self- consistent Green's function method [5] and the chiral effective many-body perturbation theory [6] using chiral nuclear forces [7]. We find that differences start to appear more strongly at higher temperatures between results for nuclear matter properties from the two effective interactions and also between these two and those from the microscopic theories. The deviations seen in the nucleon occupation probabilities have been understood from the different momentum dependence in the single-nucleon potential obtained within these approaches, while the latter is strongly suppressed at high momenta in the microscopic calculations based on chiral forces compared to those from the effective interactions, especially for Skχm∗ that has a quadratic momentum dependence. These differences in the nucleon momentum distributions lead to deviations in the kinetic energy contribution and also partially in the potential energy contribution to the nuclear equation of state. The energies per nucleon for symmetric nuclear matter and pure neutron matter from these two effective interactions, shown in the left and right windows of Fig.1, respectively, are roughly consistent with those from the self-consistent Green's function approach, although the equation of state for symmetric nuclear matter from Skχm* remains softer at higher temperatures. Using the ImMDI-GF model in the Hartree-Fock calculation reproduces remarkably well the mean-field potential from the microscopic approaches at various temperatures for both symmetric nuclear matter and pure neutron matter. Our study thus shows that effective interactions with the correct momentum dependence in the mean-field potential, such as the one from the ImMDI-GF model, can properly describe the properties of hot dense nuclear matter and is thus suitable for use in transport models to extract the equation of state of cold nuclear matter, which is needed for describing the properties of neutron stars [8], from intermediate-energy heavy-ion collisions [9,10].

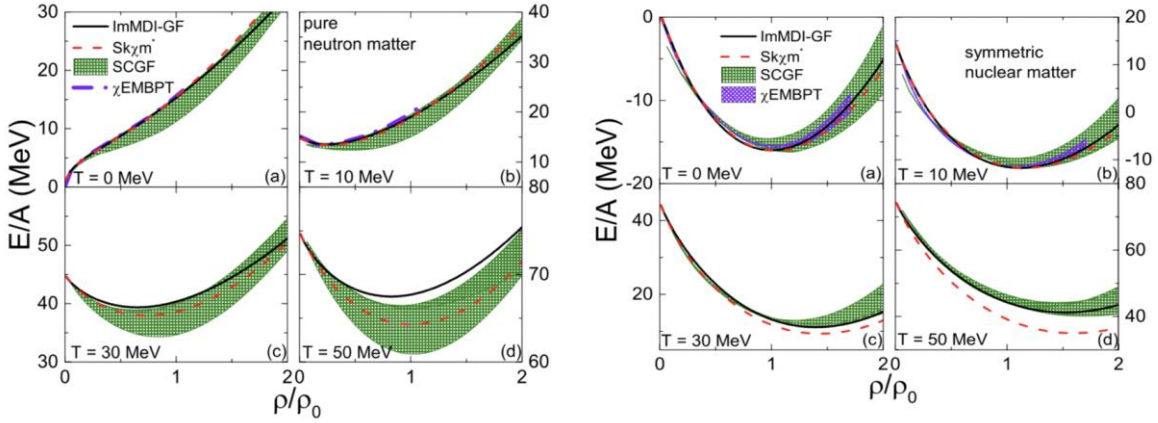

FIG. 1. Total energy per nucleon as a function of reduced nucleon density for symmetric nuclear matter (left window) and pure neutron matter (right window) at various temperatures from ImMDI-GF and Skχm∗ compared with results from the self self-consistent Green's function approach and from the chiral effective many-body perturbation theory using chiral nuclear forces.

[1] C.B. Das, S. Das Gupta, C. Gale, and B.A. Li, Phys. Rev. C **67**, 034611 (2003).

[2] J. Xu, L.W. Chen, and B.A. Li, Phys. Rev. C **91**, 014611 (2015).

[3] Z. Zhang, Y. Lim, J.W. Holt, and C.M. Ko, Phys. Lett. B **777**, 73 (2018); Phys. Rev. C **98**, 054614 (2018).

[4] J. Xu, A. Carbone, Z. Zhang, and C.M. Ko, arXiv:1904.09669 [nucl-th].

[5] A. Carbone, A. Rios, and A. Polls, Phys. Rev. C **90**, 054322 (2014).

[6] C. Wellenhofer, J.W. Holt, and N. Kaiser, Phys. Rev. C **92**, 015801 (2015); **93**, 055802 (2016).

[7] R. Machleidt and D.R. Entem, Phys. Rep. **503**, 1 (2011).

[8] Y. Lim and J.W. Holt, Phys. Rev. Lett. **121**, 062701 (2018).

[9] P. Danielewicz, R. Lacey, and W.G. Lynch, Science **298**, 1592 (2002).

[10] J. Aichelin and C.M. Ko, Phys. Rev. Lett. **55**, 2661 (1985).

Azimuthal angle dependence of the longitudinal spin polarization in relativistic heavy ion collisions

Y. Sun and C.M. Ko

Using the chiral kinetic approach [1-3] with initial phase-space distributions of quarks taken from the AMPT model [4] and their helicities randomly assigned, we have studied the effect of the transverse components of local vorticity field in the transverse plane of a heavy ion collision on the longitudinal spin polarization of quarks along the beam direction [5]. We have found that the quark longitudinal spin polarization depends not only on the longitudinal component of the vorticity field but also on its transverse components due to the resulting axial charge redistribution. Using a constant and isotropic quark scattering cross section of 10 mb, we have obtained a quark longitudinal spin polarization that has an azimuthal angle dependence and amplitude, shown in Fig. 1, similar to those measured in experiments for lambda hyperons by the STAR Collaboration at RHIC [6], as a result of the dominant effect of the in-plane component over those of the out-of-plane component and the longitudinal component of local vorticity field. We have also found that decreasing the quark scattering cross section leads to a reduction of the quark longitudinal spin polarization. Our study thus demonstrates the importance of nonequilibrium effects as well as the local structure of the vorticity field and its time evolution on the spin polarizations of quarks in relativistic heavy ion collisions. This is in contrast to results obtained from assuming local thermal equilibrium of the spin degrees of freedom in the thermal volticity field at the kinetic freeze-out of heavy ion collisions [7,8], which show an opposite sign from the measured azimuthal angle dependence.

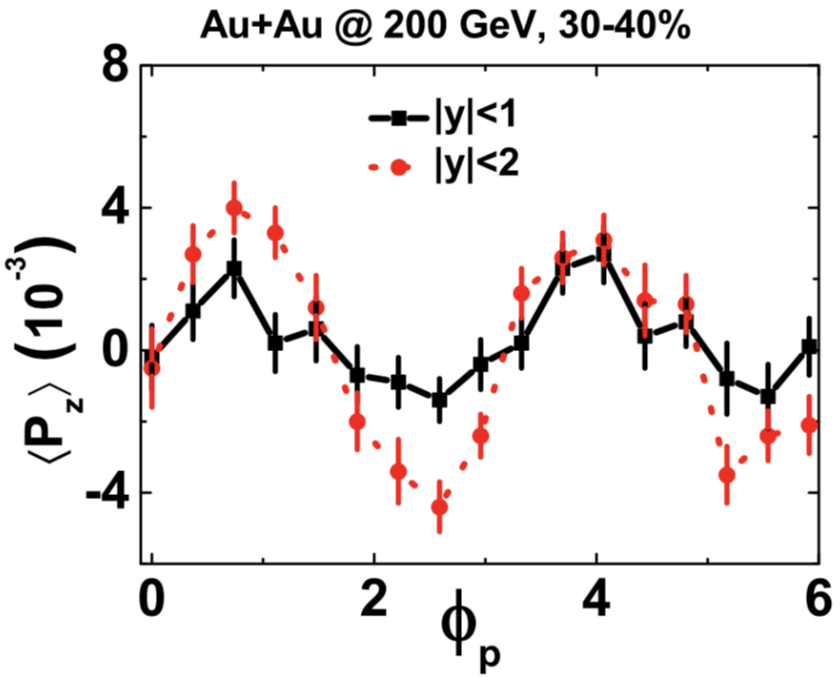

FIG. 1. Average longitudinal spin polarization of strange quarks as a function of azimuthal angle φ_p of the quark momentum in the transverse plane of heavy ion collsions for different rapidity ranges.

[1] Y. Sun, C.M. Ko, and F. Li, Phys. Rev. C **94**, 045204 (2016).
[2] Y. Sun and C.M. Ko, Phys. Rev. C **95**, 034909 (2017).
[3] Y. Sun and C.M. Ko, Phys. Rev. C **96**, 024906 (2017).
[4] Z.-W. Lin, C.M. Ko, B.-A. Li, B. Zhang, and S. Pal, Phys. Rev. C **72**, 064901 (2005).
[5] Y. Sun and C.M. Ko, Phys. Rev. C **99**, 011903(R) (2019).
[6] T. Niida (STAR Collaboration), arXiv:1808.10482.
[7] F. Becattini and I. Karpenko, Phys. Rev. Lett. **120**, 012302 , (2018).
[8] X.-L. Xia, H. Li, Z. Tang, and Q. Wang, Phys. Rev. C **98**, 024905 (2018).

Light nuclei production in Pb+Pb collisions at $\sqrt{s_{NN}}$ = 2.76 TeV

L.L. Zhu,[1] H. Zheng,[2] C.M. Ko, and Y. Sun
[1]*Department of Physics, Sichuan University, Chengdu 610064, China*
[2]*Laboratori Nazionali del Sud, INFN, via Santa Sofia, 62, 95123 Catania, Italy*

Based on an extended blast-wave model, which includes a space-momentum correlation in the phase-space distribution of high momentum nucleons and has its parameters fitted to the measured proton transverse momentum spectrum [1] and elliptic flow [2] from Pb+Pb collisions at $\sqrt{s}$=2.76 TeV for the two centralities of 10-20% and 30-40%, we have used the coalescence model to calculate the transverse momentum spectra and elliptic flows of deuteron and helium-3 [3]. As shown in Fig. 1, our results for deuterons agree with the experimental data from the ALICE Collaboration [4,5]. Although the deuteron

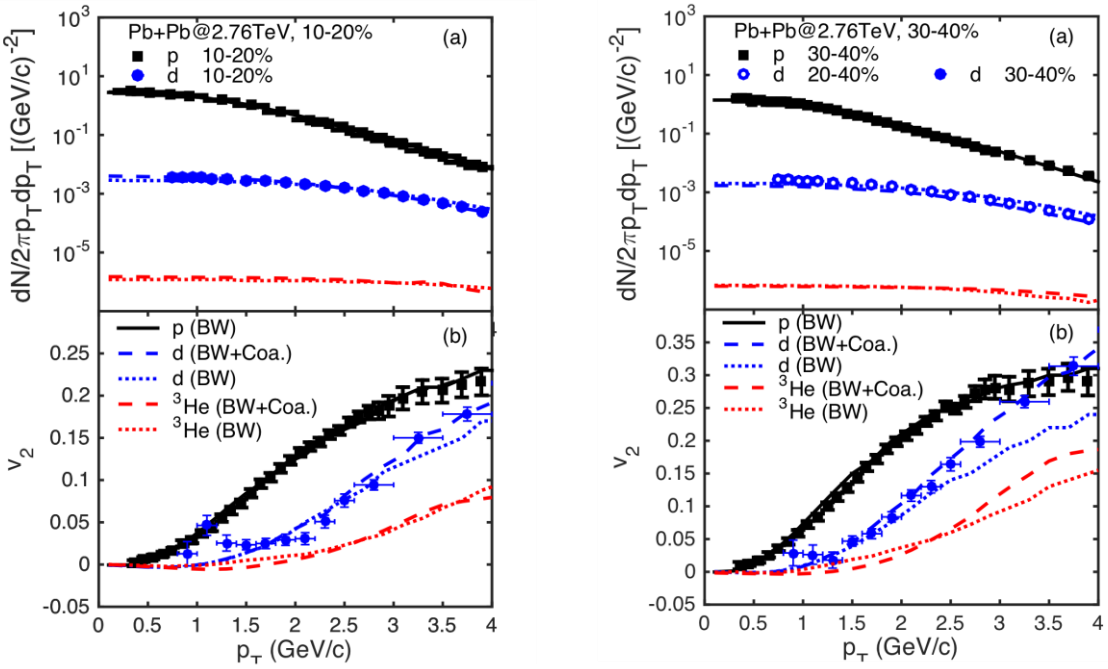

FIG. 1. Transverse momentum spectra and elliptic flows of midrapidity proton (p), deuteron (d) and helium-3 (^{3}He) from the blast-wave model (BW) and the coalescence model (BW+Coa.) for Pb+Pb collisions at $\sqrt{s_{NN}}$ = 2.76 TeV and centrality of 10-20% (left window) and 30-40% (right window). Data shown by black solid squares and blue solid circles for proton and deuteron, respectively, are taken from Ref. [1] and Ref. [4] for their respective transverse momentum spectra, and from Ref. [2] and Ref. [5] for their respective elliptic flows.

elliptic flow obtained from the blast-wave model by using the deuteron mass is roughly consistent with the data within their systematic errors for the centrality of 10-20%, it fails to describe the data at large transverse momentum for collisions at the centrality of 30-40%. A similar difference is found between the helium-3 elliptic flows at large transverse momentum obtained from the coalescence model and the

blast-wave model using the helium-3 mass. These results are similar to those shown previously for the elliptic flows of deuteron and helium-3 in Au+Au collisions at RHIC [6]. Our studies thus demonstrate that light nuclei production can provide the possibility to probe the properties of the emission source of nucleons in relativistic heavy ion collisions, complimenting the study based on the Hanbury-Brown-Twiss (HBT) interferometry of identical particles emitted at freeze-out [7,8] as originally pointed out in Refs. [9,10].

[1] J. Adam *et al.* (ALICE Collaboration), Phys. Rev. C **93**, 034913 (2016).
[2] B.B. Abelev *et al.* (ALICE Collaboration), JHEP **06**, 190 (2015).
[3] L. L. Zhu, H. Zheng, C.M. Ko, and Y. Sun, Euro. J. Phys. A **54**, 175 (2018).
[4] J. Adam *et al.* (ALICE Collaboration), Phys. Rev. C **93**, 024917 (2016).
[5] S. Acharya et al. (ALICE Collaboration) (2017), arXiv:1707.07304 [nucl- ex].
[6] X. Yin, C. M. Ko, Y. Sun, and L. Zhu, Phys. Rev. C **95**, 054913 (2017).
[7] G. Bertsch, M. Gong, and M. Tohyama, Phys. Rev. C **37**, 1896 (1988).
[8] S. Pratt, T. Csorgo, and J. Zimanyi, Phys. Rev. C **42**, 2646 (1990).
[9] S. Mrowczynski, Phys. Lett. B **277**, 43 (1992).
[10] R. Scheibl and U.W. Heinz, Phys. Rev. C **59**, 1585 (1999).

Spectra and flow of light nuclei in relativistic heavy ion collisions at energies available at the BNL Relativistic Heavy Ion Collider and at the CERN Large Hadron Collider

W. Zhao,[1] L.L. Zhu,[1] H. Zheng,[2] C.M. Ko, and H. Song[1]

[1]*Department of Physics, Peking University, Beijing 100871, China*

[2]*Department of Physics, Sichuan University, Chengdu 610064, China*

[3]*School of Physics and Information Technology, Shaanxi Normal University, Xi'an 710119, China*

Using the phase-space distributions of protons and neutrons at kinetic freeze-out from the IEBE-VISHNU hybrid model [1] with AMPT initial conditions [2], we have studied the spectra and elliptic flow of deuterons and helium-3 in relativistic heavy ion collisions at RHIC and LHC in the coalescence model [3]. Results from our coalescence model calculations are found to roughly describe the transverse momentum spectra of deuterons and the differential elliptic flow of deuterons and helium-3 at various centralities in Au + Au collisions at $\sqrt{s_{NN}} = 200$ GeV measured by the PHENIX [4] and the STAR [5] Collaboration as shown in Fig. 1. As shown in Fig.2 and Fig.3, results obtained for Pb+Pb collisions at

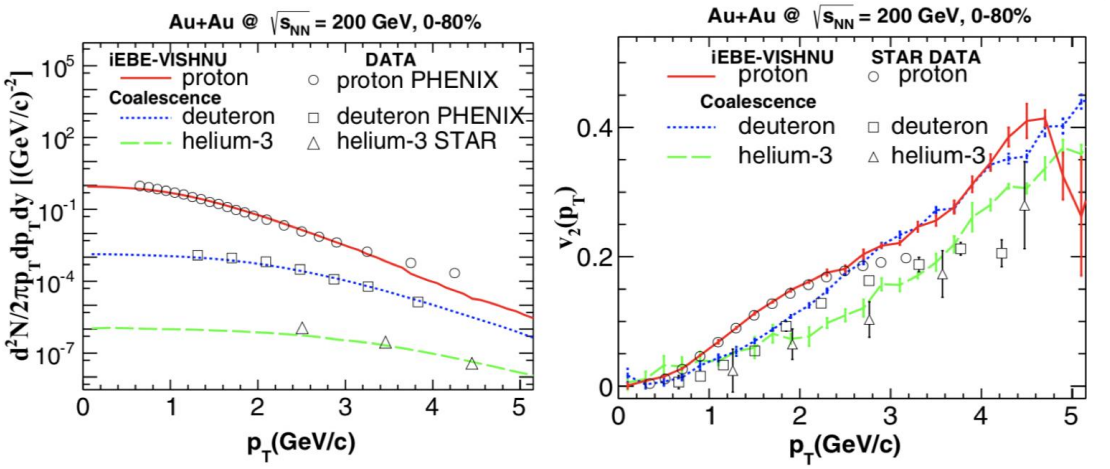

FIG. 1. Transverse momentum spectrum and elliptic flow of protons, deuterons, and helium-3 in Au + Au collisions at $\sqrt{s_{NN}} = \mathbf{200}$ GeV and 0–80% centrality, calculated from IEBE-VISHNU (protons) and from the coalescence model (deuterons and helium-3). The experimental data are taken from the PHENIX [4] and the STAR [5] Collaboration.

$\sqrt{s_{NN}} = 2.76$ TeV and 5.02 TeV at LHC can also describe the data from the ALICE Collaboration [6] except the yield of helium-3 in Pb+Pb collisions at $\sqrt{s_{NN}} = 2.76$ TeV is somewhat underpredicted. The reason for this discrepancy may be due to its earlier formation than the deuteron in collisions at higher energies.

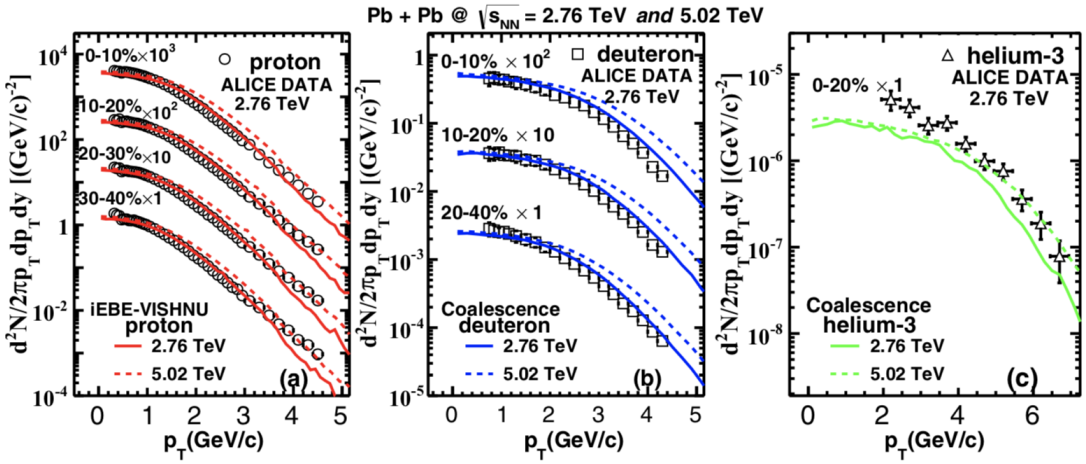

FIG. 2. Transverse momentum spectra of protons, deuterons, and helium-3 in Pb+Pb collisions at $\sqrt{s_{NN}}$ = 2.76 and 5.02 TeV, calculated from IEBE-VISHNU (protons) and from the coalescence model (deuterons and helium-3). The experimental data for protons, deuterons, and helium-3 at $\sqrt{s_{NN}}$ = 2.76 and 5.02 TeV are taken from Ref. [6].

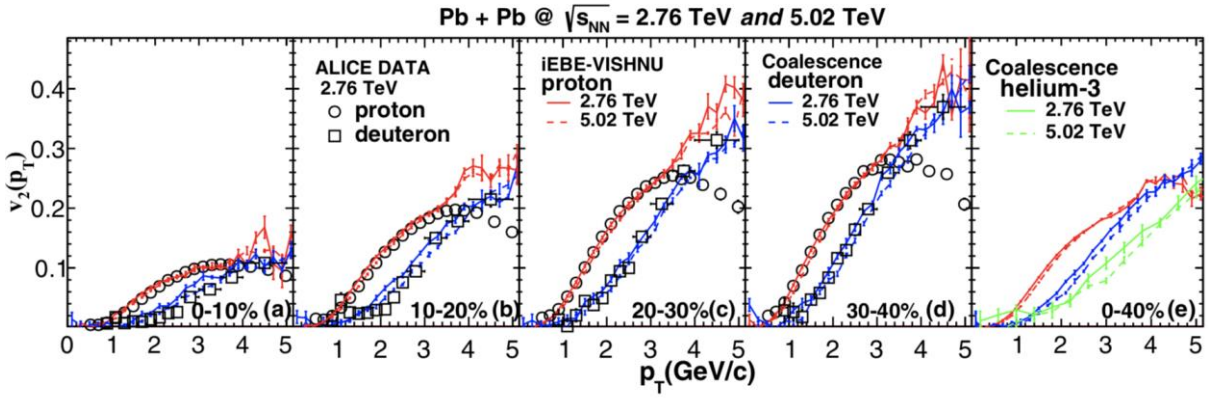

FIG. 3. Same as Fig. 2 for the elliptic flows.

[1] C. Shen, Z. Qiu, H. Song, J. Bernhard, S. Bass, and U. Heinz, Comput. Phys. Commun. **199**, 61 (2016).

[2] Z.-W. Lin, C.M. Ko, B.-A. Li, B. Zhang, and S. Pal, Phys. Rev. C **72**, 064901 (2005).

[3] W. Zhao, L. L. Zhu, H. Zheng, C. M. Ko, and H. Song, Phys. Rev. C, **98**, 054905 (2018).

[4] S.S. Adler *et al.* (PHENIX Collaboration), Phys. Rev. C **69**, 034909 (2004); Phys. Rev. Lett. **94**, 122302 (2005).

[5] B.I. Abelev *et al.* (STAR Collaboration), arXiv:0909.0566; L. Adamczyk *et al.* (STAR Collaboration), Phys. Rev. Lett. **116**, 062301 (2016); Phys. Rev. C **94**, 034908 (2016).

[6] B. Abelev *et al.* (ALICE Collaboration), Phys. Rev. C **88**, 044910 (2013); J. Adam *et al.* (ALICE Collaboration), Phys. Rev. C **93**, 024917 (2016); J. High Energy Phys. **09,** 164 (2016); S. Acharya *et al.* (ALICE Collaboration), Eur. Phys. J. C **77**, 658 (2017).

Pion production in a transport model based on mean fields from chiral effective theory

Z. Zhang and C.M. Ko

We have developed a BUU transport model based on the Skχm* interaction [1], which is constructed from fitting the equation of state and nuclear effective masses predicted by the chiral effective theory as well as the binding energies of finite nuclei [2]. This χBUU model is then used to study the effect of energy conservation in the collision (or decay) kinematics due to baryon mean-field potentials on the equilibrium properties of a N-Δ-π system in a box with periodic conditions [3]. We have found that the inclusion of baryon mean-field potentials in the energy conservation is necessary to maintain the equilibrium state of the N-Δ-π system, and neglecting this effect would significantly decrease the number of pion-like particles but only slightly decrease the effective charged pion ratio. We have also used the χBUU transport model to study pion production in central ^{197}Au + ^{197}Au collisions at the incident energy of E/A = 400 MeV, which was previously studied by us using the relativistic Vlaso-Uehling-Ulenbeck transport model [4,5]. It is found that the χBUU model can well reproduce the experimental measurement by the FOPI Collaboration [6], thus providing an empirical validation of the behavior of nuclear symmetry energy at high density predicted by the Skχm* energy density functional. We have further predicted the pion kinetic energy dependence of π^-/π^+ ratio (left window of Fig.1) and its double and subtract ratio (right window of Fig.1) as well as the isoscaling pion ratio in central collisions (b = 3 fm) of ^{132}Sn + ^{124}Sn and ^{108}Sn + ^{112}Sn at the incident energy of E/A = 270 MeV. Comparing our predictions with future experimental data from the ongoing experiments at RIKEN in Japan by the SPiRIT Collaboration [7] will provide further check on the validity of the Skχm* energy density functional at high density.

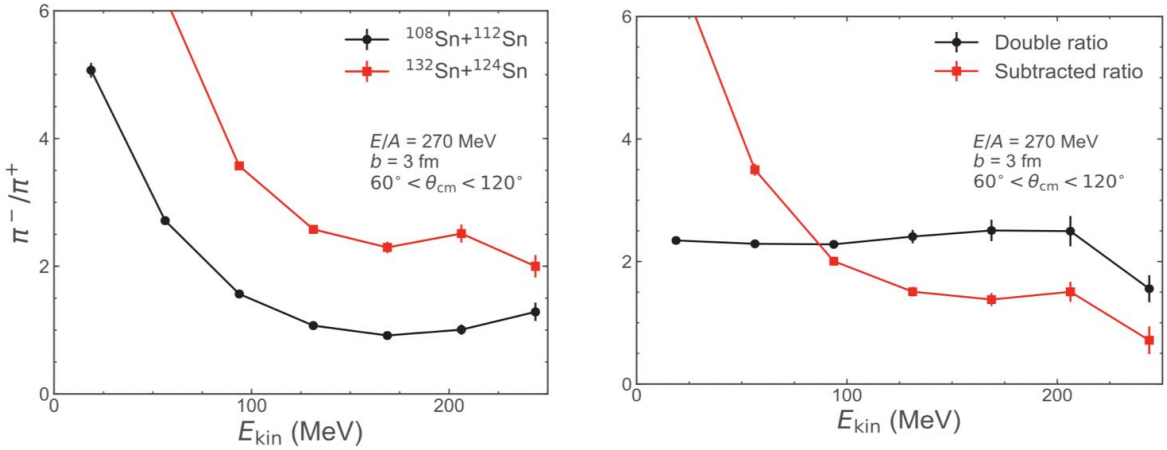

FIG. 1. π−/π+ (left window) and its double $[(\pi-/\pi+)^{132+124}/(\pi-/\pi+)^{108+112}]$ and subtracted $[(\pi-/\pi+)^{132+124} - (\pi-/\pi+)^{108+112}]$ ratios as functions of pion kinetic energy from central (b = 3 fm) collisions of ^{132}Sn + ^{124}Sn and ^{108}Sn + ^{112}Sn at the incident energy of E/A = 270 MeV. The polar angle θ_{cm} of pion momentum is relative to the incident beam direction.

[1] Z. Zhang and C.M. Ko, Phys. Rev. C **98**, 054614 (2018).
[2] Z. Zhang, Y. Lim, J.W. Holt, and C.M. Ko, Phys. Lett. B **777**, 73 (2018).
[3] X. Zhang and C.M. Ko, Phys. Rev. C **97**, 014610 (2018).
[4] T. Song and C.M. Ko, Phys. Rev. C **91**, 014901 (2015).
[5] Z. Zhang and C.M. Ko, Phys. Rev. C **95**, 064604 (2017).
[6] W. Reisdorf, A. Andronic, R. Averbeck, M. L. Benabderrahmane, O.N. Hartmann, N. Herrmann, K. D. Hildenbrand, T.I. Kang, Y.J. Kim, M. Kiš *et al.* (FOPI Collaboration), Nucl. Phys. **A848**, 366 (2010).
[7] M.B. Tsang, J. Estee, H. Setiawan, W.G. Lynch, J. Barney, M.B. Chen, G. Cerizza, P. Danielewicz, J. Hong, P. Morfouace *et al.* (SPiRIT Collaboration), Phys. Rev. C **95**, 044614 (2017).

Suppression of light nuclei production in collisions of small systems at the Large Hadron Collider

K.J. Sun, C.M. Ko, and B. Donigus[1]

[1]*Institut für Kernphysik, Johann Wolfgang Goethe-Universität Frankfurt, Max-von-Laue-Str. 1, 60438 Frankfurt, Germany*

Based on the coalescence model in full phase space, we have studied the dependence of deuteron, heilium-3, and triton production in nuclear collisions at energies available from the LHC on the charged particle multiplicity of the collisions [1]. For the nucleon distributions, they are assumed to come from a thermalized hadronic matter at the kinetic freeze-out of heavy-ion collisions with its temperature taken from the empirical fit to measured particle spectra and its size determined by assuming that the entropy per baryon is independent of the colliding system. We have found that the yield ratios d/p and ^{3}He/p are significantly reduced once the charged particle multiplicity is below about 100 as a result of the non-negligible deuteron and ^{3}He sizes compared to that of the nucleon emission source as shown by solid lines in the left window of Fig. 1. Our results thus provide a natural explanation for the observed suppression of deuteron and ^{3}He production in p+p collisions by the ALICE Collaboration at the LHC [2]. They also demonstrate the importance of the internal structure of light nuclei on their production in collisions of small systems. We have further found that the production of triton is 10%-30% larger than that of helium-3 in p+p collisions because of its smaller matter radius. This enhancement of ^{3}H/^{3}He ratio can be tested in future measurements.

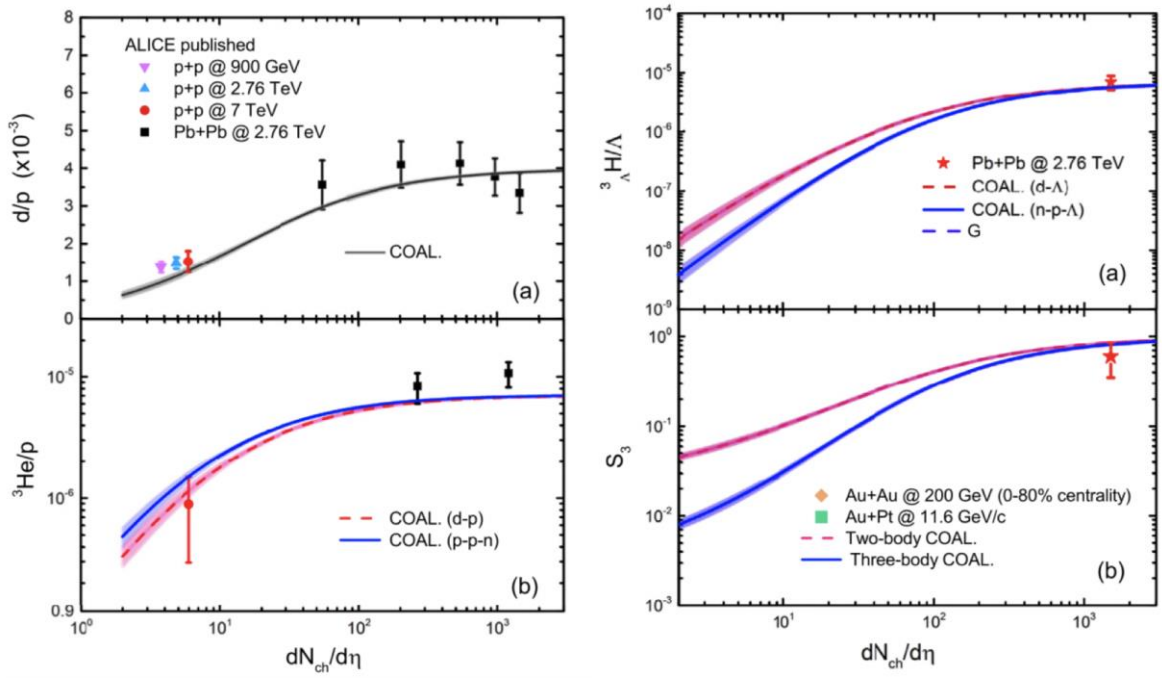

FIG. 1. Charged particle multiplicity dependence of the yield ratios d/p and ^{3}He/p (left window) as well as that of $^3_\Lambda$H/Λ and the strangeness population factor S_3 =^{3}H/(^{3}He×Λ/p) (right window). The lines denote the predictions of coalescence model with theoretical uncertainties on the emission source radius given by the shaded band. Experimental data from the ALICE Collaboration are shown by symbols with error bars [2].

We have also used this model to study the charged particle multiplicity dependence of hypertriton production in Pb+Pb collisions at the LHC by considering both the three-body process of p-n-Λ coalescence and the two-body process of d-Λ coalescence. Because of the much larger ${}^{3}_{\Lambda}$H adius than those of deuteron and ^{3}He, the yield ratio ${}^{3}_{\Lambda}$H/Λ is found to be much more suppressed in collisions with low charged-particle multiplicity, particularly for the three-body coalescence process as shown by solid lines in the upper panel of right window in Fig.1. We have further studied the charged particle multiplicity dependence of the strangeness population factor $S_3 = {}^3\text{H}/({}^3\text{He}\times\Lambda/\text{p})$, and its value in collisions with small charged particle multiplicity is found to be significantly less than one expected in collisions with large charged particle multiplicity as shown by solid lines in the lower panel of right window in Fig.1. Future experimental measurements of the yield ratio ${}^{3}_{\Lambda}H/\Lambda$ and the strangeness population factor S_3 in collisions of low charged particle multiplicity will be of great interest because it not only can check the prediction of the present study but also provide the possibility to improve our knowledge on the internal structure of ${}^{3}_{\Lambda}$H.

[1] K.J. Sun, C.M. Ko, and B. Donigus, Phys. Lett. B **792**, 132 (2019).

[2] B. Abelev *et al.*(ALICE Collaboration), Phys. Rev. C **88**, 044910 (2013); J. Adam *et al.* (ALICE Coolaboration), Eur. Phys. J. C **75**, 226 (2015); Phys. Rev. C **93**, 024917 (2016); Phys. Lett. B **754**, 360 (2016); S. Acharya *et al.* (ALICE Collaboration), Phys. Rev. C **97**, 024615 (2018).

Probing the topological charge in QCD matter via multiplicity up-down asymmetry

Y. Sun and C.M. Ko

Using the chiral kinetic approach [1-3], we have studied the effect of the vorticity field in non-central relativistic heavy ion collisions on the particle multiplicity up–down asymmetry relative to the reaction plane in order to probe the net axial charge fluctuation in the produced partonic matter [4], which is related to the topological charge in QCD [5]. Solving the chiral transport equation in the presence of a self-consistent vorticity field and including the vector charge conserved scatterings among quarks and antiquarks from the AMPT model [6], we have found that the multiplicity up–down asymmetry is sensitive to the net axial charge fluctuation in the partonic matter. As shown in Fig. 1, the ratio between the multiplicity up–down asymmetry event distributions for the cases with finite and zero net axial charge fluctuation is directly related to the inverse of the multiplicity of partons and the net axial charge fluctuation, besides depending on the strength of the vorticity field. The present study is based on the value of p = 0.4 for the ratio of the initial axial charge fluctuation to the total number of quarks in the quark matter. Since the multiplicity up–down asymmetry relative to the reaction plane is proportional to the value of p, measuring its event distribution in non-central relativistic heavy ion collisions thus provides a promising method to probe the net axial charge fluctuation in partonic matter and thus the topological charge in QCD matter.

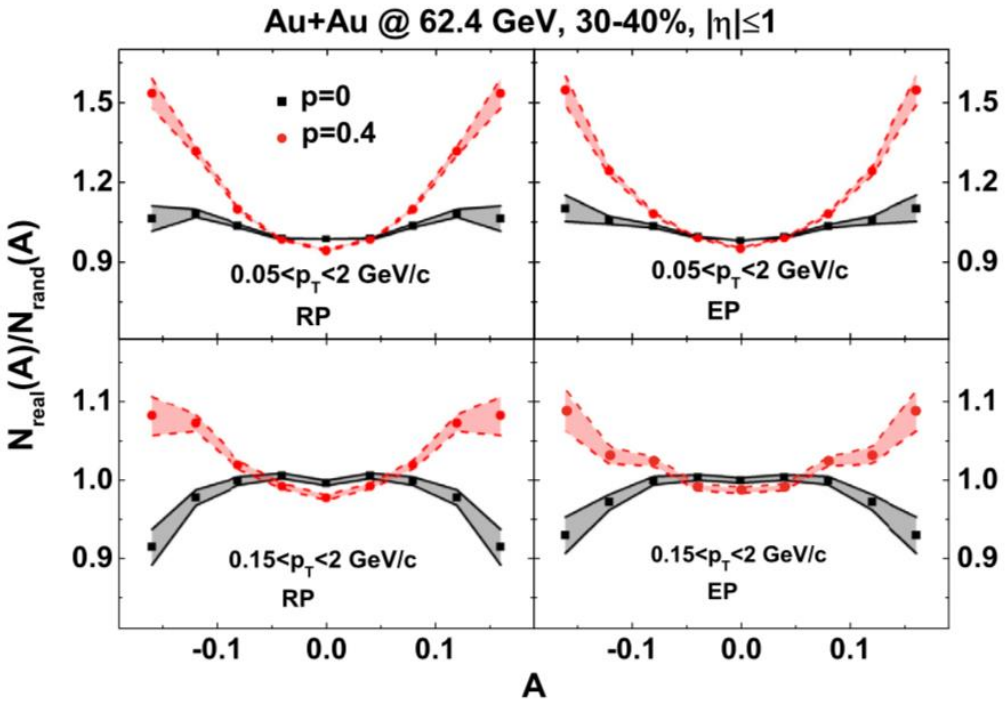

FIG. 1. Ratio of multiplicity up–down asymmetry event distribution $N_{\text{real}}(A)$ to that with random up–down momentum distributions $N_{\text{rand}}(A)$ for mid-pseudorapidity light quarks in different transverse momentum ranges in Au+Au collisions at $\sqrt{s_{NN}}$ = 62.4 GeV and centrality of 30–40%.

[1] Y. Sun, CM. Ko, and F. Li, Phys. Rev. C **94**, 045204 (2016).
[2] Y. Sun and C.M. Ko, Phys. Rev. C **95**, 034909 (2017).
[3] Y. Sun and C.M. Ko, Phys. Rev. C **96**, 024906 (2017).
[4] Y. Sun and C.M. Ko, Phys. Lett. B **789**, 228 (2019).
[5] M. Mace, S. Schlichting, and R. Venugopalan, Phys. Rev. D **93**, 074036 (2016).
[6] Z.-W. Lin, C.M. Ko, B.-A. Li, B. Zhang, and S. Pal, Phys. Rev. C **72**, 064901 (2005).

Shear viscosity of a hot hadron gas

R.J. Fries and Zhidong Yang

Last year we have reported on a the extraction of the specific shear viscosity of hot hadron gas using data from the Relativistic Heavy Ion Collider (RHIC) and the Large Hadron Collider (LHC) [1]. That work had been motivated by the paradigm that quark gluon plasma just above the crossover transition to a hadron gas is a strongly coupled liquid [2]. Its specific shear viscosity η/s has been found to be close to the conjectured lower quantum bound of $1/4\pi$. We do not expect any rapid changes of η/s of nuclear matter as a function of temperature T as it is lowered across the crossover temperature into the hot hadron gas phase. However such a rapid change is predicted by several hadronic transport models.

In [1] we had extracted η/s from the distortion $f \to f + \delta f$ of particle distributions away from equilibrium at freeze-out. These distortions emerge in the presence of shear stress and can be systematically described by a gradient expansion in the Navier-Stokes approximation. We had developed a viscous blastwave for this purpose which is discussed in detail in [1].

In the past year we have improved the values of η/s vs temperature extracted from data by accounting for the systematic bias build into the blastwave approximation in [1]. This was achieved by systematically comparing blastwave fits with relativistic fluid dynamics. Pseudodata generated with viscous fluid dynamics with known freeze-out temperature and specific shear viscosity was compared to

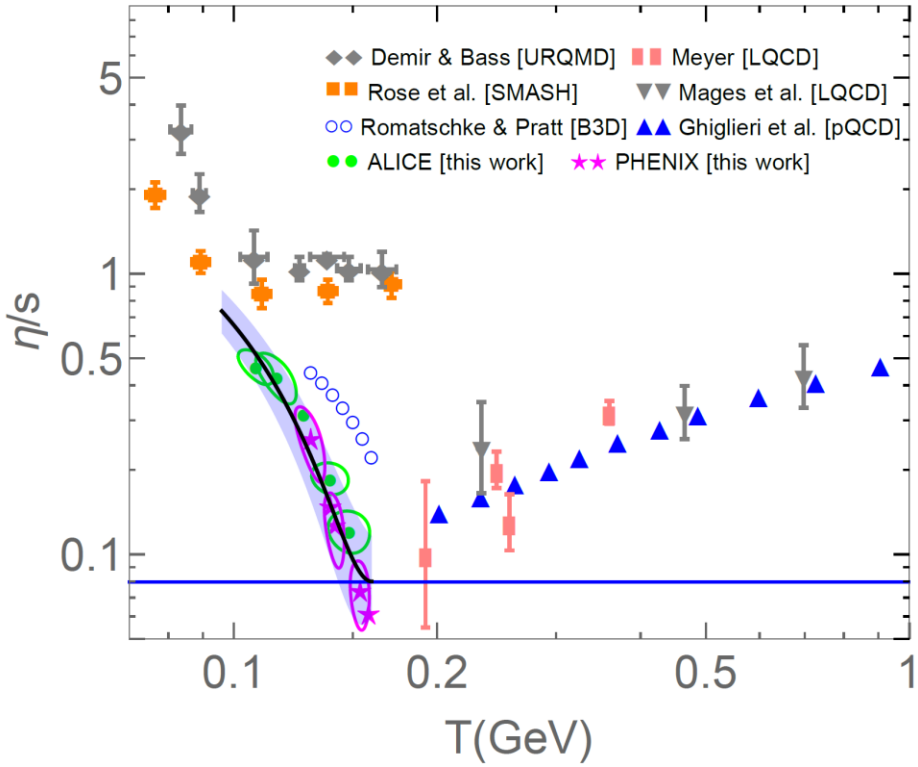

FIG. 1. The specific shear viscosity $\boldsymbol{\eta/s}$ for various temperatures in the hadronic phase extracted from freeze-out data after removal of blastwave bias. Our values are represented by circles and stars with uncertainties indicated by ellipses. For references to the other calculations shown here please see Ref. [1].

the values measured by viscous blastwave fits of the pseudodata. This distortion can be parameterized. Subsequently this map can be used to remove the bias in the temperature and specific shear viscosity extracted from real data using the viscous blastwave [3].

The results of our improved analysis can be seen in Fig. 1 together with values found in the literature calculated by both lattice QCD (for quark gluon plasma) and hadronic transport (for hadron gas). See Ref. [1] for references to the other calculations shown in this figure. We have also improved the analysis of systematic uncertainties in our approach. After removing blastwave bias the specific shear viscosity rises more slowly with dropping temperature.

[1] Z. Yang and R.J. Fries, arXiv:1807.03410.
[2] E. Shuryak, Prog. Part. Nucl. Phys. **62**, 48 (2009).
[3] Z. Yang and R.J. Fries, (in preparation).

Benchmarking the JETSCAPE 1.0 event generator in p+p collisions

R.J. Fries and JETSCAPE Collaborators

The last year has seen rapid progress in the development of the JETSCAPE event generator. In the previous report we have discussed the release v1.0 of the JETSCAPE software package [1,2]. JETSCAPE stands for *Jet Energy-loss Tomography with a Statistically and Computationally Advanced Program Envelope*. It is a collaboration funded with $3.6M through the *Software Infrastructure for Sustained Innovation* (SI2) program of the U.S. National Science Foundation. It involves theoretical and experimental physicists, computer scientists, and statisticians. R. J. Fries has been a PI on the proposal and is representing Texas A&M University in this multi-institutional effort.

Texas A&M was involved in the development and benchmark testing of the PP19 tune of JETSCAPE 1.0 intended to describe several important observables in p+p collisions. Results from p+p collisions are a critically important baseline to interpret results in collisions of nuclei. Often ratios of results in A+A and p+p, with suitable normalization, so called nuclear modification factors, are presented. It is therefore important to establish that the JETSCAPE event generator can describe measured observables in p+p to a degree comparable to established event generators.

In Ref. [3] we describe the PP19 tune in detail. We calculate single inclusive differential jet cross sections, single inclusive charged hadron cross sections, dijet mass cross sections, jet shape observables and jet fragmentation functions at three different center of mass energies, 200 GeV, 2.76 TeV and 7 TeV. We compare to calculations with default PYTHIA 8 [4] and to data from the Relativistic Heavy Ion Collider (RHIC) and the Large Hadron Collider (LHC). As an example we show in Fig. 1 the inclusive

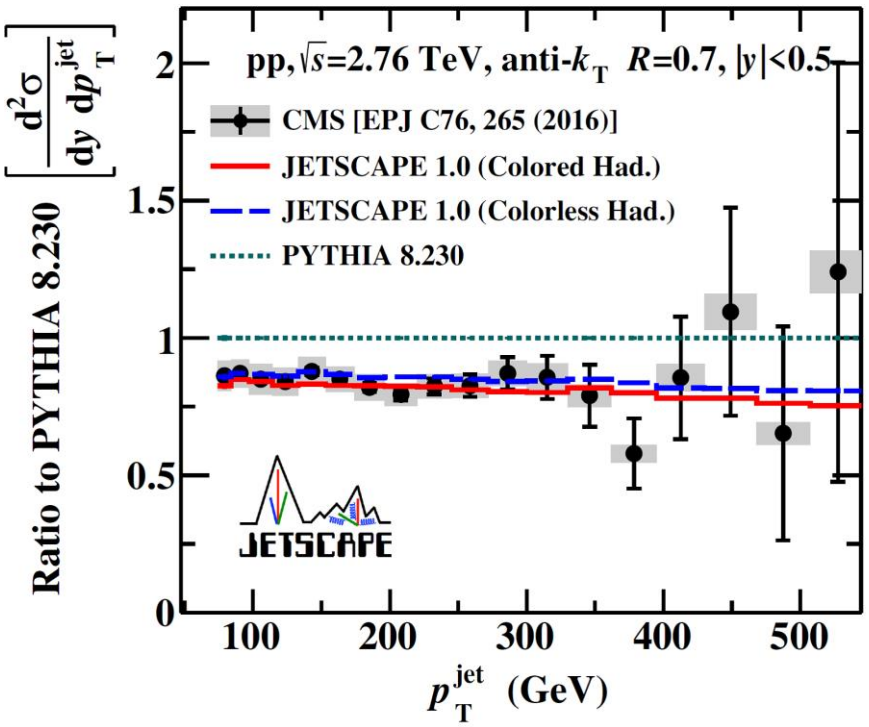

FIG. 1. One example from Ref. [3]: JETSCAPE results with both Colored and Colorless Hadronization and data from the CMS experiment [4] are compared to PYTHIA 8. The calculation was done at 2.76 TeV collision energy for jets with radius R=0.7.

cross section of jets (defined by the anti-*kt* algorithm) with radius R=0.7 at center of mass energy 2.76 TeV. The ratio of JETSCAPE results with two different hadronization options (Colorless and Colored Hadronization), and of data from CMS [4] is taken with respect to a calculation with default PYTHIA 8.

Overall we find that JETSCAPE is describing data on a level comparable to PYTHIA 8. Deviations from data increase at lower momentum and for smaller jet cone sizes, as expected. JETSCAPE does particularly well with single inclusive jet cross sections and jet shape observables. With the p+p baseline established JETSCAPE is ready to be employed in nuclear collisions.

[1] https://github.com/JETSCAPE
[2] J. Putschke *et al*. (JETSCAPE Collaboration), arXiv:1903.07706.
[3] A. Kumar *et al.* (JETSCAPE Collaboration), (in preparation).
[4] T. Sjostrand *et al.*, Comput. Phys. Commun. **191**, 159 (2015)
[5] V. Khachatryan *et al*. (CMS Collaboration), Eur. Phys. J. C **76**, 265 (2016).

Charm-baryon production in proton-proton collisions

Min He and Ralf Rapp

Recent measurements of charm-hadron production in proton-proton collisions [1] at the LHC have found a surprisingly large ratio of Λ_c baryons relative to D mesons, well above expectations from event generators or the statistical hadronization model (SHM) based on known charm-hadron states as listed by the particle data group (PDG). In the present work [2] we revisit the predictions of the SHM by employing a largely augmented set of charm-baryon states beyond the PDG listings, as predicted by the relativistic quark model (RQM) [3] and lattice QCD [4]. The problem of missing baryon resonances is well known from the light- and strange-quark sectors, and even more prominent in the heavy-quark sector where only 6 Λ_c and 3 Σ_c states are firmly established to date. Here, we implement an extra 18 excited states of Λ_c, 42 Σ_c (and further charm-strange baryons), as predicted by the RQM. These states contribute through their strong-decay feeddown to the "prompt" Λ_c production as observed in experiment. We evaluate their abundances using the standard thermal density of states, $n_i = d_i/(2\pi^2)\, m_i^2\, T_H\, K_2(m_i/T_H)$, where m_i is the hadron's mass, d_i its spin-isospin degeneracy and K_2 a modified Bessel function. The only parameter is the hadronization temperature, which we choose in the usual range of T_H=160-170 MeV as extracted from light-hadron production in both *pp* and heavy-ion collisions. For the branching ratios of the excited baryons into final states including a Λ_c, we assume 100% for states below the DN threshold, and a range of 50-100% for states above that threshold. The absolute number of charm hadrons is then fixed by introducing a charm-quark fugacity factor to match the experimentally observed total charm cross section. Several charm-hadron ratios are summarized in Table 1 for the two cases of the input charm-hadron spectrum, i.e., the one listed by the PDG and the one from the RQM, and for two hadronization temperatures. While the various D-meson ratios vary little between the two cases (and agree with experiment), the decisive difference lies in the Λ_c/D^0 ratio which increases by about a factor of 2 upon including the extra RQM states, resulting in fair agreement with the experimental value of 0.543±0.061(stat)±0.160 (sys) measured in 7 TeV *pp* collisions a midrapidity by ALICE [1].

Table I. Ratios of D^+, D^{*+},D_s^+, and Λ_c^+ to D^0 at T_H=170 and 160 MeV (including strong feeddowns) in the PDG and RQM spectrum scenarios.

r_i	D^+/D^0	D^{*+}/D^0	D_s^+/D^0	Λ_c^+/D^0
PDG(170)	0.4391	0.4315	0.2736	0.2851
PDG(160)	0.4450	0.4229	0.2624	0.2404
RQM(170)	0.4391	0.4315	0.2726	0.5696
RQM(160)	0.4450	0.4229	0.2624	0.4409

We have also evaluated the transverse-momentum (p_T) dependence of charm-hadron production, by employing a universal underlying charm-quark spectrum taken from the FONLL framework [5] with pertinent mass-dependent fragmentation functions and associated feeddown kinematics, but with

production weights from the SHM as constructed above. It turns out that the ALICE midrapidity data for the D^0, Λ_c, D^+ and D_s^+ spectra, as well as the Λ_c/D^0 ratio, can all be fairly well described, see Fig. 1 for the former two and the latter. Some discrepancy is found in comparison to the LHCb data [6] at forward rapidity, possibly due to a lower phase space density of light quarks where the applicability of the SHM might be limited.

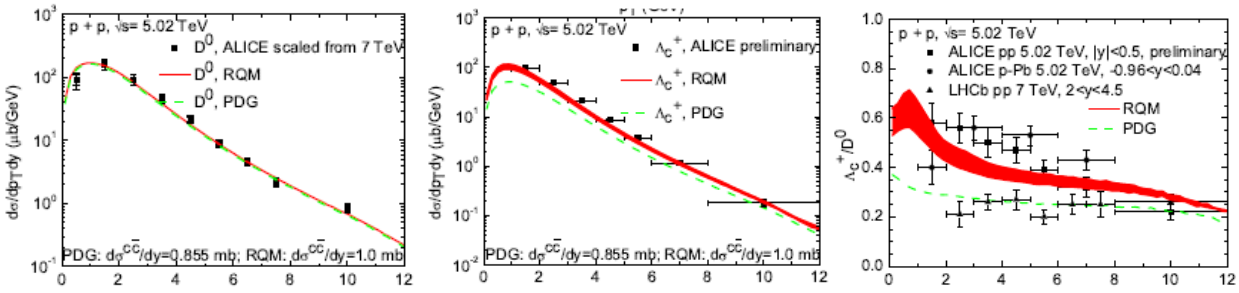

FIG. 1. Transverse-momentum dependence of the prompt D^0(left) and Λ_c (middle) spectra (including strong decay feeddown) and their ratio, compared to ALICE[1] and LHCb data. The bands illustrate the uncertainty in the branching ratios of the charm-baryon resonances.

[1] S. Acharya *et al.* [ALICE Collaboration], JHEP **1804**, 108 (2018).

[2] M. He and R. Rapp, Phys. Lett. B (in press); arXiv:1902.08889.

[3] D. Ebert, R.N. Faustov, and V.O. Galkin, Phys. Rev. D **84**, 014025 (2011).

[4] P. Madanagopalan, R.G. Edwards, N. Mathur, and M.J. Peardon, PoS LATTICE **2014**, 084 (2015).

[5] M. Cacciari, M. Greco, and P. Nason, JHEP **9805**, 007 (1998).

[6] R. Aaij *et al.* [LHCb Collaboration], Nucl. Phys. **B871**, 1 (2013).

Production of lght anti-/nuclei at thermal freezeout in ultrarelativistic heavy-ion collisions

Xinyuan Xu and Ralf Rapp

The production of light atomic nuclei (deuteron, triton, He-3, He-4 and their anti-particles) in ultrarelativistic heavy-ion collisions has posed a puzzle. While their production systematics is well produced by hadro-chemical freezeout at temperatures near the QCD pseudo-critical temperature, T_c ~ 160 MeV, their small binding energies of a few MeV per nucleon suggest that they cannot survive as bound states under these conditions (see Ref. [1] for a recent review). Here [2], we adopt the concept of effective chemical potentials in the hadronic evolution from chemical to thermal freezeout (at typically T_{fo} ~ 100 MeV), which, despite frequent elastic rescatterings in hadronic matter, conserves the effective numbers of particles which are stable under strong interactions, most notably pions, kaons and nucleons. It turns out that the large chemical potentials that build up for anti-baryons [3] result in thermal abundances of light nuclei and anti-nuclei, formed at thermal freezeout, which essentially agree with the ones evaluated at chemical freezeout. We also confirm that their transverse-momentum spectra are consistent with a kinetic decoupling near T_{fo}, which, due to the large transverse flow of the expanding fireball in the late hadronic stage of URHICs, are much harder than those evaluated at chemical freezeout, where the transverse-flow velocity is significantly smaller. Our calculations thus provide a natural explanation for the production systematics of light anti-/nuclei without having to postulate their survival at high temperatures.

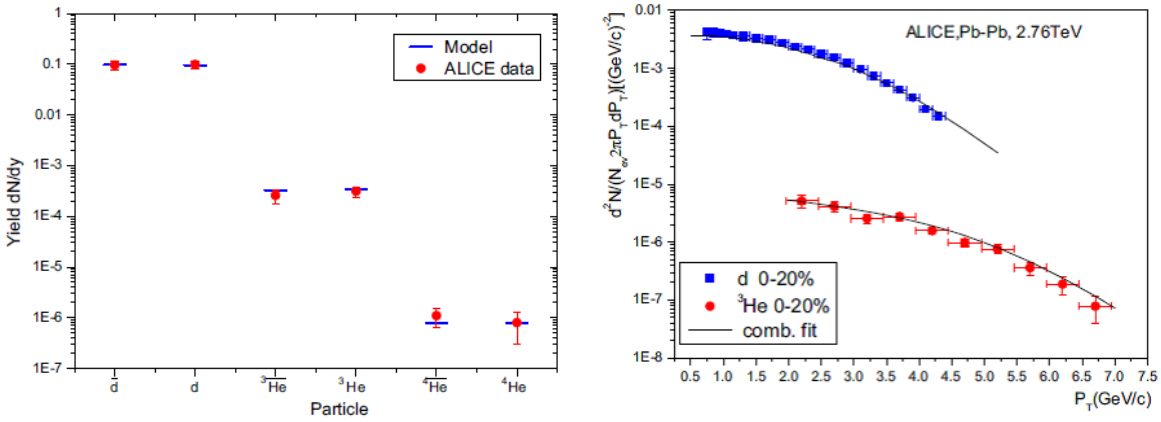

FIG. 1. Production yields of light anti-/nuclei (left panel, with an overall 3-volume adjusted to reproduce the deuteron yield) and pertinent p_T spectra (right panel) calculated at thermal freezeout (T_{fo} = 100 MeV) in 2.76TeV Pb-Pb collisions at the LHC, compared to ALICE data [3].

[1] P. Braun-Munzinger and B. Dönigus, Nucl. Phys. **A987**, 144 (2019).

[2] X. Xu and R. Rapp, Eur. Phys. J. A **55**, 68 (2019).

[3] R. Rapp, Phys. Rev. C **66**, 017901 (2002).

[4] ALICE collaboration, Phys. Rev. C **93**, 024917 (2016); Nucl. Phys. **A971**, 1 (2018).

Extraction of the heavy-quark potential from bottomonium observables in heavy-ion collisions

Xiaojian Du, Shuai Liu, and Ralf Rapp

The in-medium color potential between quarks is a fundamental quantity for understanding the properties of the strongly coupled quark-gluon plasma (sQGP). Heavy quarkonia, whose vacuum spectroscopy is well described by the Cornell potential, have long been recognized as an excellent tool to investigate the color screening of the potential in the QCD medium formed in ultrarelativistic heavy-ion collisions (URHICs). However, the production of charmonia receives large contributions from the recombination of charm quarks, which, while interesting in itself, complicates the originally envisaged suppression signature as a probe of deconfinement. On the other hand, within our previously developed transport approach [1], we have found that the suppression of the ground-state bottomonium state, Υ(1S), is a rather sensitive and robust indication of its in-medium binding energy. Based on this insight, we here [2] deploy our transport approach for the first time in a statistical analysis to extract the color-singlet potential from experimental results on Υ production in URHICs. Starting from a parameterized trial potential, we evaluate the Υ transport parameters and conduct systematic fits to available data for the centrality dependence of ground and excited states at RHIC and the LHC. As an important extra ingredient we account for nonperturbative effects in the Υ dissociation rate guided by open HF phenomenology by utilizing a "K-factor" of at least 5 in the coupling of bottom quarks to the sQGP. Our best fits with their statistical significance represented by a 95% confidence level band are shown in Fig. 1, and the pertinent potentials for selected temperatures in Fig. 2.

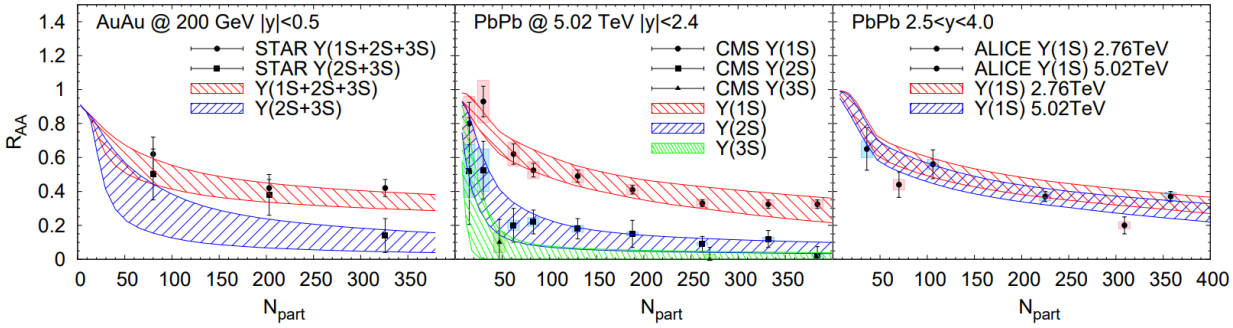

FIG. 1. Bands of 95% confidence level in our fits of Υ R_{AA}'s in the K=5 scenario, compared to Υ(1S +2S +3S, 2S+3S, 1S, 2S, 3S) data from STAR [3] , CMS [4], and ALICE [5] at RHIC and the LHC.

Our results yield a rather strongly coupled potential with substantial remnants of the long-range confining force surviving well into in the QGP. A similarly strong potential was found in previous T-matrix calculations when constrained by lattice-QCD data [6], leading to a small specific viscosity and heavy-quark diffusion coefficient. The remnants of the confining force are therefore identified as the main agent in producing the liquid-like properties of the sQGP.

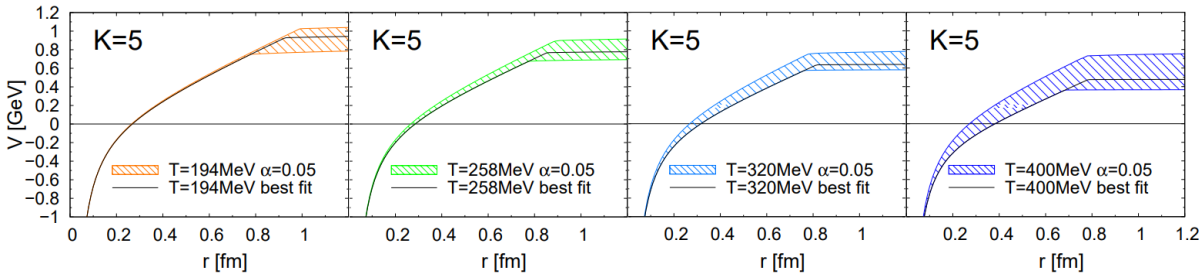

FIG. 2. Best fits (lines) and 95% confidence level bands for the extracted in-medium color-singlet heavy-quark potential at different temperatures (left to right) for K=5.

[1] X. Du, R. Rapp, and M. He, Phys. Rev. C **96**, 054901 (2017).

[2] X. Du, S.Y.F. Liu, and R. Rapp, arXiv:1904.00113; Phys. Lett. B (Submitted).

[3] Z. Ye *et al.* (STAR Collaboration), Nucl. Phys. **A967**, 600 (2017).

[4] A.M. Sirunyan *et al.* (CMS Collaboration), Phys. Lett. B **790**, 270 (2019).

[5] S. Acharya *et al.* (ALICE Collaboration), Phys. Lett. B **790**, 89 (2019).

[6] S.Y.F. Liu and R. Rapp, Phys. Rev. C **97**, 034918 (2018).

Dilepton radiation in heavy-ion collisions at small transverse momentum

M. Klusek-Gawenda, R. Rapp, W. Schäfer, and A. Szczurek

Recent measurements of dilepton production in heavy-ion collisions (HICs) at RHIC and the LHC have become feasible down to ``very low" transverse pair momenta, $P_T < 0.2$ GeV. In this regime one expects an interesting interplay of two main sources: (i) $\gamma\gamma$ fusion triggered by the coherent electromagnetic fields of the incoming nuclei and (ii) thermal radiation from the quark-gluon plasma (QGP) and hadronic phases of the fireball. The former has been established in ultra-peripheral heavy-ion collisions, where no strong-interaction overlap occurs; its spectrum is very soft and concentrated at low P_T. The latter is well established in semi-/central HICs over a wide range of collision energies, with a spectral slope governed by the temperature and the collective flow of the expanding fireball (inducing a blue-shift in the P_T but not in the mass spectra). For $\gamma\gamma$ fusion we utilize initial fluxes from the Fourier transform of charge distributions of the colliding nuclei in the equivalent-photon approximation [1] while for the thermal radiation we employ the emission from the QGP and hadronic phases with in-medium vector spectral functions which describes the mass and P_T spectra (above 0.2 GeV) of the excess radiation observed in HICs over a wide range of collision energies [2].

We have first verified that the combination of photon fusion, thermal radiation and final-state hadron decays gives a fair description of the low-P_T dilepton mass spectra as recently measured by the STAR collaboration in $\sqrt{s_{NN}}$= 200 GeV Au+Au collisions, cf. Fig. 1. The coherent contribution dominates in peripheral collisions, while thermal radiation shows a markedly stronger increase with centrality. As expected, the significance of the coherent contribution in the P_T spectrum is restricted to $P_T < 0.2$ GeV.

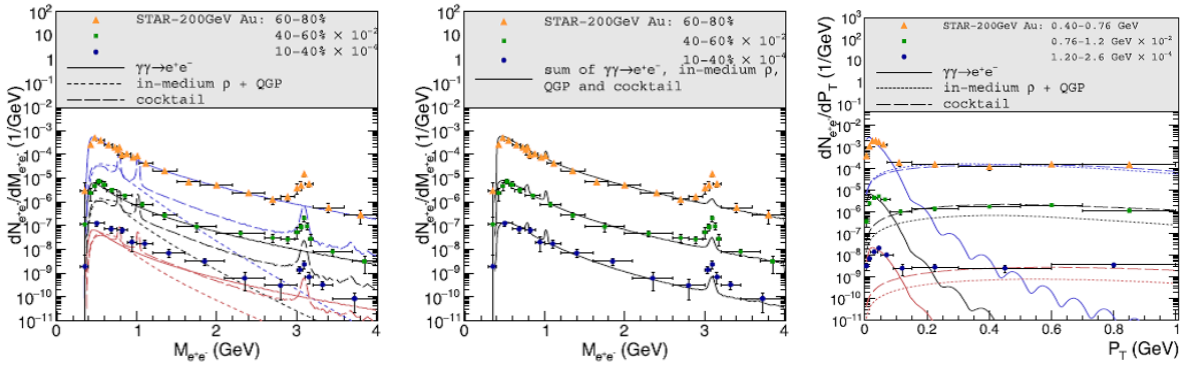

FIG. 1. Dilepton invariant-mass spectra for pair-$P_T < 0.15$ GeV in Au-Au (200GeV) collisions, including experimental acceptance cuts (left panel: individual contributions; middle panel: total) and pertinent P_T spectra in different mass regions (right panel), compared to STAR data [3].

.

We have also performed calculations for HICs over a wide range of collision energies, spanning three orders of magnitude from SPS via RHIC to the LHC regime, see Fig. 2. The resulting excitation function of low-P_T radiation shows that coherent production increases rather sharply at SPS energies and then levels off in the RHIC regime near $\sqrt{s_{NN}}$ =100 GeV, whereas thermal radiation increases more

gradually with collision energy. This leads to a non-trivial excitation function where thermal radiation is dominant at the SPS, $\gamma\gamma$ fusion dominates in peripheral collisions at RHIC, and thermal radiation becomes more important again at the LHC. These predictions will soon be tested at the LHC.

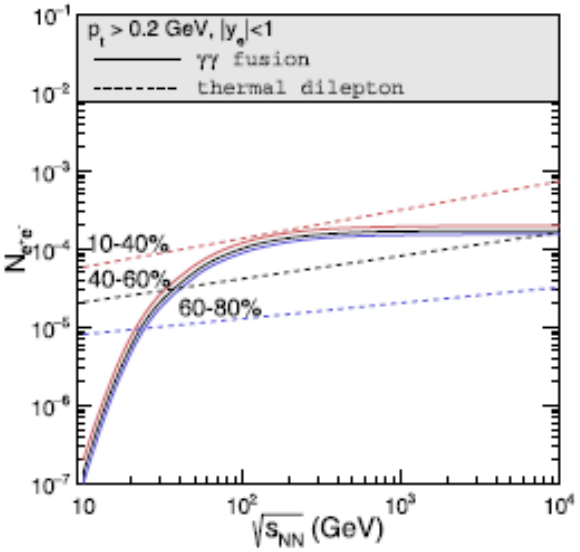

FIG. 2. Excitation function of mass-integrated low-P_T (< 0.15 GeV) dilepton spectra, including acceptance cuts on single-electrons, from the $\gamma\gamma$ fusion mechanism (solid lines) and thermal radiation (dashed lines) in collisions of two heavy nuclei with A~200 at different centralities (color coded).

[1] A. van Hameren, M. Kłusek-Gawenda, and A. Szczurek Phys. Lett. B **776**, 84 (2018).

[2] R. Rapp and H. van Hees, Phys. Lett. B **753**, 586 (2016).

[3] J. Adam *et al.* (STAR collaboration), Phys. Rev. Lett. **212**, 132301 (2018).

Radiative energy loss of heavy quarks in quark-gluon plasma within the T-matrix approach

Shuai Y.F. Liu and Ralf Rapp

When a heavy quark propagates through the quark-gluon plasma (QGP) it can either collide elastically with the thermal constituents or change its trajectory due to an acceleration that triggers the radiation of gluons, similar to the radiation of photons off accelerating electric charges. The radiation is usually concentrated in the forward direction as to slow down the heavy quark. Understanding the transition from collisional to radiative process remains a key challenge in the description of the transverse-momentum spectra of heavy-flavor particles as observed in ultrarelativistic heavy-ion collisions (URHICs). In particular, the importance of non-perturbative interactions in collisional processes in the low-momentum regime has been clearly established now [1].

Here, we extend our previously developed many-body *T*-matrix formalism [2] to study this problem, thereby treating the collisional and radiative contributions within a uniform nonperturbative framework. The theoretical formalism is based on the Kadanoff-Baym equations where the heavy-quark selfenergy in the real-time formalism can be written as

$$\Sigma_Q^>(\omega,\mathbf{p},t) = \int d\tilde{\Pi}\,\delta^{(4)}|M|^2 G_Q^>(\omega',\mathbf{p}')G_g^>(v,\mathbf{k}) = \int d\tilde{\Pi}\,\delta^{(4)}|M|^2\rho_Q(1-f_Q)\rho_g(1+f_g).$$

The $G_{Q/g}^>$ are the Green functions for quarks/gluons, $G_{Q/g}^> = \rho_{Q/g}(1 \pm f_{Q/g})$, where $\rho_{Q/g}$ denotes the pertinent spectral functions and $f_{Q/g}$ the Bose/Fermi distribution functions; *M* is the amplitude for one-to-two processes, i.e., the radiation of a gluon. This selfenergy represents the collisional rate inducing radiation in the medium. To compute the pertinent heavy-quark transport coefficients (friction coefficient or thermalization rate, *A*), an extra angular weight, $(1-\mathbf{p}\cdot\mathbf{p}'/\mathbf{p}^2)$ is required leading to

$$A(p) = \int d\tilde{\Pi}\,\delta^{(4)}|M|^2\rho_Q(1-f_Q)\rho_g(1+f_g)\left(1-\frac{\mathbf{p}\cdot\mathbf{p}'}{\mathbf{p}^2}\right) .$$

The spectral functions of ρ_Q and ρ_q are taken from our previous results within the nonperturbative selfconsistent *T*-matrix formalism (for the so-called strong-binding scenario solution which leads to a strongly coupled QGP). For the "radiation" amplitude *M*, we adopt the perturbative QCD (pQCD) form.

The friction coefficients calculated by above formalism are shown in Fig.1 where we compare several cases with different inputs. Case (1) is a baseline calculation where we use a pQCD Coulomb potential as interaction kernel and only include second order Born diagrams for the T-matrices used to calculate the spectral functions. In case (2), we include an extra confining interaction relative to case (1). For case (3), we further include the all-order resummation of *t* channel diagrams relative to case (2). For case (4), we include additional off-shell effects relative to case (3). In a short, from case (1) to (4), we subsequently account for more nonperturbative effects. As shown in Fig. 1, the friction coefficients generically increase with temperature and momentum, reflecting the opening of the phase space for the radiated gluon. As the temperature and momentum increase, the nonperturbative effects become much

less important. However, at low momentum and temperature, the nonperturbative effects largely enhance the radiative contribution to the friction coefficient. As seen from the ratios shown in the lower panels of Fig. 1, this enhancement can reach up to ~100 times when comparing the full calculations (case 4) to the baseline perturbative calculation (case 1).

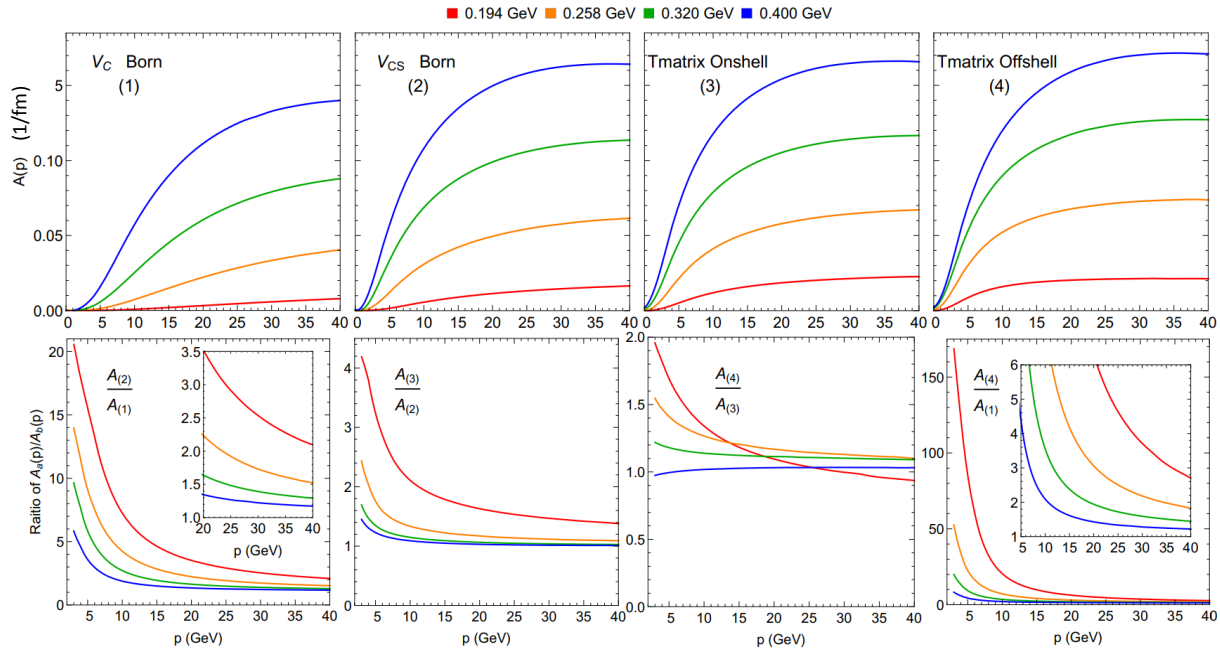

FIG. 1. Upper panels: charm-quark friction coefficients for the four different cases (1) to (4) of increasing nonperturbative effects (from left to right) as discussed in the text. The lower panels show the ratios, $\boldsymbol{A_i/A_j}$, of friction coefficients for adjacent cases (left and 2 middle panels) and for the ratio between case (4) and (1) (right panel).

The nonperturbative theoretical framework to calculate the energy loss caused by radiative processes set up in the present work complements our earlier calculations of collisional energy loss and will help us to achieve a more complete understanding of heavy-quark transport including large momentum scales, and thus arrive at a more comprehensive interpretation of heavy-flavor observables in URHICs.

[1] R. Rapp *et al.* [EMMI Rapid Reaction Task Force], Nucl. P hys. **A879**, 21 (2018).
[2] S.Y.F Liu and R. Rapp, Phys. Rev. C **97**, 034918 (2018).

SECTION IV

SUPERCONDUCTING CYCLOTRON, INSTRUMENTATION AND RIB UPGRADE

K500 operations and development

D.P. May, G.J. Kim, B.T. Roeder, H.L. Clark, and F.P. Abegglen

Introduction

During the 2018-2019 reporting period a total of 28 different beams, including 16 newly developed beams, were used for experiments, and there were a total of 36 beam tunings for these experiments. The SEE program and the radioactive-beam effort are treated separately in this progress report.

Ion Sources

In September germanium was used for the first time in ECR1. Isotopic ^{76}Ge was introduced with the high-temperature oven. During the shutdown ECR1 was opened for examination, and it was found that there had been no further deterioration in the damaged spot that had developed over a plasma flute on the aluminum wall. The plumbing for the water-cooling of the new aluminum plasma chamber has been installed, so the chamber is now ready for final assembly with the new NdFeB permanent magnets.

Cyclotron Beams

New beams of ^{10}B at 4 and 11 AMeV, ^{14}N at 7.2, 11 and 16 AMeV, ^{15}N at 22 AMeV, ^{18}O at 18 AMeV, ^{22}Ne at 6.5 and 26.5 AMeV, ^{30}Si at 24 AMeV, ^{63}Cu at 14, 18 and 22 AMeV, ^{76}Ge at 28 AMeV, ^{109}Ag at 14 AMeV, and ^{208}Pb at 10 AMeV were developed for experiments. The majority of experiments used the 2A line devoted to the recoil spectrometer MARS.

Operations

For the period April 1, 2018 through March 31, 2019, the operational time is summarized in Table I, while Table II lists how the scheduled time was divided. Unscheduled maintenance remained quite low. Scheduled time for outsider users, exclusively SEE customers remained about the same as in the last reporting period.

Table I. 2018-2019 operational time.

Time	Hrs.	%Time
Beam on target	6414	73.4
Beam development	180	2.0
Scheduled maintenance	1552	17.8
Unscheduled maint	590	6.8
Total	**8736**	**100**

Table II. 2018-2019 Scheduled Beam Time.

Time	**Hrs.**	**%Time**
Nuclear physics	2132	32.3
Nuclear chemistry	664	10.1
Outside collaboration	0	0.0
Outside users	3618	54.9
Beam development	180	2.7
Total	**6594**	**100.0**

K150 operations and development

G.J. Kim, B.T. Roeder, F. Abegglen, H.L. Clark, L. Gathings, D.P. May, and H. Peeler

We had another busy year operating the K150 cyclotron. For the reporting period we logged over 3859 hours of beam-on-target and 2772 hours for beam developments, see Table I. Included in the beam-on-target time was 3199 hours (2703 for physics and 496 for chemistry) for in-house science experiments, 396 hours for the SEE tests, and 264 hours for the LLNL-Burke experiments. The big users of the K150 beams were the LIG (light ion guide) project, the Rogachev group, and the SEE tests.

Table I. 2018-2019 operational time.

Time	Hours	% Time
Beam on target	3859	44.2
Beam development	2772	31.7
Scheduled maintenance	2104	24.1
Unscheduled maintenance	1	0.0
Total	8736	100.0

As was in the past years, proton beams from 10.3 to 28.5 MeV were produced for the LIG project throughout the year. In November of 2018, the production of the radioactive species ^{112}In (14.4 minute half-life) from a ^{114}Cd target and subsequent charge breeding and re-acceleration with K500 were investigated. Using the CB-ECR ion source the charge bred ^{112}In^{21+} ions, along with ^{16}O^{3+} which was used as a pilot beam, were accelerated to 14 AMeV from the K500 cyclotron and were then sent to the MARS spectrometer for analysis. The beam switch from ^{16}O^{3+} to ^{112}In^{21+} was accomplished by shifting the K500 RF frequency by +6.5 kHz. The MARS analysis identified the beam as ^{112}In along with two other contaminants (from the ion source) of similar intensities to the ^{112}In; it was verified that the ^{112}In was indeed produced from the LIG gas cell. Thus this 14 AMeV ^{112}In^{21+} became our first accelerated radioactive beam. This test is described in detail in a separate section.

The energies of some beams were limited by the deflector voltage, and we made some progress in better utilizing the deflector to push those beam energies higher. For example, it required 88 kV on the deflector to extract 13.7 AMeV $^{40}Ar^{14+}$ beam in Dec. 2012. Recently we were able to extract a higher 15 AMeV of the same $^{40}Ar^{14+}$ beam with 72 kV. Another example was with the $^{3}He^{2+}$ beam. In June 2018 76 kV was needed to extract a 21.5 AMeV beam, but recently we were able to extract a higher 24 AMeV at much more manageable 64 kV. The deflector consists of a high voltage electrode and a grounded septum and each is positioned independently by moving the entrance and exit pivot points. The gap between the electrode and the septum obviously depends on the positions of the electrode and the septum, and the gap size is not well determined for various possible pivot positions. (A fairly accurate ¼ scale model of the deflector exists, and it is driven at the same time as the deflector, and so the model

would track the positions of the deflector electrode and the septum. Therefore, by measuring the gap on the model, the gap on the deflector may be measured, however, the positions of the deflector parts to that of the model have not been calibrated recently.) A few years ago the deflector gap was measured at one set of pivot settings (pivot #1=50600, #3=50600, #2=49007, #4=52440), and the entrance gap was 6.5 mm and the exit gap was about 14 mm. The first thing that was tried was to close the exit gap (for example: moving only pivot #3 from 50600 to 50900, which would narrowed the exit gap from 14 mm to about 7 mm), and this greatly helped to lower the required deflector voltage. Then, while keeping the entrance and exit gaps tight, the entrance or the exit pivots for the HV electrode and the septum were moved together in or out in trying to improve the extraction efficiency and also to lower the deflector voltage if possible. These efforts have increased the energy for some beams, and in particular, raised the $^{4}He^{2+}$ beam energy up to 24 AMeV with 77 kV on the deflector.

With the improved operation of the deflector, the idea of producing 15 AMeV beams of light to heavy ions on the K150 for SEE experiments became possible. The 15 AMeV beams are heavily used on the SEE experiments on the K500 cyclotron, more so than higher 25 or 40 AMeV beams from the K500. Reallocating some 15 AMeV beams from K500 to K150 cyclotron for some SEE experiments would be useful, as it would free up valuable time on the K500 cyclotron. The SEE testing station is already in place for the K150 cyclotron; the testing station has been used with proton beams for a few years. We intend to develop a number of 15 AMeV beams with ions of charge-to-mass (z/A) around 0.35 from 14 N to 63Cu or 78Kr. The light $^{14}N^{5+}$, $^{20}Ne^{7+}$, and $^{40}Ar^{14+}$ beams have already been accelerated and extracted, and these beams required deflector voltages from 66 to 71 kV. In developing these beams, the main magnet operated above 2000 A for the first time. We still need to develop a heavier beam, such as ^{63}Cu or ^{78}Kr, to complete the 15 AMeV SEE beams for K150. The copper will be run with a sputter fixture mounted inside the ECR2 ion source. Krypton is a gas, and with 3 other gases plus oxygen gas as support gas to handle, a new gas system will be needed for the ECR2 ion source to facilitate beam changes.

In the fall of 2018, the K150 vacuum started to deteriorate, going from $1x10^{-6}$ to ~$4x10^{-6}$ torr. Then the end of 2018, due to small water leaks from cooling lines for the dee stem, the vacuum deteriorated even more and the vacuum attenuation of the beam became more noticeable. To keep the cyclotron running, cooling the cyropanel inside the cyclotron with LN2 was necessary to stabilize the K150 vacuum to about $3x10^{-6}$ torr and it allowed the completion of the scheduled beams to the end of year. During the maintenance period in the early months of 2019, a lot of time and efforts were spent to look for and then patch several small water leaks on cooling lines for the dee stem in the resonator tank. As the access to the cooling lines was very limited under the dee stem cover, it was difficult not only to locate these leaks but the repair was only possible using epoxy, likely a temporary fix. Since the repair of the leaks the K150 vacuum has improved to $7x10^{-7}$ torr, and this agrees with observed improved internal beam transmission. A few other things are planned to improve the vacuum, such as replacing a couple of 8" cryopumps on the dee tanks with 10" pumps, and a complete cleaning of the diffusion pump.

Following the K150 vacuum improvements, several beam development tunes were conducted to test if the lower measured vacuum increased beam transmission in the cyclotron and the beam intensity that could be extracted from the cyclotron. The easiest comparison to make was with the 15 MeV H^-

beam tune that is routinely used for testing the Light Ion Guide. These comparisons for beam tunes before and after the vacuum improvements are summarized in figure 1. In the plot, 15 MeV H^- beam tunes are shown as recorded in November 2015 (blue line), April 2018 (red line) and March 2019 (green line). On these occasions, the K150 measurements were $2.5*10^{-6}$, $3.0*10^{-6}$, and $9.7*10^{-7}$ respectively, and the latter tune from March 2019 was done following the vacuum improvements. In November 2015, the maximum intensity for 15 MeV H^- that could be extracted was 7 µA. For the same beam in March 2019, 24 µA was extracted. Large increases in extracted intensity were also observed for heavy ion beams from ECR2, such as the $^{40}Ar^{11+}$ tune at 6.3 AMeV. More high intensity beam developments tests are planned for the coming year.

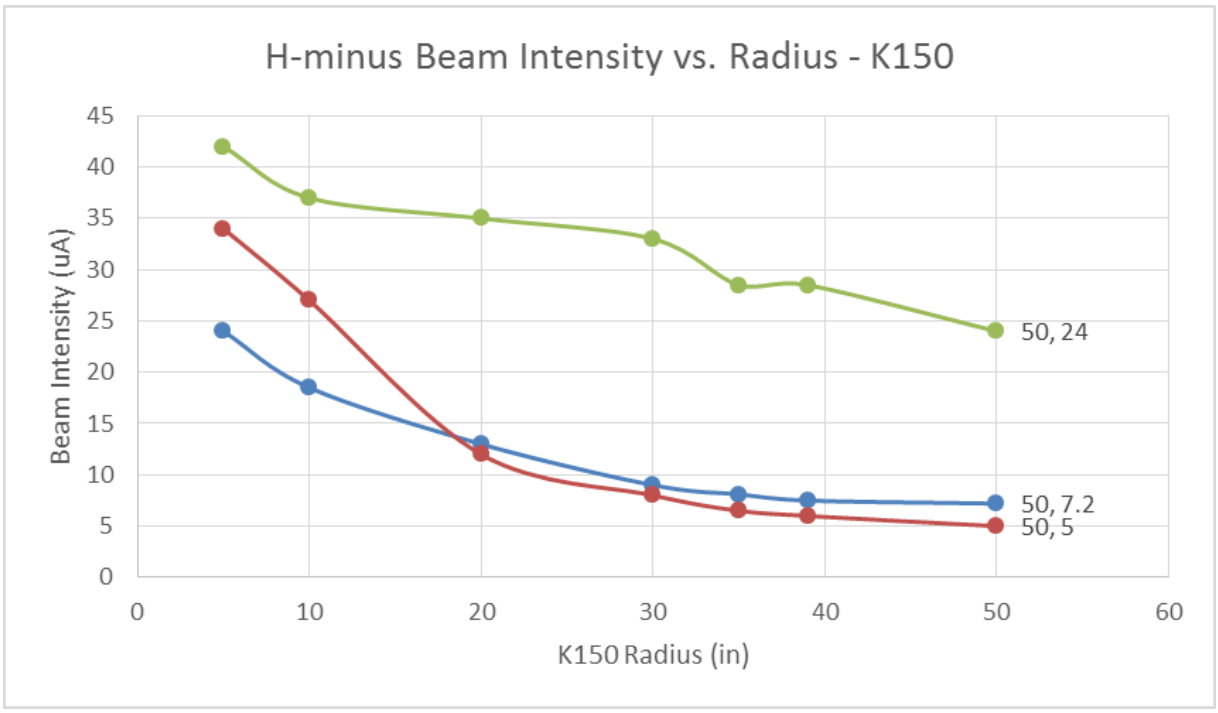

FIG. 1. Plot of beam intensity vs. radius for the K150 cyclotron for the 15 MeV H^- beam. In the plot, the blue data are from the November 2015 tune, the red data are from the April 2018 tune, and the green data are from the March 2019 tune. The radius = 50 inches in the plot represents the extracted beam from the cyclotron. Note that the March 2019 data, shown in green, shows the large improvements in transmission and extracted intensity possible with the improved K150 vacuum. See text for further explanation.

Texas A&M cyclotron radiation effects facility
April 1, 2018 – March 31, 2019

H.L. Clark, J. Brinkley, L. Chen, G. Chubarian, V. Horvat, B. Hyman, H.I. Park, B. Roeder, G. Tabacaru, and J. Thomas

The activity of the Radiation Effects Facility (REF) decreased only slightly over the previous reporting year. In this reporting period, the facility was used for 3,678 hours, which is a 0.1% decrease over the 3,681 hours used in the 2017-2018 reporting period and is the second highest usage year ever. Users of the facility (and hours used) over the past year were: Boeing Satellite Systems (436), Sandia National Lab (204), Intersil (194), NASA JPL (192), Honeywell (182), SEAKR (166), Air Force (155), Radiation Test Solutions (145.5), Texas Instruments (144), Microchip (129), Thales Alenia Space (129), Troxel Engineering (104), International Rectifier (102), Northrop Grumman (86.75), Raytheon (83), Airbus (80), Analog Devices (80), Microsemi (80), Cobham (71), VPT Inc (66), BAE Systems (64),

Table I. Radiation effects facility usage by commercial and government customers for this and previous reporting years.

Reporting Year	Total Hours	Commercial Hours (%)	Government Hours (%)
2018-2019	3678	2939(80%)	739(20%)
2017-2018	3,681	2,622 (71%)	1,059 (29%)
2016-2017	3,355	2,501 (75%)	854 (25%)
2015-2016	3,042	2,326 (76%)	716 (24%)
2014-2015	3,024	1,975 (65%)	1,049 (35%)
2013-2014	2,399	1,517 (63%)	882 (37%)
2012-2013	2,626	1,856 (71%)	770 (29%)
2011-2012	2,673	1,630 (61%)	1,043 (39%)
2010-2011	3,042	1,922 (63%)	1,121 (37%)
2009-2010	2,551	1,692 (66%)	859 (34%)
2008-2009	2,600	1,828 (70%)	772 (30%)
2007-2008	2,373	1,482 (62%)	891 (38%)
2006-2007	2,498	1,608 (64%)	890 (36%)
2005-2006	2,314	1,314 (57%)	1,000 (43%)
2004-2005	2,012	1,421 (71%)	591 (29%)
2003-2004	1,474	785 (53%)	689 (47%)
2002-2003	1,851	1,242 (67%)	609 (33%)
2001-2002	1,327	757 (57%)	570 (43%)
2000-2001	1,500	941 (63%)	559 (37%)
1999-2000	548	418 (76%)	131 (24%)
1998-1999	389	171 (44%)	218 (56%)
1997-1998	434	210 (48%)	224 (52%)
1996-1997	560	276 (49%)	284 (51%)
1995-1996	141	58 (41%)	83 (59%)

Naval Surface Warfare Center (64), Space X (61), Johns Hopkins (60), Assurance Tech Corp (56), NASA GSFC (56), Aria Labs (48), TRAD (48), Freebird (42), Millennium (40.5), Lockheed Martin (36), Teledyne DALSA (32), Astranis (31), MIT Lincoln Labs (23), CFD Research Corp (21), CoolCad (21), Applied Technology Associates (16), Ball Aerospace (16), JD Instruments (16), Trusted Semiconductor Solutions (16), Crossfield Technologies (15), Signal Analysis (14), Crane AE (12), GSI Technologies (8), HIREX (8), Martin Materials (8), NASA JSC (8), and OnSemi Conductor (8). New users included OnSemi Conductor, Microchip, Crane AE, Assurance Tech Group and Applied Technology Associates.

Table I compares the facility usage by commercial and government customers. While commercial hours still dominate, the ratio from this reporting year (80% to 20%) is similar to usage from the 2017-2018 reporting period (see Fig 1). Commercial hours increased by 12% and government hours decreased by 30%. 15 AMeV ions were the most utilized and especially 15 AMeV Au. No new beams were added to SEELine users list. Much of the testing conducted at the facility continues to be for defense systems by both government and commercial agencies. Almost 16% (474 hours) of the commercial hours were for foreign agencies from Japan, France and Germany. It is expected that the facility will continue to be as active in future years.

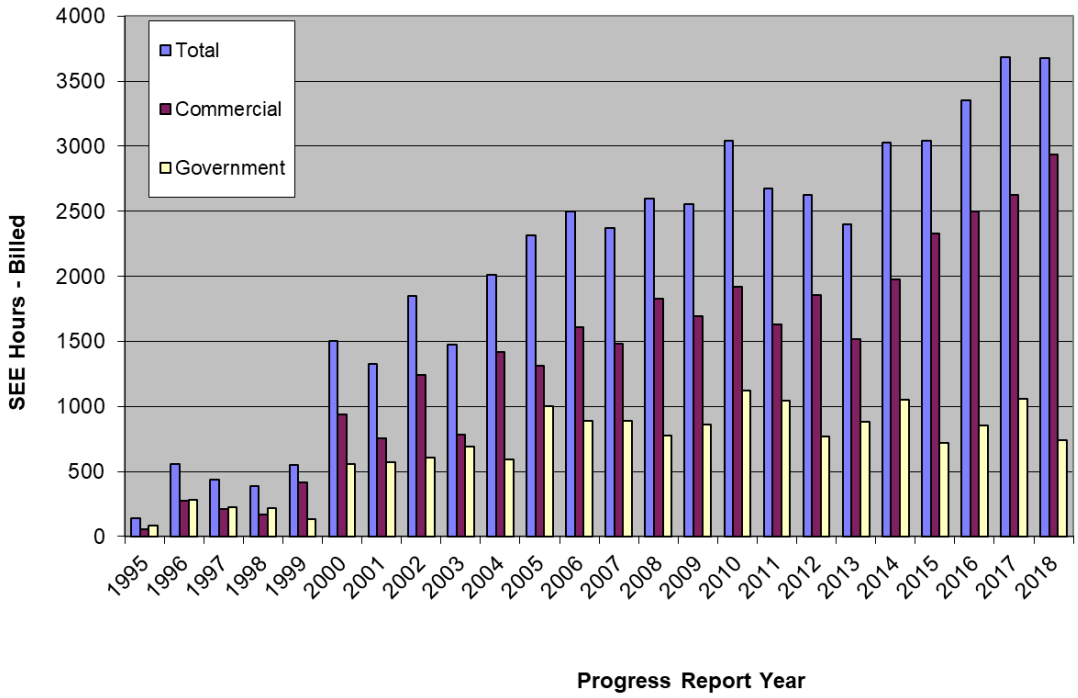

FIG. 1. Radiation Effects Facility usage by commercial and government customers for this and previous reporting years. While commercial hours still dominate, the ratio from this reporting year (80% to 20%) is similar compared to usage from the 2017-2018 reporting period. Almost 16% (474 hours) of the commercial hours were for foreign agencies from Japan, France and Germany.

Texas A&M cyclotron K150 radiation effects facility
April 1, 2018 – March 31, 2019

H.L. Clark, B. Hyman, and J. Thomas

Many updates have been made to the K150 Radiation Effects Facility during this reporting period, including a new data room and setup area and improvements to the backscatter detector system for high flux dosimetry measurements.

A data room and staging area have been constructed for use with the K150 Radiation Effects beamline. The new data room and setup area are located on the second floor between the K150 hi-bay and the office side of the Cyclotron Institute building. The data room is positioned above the entrance to the K150 vault allowing for short cabling distances between user equipment operated in the data room and their devices under test (DUTs). A patch panel has been installed in the data room with a companion patch panel located near the end of the beam line in the K150 vault. The panels include two DSUB-9 serial connections, two DSUB-25 serial connections, four usb 2.0 connections, ten BNC signal cable connections (RG-58), four BNC video cable (RG-59) connections, and five RJ45 jacks (CAT6 cable) (Fig. 1). The room is equipped with seven monitors, four for video feeds and three for customer computer

FIG. 1. Network, computer, and data patch for communication between K150 Data Room, K150 Radiation Effects Beamline, and the Control Room.

use. Work tables and chairs are also provided for testing needs (Fig. 2). A supply of USB, BNC, HDMI, and CAT6 cables of various lengths are also available if needed. Two cameras have been installed and integrated into our video system. For safety, these are viewable in the K150 control room. Fourteen hardwired network connections have been installed so that customers can connect to our computer network. Wireless network connections to the TAMULINK network are also available if needed.

A small staging area has been set up just outside the south exit of the new data room. This area is used to accommodate customers who need space to prepare their DUTs or just a place to work outside of the data room. The area has three workbenches (with overhead lights) and includes a stocked tool box and equipment cabinet. Carts for transporting equipment between the staging area and the K150 vault are also provided (Fig. 2). A refrigerator, microwave oven, and coffee maker are also provided for customer use. A new secured door was installed for access to the freight elevator located in the office side of the building. This allows for equipment to be moved between the data room and the K150 vault as needed.

FIG. 2. (Top) Full view of the inside of the K150 Data Room. (Bottom) K150 Radiation Effects Staging Area. Carts and extra chairs for larger testing groups. The entrance of the K150 Data Room. Work surfaces with overhead work lights, Shop-Vac, tool box, and equipment cabinet.

Improvements have also been made near the beam line in the K150 vault. Space for customer equipment and beam line access has been cleared by removing a beam pipe storage rack and equipment shelf. The sister patch panel to the data room patch panel has been mounted on the north wall near the

in-air positioning system. A toolbox containing 80/20 extrusions and hardware has been added for custom DUT mounting requirements. The cart used for computer access to our SEUSS positioning software has been relocated to the right side of the beam line.

Updates to beam line components have been made to help dosimetry accuracy and reduce residual radioactivity along the beamline. A new, thinner aluminum 4”-diameter beam collimator was installed directly in front of the beam line isolation valve. This collimator is designed to reduce beam exposure to the stainless steel valve. The collimator was thinned to minimize beam scattering along the inside circumference. A second 4”-diameter beam collimator has been installed between shutter #1 and the beam viewer to help reduce unanticipated irradiation on the backs and sides of the backscatter detectors. Extra aluminum shielding has been placed around the backscatter detector holders for additional protection. Material for shutter #2B has been changed from aluminum plate to conductive carbon with an aluminum support. This has been done to reduce the residual radioactivity of the beamline and prevent the inadvertent measuring of this radiation by the backscatter detectors.

These improvements and additions to the K150 Radiation Effects Facility should make testing at our facility more convenient, comfortable, and safer for our customers as the use of the facility increases moving forward.

Recent progress on the ECR4 ion source

D.P. May, S. Molitor, F.P. Abegglen, H. Peeler, and R. Ohlsen

Progress on the new 6.4 GHz ECR4 ion source has been somewhat slow in this reporting period, but plans for final installation are now underway. Most significantly, plumbing for water-cooling has been fitted to and mounted on the new ECR4 plasma chamber as well as for the new ECR1 plasma chamber (Fig. 1). Also, the assembly of the Glaser lenses has been completed (Fig. 2).

The scheme for the placement of the ECR4 ion source and injection line has been laid out next to ECR1. The power supplies, transmitters, stands and injection-line elements will soon be brought into place. The plasma chamber is still to be fitted with its permanent magnets and then inserted into the coil-and-yoke assembly before final positioning.

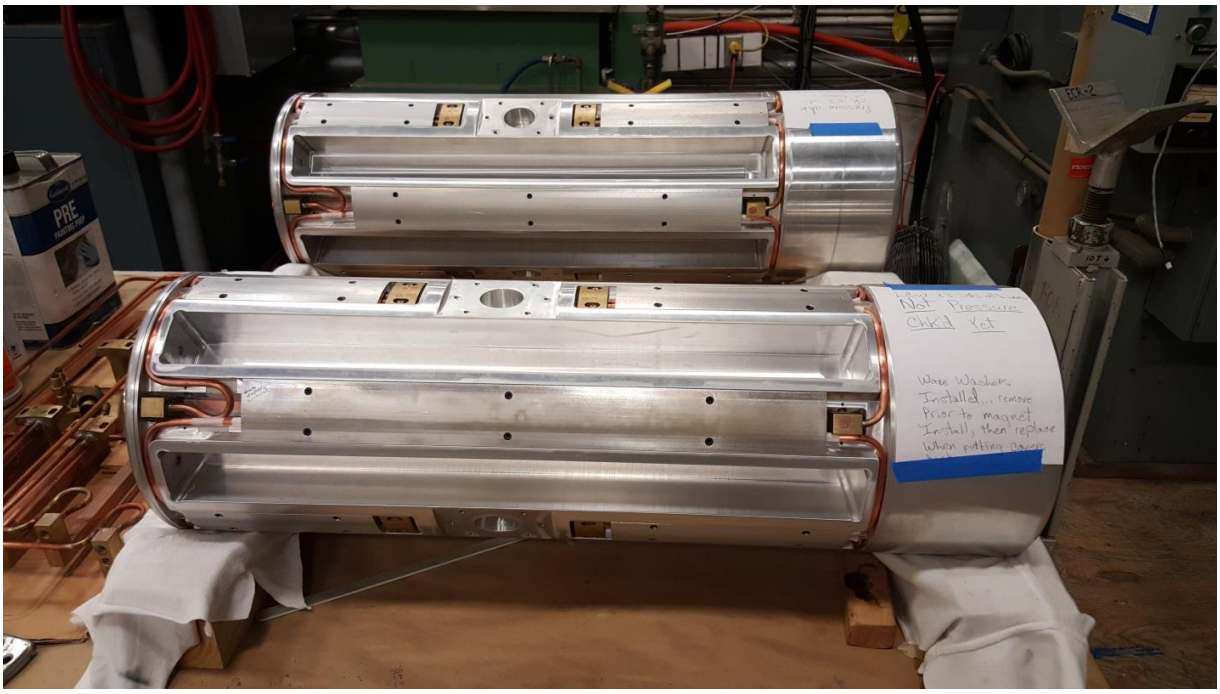

FIG. 1. Plasma chambers for ECR4 and ECR1 with water-cooling channels.

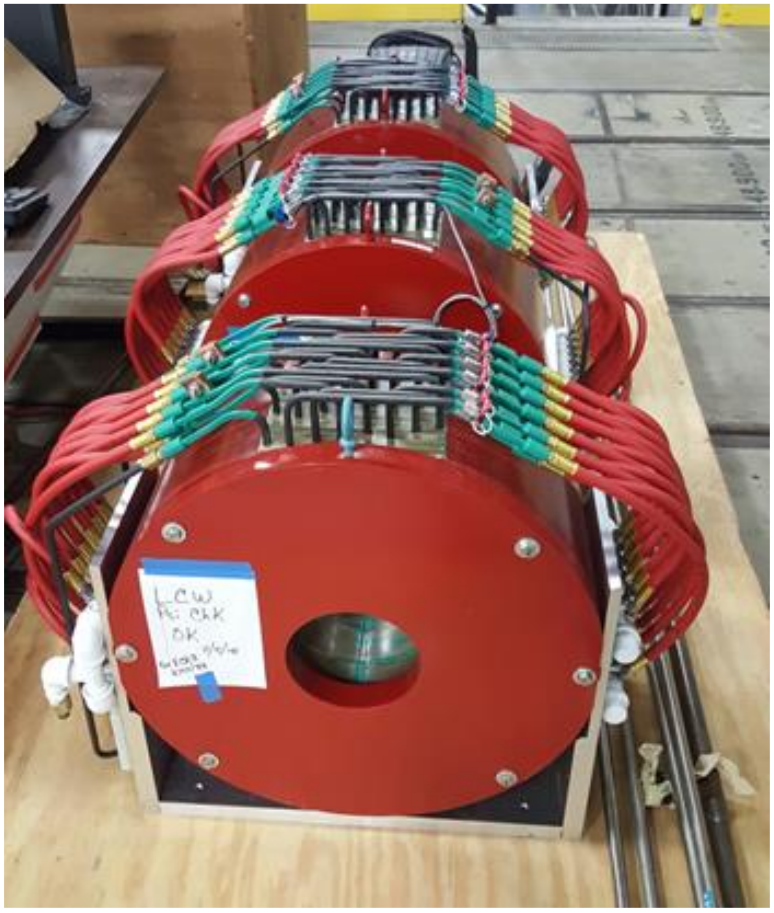

FIG. 2. Glaser lenses.

Light ion guide - a new approach

G. Tabacaru, J. Ärje, D.P. May, A. Saastamoinen, F.P. Abegglen, G.J. Kim, S. Molitor, and B.T. Roeder

Introduction

Accel-decel injection from the light-ion guide (LIG) target cell to the plasma chamber of the charge-breeding ECR ion source (CB-ECRIS) was studied intensively in the previous reporting period [1]. A number of radioactive ion beams were developed for acceleration by the K500 cyclotron as summarized below:

Reaction studied	History
^{58}Ni(p,n)^{58}Cu	$^{58}Cu^{14+}$ was separated with a total yield of 21 ions/μC.
^{27}Al(p,n)^{27}Si	$^{27}Si^{5+}$ first time observed and separated with a very low efficiency 0.03 ions/μC.
^{64}Zn(p,n)^{64}Ga	Multiple experiments were performed on this reaction. $^{64}Ga^{17+}$ had a total yield of approximately 62 ions/μC. Contaminants in CB-ECRIS made it impossible to separate radioactive ^{64}Ga after acceleration.
^{64}Zn(p,d)^{63}Zn	Radioactive $^{63}Zn^{17+}$ was separated and an attempt to accelerate was made. Contaminants from CB-ECRIS (^{63}Cu) made it impossible to clearly identify radioactive ^{63}Zn after acceleration.
^{114}Cd(p,n)^{114}In	$^{114}In^{19+}$ was separated with an estimated charge-breeding efficiency of 1%.

These results were clearly disappointing. However, the previously reported study of direct injection via a 40 cm long rf-only, sextupole ion guide (SPIG) [1] demonstrated much higher efficiency for charge-breeding of ions produced by an alkali button source, so the decision was made to attempt direct injection via SPIG from the LIG target chamber to CB-ECRIS.

Direct injection from LIG to CB-ECRIS

A SPIG system with 5 sections and approximately 2.5 m long, spanning the distance from the LIG target-cell to the plasma chamber entrance of CB-ECRIS, was installed in the chambers of the existing transfer line with the purpose of simplifying injection and increasing the efficiency of charge-breeding ions coming from the target cell (Figs. 1 and 2). The dividing of the SPIG into sections allowed for the efficient bypassing of the helium gas from the target cell into pumps along the line such that no elevated pressure from the helium flow through the target cell could be detected in the chamber immediately before CB-ECRIS injection.

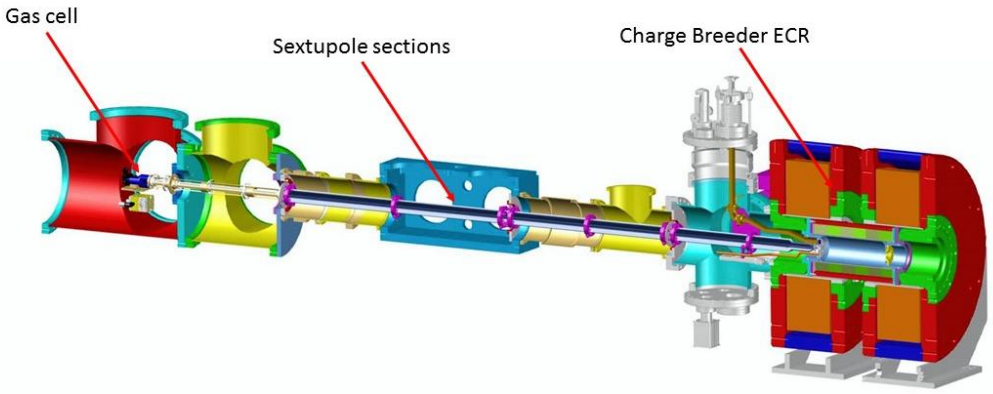

FIG. 1. View of the new SPIG injection system.

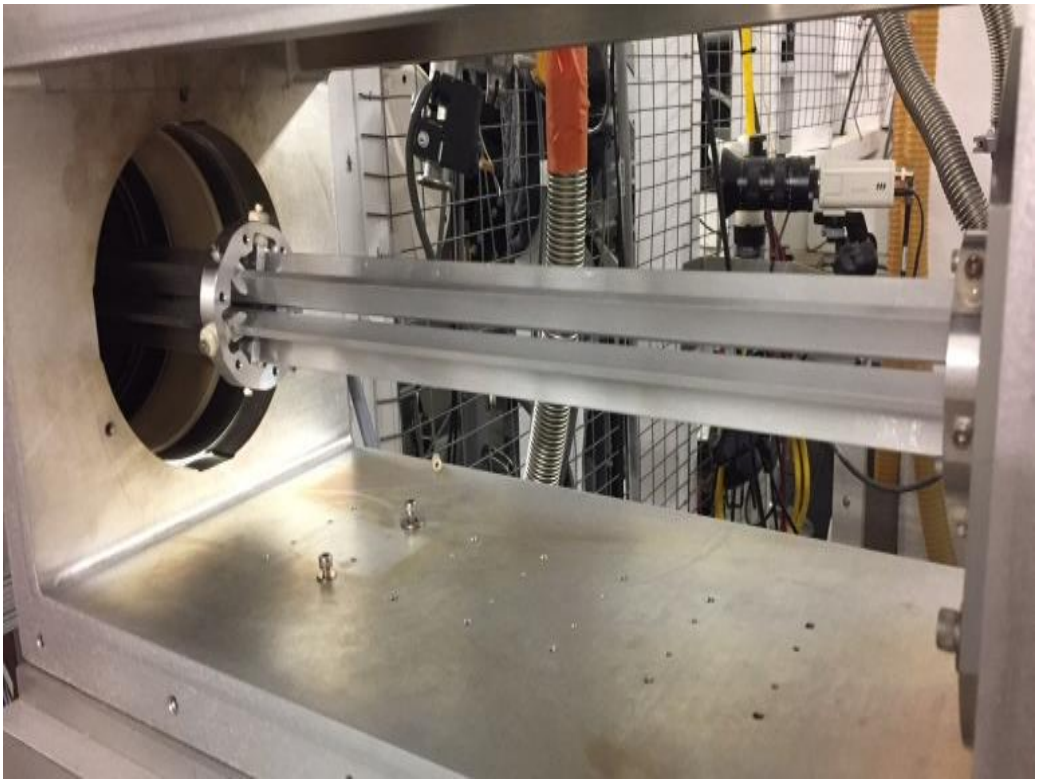

FIG. 2. Middle section of the SPIG.

The first experiment made with this new injection system was the charge-breeding of Cs 1^+ ions from an alkali source. The charge-breeding efficiency was high, estimated to be approximately 50%. The charge-state distribution of Cs peaked around 24^+, 25^+ and 26^+ (Fig. 3).

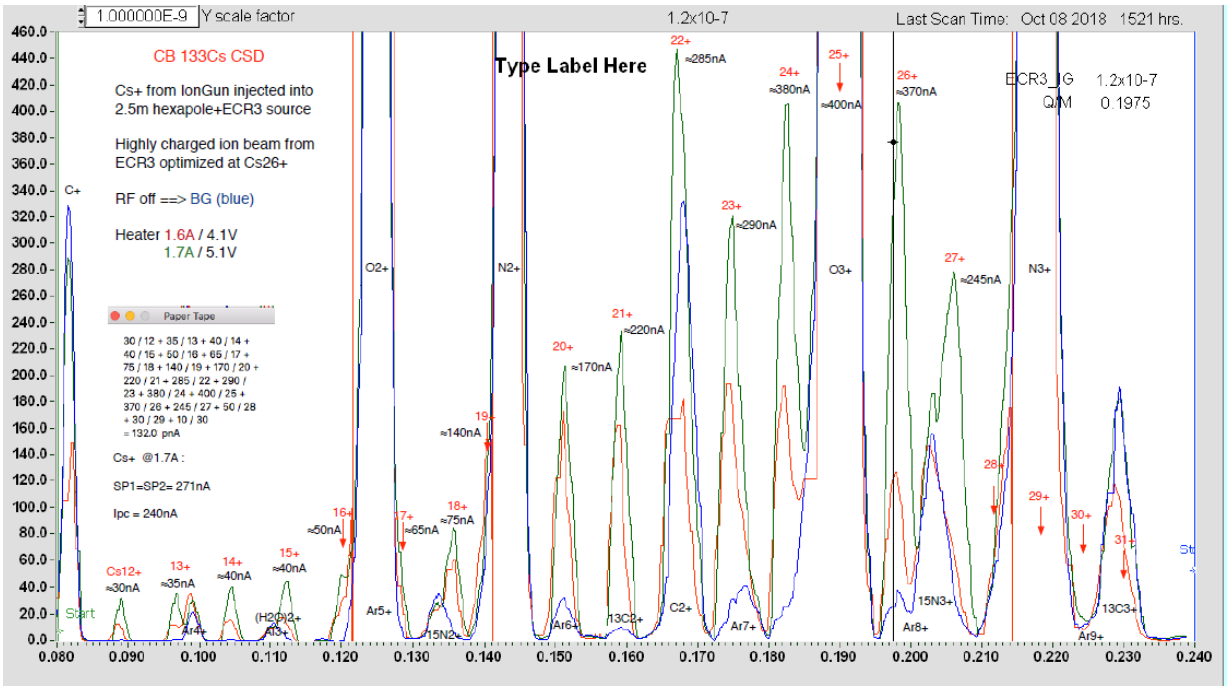

FIG. 3. Scan of the charge-state distribution in the CB-ECRIS with red labels showing locations of the Cs peaks.

Next a ^{228}Th radioactive source was used to test the system using helium gas. Alpha particles from the radioactive products ^{220}Rn and ^{216}Po of various charge states were detected. The charge-breeding efficiency was very high, estimated to be around 50 % as well. The operation of the entire apparatus was stable and the results were reproducible for the entire period of the experiment.

The next step in the development of the light-ion guide was the use of the proton beam to produce radioactive ions injected in CB-ECRIS via the new SPIG. The first reactions used were ^{114}Cd(p,n)^{114}In and ^{114}Cd(p,3n)^{112}In. The maximum outputs of ^{114}In and of ^{112}In were approximately 600 ions/μC and 900 ions/μC, respectively. The ion $^{112}In^{21+}$ was successfully accelerated by the K500 Cyclotron, as reported elsewhere in this progress report. Lighter nuclei production was attempted in the next campaigns: production of ^{64}Ga, ^{63}Zn, ^{90}Nb, ^{58}Cu, and ^{46}V. The most successful production was ^{64}Ga, ^{63}Zn, and relatively ^{90}Nb. Acceleration of ^{63}Zn could not be verified due to the high contamination with ^{63}Cu (stable) in the injected beam from the CB-ECRIS. Production of ^{58}Cu and ^{46}V was low and further investigations should be performed.

Conclusions

Direct injection via SPIG is proving to be a good method to increase the charge-breeding efficiency of ions coming from the light-ion guide. However, some of the inconsistencies in the operation

need to be further studied and understood. Future work will be focused on resolving the irregularities in the operation and on the development of the lighter radioactive products. Fitting the SPIG into the existing transfer line has resulted in making alignment and servicing difficult and time consuming. In an effort to solve this problem, a new chamber is now being designed specifically for the SPIG. It will incorporate a single, long port through which the SPIG can easily be removed, or inserted and aligned. Also, room for diagnostics with a possible moveable section of the SPIG is being considered.

[1] G. Tabacaru *et al.*, *Progress in Research*, Cyclotron Institute, Texas A&M University (2017-2018), p. IV-10.

Identification of ^{112}In: First re-accelerated radioactive light-ion guide beam

B.T. Roeder, F. Abegglen, J. Arje, G.J. Kim, A. Saastamoinen, and G. Tabacaru

This year, following the installation of a 2.5m long Sextupole Ion Guide (SPIG) upstream of the CB-ECRIS, the first charge-bred and reaccelerated radioactive beam from the Light Ion Guide project was realized. Leading up to the attempt to re-accelerate the ions through the K500, $^{114}In^{19+}$ from $^{114}Cd(p,n)^{114}In$ with 10 MeV protons from the K150 cyclotron was observed after the CB-ECRIS at a rate of ~1200 decays/sec per μA of proton beam on the LIG target. This represented a large improvement over previous results. However, following the re-acceleration of ^{114}Cd ions last year [1], it was noted that a reaction product with different mass than the production target was needed. ^{112}In is produced from the same ^{114}Cd target with high cross section if the proton beam energy is increased to 28 MeV [2].

The experiment was carried out in a similar way as the previous experiments to measure ^{85}Rb, ^{64}Zn, and ^{114}Cd from the CB-ECR [1,3,4]. To calibrate the detectors at the focal plane of the Momentum Acromat Recoil Separator (MARS) [5], a beam of ^{109}Ag at 14 MeV/u was accelerated with the K500 cyclotron and was transported to the target chamber of MARS. The ^{109}Ag beam impinged on a thin ^{12}C stripper foil that was 47.7 μg/cm^2 thick. The stripper foil removed electrons from the beam such that the resulting charge states of the beam could be tuned through MARS at rigidities calculated with the LISE++ model of MARS [6,7]. Once each charge state was tuned through MARS, it was measured at the focal plane with detectors consisting of a ΔE-E silicon telescope. The ΔE detector was a 64 μm thick, position sensitive silicon strip detector and the E detector was a single pad detector that was 500 μm thick. The type and thicknesses of the detectors were chosen such that the ^{109}Ag, and also the desired ^{112}In, could be detected and identified using their energy loss in the silicon detectors and their position at the MARS focal plane. During the calibration, charge states 38+ and 39+ for ^{109}Ag were measured. An average energy of 1502 ± 2 MeV was observed by calculating the beam energy based on a prior calibration of the MARS D1 dipole field and comparing the energy deposits in the silicon telescope for each charge state. An excellent energy resolution of about 10 MeV FWHM was obtained for the ΔE detector which allowed for the identification of individual elements with the same mass.

To search for ^{112}In ions that had been accelerated by the K500, first a pilot beam of $^{16}O^{3+}$ at 14 MeV/u was tuned through the K500 cyclotron. The charge-to-mass ratios (Q/M) for $^{16}O^{3+}$ and $^{112}In^{21+}$ are 0.18758 and 0.18768 respectively. Taking into account that the percent change in the charge to mass ratio here is +0.053%, to shift the frequency for $^{16}O^{3+}$ to $^{112}In^{21+}$ corresponding to $\Delta Q/\Delta M \approx 0.00010$, a frequency shift of about +6.5 kHz was expected. However, it was also noted in the ^{85}Rb experiment that the $^{16}O^{3+}$ pilot beam could still be observed as much as 12 kHz away from the optimum frequency. As a result, it was expected that both $^{16}O^{3+}$ and $^{112}In^{21+}$ would be transported to the MARS target chamber simultaneously despite the slight change in the frequency of the K500 cyclotron. But, after being stripped with the thin carbon stripper foil, the ^{112}In for the charge states where the Q/M were different would be cleanly separated in rigidity from the ^{16}O pilot beam.

The ^{112}In ions were produced by bombarding a thin, enriched ^{114}Cd target with about 2 μA of 28 MeV protons from the K150 cyclotron. The ^{112}In ions, produced from the $^{114}Cd(p,3n)^{112}In$ reaction, were

stopped in pure He gas and transported by the Light Ion Guide (LIG) [6] to the CB-ECR. Inside the CB-ECRIS, the ions were charge-bred in the plasma to $^{112}In^{21+}$ ions. Since $^{16}O^{3+}$ is also extracted from the CB-ECRIS with the same extraction voltage and magnet settings as the $^{112}In^{21+}$ ions, the $^{16}O^{3+}$ was used as a pilot beam to develop the tune from the CB-ECRIS through the K500 cyclotron and eventually to MARS. Then, once the $^{16}O^{3+}$ beam was tuned to the entrance of MARS, the frequency of the K500 cyclotron was shifted +6.5 kHz (to optimize for the $^{112}In^{21+}$) to begin the search for the re-accelerated ions.

MARS was tuned with magnetic rigidity settings optimized to observe the ^{112}In in charge states 34+ though 41+ as predicted by the LISE++ charge stripping models. The magnetic rigidity of MARS was set with the currents on the magnets as determined by the LISE++ model of MARS [7,8]. The ΔE vs. E spectrum obtained with MARS set to measure the $^{114}In^{38+}$ after the stripper foil is shown in Fig. 1. Particles with Mass 112 dominate the spectrum and $^{112}In^{38+}$ is visible in the Mass 112 group. ^{112}Cd and ^{112}Sn, likely originating from CB-ECRIS plasma chamber contamination, were also present. A few other ions with Q/M ≈ 3/16, similar to the $^{16}O^{3+}$ pilot beam, were also observed.

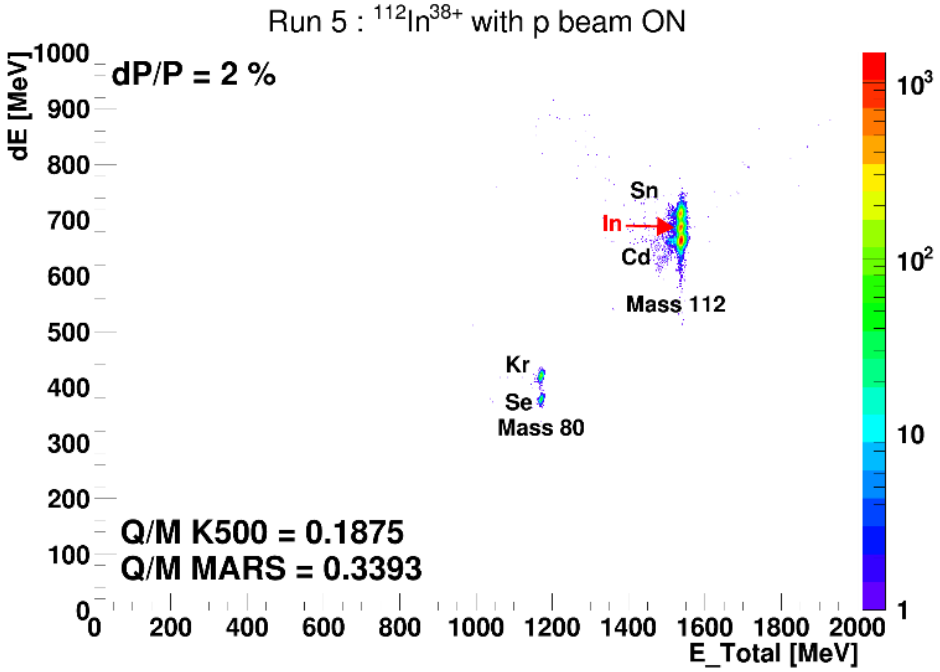

FIG. 1. Energy Loss (ΔE) vs. Total Energy spectrum obtained for the $^{112}In^{38+}$ MARS tune.

Measurements were conducted with the proton beam "on" and "off" the LIG target for 3 minutes each. Some results of these measurements are shown in Fig. 2 for the $^{112}In^{39+}$ setting. The peak corresponding to ^{112}In disappears if the K150 proton beam is stopped while the others remain. A maximum rate of 100 counts/sec for ^{112}In was observed on the MARS silicon detector telescope with MARS tuned for $^{112}In^{39+}$ and 2 μA of proton beam on the LIG target.

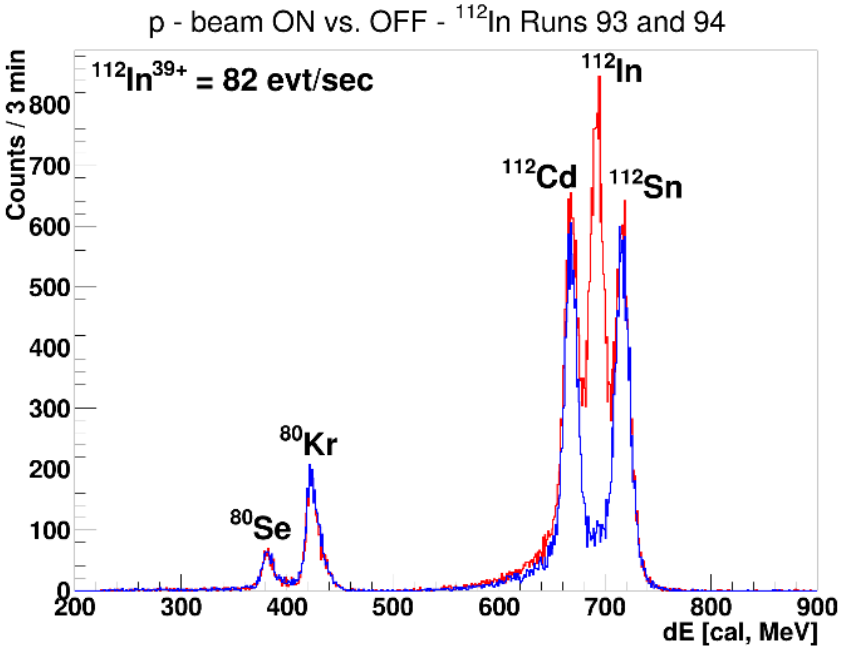

FIG. 2. ΔE Spectra showing the ^{112}In measured at the MARS focal plane for the 39+ charge state settings. The measurements for the proton-beam "off" (shown in blue) and the proton beam "on" (shown in red) were measured for 3 minutes each. The peak corresponding to ^{112}In is clearly visible with the K150 proton beam "On" versus when the proton beam was "Off".

Considering the charge state scan measured at the MARS focal plane, about 30% of the re-accelerated ^{112}In was observed at the MARS focal plane with the $^{112}In^{39+}$ magnet settings. Also, the transmission of the beam through the K500 cyclotron was estimated to be about 10%, based on the measurements of the $^{16}O^{3+}$ pilot beam on faraday cups before and after the cyclotron. Thus, it can be implied about 3.3×10^3 p/s of $^{112}In^{21+}$ was produced before the K500 cyclotron by the LIG+CB-ECRIS with 2 μA of proton beam on the production target.

In conclusion, ^{112}In from the LIG and CB-ECRIS has been re-accelerated by the K500 cyclotron and observed at the MARS focal plane. Peaks $^{112}Cd^{39+}$, $^{112}In^{39+}$ and $^{112}Sn^{39+}$ ions, obtained after passing the beam through a stripper-foil, were clearly observed confirming that the tune of the K500 cyclotron, the beam-line optics, and MARS was correct. The peak arising from the $^{112}In^{39+}$ ions varied in intensity depending on if the K150 proton beam was "on" or "off", if the LIG was "on" or "off", and also the intensity increased linearly if the amount of proton beam on the LIG was increased. The observation of the ^{112}In ions represents the first confirmed re-accelerated radioactive ions from the LIG and the CB-ECRIS. Following this result, the re-acceleration of lighter ions, such as ^{57}Ni, is planned for coming year.

[1] B.T. Roeder *et al.*, *Progress in Research*, Cyclotron Institute, Texas A&M University (2017-2018),p. IV-63; http://cyclotron.tamu.edu/progress-reports/2017-2018/SECTION IV.html.

[2] *TENDL-2017*, https://tendl.web.psi.ch/tendl_2017/tendl2017.html.

[3] B.T. Roeder *et al.*, *Progress in Research*, Cyclotron Institute, Texas A&M University (2015-2016), p.IV-16; http://cyclotron.tamu.edu/progress-reports/2015-2016/SECTION IV.html.

[4] B.T. Roeder *et al.*, *Progress in Research*, Cyclotron Institute, Texas A&M University (2016-2017), p. IV-17; http://cyclotron.tamu.edu/progress-reports/2016-2017/SECTION IV.html.

[5] R.E. Tribble, R.H. Burch, and C.A. Gagliardi, Nucl. Instrum. Methods Phys. Res. **A285**, 441 (1989).

[6] G. Tabacaru *et al.*, *Progress in Research*, Cyclotron Institute, Texas A&M University (2018-2019), p. IV-13; *Cyclotron Institute upgrade project: Section IV: Progress on the Light Ion Guide*, http://cyclotron.tamu.edu/progress-reports/2018-2019/SECTION IV.html.

[7] B.T. Roeder *et al.*, *Progress in Research*, Cyclotron Institute, Texas A&M University (2013-2014), p. IV-40; http://cyclotron.tamu.edu/progress-reports/2013-2014/SECTION IV.html.

[8] O.B. Tarasov and D. Bazin, Nucl. Instrum. Methods Phys. Res. B**266**, 4657 (2008).

Cyclotron computing

R. Burch, J. Gauthier, and K. Hagel

Continuing to provid the Cyclotron Institute with the secure computational and networking infrastructure necessary to teach and execute research programs, we increased the Institute's computing capacity and infrastructure over this past year by adding four computational servers. We upgraded our authentication service hardware. To enhance our security posture, we migrated the Institute's offsite fileserver and data management server to the WCDC (West Campus Data Center) and updated our TAMU NetID configurations.

To increase productivity and reduce turn-around time we added four general lab computational servers, now totaling twenty. This increases our capacity by 8 2.9GHz late model processors or from 388 to 484 concurrent jobs. Each added server has 64GByte of RAM, allowing users to analyze memory intensive jobs quickly. These servers are provisioned and are in production.

These changes and additions allow us to supply the Institute with the resources it needs to execute its mission by increasing our computational and data serving capacity, providing more security by utilizing TAMU authentication services.

Data acquisition upgrades at the Cyclotron Institute

K. Hagel, A. Jedele, A.B. McIntosh, R. Burch, and J. Gauthier

We have implemented a number of new capabilities into our data acquisition system in the last several years in order to leverage more modern technology. This has recently included waveform digitizers and the MASE system [1].

We began to employ waveform digitizers several years ago in order to leverage present improvements in technology that provide opportunities to acquire more information from our experiments. The implementation of these digitizers has allowed us to gain information that would be otherwise inaccessible [2] as well as to consolidate a complete wall of electronics and delay lines into a single VME crate [3] that provides triggering, time information as well as several integration windows of signals for pulse shape analysis.

The early versions the software to operate the digitizers relied on calls to the access functions inside the data acquisition code. This proved usable and was, in fact, indispensable in learning how to use the digitizers, but had the effect that any change to the digitizer configuration had to be performed by an expert and the data acquisition had to be exited, recompiled and started again each time the configuration was changed.

In order to mitigate this problem we developed a control GUI for the digitizers that is integrated seamlessly into the front-end data acquisition system. This allows a fast change of the configuration by simply stopping the acquisition during a run, clicking on the control GUI, clicking on what needs to be changed and continuing the next run with the new configuration. The GUI also saves the previous configuration to allow reverting to that configuration if that becomes necessary.

We are also in the process of upgrading NIMROD [3] to replace aged radiation damaged silicon detectors as well as to increase the number of super telescopes. The previous system for the silicon detector readout does not have sufficient capacity in order to allow readout of all of the new silicon detectors.

To be able to read out the larger number of detectors, we have borrowed the MASE [1] system from the group in Indiana. In the same spirit as the waveform digitizers, we have developed GUI based on the one developed by the Indiana group. This GUI is also incorporated seamlessly into the data acquisition system and works in a similar spirit to the digitizer GUI.

[1] C. Metelko, A. Alexander, S. Hudan, J. Poehlman, R.T. de Souza, Nucl. Instrum. Methods Phys. Res. **A569**, 815 (2006).

[2] S. Wuenschel, K. Hagel, M. Barbui, J. Gauthier, X.G. Cao, R. Wada, E.J. Kim, Z. Majka, R. Płaneta, Z. Sosin, A. Wieloch, K. Zelga, S. Kowalski, K. Schmidt, C. Ma, G. Zhang, and J.B. Natowitz, Phys. Rev. C **97**, 064602 (2018).

[3] S. Wuenschel, K. Hagel, R. Wada, J.B. Natowitz, S.J. Yennello, Z. Kohley, C. Bottosso, L.W. May, W.B. Smith, D.V. Shetty, B.C. Stein, S.N. Soisson, Nucl. Instrum. Methods Phys. Res. **A604**, 578 (2009).

Studies of the CB-ECRIS beam background

B.T. Roeder, F. Abegglen, J. Ärje, G.J. Kim, D.P. May, A. Saastamoinen, and G. Tabacaru

Re-accelerated Rare Isotope Beams (RIBs) prepared with the Light Ion Guide (LIG), charge-bred with the Charge Breeding Electron Cyclotron Resonance Ion Source (CB-ECR), and re-accelerated with the K500 cyclotron are becoming feasible at the Cyclotron Institute at Texas A&M. The desired characteristics of these beams are energies of 10 AMeV to 30 AMeV, low momentum and energy spreads of ~0.1%, and beam purities approaching 100%.

The following RIBs have been developed with the LIG and CB-ECRIS for attempts at Re-acceleration: ^{64}Ga [1], ^{63}Zn, ^{114}In [2], ^{112}In[3]. Of these beams, so far only the ^{112}In has been successfully observed after acceleration by the K500. The other three species, in particular the ^{64}Ga, have been obscured by stable beams with the same mass, so-called mass isobars. This stable beam background has intensities of orders of magnitude higher than the expected rates for the RIBs.

Following the attempt to observe re-accelerated ^{64}Ga, which was lost amongst 10^4 p/s of ^{64}Zn background, it was discovered that the plasma chamber of the CB-ECR was constructed with aluminum alloy, series 7075 [4]. This alloy contains the following impurities, which increase its strength: Zn (~6%), Mg (~2%), Cu (~1.5%) and Si, Fe, Mn, Ti, Cr (total < 0.5%) amongst other metals. The plasma in the CB-ECRIS sputters these metals, in particular the Zn and the Cu, from the surface of the plasma chamber and ionizes them, making them part of the beam that is injected into the K500 cyclotron.

In the past year, a few attempts have been made to observe the beam background arising from the impurities in the aluminum alloys of both the CB-ECRIS and ECR1, the stable beam ion source normally used with the K500 cyclotron. In May 2018, a pilot beam of $^{15}N^{4+}$ at 22 AMeV was used to provide the initial tune of the K500 cyclotron and of the beamline optics to MARS [5]. In that case, the goals were to observe $^{64}Ga^{17+}$ and/or $^{63}Zn^{17+}$ by making the appropriate K500 frequency changes. The beam mixture is stripped to higher charge states by a thin carbon foil at the entrance of MARS and the resulting charge states are tuned to the MARS focal for particle identification. The ^{64}Ga was not observed under the intense ^{64}Zn background from the CB-ECRIS. In the worst case, $^{64}Zn^{28+}$ was measured at the MARS focal plane with a rate of about $9*10^3$ p/s, while the expected rate of $^{64}Ga^{28+}$ was around 10 p/s. Similarly, the ^{63}Zn was not observed due to background from ^{63}Cu, although the K500 frequency change was much larger in that case. This made the observation difficult and ^{63}Zn was also not observed.

In December 2018, a pilot beam of $^{14}N^{4+}$ at 24.8 MeV/u was tuned to investigate if the different possible contaminant beams from the CB-ECRIS could be observed with MARS. By tuning the K500 frequency 20.8 kHz higher than the frequency for the $^{14}N^{4+}$, several contaminant beams were measured with MARS including ^{70}Zn, ^{56}Fe, ^{49}Ti and ^{28}Si. A spectrum showing these contaminants is shown in Fig. 1. In addition, a relatively intense ^{35}Cl contaminant beam was also seen with a different MARS spectrometer tune.

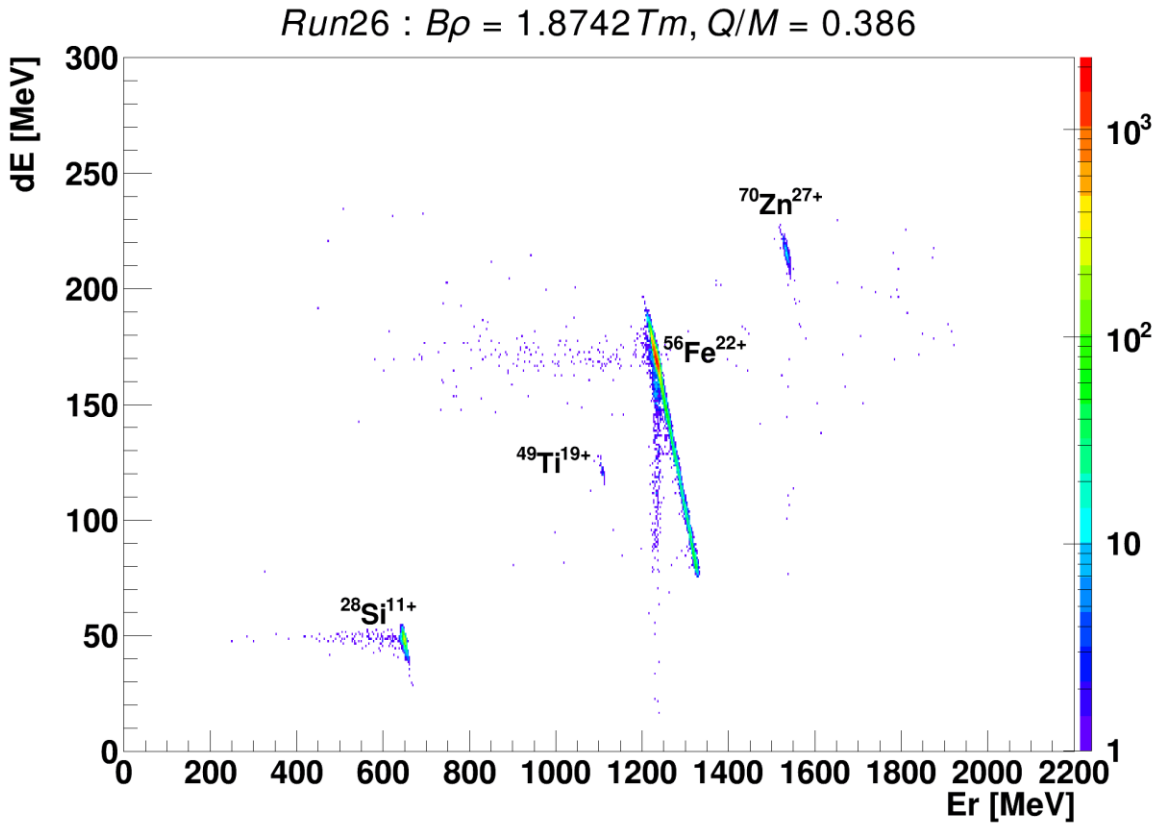

FIG. 1. Measurement of beam contaminants from the CB-ECR with $^{14}N^{4+}$ pilot beam at 14 MeV/u as observed at the MARS focal plane. See text for further explanation.

To combat this problem, we plan to try using pure aluminum liners or redesigning some components of the ECR plasma chambers to attempt to remove some of this contamination. The results of these efforts will be reported in next year's progress report.

[1] B.T. Roeder *et al.*, *Progress in Research*, Cyclotron Institute, Texas A&M University (2016-2017), p. IV-17; http://cyclotron.tamu.edu/progress-reports/2016-2017/SECTION IV.html.

[2] B.T. Roeder *et al.*, *Progress in Research*, Cyclotron Institute, Texas A&M University (2017-2018), p. IV-63; http://cyclotron.tamu.edu/progress-reports/2017-2018/SECTION IV.html.

[3] B.T. Roeder *et al.*, *Progress in Research*, Cyclotron Institute, Texas A&M University (2018-2019), P. IV-17;http://cyclotron.tamu.edu/progress-reports/2018-2019/SECTION IV.html.

[4] https://en.wikipedia.org/wiki/Aluminium_alloy

[5] R.E. Tribble, R.H. Burch, and C.A. Gagliardi, Nucl. Instrum. Methods Phys. Res. **A285**, 441 (1989).

MARS status report: Tuning of rare isotope beams of ^{10}C, ^{14}O, ^{42}Ti, ^{29}P, ^{8}B, ^{12}N, ^{9}Li and ^{76}Ge fragmentation

B.T. Roeder and A. Saastamoinen

This year, we continued the program of providing rare isotope beams for the physics program at the Cyclotron Institute at Texas A&M University with the Momentum Achromat Recoil Separator (MARS) [1]. The beams that have been developed in previous years that were employed in physics experiments this year are as follows: A ^{42}Ti beam, made with the ^{40}Ca+^{4}He reaction at 32 MeV/u, was provided to Dr. Hardy's research group for their continuing studies of super-allowed β-decay; ^{10}C, ^{14}O, and ^{9}Li beams were prepared for experiments with Dr. Rogachev's research group for experiments with the TexAT active target; and also, a low energy ^{8}B beam was prepared for Dr. Rogachev's group for use in an experiment in collaboration with the University of São Paulo in Brazil.

Two new rare isotope beams were developed this year: ^{12}N and ^{29}P. Also, ^{76}Ge fragmentation at 28 AMeV on Be, Al and Ni targets was investigated to test what could be produced with that primary beam. These new MARS tunes are described below.

The low energy ^{12}N beam was requested by Dr. Rogachev's group for an experiment in collaboration Washington University in St. Louis. The goal was to implant ^{12}N into the gas of the TexAT active target and observe the β-delayed 3α decay. ^{12}N was prepared with a ^{10}B primary beam at 11 AMeV from the K500 cyclotron bombarding the MARS gas target filled with ^{3}He gas at a pressure of 800 torr and a temperature 77K. With the MARS momentum slits at ± 1.0cm, a production rate of 5.6 event/nC was measured for the ^{12}N. About 3% of the total secondary beam was from a tail of ^{7}Be contamination. This production rate was sufficient for the requested ^{12}N rate of about 100 p/s for the experiment. The secondary beam energy was 81 MeV. This beam energy was further degraded with a rotatable aluminum degrader such that the ^{12}N could be stopped in the gas volume of TexAT.

The ^{29}P beam was requested by Dr. Melconian's group for an experiment to measure its half-life with the TAMU Tape Drive system. Several methods of production were proposed. The p(^{30}Si,^{29}P)2n reaction was chosen as the (*p*,2*n*) reaction has been known to provide nearly pure rare isotope beams in the past and was predicted to have high production cross section. During the beam development, a ^{30}Si beam at 24 MeV/u bombarded the MARS gas target filled with H_2 gas at a pressure of 2 atm and a temperature of 77K. The result was a nearly pure secondary beam of ^{29}P with a production rate of 1427 event/nC with the MARS momentum slits at ± 0.5 cm. A tail of ^{27}Si contributed 0.13% to the total rate of the secondary beam, and the total secondary beam contamination was less than 0.5%. Despite the relatively low intensity available for the ^{30}Si primary beam, ^{29}P rates of about $2*10^4$ p/s were typical. The ^{29}P half-life experiment was completed in November 2018 and the analysis is ongoing.

Finally, ^{76}Ge fragmentation at 28 MeV/u on solid targets of Be, Al and Ni was tested for Dr. Christian's group. The goal was to develop neutron-rich rare isotope beams in the region of ^{73}Cu. However, development of heavy mass beams with A > 60 with MARS is problematic because the reaction products are not fully stripped of their electrons. This makes identification of the reaction products difficult. Also, 28 AMeV beam energy was too low to efficiently remove more than 3 nucleons

from the ^{76}Ge beam, especially in the case of the Ni target which has a higher Coulomb barrier. Thus, no rare isotopes were observed in the case of the Ni target. For the Al and Be targets, 1 and 2 nucleon removal were favored. Nuclei in charge states with 1 or 2 electrons were populated. There were some events of particles with the correct energy loss in the silicon detectors that could be identified as ^{73}Cu at low rate. ^{72}Ni was not observed. Also, the high rate of undesired reaction products with similar charge-to-mass ratio as the ^{73}Cu would make an experiment with the low rate of ^{73}Cu difficult. Future attempts at the production of ^{73}Cu or ^{72}Ni would greatly benefit from higher energy and higher intensity of the ^{76}Ge primary beam. Perhaps energies 40 MeV/u or greater and intensities above 1 particle-nA would be needed to produce ^{72}Ni.

[1] R.E. Tribble, R.H. Burch, and C.A. Gagliardi, Nucl. Instrum. Methods Phys. Res. **A285**, 441 (1989).

Development of electron cyclotron emission imaging optics

L.E. Henderson, H.L. Clark, C.A. Gagliardi, and D.P. May

We are developing optics that function in the 15-65 GHz band in order to image Electron Cyclotron Emission (ECE) from the plasma inside the Cyclotron Institute's Electron Cyclotron Resonance Ion Sources (ECRIS). ECE correlates directly to the energy, number density, and magnetic confinement of plasma electrons, so these optics will allow us to characterize the dominant dynamical population in the plasma interior with spatial resolution not previously available.

Given that the operating wavelengths are comparable to lens dimensions, conventional optical calculations for the lenses had to be supplemented with simulations of Maxwell's equations in the MEEP software package.

The optics inside the plasma chamber take advantage of existing radial ports in our ECRIS, so no ion source modifications are necessary. A cemented stack of alumina and PTFE lenses will couple ECE from the plasma midplane into an alumina-filled waveguide array, which will then transport the image out of the ECRIS. Conventional relay optics were ruled out by the small diameter of the access pipe (dia. 3.81 cm) and comparable operating wavelengths (λ = 0.46 - 2.0 cm). In fact, obtaining an image with any useful resolution would be impossible without filling the radial port opening (dia. 1.905 cm) with a high-index material like alumina (n = 3.1) to temporarily reduce the image wavelengths. Alumina and PTFE also have known, minimal dispersions in the desired frequency band.

Outside the ECRIS, the image will be routed to the receiver array by PTFE lenses and aluminum mirrors, as shown in Fig. 1.

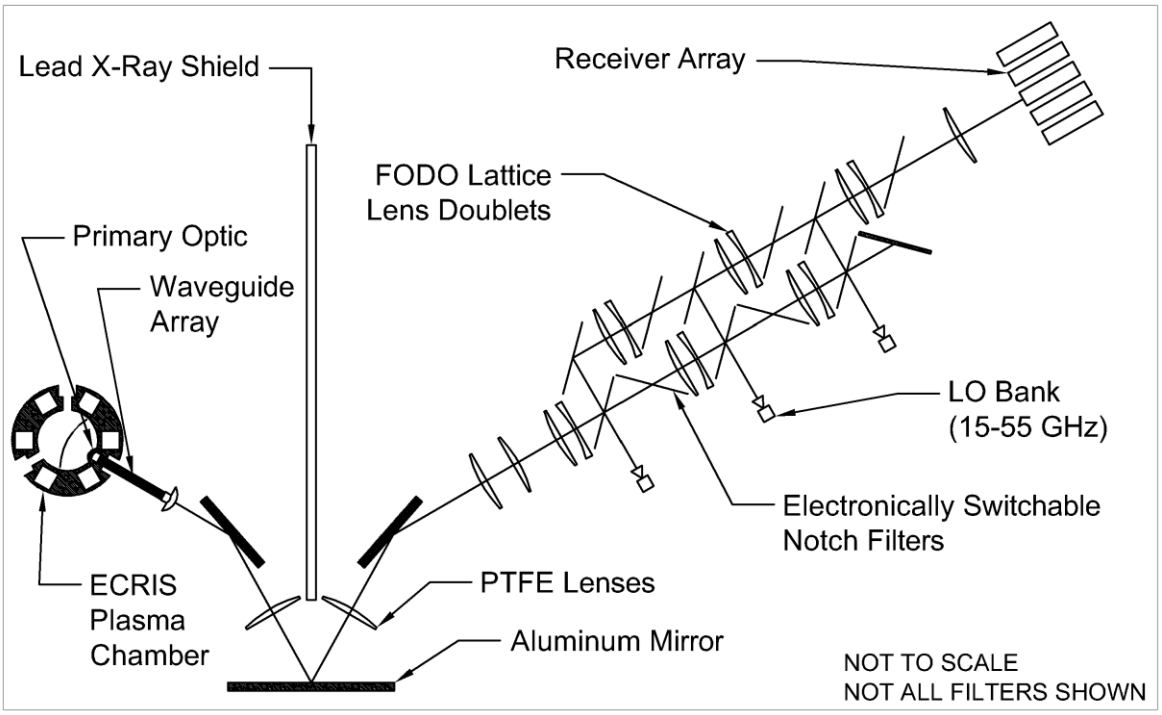

FIG. 1. ECE optical train.

Each receiver in the receiver array will convert the signal to much lower frequencies before digital sampling, which is known as a heterodyne receiver. However, since a fully electronic receiver array for the entire 15-65 GHz band would require the duplication of many expensive components in an unwieldy waveguide network, some of the electronics that typically follow the receiver antennas will be replaced with equivalent optical elements preceding the receiver antennas.

To enable this receiver design, the recent work has been focused on developing novel optical elements: a suite of free-space microwave notch filters with electronically controllable reflectivity. Activating one set of filters routes both the desired signal band and a known 'local oscillator' onto the receiver array's optical path (at a reasonable signal-to-noise ratio), and the filter design allows for switching thousands of times per second. Performing this signal preparation in free space means that the first stage mixing, from 15-65 GHz down to 0-8 GHz, can be completed with a single diode attached to each receiver antenna. Secondary mixing and amplification stages can then be built with more conventional electronics.

Each filter is a 2D array of copper antennas, connected by PIN diodes and resistive carbon traces, which will be fabricated on a PTFE substrate using standard printed circuit board manufacturing techniques. The resistive carbon traces are essentially invisible to incident electromagnetic radiation, so they are useful for supplying a bias current to the PIN diodes. The DC bias current controls the AC impedance of the PIN diodes, which in turns controls the damping of each antenna. Since a damped antenna cannot re-radiate EM radiation efficiently, the reflectivity of the filter is therefore controlled by the bias current. Given the wide range of AC impedances that PIN diodes can achieve ($0.7\ \Omega < R_{AC} < 5000\ \Omega$), MEEP simulations have shown the existence of essentially non-reflective (~3%) and reflective (>95%) filter operating modes. Additionally, simulations show high reflectivity only manifests in a single, specified band (-3dB width of ~4 GHz) within the nominal 15 - 65 GHz design band. Each filter for this camera will have at least two layers to extend the bandwidth.

Installation and characterization of the AGGIE gas-filled separator

C.M. Folden III[1,2] and C.S. Salas[1,2]
[1]*Cyclotron Institute, Texas A&M University, College Station, TX 77843*
[2]*Department of Chemistry, Texas A&M University, College Station, TX 77843*

The gas-filled separator formerly known as SASSYER [1], which was previously installed at Yale University [2], has been installed on a beamline in Cave 4 at the Cyclotron Institute. As part of the recommissioning, it has been renamed Al Ghiorso's Gas-filled Ion Equipment (AGGIE). When commissioning is complete, it is expected to substantially increase the sensitivity of fusion-evaporation experiments, since the gas-filled separation technique [3] reduces the width of the magnetic rigidity distribution of the products, resulting in an increased transmission efficiency. The separator was previously reported to have separation factor of 10^{15} for full-energy projectiles [3].

Initial installation occurred in parallel with improvements to the NIMROD array and relocation of the Hyperion array during Fall 2018. The installation required a significant effort from the Operations Group, as the Cave 4 roof planks were temporarily removed, the main magnets were installed, and power and water cables were installed. A new target box was also fabricated. The corresponding beamline has been reassembled and a preliminary test has confirmed that beam delivery is possible. The downstream side of the separator is shown in Fig. 1(left).

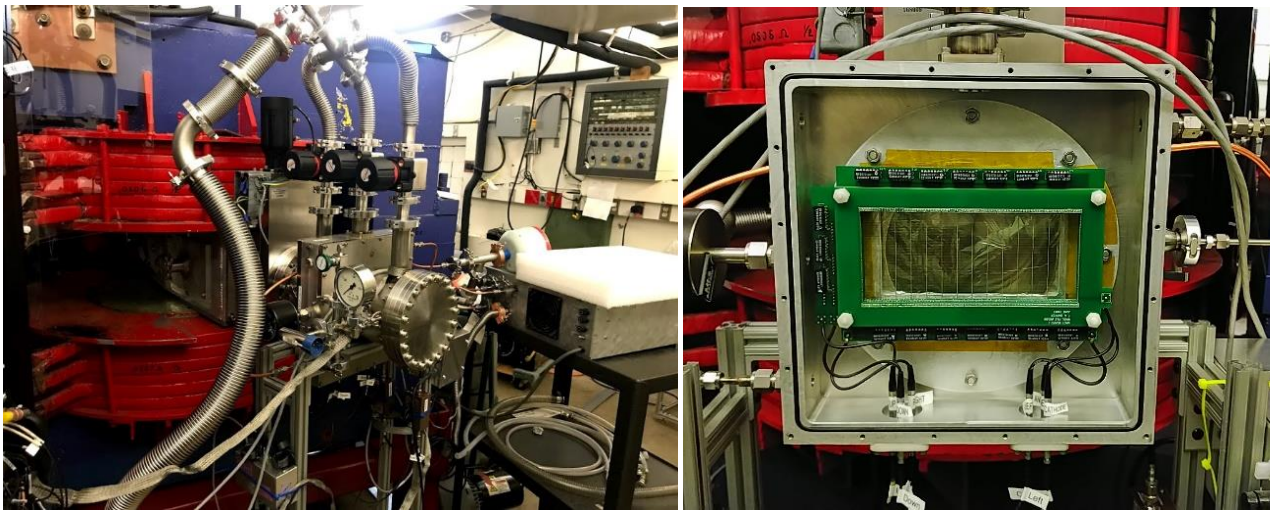

FIG. 1. Left: Downstream end of the gas-filled separator AGGIE installed on a beamline in Cave 4. MACY is installed inside the square box near the end of the beamline. Right: Interior view of MACY. The black boxes are delay-line resistors that create a time difference between the left/right and up/down signals.

Additional equipment received from Yale University included the Multiwire Avalanche Counter at Yale (MACY, a gas-filled position-sensitive implantation detector), a multiplexing set of electronics, a pair of double-sided silicon detectors (DSSDs), gas-handling equipment, and other ancillary equipment. During Spring 2019, MACY received extensive repairs, as it arrived with both of its Mylar® windows

and several of its wires broken. The detector was installed at the end of AGGIE [see Fig. 1(right)] and has been characterized with alpha and fission products sources using isobutane as a fill gas. The multiplexing electronics and DSSDs were tested during a previous reporting period and have been successfully interfaced to the existing data acquisition system. Commissioning experiments with the full setup are scheduled for Fall 2019.

[1] A. Ghiorso and J. Radioanal. Nucl. Chem. **124**, 407 (1988). doi:10.1007/bf02041331.

[2] J.J. Ressler *et al.*, Nucl. Instrum. Methods Phys. Res. **B204**, 141 (2003). doi:10.1016/S0168-583X(02)01906-7.

[3] A. Ghiorso *et al.*, Nucl. Instrum. Methods Phys. Res. **A269**, 192 (1988). doi:10.1016/0168-9002(88)90877-7.

Studies of systematic effects of the AstroBox2 detector in online conditions

A. Saastamoinen, E. Pollacco,[1] B.T. Roeder, R. Chycz, L. Trache,[2] and R.E. Tribble
[1] *IRFU, CEA Saclay, Gif-sur-Yvette, France*
[2]*National Institute of Physics and Nuclear Engineering, Bucharest-Magurele, Romania*

After commissioning, the AstroBox2 detector [1] has been used already for several physics experiments. During some of the experiments systematic effects in the measured decay spectra have been observed and related to gain shifts due to the environment, the chemical nature of the isotope under investigation, and to the beam implantation rate [2].

Gas gain, especially in the exponential regime of a Micromegas, can be very sensitive to various changes in the detection medium such as gas impurity levels and gas density changes due to either pressure or temperature fluctuations. In the experimental cave which remains closed during the beam time, the temperature stabilizes during beam tuning and is monitored during experiments. To track possible gain drift we have implemented multiple independent ways to monitor the stability of the detector: (1) an α-source on an active side pad of the detector, (2) a separate chamber for a ~1 cm^2 Micromegas detector using an ^{55}Fe X-ray source at the gas exhaust, (3) a pulser in the AstroBox electronics, and (4) possible strong decay branches of the species under study. In most cases when the environment is under control, no gain shifts beyond the typical instrument resolution are observed. In case gain shifts are observed, those can be corrected by using the the simultaneously collected α-source data from an active side pad [2].

Within the present operating conditions in use with AstroBox2 the implanted ions if rapidly neutralized will exercise a Brownian motion and will be localized within a sphere of few mm of the stopping position at decay. However, for relatively low electron affinities with respect to the P5 constituents, the ions will drift towards the cathode. In some cases, such as βα-decay of ^{20}Na, we have observed a clear signature of decays occurring on the cathode: As shown in Fig. 1, ^{16}O recoils are clearly seen in data and in calorimetric measurement this is only possible from decay on a surface. The α will be deposited into the cathode while the ^{16}O recoil ionization is detected. In addition the drift time difference from the two pads indicates particle tracks mostly towards the anode. If the decay occurs in gas, there should be equal amounts of particle tracks towards the cathode, a signature missing from these data. Our observations [2] are in agreement from earlier studies done at GANIL in the 1990s [3] but would need a separate study to be fully characterized.

In the AstroBox experiments, when everything is under control, we have not observed any rate related effects up to about kHz total implant/decay rates (rates limited mostly due to amount of primary beam available). However, during one of our experiments the standard MKS piPC99 gas controller failed during the setup stage and we had to use instead the gas handling system used for the Oxford detector. During the run it became evident that unknown chemical history and component quality of this gas system, even after flushing for several days, brought up implant / decay related pulse height defect even at below kHz rates. This effect was localized into pads with highest implant rates which translates to

highest β-activity during the decay phase [2]. A separate study with proper gas handling system to study this effect with higher rates is under planning.

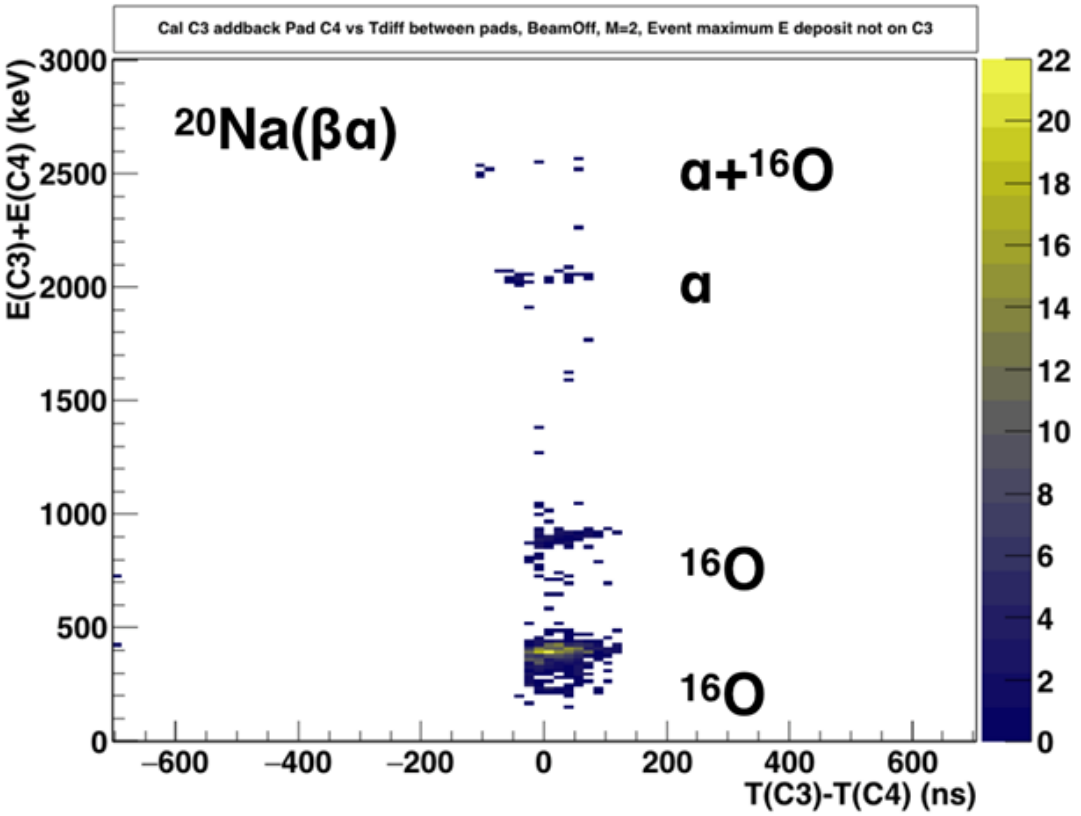

FIG. 1. The total decay energy collected with two neighboring pads from the central region (labeled C3 and C4) versus the time difference of the same pads in case of ^{20}Na measured with AstroBox2. Here the positive time difference in pad drift times corresponds to particle trajectory towards the anode and the negative time difference to a trajectory towards the cathode. The spectra are produced from beam off period with requirement of exactly two pads firing, and that the maximum energy deposition of the event is not on the pad where decay occurred.

[1] A. Saastamoinen *et al.*, Nucl. Instrum. Methods Phys. Res. B**376**, 357 (2016).

[2] A. Saastamoinen *et al.*, Nucl. Instrum. Methods Phys. Res. B (in press); DOI: 10.1016/j.nimb.-2019.05.026.

[3] B. Blank *et al.*, Nucl. Instrum. Methods Phys. Res. **A330**, 83 (1993).

Development of TexCAAM: Texas CsI Array for Astrophysical Measurements

E. Aboud, L. Jeffery, E. Koshchiy, M. Barbui, C. Hunt, G.V. Rogachev, S. Ahn, and E. Lester

High efficiency, compact CsI(Tl) gamma-ray array is being developed at TAMU. It will be primarily utilized for indirect nuclear astrophysics studies with stable and rare isotope beams. The main focus of these studied will be astrophysically relevant α-capture reactions. With stable beams the TexCAAM will be used in conjunction with the MDM spectrometer, and with rare isotope beams thick target and Si detector will be used to provide an event ID using coincidence with charged particles from (^{6}Li,d) or (^{7}Li,t) reactions. γ-ray spectroscopy will be used to determine excitation energies, α-ANCs, and spin-parities for the near α-threshold states relevant for astrophysics.

TexCAAM (the **T**exas **C**sI **A**rray for **A**strophysical **M**easurements) consists of 32 Scionix CsI(Tl) (5x5x4 cm^{3}) detectors readout by Si pin-diodes with the preamps directly attached to them for optimal noise conditions. The crystals are arranged as shown in Fig. 1. SIS3316 Struck wave-form digitizers are used to digitize and record the signals from the preamps directly.

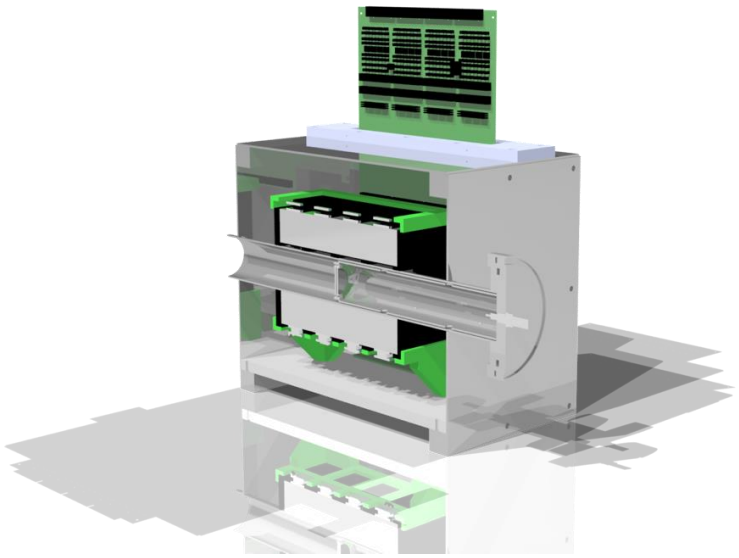

FIG. 1. Cutaway CAD drawing of TexCAAM. The target is inserted so that it is directly halfway into the CsI array. The array of CsI is designed to maximize the solid angle covered while allowing the beam-pipe to go through the array. The black and green parts are a 3D printed skeleton that holds the CsI in place around the beamline.

The commissioning experiment of TexCAAM is planned to be the ^{7}Be(^{6}Li,dγ)^{11}C* reaction to determine the contribution of the sub-threshold 3/2^{+} state to the production of ^{12}C in astrophysical environments, particularly in zero metallicity population-III stars [1,2]. Another early TexCAAM

experiment will be focusing on constraining the spin-parity assignments for astrophysically relevant states in ^{26}Mg that contribute to the ^{22}Ne(α,n) and ^{22}Ne(α,γ) reactions.

At present the array is being tested using gamma-ray sources to optimize data acquisition parameters for energy resolution, and determine efficiency of the setup. Further tests will be done to determine TexCAAM's ability to measure γ-γ angular correlations. The design of the target assembly has been completed and construction of it is set to begin shortly.

[1] M. Wiescher *et al*., Astrophys. J. **343**, 352 (1989).
[2] M. Hartos *et al.*, Astrophys. J. **862**, 62 (2018).

Performance of GEM-Micromegas detector with TexAT

E. Koshchiy, S. Ahn, J. Bishop, C. Hunt, A. Saastamoinen, G.V. Rogachev, and E. Pollacco[1]
[1]*IRFU, CEA Saclay,Gif-Sur-Ivette, France*

Texas Active Target (TexAT) is in active operation at the Cyclotron Institute since 2017. See Ref. [1] for general outline of the detector. It is designed for direct measurements of the excitation functions for proton, deuteron and alpha particle elastic and inelastic scattering and transfer reactions such as (*d*,*p*), (*d*,*t*), (*p*,*d*), (*p*,*t*), (p,α), (p,^{3}He) and (d,^{3}He) in inverse kinematics using radioactive ion beams.

The key element of TexAT is a Time Projection Chamber (TPC) with highly segmented Micromegas bulk detector. While several successful experiments have been performed with TexAT, some limitations have been identified during the first year of operation: to achieve a desired gain for high energy protons a fairly strong electric field, at the level of 40 to 50 kV/cm, in the Micromegas detector must be created. Such operation conditions can generate severe sparks in the Micromegas detector and damage sensitive readout electronics. This occurs in spite of the protective circuits implemented with the TexAT. To overcome this issue and to reduce the possibility of discharge, an additional Gas Electron Multiplier (GEM) [2] detector was installed as a preamplifier prior to the Micromegas mesh. GEM preamplification allows a substancial decreased of Micromegas tension while keeping the gas gain at the desired level. As a result the discharge effects in Micromegas are significantly reduced and the dynamic range of TexAT detector is enhanced.

Two different GEM-Micromegas configurations were tested:

1. A thick GEM (TGEM), fabricated in CERN by standard PCB techniques - the 0.75 mm diameter holes mechanically drilled through the 1.5 mm thick FR4 double sided copper clad PCB board. The distance between the holes is 1.25 mm. Chemical etching was used to make a small rim (0.1 mm) around each hole to reduce the discharging. The overall geometry of an active area is matched to TexAT Micromegas detector: 240mm (W) x 224mm (L);
2. A GEM (produsedby CERN) – consists of a thin (50μ) double copper clad kapton foil, chemically perforated by high density (50 holes/mm^2) holes of φ=50μ. The geometry of the active area is designed to fully match the segmented TexAT's Micromegas detector. The GEM foil has an optional central zone (20.4 mm wide) along the beam axis and two side zones of 224 mm x 101.5 mm. Such segmentation allows the creation of an avalance areas with different gas gain.

The schematic of the modified TexAT TPC detector is shown in Fig.1. It was tested with an alpha source in full TexAT configuration. Signals from GEM/TGEM and MM mesh were read out by spectroscopic preamplifiers and monitored on an oscilloscope. Thus voltage operation conditions for both gaseous detectors are controlled. This option also allows an independent external trigger from GEM or MM mesh to be used with GET electronics.

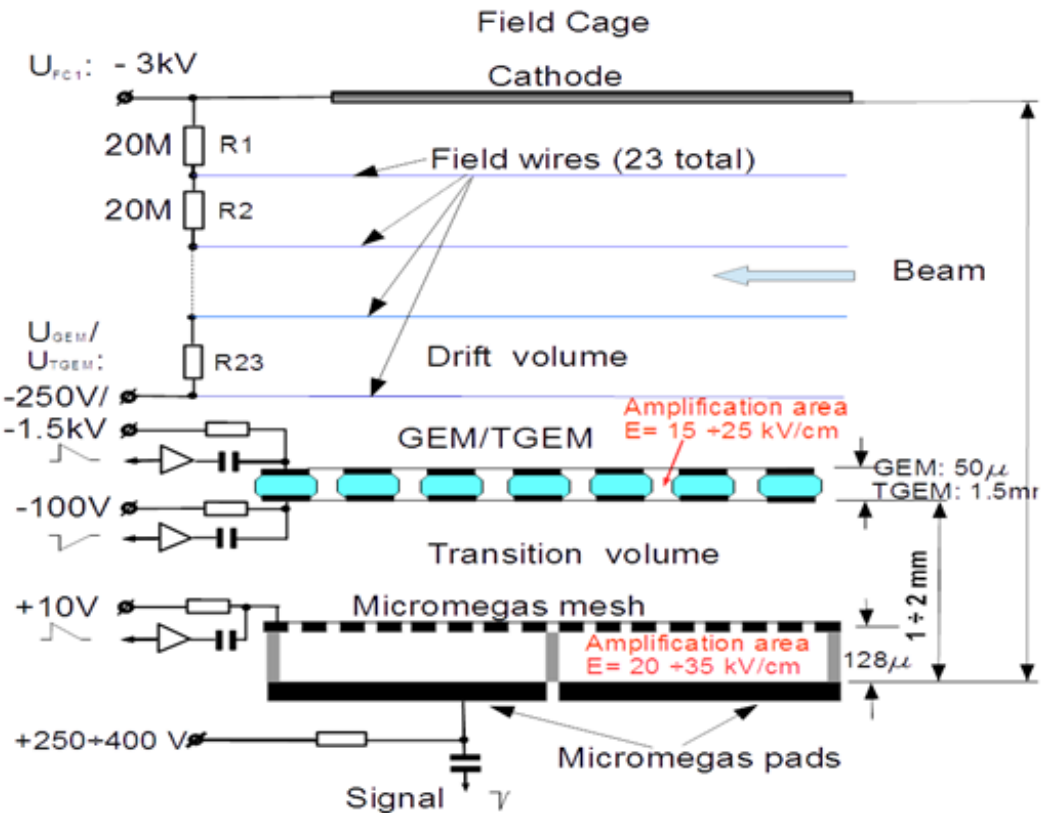

FIG. 1. Scematic of the setup used for testing/operation of GEM+Micromegas detector for TexAT.

Two areas of application were explored:

1. The configuration of TGEM+Micromegas: CO_2, P5, and quenched noble gases (He/CO_2(1-2%), He/CH_4(1-2%)) at the low pressure of 15 - 40 torr. This mode is used for β - delayed particle emission experiments with exotic nuclei;
2. The configuration of GEM+Micromegas: standard hydrogen and helium containing gases: H_2, CH_4, C_4H_{10} at the "high" pressure range of interest for experiments with rare isotope beams – resonance elastic and inelastic scattering of protons and α - particles and transfer reactions.

As a result of extensive tests the optimum working conditions for both configurations were defined and limits for spark- safe detector operation established. It was determined that at the same gain the spark probability of the GEM-Micromegas detector is substantially reduced compared to the standard Micromegas detector, and a higher gain (factor of 10) could be obtained at relatively low applied voltages.This indicates that the GEM-Micromegas detector works better than the standard bulk-Micromegas, as expected.

Both configurations were already tested in the in- beam experiments at the Cyclotron Institute in 2019:

1. TGEM+Micromegas setup - for the study of Hoyle state using β - decay of ^{12}N [3].

Gas: CO_2 (20 torr). One of the typical XY- track's projection of events of interest (3α- decay of excited $^{12}C^{*}_{7.27}$ nuclei) is shown in Fig. 2.

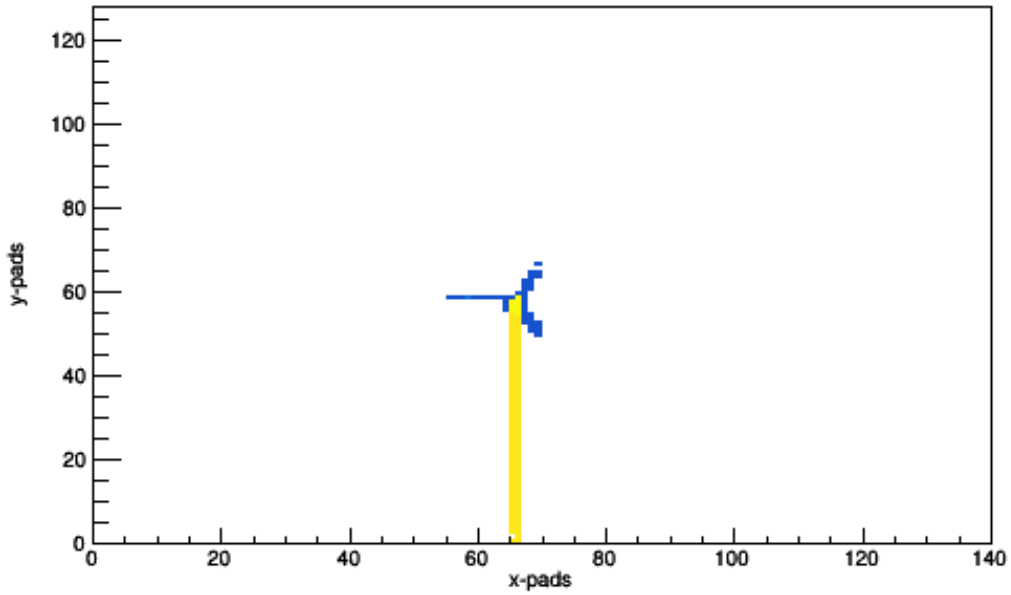

FIG. 2. Event of 3α- decay, measured with TGEM+ Micromegas TexAT configuration. Implanted ion of ^{12}N is shown in yellow; Hoyle- decay (delayed by 30 ms) is shown in blue.

2. GEM+Micromegas setup – for the study of $^{12}B(d,^{3}He)$- transfer reactions. This experiment was conducted in "active gas target"- mode. The track (XY- projection) of one of events is shown in Fig.3.

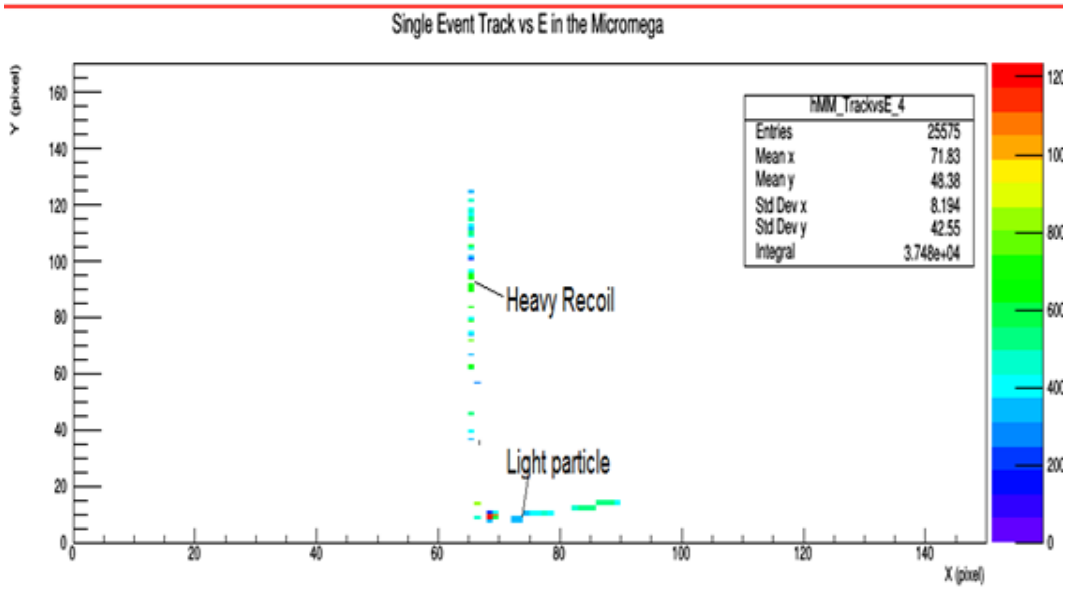

FIG. 3. Scattering/reaction (currently under analysis) event. Beam: ^{12}B, E=21.6 AMeV; Target gas: deuterated methane (CD_4); P= 250 torr.

The upgraded TexAT has demonstrated an improved electrical performance, high gain and enhanced stability. No sparks and voltage trips were observed in the detector during a two 2- week long in- beam experiments. The results of experiments are now under analysis.

[1] E. Koshchiy, G.V. Rogachev, E. Pollacco, S. Ahn, E. Uberseder, J. Hooker, J. Bishop, E. Aboud, M. Barbui, V.Z. Goldberg, C. Hunt, H. Jayatissa, C. Magana, R. O'Dwyer, B.T. Roeder, A. Saastamoinen, and S. Upadhyayula, arXiv:1906.07845 (2019).

[2] F.Sauli, Nucl. Instrum. Methods Phys. Res. **A805**, 2 (2016).

[3] J. Bishop, G. V. Rogachev, E. Aboud, S. Ahn, M. Barbui, A. Bosh, C. Hunt, J. Hooker, D. Jayatissa, E. Koshchiy, C. Pruitt, E. Pollacco, B. T. Roeder, A. Saastamoinen, L. Sobotka, and S. Upadhyayula. *Progress in Research*, Cyclotron Institute, Texas A&M University (2018-2019), p. I-45.

Toward the development of a next generation fast neutron portal monitor

E. Aboud,[1,2] G.V. Rogachev,[1,2] E. Koshchiy,[1] J. Hooker,[1,2] S. Ahn,[1] C. Parker,[1] G. Christian,[1,2]
P. Kuchment,[3] W. Baines,[3] LG. Sobotka,[4] A. Thomas,[4] S. Ota,[1] and V. Johnson[5]
[1]*Cyclotron Institute, Texas A&M University, College Station, Texas*
[2]*Department of Physics & Astronomy, Texas A&M University, College Station, Texas*
[3]*Department of Mathematics, Texas A&M University, College Station, Texas*
[4]*Departments of Chemistry, Washington University, St. Louis, Missouri*
[5]*Department of Statistics, Texas A&M University, College Station, Texas*

The non-proliferation of fissile materials is an important goal for global security. Current generation neutron portal monitors mainly utilize ^{3}He detector counters to detect thermal neutrons. A shortage of ^{3}He has made this technique expensive. Also, the neutron thermalization prevents the use of thermal neutron sources, that can otherwise be employed for active interrogation that is especially useful for detection of ^{235}U. Additionally, all of the directionality information from the neutrons is lost in the thermalization process. Taking inspiration from the Gamma-Ray Burst Monitor [1], we are developing a fast neutron detector that will surpass these limitations. By utilizing a large array of small (2.5cmx2.5cmx2.5cm) p-terphenyl scintillators we can distinguish ambient background neutrons from source neutrons and we can also localize a fissile source. Detecting fast neutrons preserves directional information while also minimizing the sensitivity limitations from the ambient neutron background. The development of this detector is a collaborative effort between the Cyclotron Institute, the department of mathematics, the department of statistics and Washington University. The focus of this report is Monte Carlo simulations of the proposed detector configuration for security applications.

The double neutron scattering technique described in the previous report, [2], was found to be inefficient because of the low frequency of events above a reasonable detector threshold. The new concept was introduced and the simulations have indicated that the downfalls of the previous design can be alleviated. By creating a large array of the p-terphenyl crystals (~2 mean free paths thick) we can continuously sample the ambient neutron background on one half of the detector while measuring neutrons coming from a fissile source on the other half. Each of the crystals are attached to EJ-282 wavelength shifters which have photomultiplier tubes attached at the end. We can readout each of the scintillators to get the neutron flux in each crystal which allows us to determine the direction of the source regardless of the location with respect to the detector. Utilizing multiple of these detectors will provide a powerful apparatus in the detection of fissile materials. Fig.1 is a visualization of the assembled detector array.

Simulations are being conducted in MCNP6 [3] with a Watt fission spectrum sampled ^{235}U+n source and a realistic ambient neutron background taken from data obtained near New Orleans. Simulations have provided encouraging results. Using a basic analysis technique of looking at the number of neutrons scattering per layer of scintillators as a function of the penetration depth, we can clearly identify presence of a localized neutron source. Fig. 2 shows an example of what the simulated

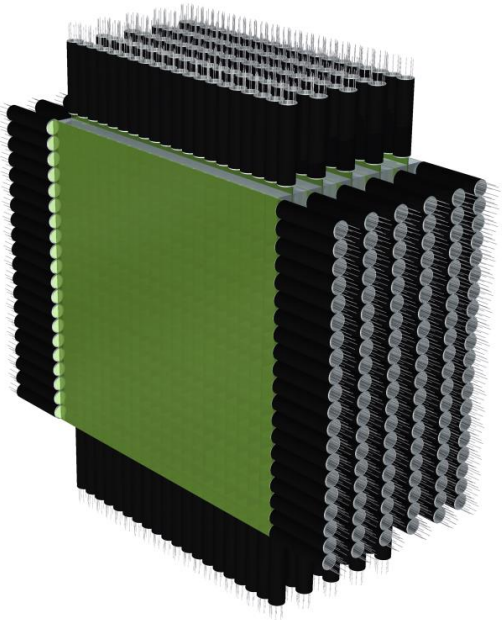

FIG. 1. CAD drawing of the assemble neutron detector. Ideally the source would be emitting towards the exposed face of the apparatus. The black cylinders are the photomultiplier tubes, the green sheets are the EJ-282 wavelength shifters, and the grey cubes are the para-terphenyl scintillators.

data looks like. From this figure, it is clear that for certain source strength it is easy to differentiate the source and the background neutrons.

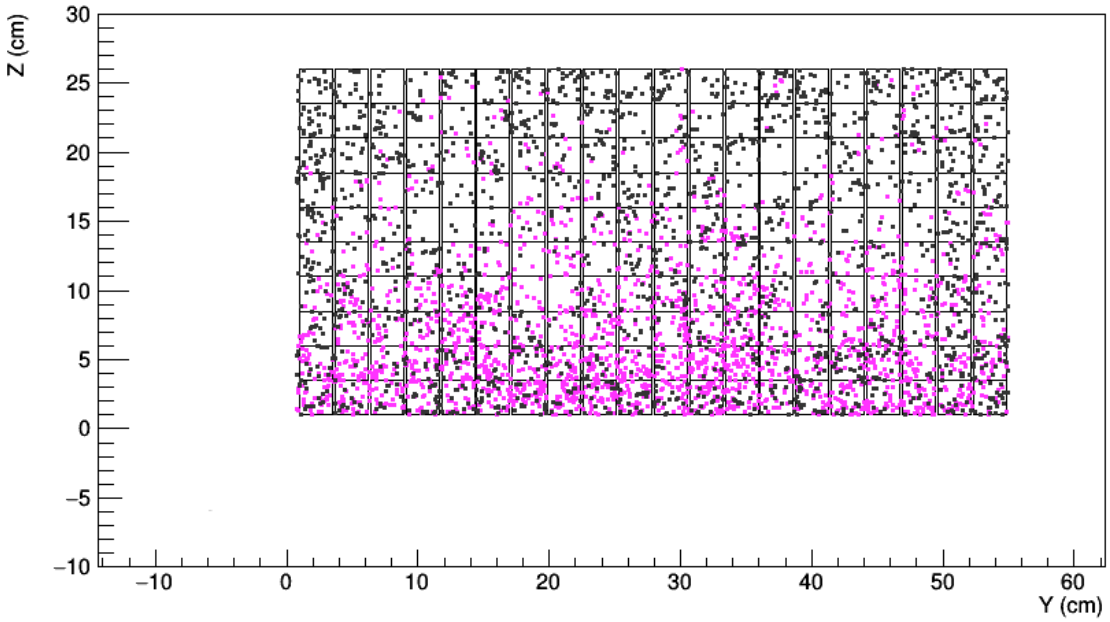

FIG. 2. Example of the MCNP6 simulation data. The square segments are para-terphenyl cubes projected onto a y-z plane. The black dots are neutron scattering events from the ambient neutron background and the magenta dots are neutron scattering events from the ^{235}U+n source. The source is located at negative one meter along the z-axis.

Current progress is being made to determine the minimum source strength that we can accurately identify. To do this we have two parallel methods in progress: one is a statistical model and the other is a deep learning technique. Both of these methods utilize the neutron flux in each crystal, allowing for source recognition regardless of source location.

[1] C. Meegan *et al.*, Astrophys.l J. **702**, 791 (2009).
[2] E. Aboud *et al., Progress in Research*, Cyclotron Institute, Texas A&M University (2017-2018), p. IV-79.
[3] T. Goorley *et al.*, Nucl. Tech. **180**, 298 (2012).

Parallel-plate avalanche counter (PPAC) detector as an MDM focal plane detector

H. Jayatissa, G. Chubaryan, E. Koshchiy, and G.V. Rogachev

Two parallel-plate avalanche counter detectors (PPACs) have been designed and built for MDM focal plane. The main purpose of this detector is to provide a tool to measure tracks of low energy (~1 MeV/u) heavy ions with the MDM spectrometer. It will be utilized for experiments with low energy stable beams to constrain the reaction rates relevant for nuclear astrophysics. The time of flight (ToF) of low energy charged particles traveling between the two PPAC detectors can be used in conjunction with magnetic rigidity for particle ID – separating by A/Z ratios.

In PPAC an electron amplification occurs in two uniform electric fields: between two planar electrodes (cathodes) placed on either side of a common electrode (anode). The two cathodes are composed of a uniform grid of wires made of 50 μm Be-Cu alloy with a pitch of 1 mm. One cathode has wires placed vertically (X-plane) and the other has horizontal wires (Y-plane). The cathode consists of a Mylar foil of thickness 220 μg/cm2 with an aluminum layer of a thickness of 80 μg/cm2 on either side of the Mylar foil. The anodes and the cathode have a separation of ~3 mm defined by the thickness of the printed circuit board (PCB) used to hold the wires and Mylar foil. The detector has an active area of 40 cm x 10 cm. These PPAC detectors have been built and assembled as shown in Fig. 1, and testing is currently underway.

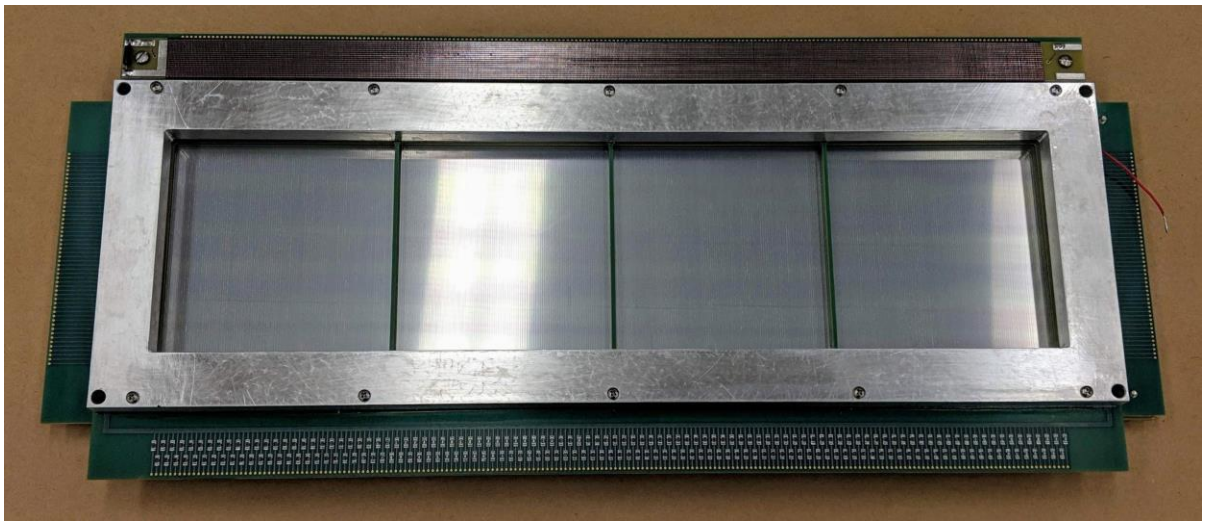

FIG. 1. Picture of an assembled parallel-plate avalanche counter detector.

Control system for TAMUTRAP

M. Nasser, V. Iacob, V.S. Kolhinen, D. McClain, D. Melconian, A. Ozmetin,
B. Schroeder, and P.D. Shidling

TAMUTRAP is upgrading from the 90-mm prototype to the full 180-mm diameter cylindrical Penning trap [1, 2] and which has been installed in the 7-T superconducting solenoid by June 2019. In preparation for it, there have been a number of hardware and software upgrades. These upgrades are for a mixture of improved capabilities and further ease of use for the user.

The first is the furthering of our scan automation for mass resonance measurements using the standard time-of-flight ion cyclotron resonance (TOF-ICR) technique. The original approach of patching LabVIEW and Python together [3] has been altered to a Python-oriented implementation, with LabVIEW being secondary. The upgrades to our scan automation are coded entirely in a Python program referred to as the Scan Automation System (SAS). The SAS allows us to get a wide range of measurements and configurations, and outputs the data in an easy-to-parse format for offline analysis.

We analyze the data collected using the SAS using the Time-of-Flight Fitter and Integrator (TOFFI) program. In a majority of publications, the TOF for an ion in a fit to the resonance curve is calculated as either being proportional to the radial energy, or is an integration based on an approximation to the electromagnetic fields. TOFFI however does its fitting through either numerical integration (such as Gaussian quadrature and trapezoidal summing), or through anti-derivatives and approximations like in the literature. The last phase of TOFFI's development is the inclusion of damping due to the cooling gas in the trap. This has been mostly achieved and can be seen in Fig. 1.

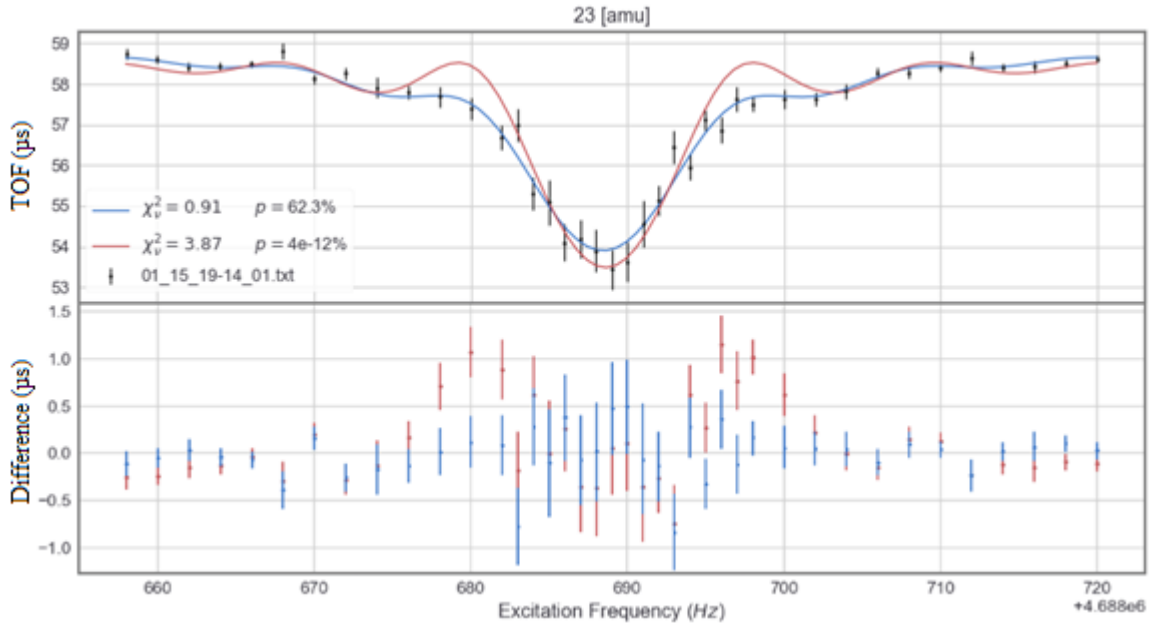

FIG. 1. Resonance spectrum for mass measurement of ^{23}Na. The red curves are fits without dampened structure due to gas pressure, whereas blue are with such structure. The blue is a recent upgrade of May '19, which as the χ^2 indicates represents a significant improvement to the model.

The last large control system project is our PulseBlaster Signal Controller (PBSC). Previously, an FPGA was used to handle pulse timings for controlling electrodes and such. A standing issue though was that its logic TTL was around 2.5V and noisy. For some equipment we required at least 3.3V to operate in certain manners, in particular we were not able to run our function generator in gated mode, complicating our scans as a function of rf frequency. In purchasing a PB24-100-4k-USB timing card, we now have a 5V TTL with the additional benefit of ns resolution on pulse initiation/termination. An enclosure (see Fig. 2.) was constructed for it and software was homebuilt (excluding some pre-made libraries) for use.

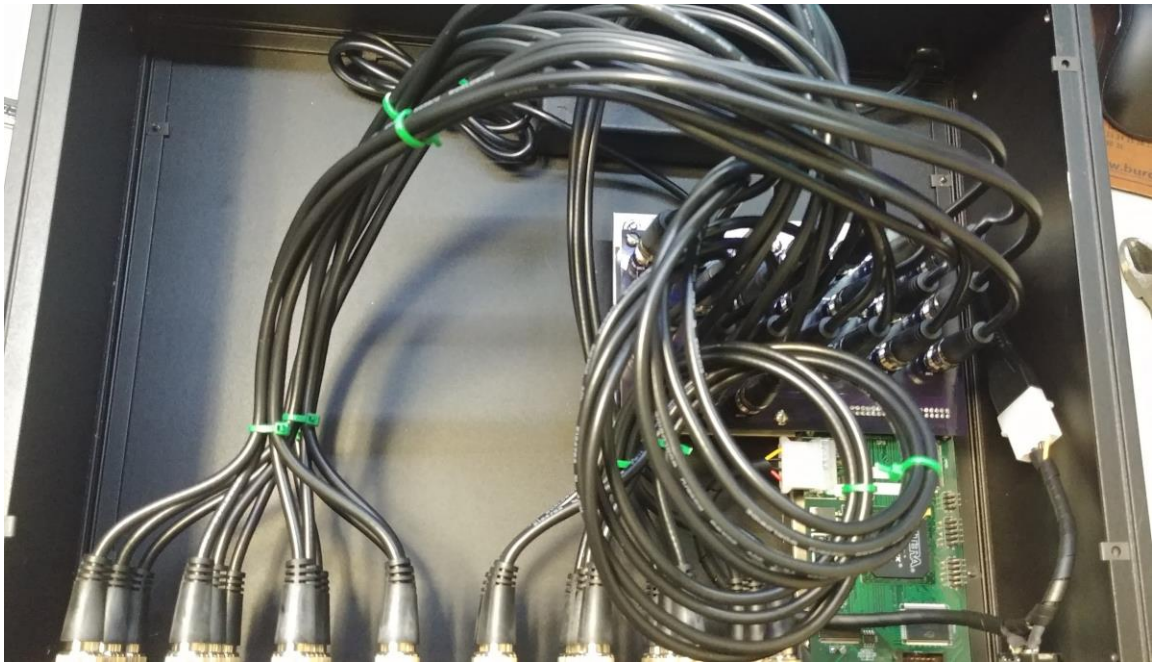

FIG. 2. Inside of the PBSC enclosure during construction. It has 24 channels for signal control run through a USB connection.

[1] V.S. Kolhinen *et al.*, *Progress in Research*, Cyclotron Institute, Texas A&M University (2017-2018), p. IV-42.

[2] V.S. Kolhinen *et al.*, *Progress in Research*, Cyclotron Institute, Texas A&M University (2018-2019), p. IV-45.

[3] R. Burch *et al.*, *Progress in Research*, Cyclotron Institute, Texas A&M University (2017-2018), p. IV-46.

Making the world's largest Penning trap 2x bigger for beta-delayed proton decay studies

V.S. Kolhinen, V.E. Iacob, D. McClain, D. Melconian, M. Nasser, A. Ozmetin, B. Schroeder, and P.D. Shidling

Precision measurements of the correlation parameters and *ft* values of β-decaying nuclei continue to improve our understanding of the fundamental symmetries of the weak interaction. The initial goal of the TAMUTRAP facility is to carry out precision studies of superallowed $T = 2$ β-delayed proton transitions in order to gain information on the β-ν correlation parameter by observing the angular distribution of β and p. The aim is to start with one of ^{20}Mg, ^{24}Si or ^{32}Ar, whichever the Institute is first able to provide with the highest rates.

The cylindrical prototype trap, which has the inner diameter of 90 mm and thus is presently the world largest Penning trap, has been built and commissioned. We have performed mass measurements with stable ^{23}Na, ^{39}K, ^{85,87}Rb and ^{133}Cs singly-charged ions for the test purposes [1, 2]. However, in order to be able to carry out the planned measurement program, we need a cylindrical Penning trap that is double the size to contain the β-delayed protons which have a Larmour radius up to 90 mm.

The new trap, which has a 180-mm inner diameter (see Ref. [3] for its design specifications), has been manufactured and built. Fig. 1 shows a photograph of the assembled trap. The electrodes are made from oxygen-free (OFE) copper and are gold plated (5 μm). Different electrodes are separated by ceramic (Aluminium Oxide) insulators. The lengths of the electrodes are based on a novel design [4] that has larger radius-to-length ratio compared to the typical open-ended cylindrical Penning trap.

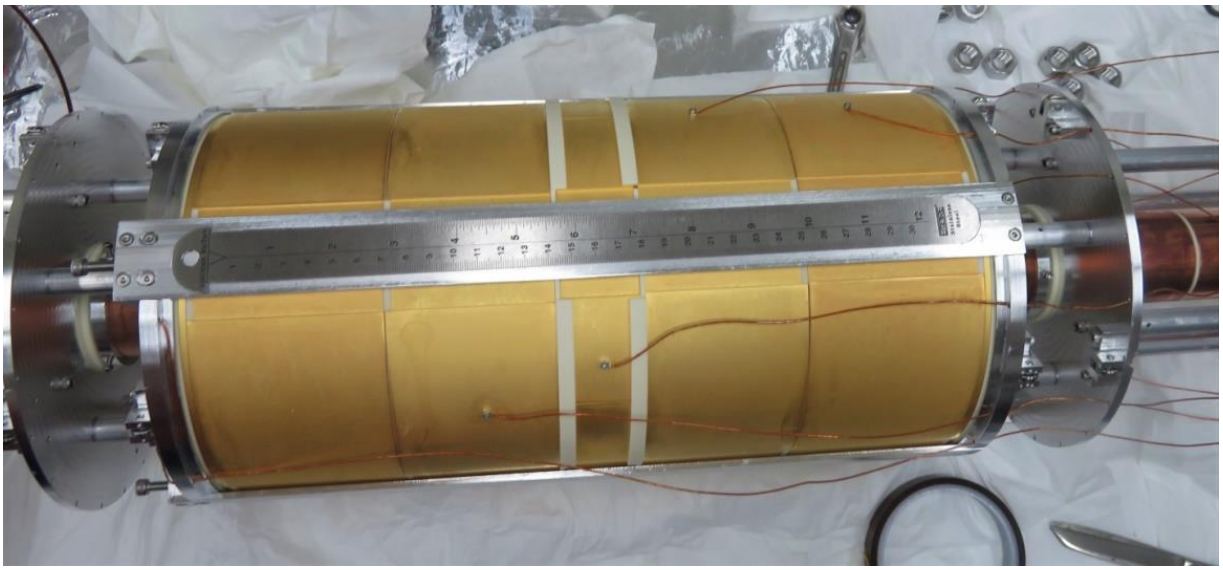

FIG. 1. The electrode structure of 180 mm diameter TAMUTRAP. The ruler on the top of the trap structure is there to demonstrate the size of the trap.

We have also modified the injection drift tube and the extraction electrodes in order to have better control, especially for the extraction of the ions to improve the precision of the time-of-flight from

the trap to a Micro-Channel Plate (MCP) detector as we commission it with mass measurements of stable ions.

The completely assembled trap, including the injection/extraction components and all electronics, has been inserted in a new 197-mm diameter 316L-grade steel vacuum tube and installed in the bore of the 7-T superconducting solenoid from Agilent Technologies. We will commission the new device with offline mass measurements as the coupling of TAMUTRAP to the K150 Cyclotron is developed.

[1] V.S. Kolhinen *et al*., *Progress in Research*, Cyclotron Institute, Texas A&M University (2017-2018), p. IV-39.

[2] P.D. Shidling *et al*., *Progress in Research*, Cyclotron Institute, Texas A&M University (2018-2019), p-IV-47.

[3] V.S. Kolhinen *et al*., *Progress in Research*, Cyclotron Institute, Texas A&M University (2017-2018), p. IV-42.

[4] M. Mehlman *et al*., Nucl. Instrum. Methods Phys. Res. **A712,** 9 (2013).

Update on the TAMUTRAP facility

P.D. Shidling, V.E. Iacob, V. Kolhinen, D. McClain, D. Melconian, N. Morgan,
A. Ozmetin, and B. Schroeder

The initial program of the TAMUTRAP facility is to search for scalar currents in the weak interaction via the measurement of $\beta - \nu$ angular correlation parameter, $a_{\beta\nu}$, for $T = 2, 0^+ \rightarrow 0^+$ superallowed beta-delayed proton emitters. The great advantage of beta-delayed proton emitters for such a study is that the proton energy distribution contains the information about the angle between β and $\nu, \theta_{\beta\nu}$. By observing the proton energy distribution the value of $a_{\beta\nu}$ will be deduced, which can then indicate the existence of a scalar current if it exists. Additional scientific goals for this system are mass measurements, and providing a low-energy radioactive ion beam (RIB) for various other applications.

After demonstrating the ability to perform high-precision mass measurements in a cylindrical Penning trap, we began the year by aligning Section 1 of the TAMUTRAP facility (see Fig. 1) to the T-

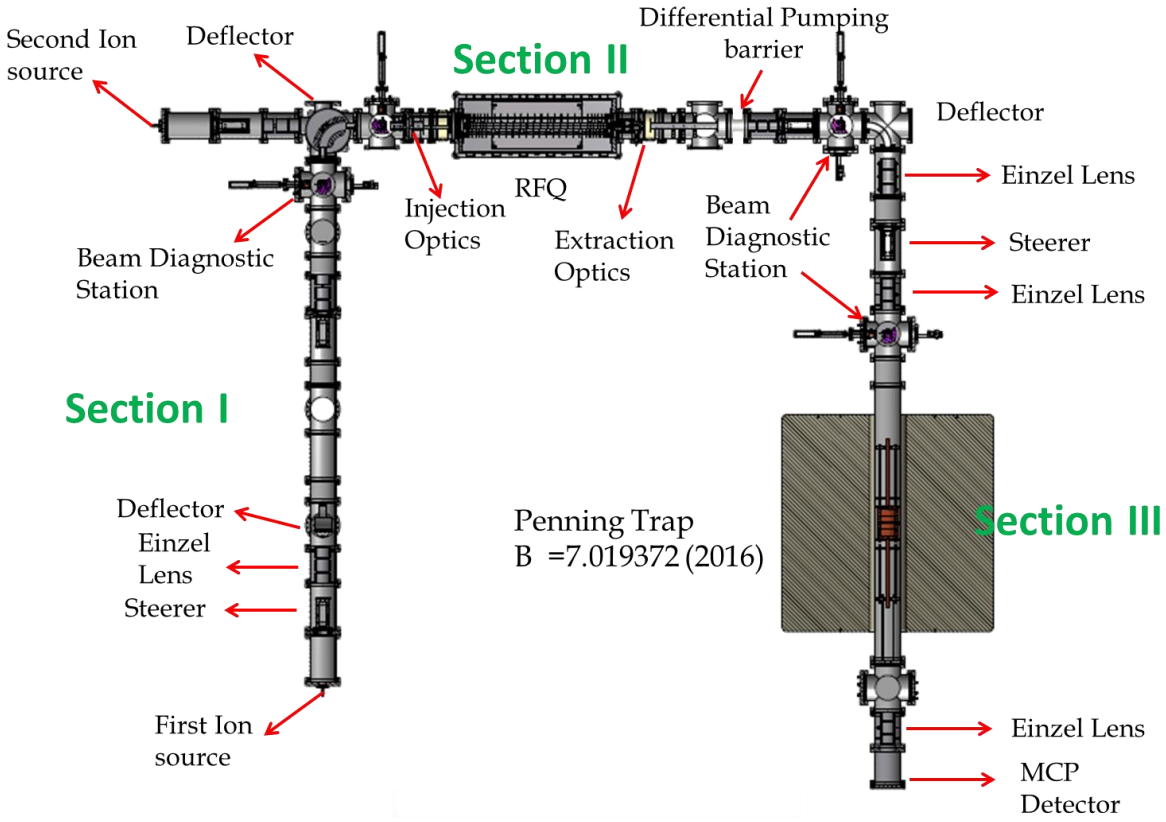

FIG. 1. Texas A&M University Penning Trap Facility (TAMUTRAP).

REX upgrade project and by installing gate valves at two different locations of the beamline. The third cylindrical deflector (Section 3 in Fig. 1) was replaced by spherical deflector to improve the bending efficiency without changing the longitudinal and transverse emittance of the beam. The vacuum in the Section III has been improved by factor of two by installing a differential pumping barrier at the exit of

the He-gas-filled RFQ (see Fig. 1). The differential pumping barrier is a 5"-long tube with an inner diameter of 1.5". The factor of two improvement in the vacuum in Section III of Figure 1 allowed us to perform mass measurements for longer excitation times.

Mass measurements with an excitation time, $T_{RF} = 200$ ms, were performed for several stable isotopes, ^{23}Na, ^{85,87}Rb and ^{133}Cs with ^{39}K as reference mass. The measured masses of ^{23}Na, ^{85,87}Rb and ^{133}Cs agrees with the literature value within a precision of 1.2×10^{-8} with a measurement precision at the 10^{-8} level. In the case of rubidium (^{85,87}Rb) isotopes, a new excitation scheme was implemented for selecting and centering the chosen rubidium isotope in the Penning trap. This technique allows us to operate the Penning trap in a dual mode (purification & measurement trap) and does not rely on the application of buffer gas for selecting and centering the ions. In this method, all trapped ions are first excited with a dipolar field to a large magnetron radius. The ions of interest are then excited resonantly with a quadrupolar field at the sum of the magnetron and the reduced cyclotron frequency. After coupling the radial motions, ions are cooled for 100 ms. During the cooling process, ions of interest are brought back to the trap axis whereas all others move even further out to larger magnetron radii. Once the ions of interest are on the trap axis, the ions are then excited resonantly with a quadrupolar field to measure the cyclotron frequency by time-of-flight resonance technique [2].

The performance of RFQ in bunched mode was improved by rewiring the RFQ electronics and changing the resistors value of last segment which is used to bunch the beam. The change in resistor value of the last segment improved the switching of the last segment during ejection and gave a satisfactory results.

The current prototype Penning trap has an inner diameter of 90 mm and is presently the world's largest Penning trap [1]. However, in order to perform the planned measurement the diameter of the Penning trap needs to be twice the dimension of prototype Penning trap. The assmebly of the TAMU-Penning trap (180 mm diameter) is completed and will be installed in the bore magnet by end of June, 2019. The TAMU-Penning trap system consists of 40 cm long drift tube in the injection side and three drift tube of 15 inch long on the extraction side. The purpose of the three short drift tubes is to guide the ion bunch out of the Penning trap, through the magnetic field to the micro channel plate (MCP) detector located at 1 m distance away from the exit of magnet with higher efficiency. The three short drift tubes will be floated at different voltages to increase the time of flight separation between ions that have gained radial energy during quadrupolar excitation (on-resonance frequency) and the base line (off-resonance frequencies). More details about the 180 mm diameter Penning trap has been described in Ref. [3].

GEANT4 Monte Carlo simulations for the TAMUTRAP Penning trap setup is a work in progress and more detail can be found in Ref. [4]. We also made significant progress in automating the frequency scan for performing mass measurements and have also updated the timing card for TAMUTRAP beamline. Details on automation scan and timing card has been described in Ref. [5].

The immediate outlook for the TAMUTRAP facility involves installing 180 mm inner diameter TAMU-Penning trap system and demonstrate the ability to perform high precision mass measurements. We expect to complete the simulation and finalize the dimensions of the detectors by fall 2019.

[1] P.D. Shidling *et al.*, Hyperfine Interaction, **240**, 40 (2019).

[2] V.S. Kolhinen *et al.*, *Progress in Research*, Cyclotron Institute, Texas A&M University (2017- 2018), p. IV-39.
[3] V.S. Kolhinen *et al.*, *Progress in Research*, Cyclotron Institute, Texas A&M University (2018-2019), p. IV-45.
[4] B. Schroeder *et al*., *Progress in Research*, Cyclotron Institute, Texas A&M University (2018-2019), p.IV-50.
[5] M. Nasser *et al.*, *Progress in Research*, Cyclotron Institute, Texas A&M University (2018-2019), p. IV-43.

GEANT4 simulations of the TAMUTRAP facility

B. Schroeder, V.E. Iacob, V.S. Kolhinen, D. McClain, D. Melconian, M. Nasser,
A. Ozmetin, and P.D. Shidling

The TAMUTRAP facility [1] has the primary goal of measuring the electroweak interaction's beta-neutrino correlation parameter, $a_{\beta\nu}$. This parameter is sensitive to scalar currents in the electroweak charged-current interaction which would be a sign of physics beyond the standard model. We will determine the parameter by measuring the proton spectrum of T=2 superallowed $0^+ \rightarrow 0^+$ beta-delayed proton emitters and separating the spectrum based on whether the proton is detected in the same or opposite hemisphere as the beta particle. In addition, we expect to be able to measure the β-p branching ratios in our system which, with the known lifetimes, would allow us to determine the ft value and perhaps contribute to the evaluation of V_{ud}, the up-down element of the Cabibbo-Kobayashi-Maskawa (CKM) matrix [2].

Circular double-sided silicon strip detectors with central holes will replace the end cap electrodes in the current configuration of the 180-mm diameter Penning trap [3]. Charged particles inside the trap are constrained to an axial position within one Larmor diameter ($D = \frac{2v}{\omega} = \frac{2\beta\gamma mc}{qB}$). With the betas being light and relatively low energy (T ~4 MeV) they are kept within a Larmor diameter of ~10 mm. Because of this, decays taking place on the trap's central axis have a high probability of the beta escaping detection through the central hole. To avoid these losses, we will excite the magnetron motion of the ions, moving them off-axis farther than the 6-mm holes in the end cap electrodes. Distributions of the radii where protons and betas from the superallowed p_0 proton emitting channel hit the detector in simulation are shown below in Fig. 1.

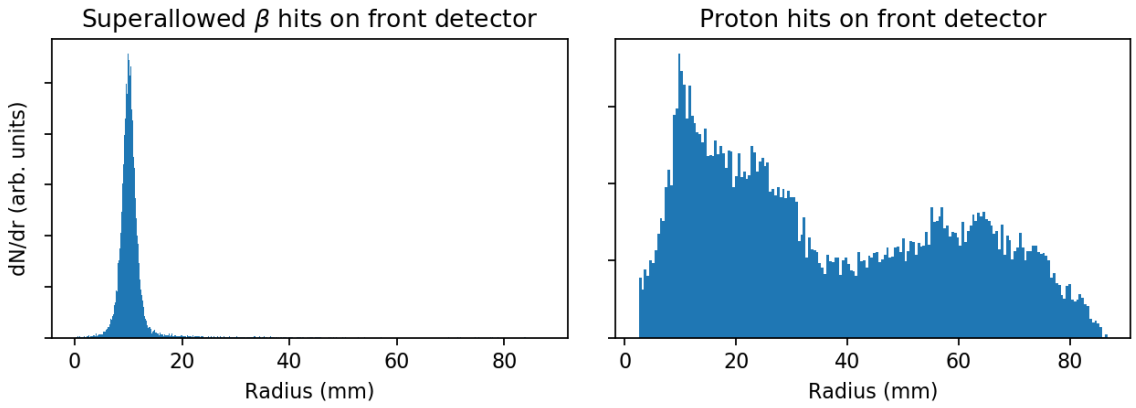

FIG. 1. Simulation of the radial position of the beta (left) and proton (right) in Si detectors following a β-p decay of ^{32}Ar. The βs have a small Larmor radius, so their distribution is essentially the initial radius (in this case, magnetron excitation move them to R=10mm). The protons may have a large helical path and so illuminate more of the detector.

Our simulations [4], which previously simulated only the main beta-delayed-proton branch in the ^{32}Ar decay scheme (with branching ratio 20.50% [5]), have been expanded to allow for a second beta to be produced by the radioactive daughter isotope. Ions are loaded into TAMUTRAP in the 1^+ charge state, so ^{32}Cl ions will be neutral unless there are shake-off electrons. Because the ^{32}Cl ions are neutral in this case, they unaffected by both the electric and magnetic fields which trap the ^{32}Ar. Therefore, the geometric efficiency is effectively much smaller for the betas produced by ^{32}Cl decays than ^{32}Ar decays (approximately 12% efficiency).

Though this simulation does not implement the full decay scheme of ^{32}Ar, the energy spectrum of the ^{32}Cl daughters is not the focus of the study, as the TAMUTRAP detectors will not capture the full energy of the betas. Thus, we have selected samples of 80% decays through the ^{32}Cl (1.1 MeV) state producing two betas and 20% superallowed beta-delayed-proton events producing one beta and one proton.

We are currently analyzing the results of these simulations to determine the precision with which TAMUTRAP will be able to measure the *ft* values of the superallowed transitions, as well as the best strategy for time and spatial separation of the counts due to daughter decays.

[1] P.D. Shidling *et al.*, *Progress in Research*, Cyclotron Institute, Texas A&M University (2018-2019), p. IV-47.

[2] J.C. Hardy and I.S. Towner, Phys. Rev. C **91**, 025501 (2015).

[3] V.S. Kolhinen *et al.*, *Progress in Research*, Cyclotron Institute, Texas A&M University (2018-2019), p. IV-45.

[4] V.S. Kolhinen *et al.*, *Progress in Research*, Cyclotron Institute, Texas A&M University (2017-2018), p. IV-44.

[5] M. Bhattacharya *et al.*, Phys. Rev. C **77**, 065503 (2008).

Development and prototyping of a new highly-segmented neutron detector

C.E. Parker, G.A. Christian, D.P. Scriven, E. Aboud, G.V. Rogachev, S. Ahn, and E. Koshchiy

Developing a highly-pixelated neutron detector made of organic scintillator with good efficiency for 1- to 30-MeV neutrons, fast timing, pulse-shape discrimination (PSD), and ~cm position resolution greatly benefits both national security applications and basic nuclear science. A detector of this type would greatly benefit portal monitors as it would measure fast neutron flux above ambient background, as opposed to easily-shielded γ-rays, without depending on ^{3}He detectors that are only sensitive to thermal neutrons. On the basic science front, studying the invariant mass breakup of n-rich systems, as well as (d,n) or (^{3}He,n) reactions are important both in nuclear astrophysics and the structure of nuclei away from stability.

For the detector, p-Terphenyl ($C_{18}H_{14}$) will be used as the scintillator material because it has a fast decay time, is very bright, and has excellent n/γ PSD. However, there are downsides to selecting p-Terphenyl as it is expensive and difficult to grow in large sizes. These downsides can be mitigated by building a detector array of many smaller cubes and using wavelength shifter (WLS) bars to "pipe" the light to photomultipliers on either end to be read out by PSD-capable ASIC chips.

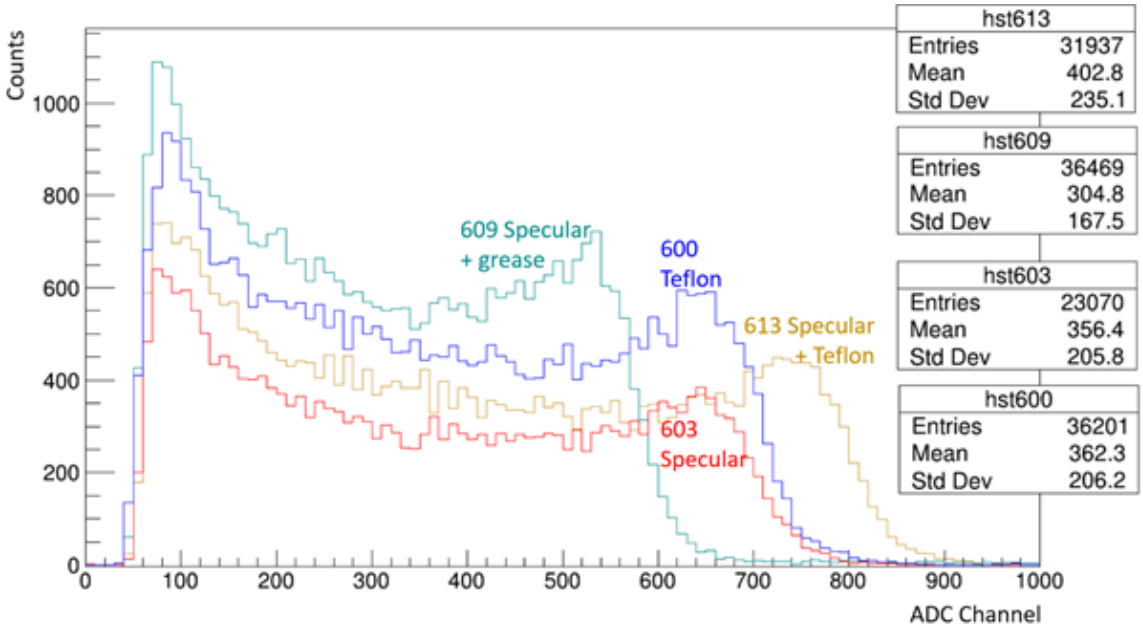

FIG. 1. Comparison of four different cube-wrapping techniques using a ^{137}Cs source; the three-digit numbers correspond to the run number.

To test the concept, small prototype detectors were constructed and tested. These consisted of 10x10x10 mm^3 scintillator cubes with photomultiplier tubes (PMTs) oriented 180° apart in a 3D-printed light-tight plastic housing. The first task was to understand the response of a single cube and a single PMT. To capture the light from the scintillator, a reflective material would need to be selected for the tests. The p-Terphenyl cube was carefully wrapped in either 3M™ Vikuiti™ Enhanced Specular

Reflector film, Teflon tape, or both, on five sides, then coupled with optical grease directly to a PMT. Each wrapping configuration was tested using a ^{137}Cs source placed ~2 cm from the center of the detector to determine which would be used for subsequent tests.

Results of this test are shown in Fig. 1, Upon the results that adding the additional Teflon layer over top of the specular reflector provided the best light collection, the ^{207}Bi and ^{137}Cs sources were used to obtain a rough energy calibration using the Compton edges of the known γ-rays; the conversion electrons (CEs) could not be measured due to the plastic housing. Next, the n/γ PSD of the single-cube setup was tested with a ^{252}Cf source. Adjustments were made to the integration times of the digital acquisition system to separate the neutron and γ-ray events online. Concurrently, waveforms for each event were saved for additional offline analysis.

To test the light pipe technique, a WLS bar was affixed to one side of the cube using Teflon tape while the edges of the WLS bar were optically coupled to the PMTs, as shown in Fig. 2. The signal

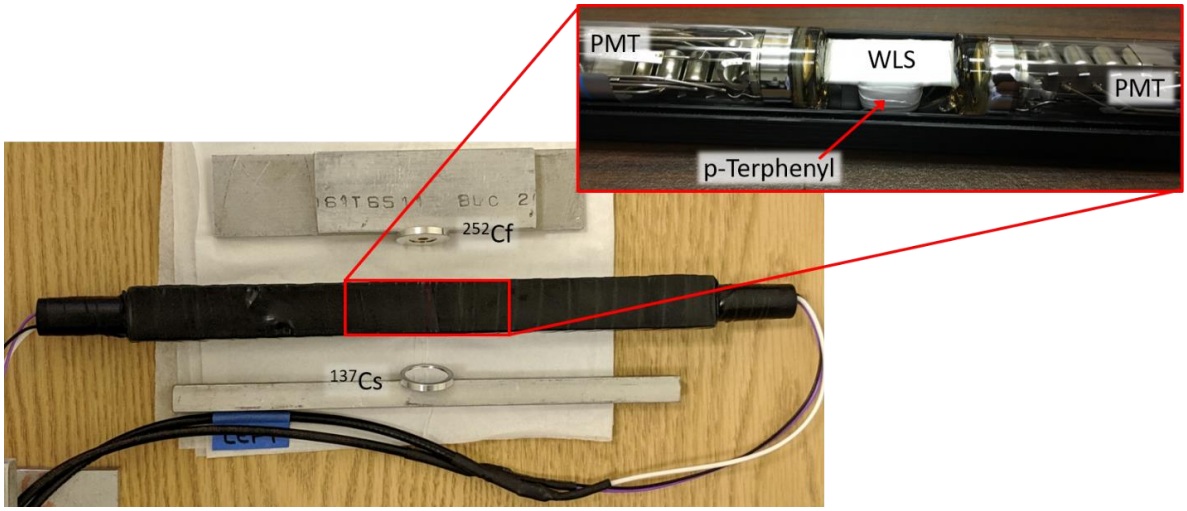

FIG. 2. Experimental set-up for the ^{252}Cf + ^{137}Cs run. The insert shows the specular reflector + Teflon tape-wrapped 10x10x10-mm^3 p-Terphenyl cube and WLS bar and the PMTs with the top of the housing removed.

amplitude was expected to drop when adding the WLS to the system as the emission wavelength of the WLS is higher than the peak absorption wavelength for the PMT. This was visually confirmed on the oscilloscope prior to data collection. The ^{137}Cs and ^{252}Cf sources were fielded at the same time, one on either side of the detector housing, ~2 cm away. This would allow for a known calibration point as the ^{137}Cs source consistently provides the same energy Compton edge and intensity. Fig. 3 shows the PSD results of the summed PMT signals for this experimental set-up.

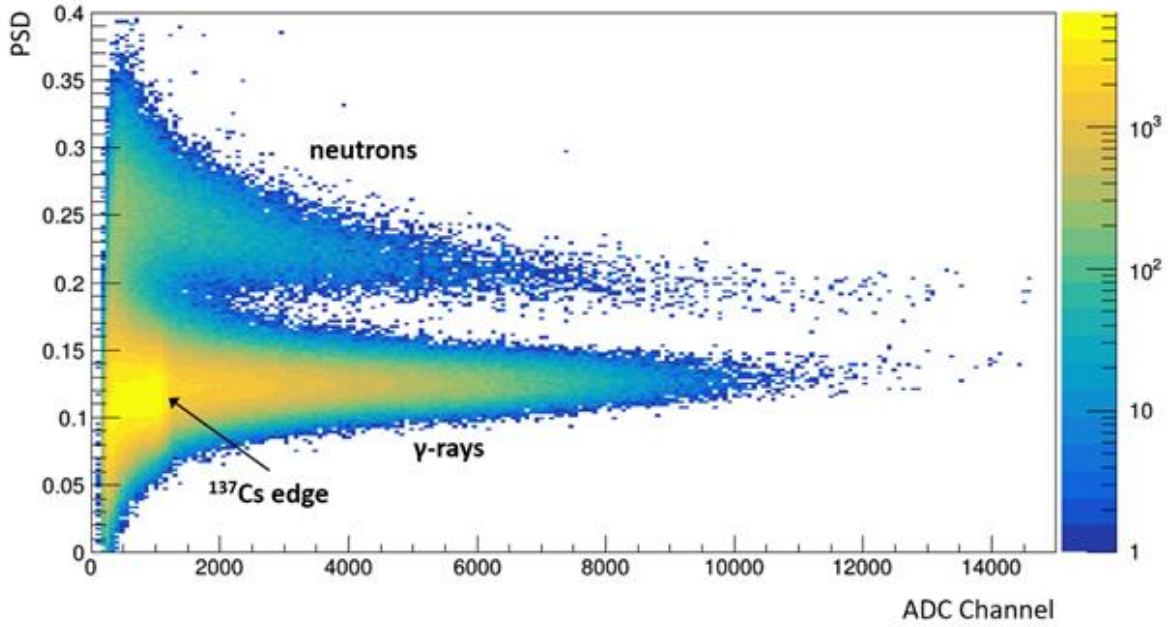

FIG. 3. Summed PSD plot for a 15-hour ^{252}Cf + ^{137}Cs run. The ^{137}Cs edge corresponds to ~470keV.

The path forward will be to measure the signal with the WLS and multiple cubes with two PMTs using the ^{137}Cs and ^{252}Cf sources, followed by testing the configuration with a modified housing to allow the CEs from the ^{207}Bi and ^{137}Cs sources to directly interact with the cube(s). Further development will be to attempt to measure signal in both the X and Y directions using multiple cubes, WLS bars, and PMTs with the offline sources and ultimately at a neutron-producing facility. Parallel efforts to obtain PSD and fast timing using silicon photomultipliers with custom ASIC chips, which would decrease the cost per channel of the large-scale array, are currently being led by collaborators at Washington University, St. Louis.

Optimizing the design of a highly-segmented neutron detector with Geant4

D.P. Scriven and G. Christian

Motivation

Detecting neutrons in the 1-30 MeV range has a wide range of applications to basic nuclear science and national security. Many materials have been optimized for neutron detection, but many are toxic or volatile liquids, and many solid scintillators don't compete. In the last few years, new materials have been formulated to move away from poor performing solids, and hazardous liquids. Development of a new neutron detector array is underway at Texas A&M University. This detector is ultra-segmented and utilizes a new fast, bright, organic scintillator, para-terphenyl. To contrast, p-terphenyl is comparably bright to liquids (brighter than anthracene, stilbene and most plastics), has a fast decay time of 3.7 s, and has excellent PSD. The high degree of segmentation coupled with the properties of the scintillator allow for high-resolution timing and position measurements. The detector (and possible derivatives) have many applications, from Standard Model- and astrophysics, to medicine and stockpile stewardship. In this work we present results from initial simulations using Geant4 to characterize and guide the design process of this instrument.

Investigation

Geant4 has been used to assemble an array 1x1x0.1 m^3, of cubic p-terphenyl crystals. This wall is segmented in x, y, and z; each segment acts as a 3D pixel (a voxel). We were interested how different voxel sizes effect measurements of the detector across a range of timing resolutions and initial neutron energy. Many simulations were performed (210 in total), varying these parameters independently. After all simulations, it was determined that a timing resolution of σ = 200 ps (FWHM of 471 ps) was a reasonable real-life expectation and would suffice for further analysis.

Our Geant code was modified to use MENATE_R [2] scattering models. This detector is designed to detect fast neutrons down to some fractions of 1 MeV. Therefore, the low energy neutron behavior must be modelled correctly. The models in MENATE_R more accurately reproduced scattering cross sections and angular distributions for ^{1}H and ^{12}C, spanning the energy range 1 MeV – 300 MeV. This simulation accounts only for neutron scattering. Light transport and transport efficiencies are not yet implemented. Future simulations with light transport are scheduled, as well as studies of invariant mass measurements.

Results

Several parameters were measured in each simulation to ensure their robustness. These measurements are shown in Fig. 1. Measured kinetic energies are calculated from TOF and were in good agreement with source energies. The kinetic energies used for KE_{obs} are those energies given by the mean of the fit in Fig. 2 left. Our greatest interest is in the energy resolution of the detector with various geometries. To quantify this, two measurements are made; θ_{obs}-θ_{emit}, and $x_{i,real}$-$x_{i,det}$. Here θ is the angle around the z-axis that the neutron is emitted from, and x_i x, y, and z coordinates. These measurements

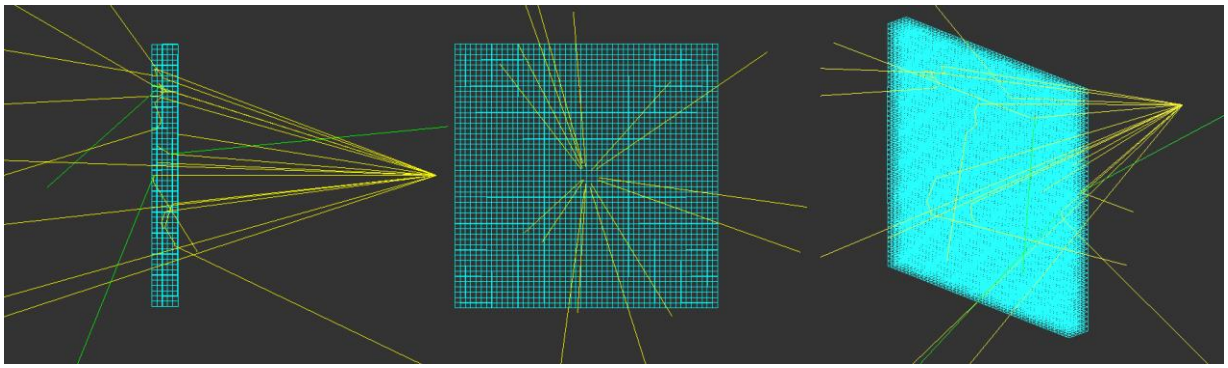

FIG. 1. An image from Geant4 of a 1x1x0.1 m array of 2 cm/side voxels of p-terphenyl. A conic, monoenergetic 10 MeV source of neutrons (shown in yellow) is emitted 1 m from the array. Gammas liberated from Compton scattering are also shown (green).

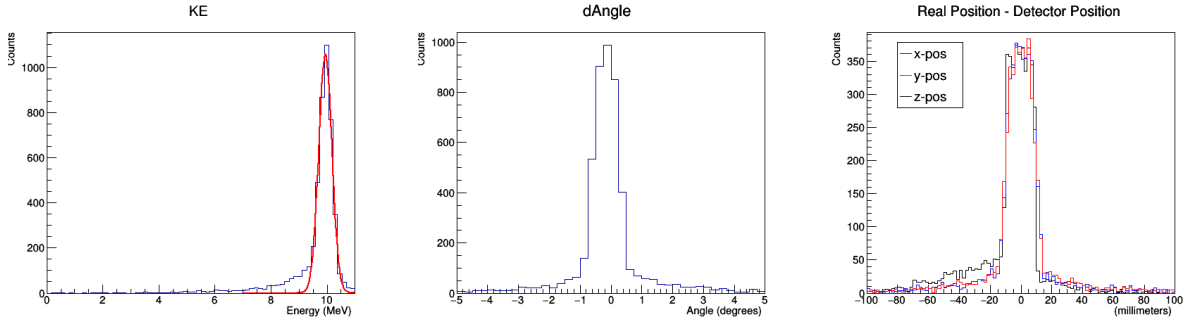

FIG. 2. Measurements from one simulation where 20 mm voxels were used with 10 MeV neutron energy. Left: Measured neutron kinetic energies. Center: the difference in measured vs emitted angle. Right: Difference in crystal location vs real hit location.

were carried out in simulation, and in an analysis routine was created to fit and measure full width half maxima for each simulation. Fig. 3 shows results of this routine.

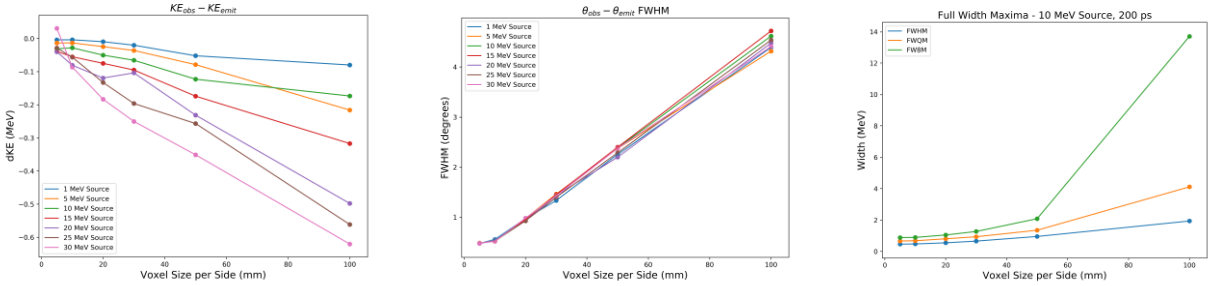

FIG. 3. Left: The emitted source kinetic energy minus the fitted kinetic energy results for different source energies and voxel sizes. Center: The FWHM of the difference in observed angle vs emitted source angle for various voxel sizes and energies. Right: The FWHM of KE for various voxel sizes with a source energy of 10 MeV. This result is representative of all simulations in the range of 1 – 30 MeV energy source neutrons.

One factor of importance in the design of this detector is to be able to ensure a low threshold and reduce multiple scatters. The low energy tail in Fig. 2 left comes from dark scatters in the detector. A dark scatter being an inelastic scatter of the neutron, typically off of carbon in the scintillator, which gives little to no light output. As the neutron is inelastically scattered it will have its direction and kinetic energy changed. Subsequently, this neutron can interact somewhere else in the detector. The now scattered neutron's time of flight has been increased and it is observed somewhere else in the detector. The changed time and interaction coordinate yield a lower KE, and hence a low energy tail. In the case of Fig. 2, (10 MeV neutrons, and 10 mm crystals) about 65% of the detected neutrons lie under the fit, while the low energy tail makes up about 30% of the data. These fractions are heavily dependent on the neutron energy and the voxel size.

Conclusion

Measurements from these Geant4 simulations indicate that voxel sizes below 20 mm begin to give diminishing returns, and yield sub - 1° difference in angle measurement. More simulations are in progress to study how the detector will perform with invariant mass measurements. We also plan to incorporate light transport, as this array will utilize a light piping system. The results of this work are currently being used to guide the design of prototypes under construction at the Cyclotron Institute in collaboration with Washington University in St. Louis. Much progress has been made in the last few months on the experimental side to characterize wavelength-shifting light pipes coupled to PMTs and p-terphenyl scintillators.

This work is supported by the DOE/NNSA CENTAUR grant DE-NA0003841.

[1] Geant4 Collaboration (S. Agostinelli *et. al.*), Nucl. Instrum. Methods Phys. Res. **A506**, 250 (2003).

[2] B. Roeder, "Development and validation of neutron detection simulations for EURISOL", EURISOL Design Study, Report: [10-25-2008-006-In-beamvalidations.pdf, pp 31-44] (2008). URL www.eurisol.org/site02/physics and instrumentation/

[3] Z. Kohley, *et al.*, Nucl. Instrum. Methods Phys. Res. **A682**, 59 (2012).

Progress with the TAMU-ORNL BaF_2 array re-coupling

J. Gauthier, A.B. McIntosh, and I. Jeanis

The re-coupling of the TAMU-ORNL BaF_2 Array detectors [1] is still underway and progresses well. We encountered some issues during the process and figured out solutions. The light leak due to the peeling off of the isolating electrical tape at the junction of the crystal and the photomultiplier tube (PMT) has been resolved by surrounding it with black heat shrink tube. The other main issue that we have is the energy resolution. It's well known that the typical BaF_2 energy resolution for the 662 KeV gamma photoelectric peak from the ^{137}Cs is about 12% [2] but the resolution of our detectors is consistently between 15 and 25%. The most likely explanation is the age of the phototubes that may have caused vacuum and photocathode sensitivity degradation. To test this hypothesis, we ordered two specially designed brand new PMTs from Hamamatsu and tested them with two of our BaF_2 crystals. The energy resolution test comparison is shown in Fig. 1. The same crystal coupled with one of the old PMT has a resolution of 17.7%. With the new PMT, it improves to 11.6%. The other new PMT coupled with another crystal gives a similar result (11.5%).

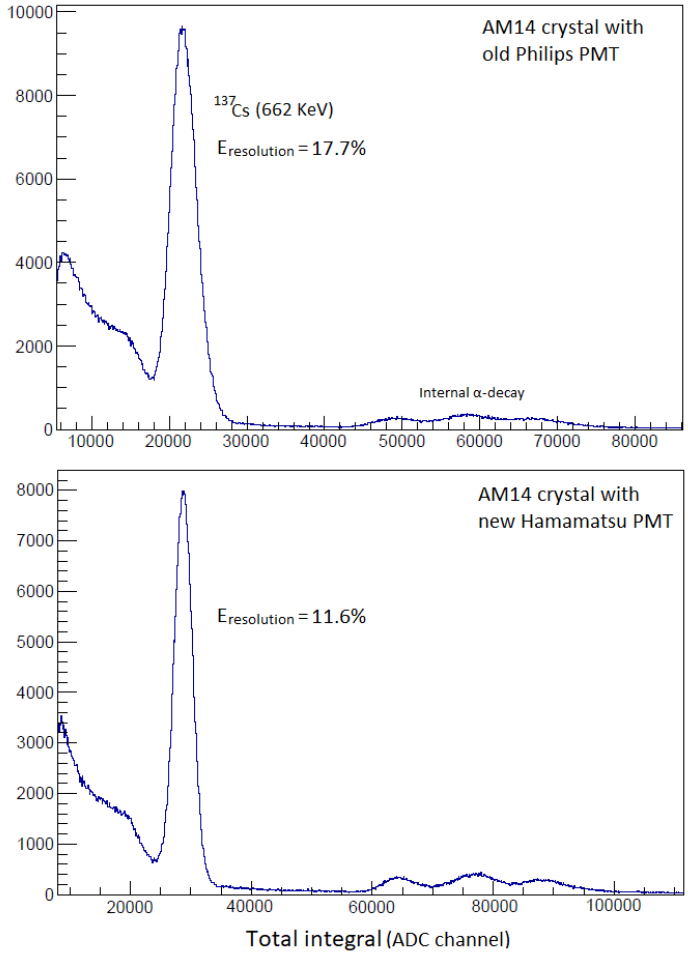

FIG. 1. Old and new PMT energy resolution comparison.

In Fig. 2, we show the calibrated spectra from the ^{137}Cs and ^{60}Co sources acquired by the new PMT coupled with the AM14 crystal. The better resolution provides good separation of the two cobalt peaks.

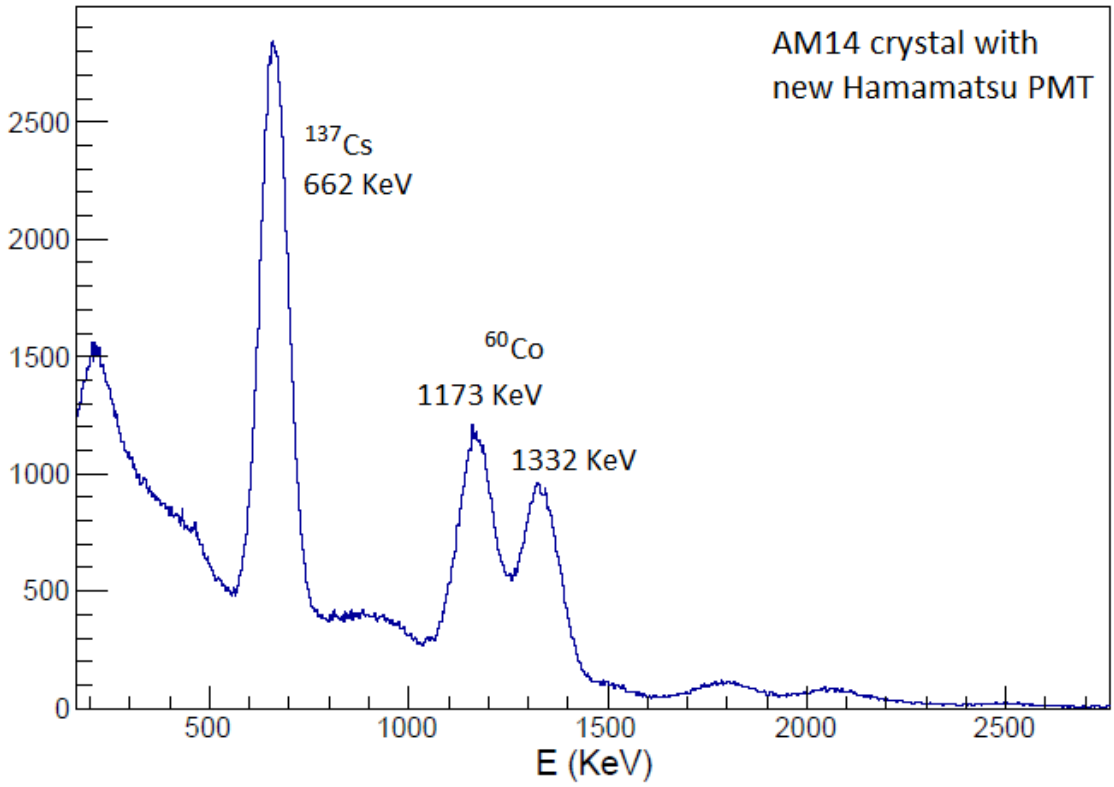

FIG. 2. New PMT calibrated spectra of ^{137}Cs and ^{60}Co sources. Calibration is calculated from the total integral.

Moreover, we determined that the cause of the problem with the pulse shape particle separation was the RTV (*Room-Temperature-Vulcanizing* silicone) we used to re-couple the detectors. Since RTV has a cutoff wavelength very close to the wavelength of the UV light from the BaF_2, a too-thick layer applied induces a suppression of the fast component that is enough to degrade the separation and in some case, completely cancel it. We used heating tape to warm up the crystal-PMT junction at 100^o C in order to decouple the detectors with RTV and replaced it with silicon oil. As we can see in Fig. 3 (top and middle panels) this operation allowed us to recover the particle separation. The bottom panel of Fig. 3 shows the new PMT with oil coupling. The separation is slightly better than the one with the old PMT and we can clearly see the better energy resolution on the x axis.

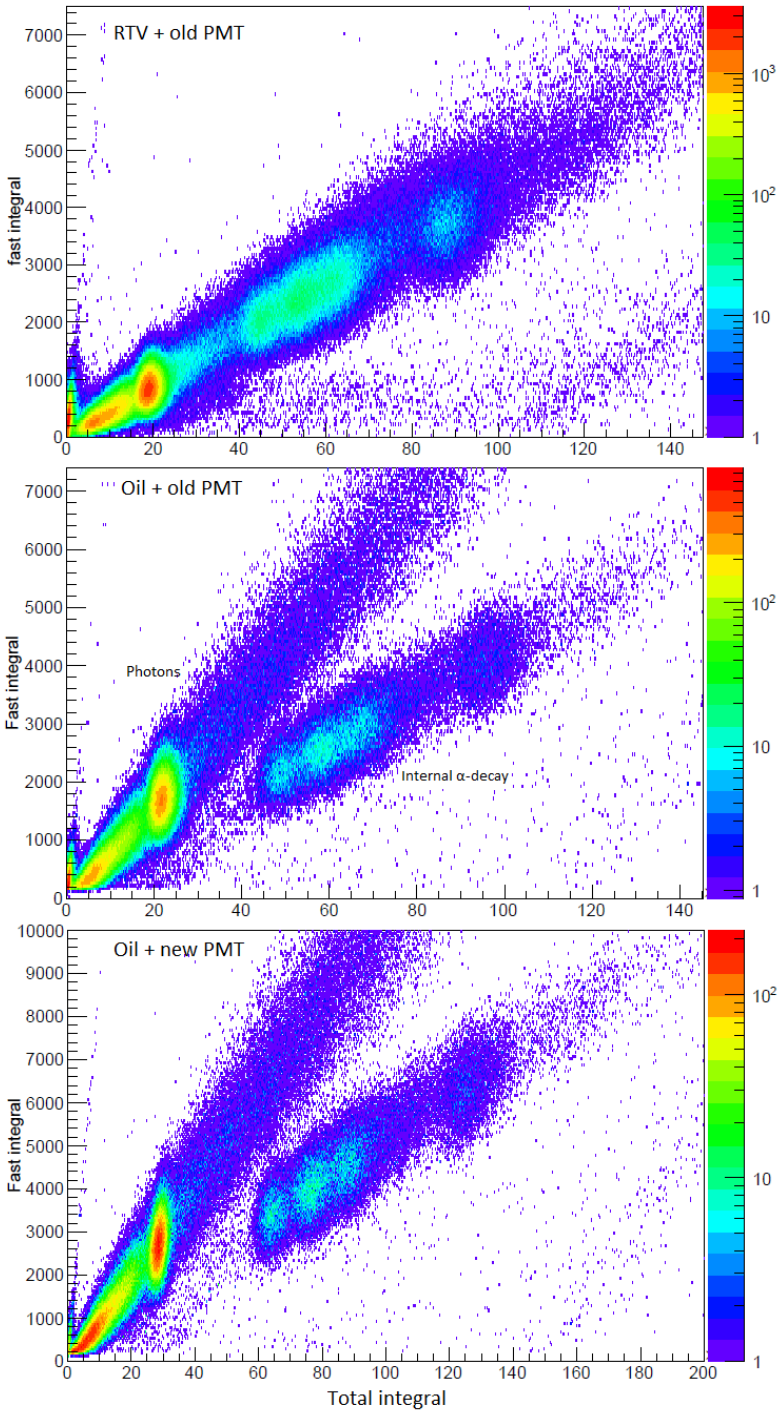

FIG. 3. Fast vs Total integral comparison. Old PMT with RTV coupling is compared with old PMT with silicon oil. The spectrum from the new PMT with oil is shown as well. A ^{137}Cs source was used in all three cases.

[1] A.B. McIntosh *et al.*, *Progress in Research*, Cyclotron Institute, Texas A&M University (2016-2017), p. IV-40.

[2] P. Kozma *et al.*, Nucl. Instrum. Methods Phys. Res. **A314**, 26 (1992).

Experimental implication of PIGE (Particle Induced Gamma Ray Emission) and standard modifications

M. McCarthy, E. Salas, A. Rodriguez Manso, J. Gauthier, and S.J. Yennello

PIGE (Particle Induced Gamma Ray Emission) is an ion beam analysis technique that is used to determine the composition of a sample, and has been implemented.

When low MeV protons interact with the nucleus of a target atom, excitation of the nucleus occurs due to proton induced nuclear reactions. Upon de-excitation, characteristic gamma rays are emitted. PIGE can be used for low Z elements and is sensitive up to parts per million (ppm) [1]. PIGE has been used for identifying per- and polyfluoroalkyl substances (PFAS). PFAS are commonly used in commercial products for waterproofing and fireproofing consumer products. These include food containers, curtains, couch cushions, fireproof foam. However, health and environmental concerns have been linked to PFAS [2].

In November 2018, we used a 3.4 MeV proton beam delivered by the K150 TAMU cyclotron to study a set of cosmetic products to determine if PFAS were contained in the products, in particular products that were marketed as being waterproof. Gamma rays were detected by a XR-100 CdTe diode detector placed 45^{o} from the beam axis. Fluorine has two gamma lines at 110 and 197 keV that are used as a marker for PFAS. Fig. 1 shows an example of a Teflon gamma ray spectra with the distinctives peaks.

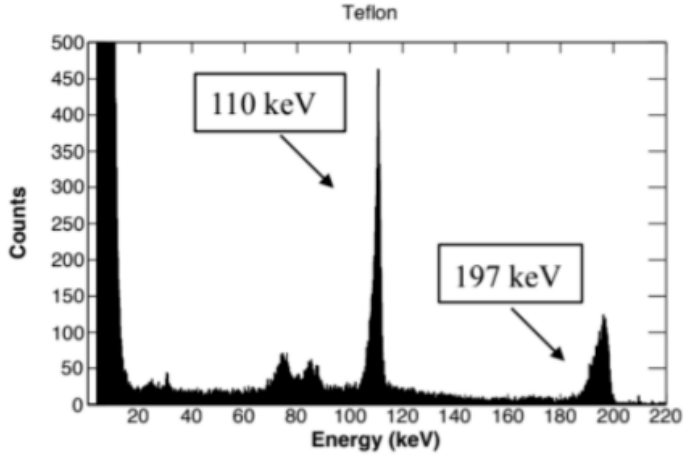

FIG. 1. An example gamma spectra of Teflon. The two distinct Fluorine peaks are marked at 110 and 197 keV.

An example gamma spectra of Teflon. The two distinct Fluorine peaks are marked at 110 and 197 keV.

The summary of the cosmetic products tested for fluorinated compounds concentrations by utilizing the calibration curve in Fig. 2, is shown in Table I. The samples were prepared by swatching a

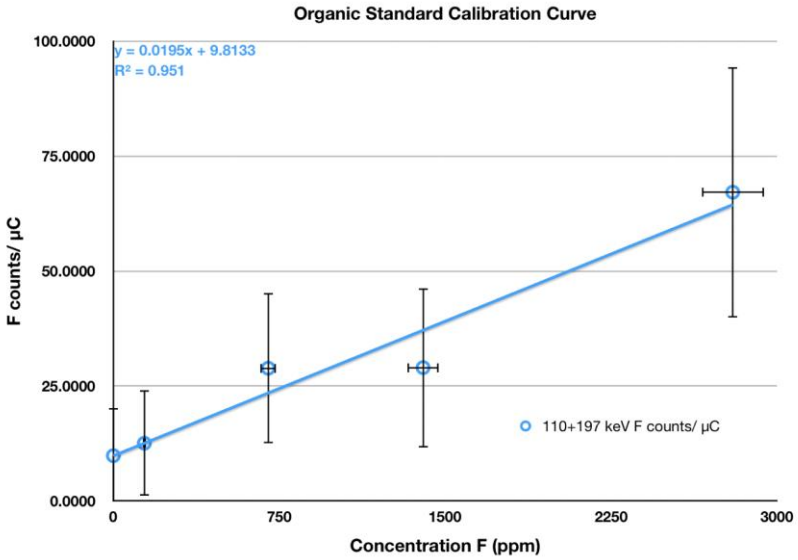

FIG. 2. Organic Standard Calibration Curve. The standards ranged from 0-2800 ppm of F. The plot shows the concentration of the standards versus the normalized Fluorine counts. Errors were computed using statistical and beam errors. The errors are relatively large due to degradation of the standards over the beam exposition.

thin layer on a non fluorinated filter paper. A similar procedure is used where the fluorine gamma lines were integrated and normalized. The trendline in the calibration curve allows the backtrack and determine the concentration from the fluorine counts. These results show a considerable amount of Fluorine was present in multiple cosmetic products labeled as waterproof.

The standards used for the analysis were prepared with PFOA (Perfluorooctanoic acid). PFOA is relatively volatile, and degradation of the standards over beam use has been observed. As a consequence, two new sets of standards were prepared with PFOA and were diluted with methanol and water, and then pipetted on non-flourinated filter paper. Both sets of standards ranged over 0 - 12k ppm of F over two months. These will be tested to determine the longevity of the standards and the degradation due to beam use in future experiments.

Table I. Summary results of the cosmetic products. Over a third of the set shows significant amount of Fluorine present.

Sample Name	Determined Fluorine Concentration (ppm)
Popcorn Bag	4650.0
C10 Pet Proof	Undetectable
Oven Bags	Undetectable
Urban Decay Foundation	Undetectable
Urban Decay Water Proof Powder	2209.74
Clinique Foundation Ever better	Undetectable
Coverfix Foundation	5390.50
Fenty 130 Foundation	Undetectable
Sephora 27 Foundation	Undetectable
Nars Gobi Foundation	Undetectable
Smashbox Concealer Waterproof	Undetectable
Clinique Beyond Perfection Concealer	279.93
Sephora Concealer	1991.19
Muf Primer	Undetectable
Clinique Super Primer	Undetectable
Nars Primer	Undetectable
Laura Geller Matte Primer	Undetectable
Xo Beauty Haroika	658.42
Tarte Shape Tape Concealer	Undetectable
Nars American Women Liquid Lipstick	Undetectable
Jeffree Star Liquid Lipstick	578.75
Wet n Wild Liquid Catsuit	1883.14
Milani Liquid Lipstick	129.37
NYX Stockholm Lipstick	1608.29
Kat Von D Bauha 5	1260.07
Anastasia Beverly Hills Liquid Lipstick	139.24
Dose of Colors Stone Liquid Lipstick	1497.26
Mac Lipstick	Undetectable
Stila Liquid Eyeshadow	Undetectable
Urban Decay Eye Primer	1098.84
Too Faced Melted Lipstick	Undetectable
Tarte Lip Paint Man Bun	Undetectable
Pixi Au Naturelle Liquid Lipstick	Undetectable
Tarte Blush Art Deco	1602.60
Tarte Eyeshadow Caretaker	Undetectable
Fenty Contour	Undetectable
Anastasia Beverly Hills Eyebrow Gel	Undetectable
Anastasia Beverly Hills Brow Pomade	Undetectable

[1] M.B.H. Breese, D.J. Jamieson, and P.J.C. King, *Materials Analysis using a nuclear microprobe*, (John Wiley & Sons, New York, 1996).

[2] Zhanyun Wang, Jamie C. DeWitt, Christopher P. Higgins, and Ian T. Cousins, Environ. Sci. Tech. **51**, 2508 (2017); 10.1021/acs.est.6b04806.

Neutron ball background testing

A. Jedele, K. Hagel, and S.J. Yennello

In the summer of 2018, the configuration of cave 4 was changed to accommodate the AGGIE spectrometer. The concrete wall shielding around the beam dump and the concrete half-wall located right behind the neutron ball were removed, and a new beam dump was designed and installed. Due to the new configuration, the neutron distribution within the cave has changed.

The neutron ball[1] is a neutron detector and is part of the NIMROD multi-detector array. It consists of six segments filled with EJ-335 (pseudocumene and mineral oil) doped with 0.25% wt Gd[2]. In NIMROD experiments, the neutron multiplicity is measured by counting the number of signals within two consecutive 100 μs gates. Understanding the background rate within each gate is essential to accurately measuring the neutron multiplicity.

Initial measurements were taken with a Ne-22 beam @ 19 MeV/nuc on the K150 beam in July (before the cave was reconfigured). Results showed a 1000 counts/sec background without beam with a 10% efficiency. Upon tuning the beam through a blank target frame, the background rate increased to ~2000 counts/sec. Results from a 5.0 mg/cm^2 Sn target showed a rate of 60,000 counts/sec.

In September, the experiment was repeated with the new configuration consisting of a new beam dump and the removal of the half-wall behind the neutron ball. The background rate without beam was still 1000 counts/sec. Initially, when the beam was tuned through the blank target, the beam on background rate was 6000 counts/sec. The Sn target produced a rate of 200,000 counts/sec with 0.3 nA on FC02. When the beam viewer was placed in the beam line, right upstream of the beam dump, it was concluded the dispersion in the x-direction was larger than the target frame at the target position. The beam viewer, located where the half-wall used to be, showed the dispersion in the x-direction was large, however it did not completely cover the viewer. The beam was re-tuned onto the beam dump without a target in the target position. The beam-on background rate was 1500 counts/sec. The beam was also tuned to align the Maryland magnet and two quadrupole magnets (in the cave) and the rate through the blank target frame was 2400 counts/sec and 3000 counts/sec for a Zn target.

The K500 was used to further test the beam dump due to the less dispersive nature of the beam. The background measurement without beam was 8,000 counts/sec at an efficiency of 55% and the beam-on background rate was 10,000 counts/sec with 600 nA on the beam dump. The neutron count was measured in six 100 μs gates. The results are seen in Table I. Each row corresponds to a different attenuation setting with no attenuation corresponding to 600 nA. The neutron gates were triggered using a Si detector. Two measurements were taken for the 1 x 10^{-2} attenuation setting, corresponding to the phase shifter being turned off and on.

Table I. Neutron count in six consecutive 100 μs gates triggered by an event in a Si detector. Results show a large initial neutron rate followed by a large asymptotic drop off. The last column is the difference between the 1st window and the average of the next 5.

Neutron Count							
Attenuation	1st window	2nd window	3rd window	4th window	5th window	6th window	$\Delta x = (x_1 - (\overline{x_{2-6}}))$
1×10^{-2}	10.96 ± 0.15	2.35 ± 0.09	2.13 ± 0.08	2.00 ± 0.08	1.91 ± 0.08	2.16 ± 0.10	8.85 ± 0.17
10^{-2} - ps off	11.02 ± 0.11	4.39 ± 0.11	4.36 ± 0.11	4.22 ± 0.11	3.90 ± 0.09	4.18 ± 0.11	6.81 ± 0.14
3×10^{-3}	9.63 ± 0.24	1.77 ± 0.12	1.84 ± 0.16	2.29 ± 0.22	2.00 ± 0.18	1.91 ± 0.19	7.67 ± 0.30
1×10^{-3}	9.02 ± 0.17	2.21 ± 0.17	2.15 ± 0.16	2.20 ± 0.16	2.14 ± 0.16	1.84 ± 0.13	6.91 ± 0.23
3×10^{-4}	8.56 ± 0.24	1.76 ± 0.17	2.14 ± 0.22	1.97 ± 0.27	1.84 ± 0.17	1.82 ± 0.20	6.65 ± 0.32

Beam shielding studies were performed looking at the effect of adding bags of borated polyethylene ("green board") shavings around the beam pipe right upstream of the beam dump. Table II shows the results in the first two 100 μs gates. The results shown are for no shielding, one layer (3 bags) of green board shavings, 2nd layer around initial layer and a layer upstream, a 2nd layer around the more upstream layer, and a lead brick wall. The lead wall was placed right upstream from the 2nd layer of green board shavings. The results indicate adding layers of green board shavings decreases the neutron rate slightly. The addition of a lead wall did increase the rate in the 1st 100 μs gate, which does not rule out the possibility that the beam is hitting the pipe upstream of the wall. It is believed that the increase in neutron count after the lead brick indicates gamma rays produced from neutron capture is not a large contributor in the neutron ball background rate.

Table II. Results for beam shielding studies. The 1st column consists of the neutron count in the first 100 μs gate and the 2nd column is the neutron count in the 2nd 100 μs gate.

Beam Shielding Effects - Neutron Count		
Beam Shielding	1st window	2nd window
No shielding	8.86 ± 0.13	2.89 ± 0.16
1 layer of green board bags	8.76 ± 0.07	2.63 ± 0.07
2nd layer of bags and 1 layer upstream	8.67 ± 0.12	2.35 ± 0.10
2nd layer of bags upstream	8.48 ± 0.11	2.58 ± 0.12
Lead brick wall upstream of bags	8.80 ± 0.08	2.61 ± 0.09

The neutron ball background rate was characterized for the new cave 4 configuration and beam shielding studies were conducted. The results indicate that the beam dump is successful at thermalizing and capturing neutrons. However, the neutron rates indicate that the beam is hitting the beam pipe, creating a larger background rate than the previous configuration. We are studying how to mitigate these issues.

Comparing the K500 beam pulser and phase shifter: A timing study

A. Jedele, K. Hagel, and S.J. Yennello

There are currently two methods to turn off the beam on the K500 on a "fast" time scale in real time during data taking. The beam pulser consists of two plates located on the injection line just downstream of the ECR ion source. An electrical field is applied to divert the beam from the cyclotron. The time of the beam to turn off at the target is limited by the time it takes for the remaining beam after the plates to cycle through the cyclotron and travel to the cave. The phase shifter, in contrast, changes the phase of the cyclotron, causing the beam to be stopped within the cyclotron. The limiting factor is the time needed to change the phase of the cyclotron.

The time required to turn off the beam is of great concern for NIMROD experiments. The free neutron multiplicity is measured using the neutron ball detector [1] through neutron capture on Gd. Scalers are used to measure the number of hits within 2 consecutive 100 μs gates. As soon as the data acquisition is triggered, a signal is sent to turn the beam off to mitigate the background rate during the capture time of the neutron ball. The beam must be turned off as quickly as possible to ensure a free neutron multiplicity measurement with minimum contamination from background.

A Si detector was placed at directly in the beam in the NuStars chamber. The computer was triggered using the Si signal. The RF signal was input into a scaler to create a clock. This scaler was cleared at the same time that the signal was sent to turn the beam off. The beam was turned on for 30 ms and then turned off for 30 ms. The RF frequency was multiplied by the scaler value to obtain the time of further hits in the Si detector.

The results are shown in Fig. 1. The beam pulser (left side) turns off within 50 μs and the phase shifter (right) turns off within 100 μs. The first peak appears in at 20 μs due to VME timing, which

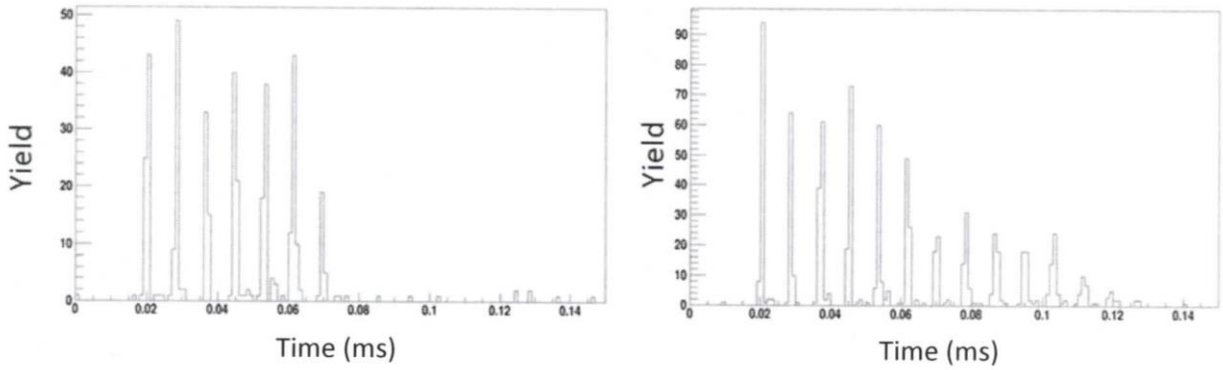

FIG. 1. Timing of the beam pulser (left) and the phase shifter (right). The timing is plotted in microseconds. The beam pulser turns off in 40 μs with some beam leaking through up to 50 μs . The phase shifter turns out within 100 μs with most turning off within 80 μs. The first peak comes in 20 μs late due to VME dead times. The 7 μs interval between peaks also corresponds to VME read out time.

correlates to the last peak coming 20 μs later than the actual value. Most of the beam is absent within 40 μs for the beam pulser with a small amount of beam leaking in up to 10 μs later. The phase shifter turns off within 80 μs with some beam leaking in up to 100 μs. The 7 μs spacing between peaks is due to

VME read-out timing. The percentage of beam leaking through after the beam has been completely turned off was not tested in this experiment due to threshold changes between measurements and the amount of noise was not quantified.

SECTION V

PUBLICATIONS

PAPERS PUBLISHED
April 1, 2018– March 31, 2019

Connection between asymptotic normalization coefficients and resonance widths of mirror states, A.M. Mukhamedzhanov, Phys. Rev. C **99**, 024311 (2019).

Equilibration chronometry and reaction dynamics, A.R. Manso, A.B. McIntosh, K. Hagel, L. Heilborn, A. Jedele, A. Wakhle, A. Zarrella, and S.J. Yennello, Il Nuovo Cimento C **41**, 180 (2019).

Examination of evidence for resonances at high excitation energy in the 7α disassembly of ^{28}Si, X.G. Cao, E. Kim, K. Schmidt, K. Hagel, M. Barbui, J. Gauthier, S. Wuenschel, G. Giuliani, M.R.D. Rodrigues, S. Kowalski, H. Zheng, M. Huang, A. Bonasera, R. Wada, N. Blando, G. Zhang, C.Y. Wong, A. Staszczak, Z.X. Ren, Y.K. Wang, S.Q. Zhang, J. Meng, and J.B. Natowitz, Phys. Rev. C **99**, 014606 (2019).

Experimental liquid-gas phase transition signals and reaction dynamics, R. Wada, W. Lin, P. Ren, H. Zheng, X. Liu, M. Huang, K. Yang, and K. Hagel, Phys. Rev. C **99**, 024616 (2019).

Isospin effects in nuclear reactions, S. Yennello, Il Nuovo Cimento C **41**, 170 (2019).

Spectral characterization by CVD diamond detectors of energetic protons from high-repetition rate laser for aneutronic nuclear fusion experiments, M. Cipriani, F. Consoli, P.L. Andreoli, D. Batani, A. Bonasera, G. Boutoux, F. Burgy, G. Cristofari, R.D. Angelis, G.D. Giorgio, J.E. Ducret, A. Flamigni, D. Giulietti, K. Jakubowska, C. Verona, G. Verona-Rinati, J. Instrum. **14**, C01027 (2019).

The partial truncated icosa- hedron phoswich array for detection of low energy charged pions and light charged particles, A. Zarrella, E. Churchman, J. Gauthier, K. Hagel, L. Heilborn, A. Jedele, Y. Lui, A.B. McIntosh, A.R. Manso, A. Wakhle, M.D. Youngs, and S.J. Yennello, Nucl. Instrum. Methods Phys. Res. **A915**, 47 (2019).

β-delayed γ decay of ^{20}Mg and the ^{19}Ne(p, γ)^{20}Na breakout reaction in Type I X-ray bursts, B.E. Glassman, D. Pérez-Loureiro, C. Wrede, J. Allen, D.W. Bardayan, M.B. Bennett, B.A. Brown, K.A. Chipps, M. Febbraro, M. Friedman, C. Fry, M.R. Hall, O. Hall, S.N. Liddick, P.O'Malley, W.J. Ong, S.D. Pain, C. Prokop, S.B. Schwartz, P. Shidling, H. Sims, P. Thompson, H. Zhang, Phys. Lett. B **778**, 397 (2018).

^{7}Li(^{15}N,^{14}C)^{8}Be reaction at 81 MeV and ^{14}C +^{8}Be interaction versus that of ^{13}C +^{8}Be, A.T. Rudchik, A.A. Rudchik, L.M. Muravynets, K.W. Kemper, K. Rusek, E.I. Koshchy, E. Piasecki, A. Trzcińska, V.M. Pirnak, O.A. Ponkratenko, I. Strojek, A. Stolarz, V.A. Plujko, S.B. Sakuta, R. Siudak, A.P. Ilyin, Y.M. Stepanenko, Y.O. Shyrma, and V.V. Uleshchenko, Nucl. Phys. **A971**, 138 (2018).

AstroBox2E: a detection system for very low energy β-delayed proton decay, I.C. Stefanescu, A. Spiridon, L. Trache, E. Pollacco, A. Saastamoinen, and B. Roeder, J. Phys. Conf. Series **1024**, 012007 (2018).

Computational and experimental forensics characterization of weapons-grade plutonium produced in a thermal neutron environment, J.M. Osborn, K.J. Glennon, E.D. Kitcher, J.D. Burns, C.M. Folden, S.S. Chirayath, Nucl. Eng. Technology **50**, 820 (2018).

Constraining neutron capture cross sections for unstable nuclei with surrogate reaction data and theory, J.E. Escher, J.T. Burke, R.O. Hughes, N.D. Scielzo, R.J. Casperson, S. Ota, H.I. Park, A. Saastamoinen, T.J. Ross, Phys. Rev. Lett. **121**, 052501 (2018).

Direct measurement of astrophysically important resonances in ^{38}K(p, γ)^{39}Ca, G. Christian, G. Lotay, C. Ruiz, C. Akers, D.S. Burke, W.N. Catford, A.A. Chen, D. Connolly, B. Davids, J. Fallis, U. Hager, D. Hutcheon, A. Mahl, A. Rojas, and X. Sun, Phys. Rev. C **97**, 025802 (2018).

Entry-level spin distributions and relative γ-neutron branching ratios of samarium isotopes populated by the (p, t) reaction, N. Cooper, C.W. Beausang, P. Humby, A. Simon, J.T. Burke, R.O. Hughes, S. Ota, C. Reingold, A. Saastamoinen, E. Wilson, Phys. Rev. C **98**, 044618 (2018).

Evidence for prevalent Z = 6 magic number in neutron-rich carbon isotopes, D.T. Tran, H.J. Ong, G. Hagen, T.D. Morris, N. Aoi, T. Suzuki, Y. Kanada-En'yo, L.S. Geng, S. Terashima, I. Tanihata, T.T. Nguyen, Y. Ayyad, P.Y. Chan, M. Fukuda, H. Geissel, M.N. Harakeh, T. Hashimoto, T.H. Hoang, E. Ideguchi, A. Inoue, G.R. Jansen, R. Kanungo, T. Kawabata, L.H. Khiem, W.P. Lin, K. Matsuta, M. Mihara, S. Momota, D. Nagae, N.D. Nguyen, D. Nishimura, T. Otsuka, A. Ozawa, P.P. Ren, H. Sakaguchi, C. Scheidenberger, J. Tanaka, M. Takechi, R. Wada, and T. Yamamoto, Nature Communications **9**, 1594 (2018).

Excited levels in the multishaped ^{117}Pd nucleus studied via β decay of ^{117}Rh, J. Kurpeta, A. Płochocki, W. Urban, T. Eronen, A. Jokinen, A. Kankainen, V.S. Kolhinen, I.D. Moore, H. Penttilä, M. Pomorski, S. Rinta-Antila, T. Rząca-Urban, J. Wiśniewski, Phys. Rev. C **98**, 024318 (2018).

Experimental survey of the production of α-decaying heavy elements in ^{238}U + ^{232}Th reactions at 7.5-6.1 MeV/nucleon, S. Wuenschel, K. Hagel, M. Barbui, J. Gauthier, X.G. Cao, R. Wada, E. Kim, Z. Majka, R. Płaneta, Z. Sosin, A. Wieloch, K. Zelga, S. Kowalski, K. Schmidt, C. Ma, G. Zhang, J.B. Natowitz, Phys. Rev. C **97**, 064602 (2018).

High-precision half-life measurement of the β+ decay of ^{21}Na, P.D. Shidling, R.S. Behling, B. Fenker, J.C. Hardy, V.E. Iacob, M. Mehlman, H.I. Park, B.T. Roeder, and D. Melconian, Phys. Rev. C **98**, 015502 (2018).

Neutron-proton equilibration in 35 MeV/u collisions of ^{64,70}Zn +^{64,70} Zn and ^{64}Zn, ^{64}Ni +^{64}Zn, ^{64}Ni quantified using triplicate probes, L.W. May, A. Wakhle, A.B. McIntosh, Z. Kohley, S. Behling, A. Bonasera, G. Bonasera, P. Cammarata, K. Hagel, L. Heilborn, A. Jedele, A. Raphelt, A.R. Manso, G. Souliotis, R. Tripathi, M.D. Youngs, A. Zarrella, S.J. Yennello, Phys. Rev. C **98**,044602 (2018).

Neutron-rich rare isotope production with stable and radioactive beams in the mass range A ∼ 40 − 60 at beam energy around 15 MeV/nucleon, A. Papageorgiou, G.A. Souliotis, K. Tshoo, S.C. Jeong, B.H. Kang, Y.K. Kwon, M. Veselsky, S.J. Yennello, and A. Bonasera, J. Phys. G **45**, 095105 (2018).

New result for the neutron β-asymmetry parameter A_0 from UCNA, M.A. Brown, E.B. Dees, E. Adamek, B. Allgeier, M. Blatnik, T.J. Bowles, L.J. Broussard, R. Carr, S. Clayton, C. Cude-Woods, S. Currie, X. Ding, B.W. Filippone, A. García, P. Gel- tenbort, S. Hasan, K.P. Hickerson, J. Hoagland, R. Hong, G.E. Hogan, A.T. Holley, T.M. Ito, A. Knecht, C. Liu, J. Liu, M. Makela, J.W. Martin, D. Melconian, M.P. Mendenhall, S.D. Moore, C.L. Morris, S. Nepal, N. Nouri, R.W. Pattie, A. Pérez Galván, D.G. Phillips, R. Picker, M.L. Pitt, B. Plaster, J.C. Ramsey, R. Rios, D.J. Salvat, A. Saunders, W. Sondheim, S.J. Seestrom, S. Sjue, S. Slutsky, X. Sun, C. Swank, G. Swift, E. Tatar, R.B. Vogelaar, B. VornDick, Z. Wang, J. Wexler, T. Womack, C. Wrede, A.R. Young, B.A. Zeck, Phys. Rev. C **97**, 035505 (2018).

Nuclear beta decays and CKM unitarity, J.C. Hardy and I.S. Towner, eConf **C18-05-09**, 63 (2018).

Precise half-life measurement of the superallowed emitter ^{30}S, V.E. Iacob, J.C. Hardy, L. Chen, V. Horvat, M. Bencomo, N. Nica, H.I. Park, B.T. Roeder, A. Saastamoinen, Phys. Rev. C **97**, 035501 (2018).

Precise measurement of α_K and α_T for the 39.8-keV E3 transition in ^{103}Rh: Test of internal-conversion theory, N. Nica, J.C. Hardy, V.E. Iacob, V. Horvat, H.I. Park, T.A. Werke, K.J. Glennon, C.M. Folden, V.I. Sabla, J.B. Bryant, X.K. James, M.B. Trzhaskovskaya, Phys. Rev. C **98**, 054321 (2018).

Precise test of internal- conversion theory: α_K measurements for transitions in nine nuclei spanning $45 \leq Z \leq 78$, J.C. Hardy, N. Nica, V.E. Iacob, and M.B. Trzhaskovskaya, Appl. Radiat. Isot. **134**, 406 (2018).

Nuclear Data Sheets for A = 140, N. Nica, Nucl. Data Sheets **154**, 1 (2018).

Reexamination of a novel determination of density, temperature, and symmetry energy based on a modified Fisher model, X. Liu, H. Zheng, W. Lin, M. Huang, Y.Y. Yang, J.S. Wang, R. Wada, A. Bonasera, and J.B. Natowitz, Phys. Rev. C **97**, 014613 (2018).

Use of a nucleation based ternary fission model to reproduce neck emission in heavy-ion reactions, J. Gauthier, M. Barbui, X.-G. Cao, K. Hagel, R. Wada, S. Wuenschel, and J.B. Natowitz, AIP Conference Proceedings **2038**, 020036 (2018).

Searching for states analogous to the ^{12}C Hoyle state in heavier nuclei using the thick target inverse kinematics technique, M. Barbui, K. Hagel, J. Gauthier, S. Wuenschel, R. Wada, V.Z. Goldberg, R.T. de Souza, S. Hudan, D. Fang, X.-G. Cao and J.B. Natowitz, AIP Conference Proceedings **2038**, 020027 (2018).

Evidence for resonances in the 7α disassembly of ^{28}Si, X.G. Cao, E.J. Kim, K Schmidt, K. Hagel, M. Barbui, J. Gauthier, S. Wuenschel, G. Giuliani, M.R.D. Rodriguez, S. Kowalski, H. Zheng, M. Huang, A. Bonasera, R. Wada, G.Q. Zhang, C.Y. Wong, A. Staszczak, Z.X. Ren, Y.K. Wang, S.Q. Zhang, J. Meng, and J.B. Natowitz, AIP Conference Proceedings **2038**, 020021 (2018).

γ-ray strength function for thallium isotopes relevant to the ^{205}Pb–^{205}Tl chronometry, H. Utsunomiya, T. Renstrøm, G.M. Tveten, S. Goriely, T. Ari-izumi, D. Filipescu, J. Kaur, Y.-W. Lui, W. Luo, S. Miyamoto, A.C. Larsen, S. Hilaire, S. Péru, and A.J. Koning, Phys. Rev. C **99**, 024609 (2019).

Photoneutron cross sections for Ni isotopes: Toward understanding (n,γ) cross sections relevant to weak s-process nucleosynthesis, H. Utsunomiya, T. Renstrøm, G.M. Tveten, S. Goriely, S. Katayama, T. Ari-izumi, D. Takenaka, D. Symochko, B.V. Kheswa, V.W. Ingeberg, T. Glodariu, Y.-W. Lui, S. Miyamoto, A.C. Larsen, J.E. Midtbø, A. Görgen, S. Siem, L. Crespo Campo, M. Guttormsen, S. Hilaire, S. Péru, and A.J. Koning, Phys. Rev. C **98**, 054619 (2018).

Verification of detailed balance for γ absorption and emission in Dy isotopes, T. Renstrøm, H. Utsunomiya, H.T. Nyhus, A.C. Larsen, M. Guttormsen, G.M. Tveten, D.M. Filipescu, I. Gheorghe, S. Goriely, S. Hilaire, Y.-W. Lui, J.E. Midtbø, S. Péru, T. Shima, S. Siem, and O. Tesileanu, Phys. Rev. C **98**, 054310 (2018).

Search for dark matter decay of the free neutron from the UCNA experiment: $n \rightarrow \chi + e^+e^-$, X. Sun, E. Adamek, B. Allgeier, M. Blatnik, T.J. Bowles, L.J. Broussard, M.A. Brown, R. Carr, S. Clayton, C. Cude-Woods, S. Currie, E.B. Dees, X. Ding, B.W. Filippone, A. García, P. Geltenbort, S. Hasan, K.P. Hickerson, J. Hoagland, R. Hong, G.E. Hogan, A.T. Holley, T.M. Ito, A. Knecht, C. Liu, J. Liu, M. Makela, R. Mammei, J.W. Martin, D. Melconian, M.P. Mendenhall, S.D. Moore, C.L. Morris, S. Nepal, N. Nouri, R.W. Pattie, A. Pérez Galván, D.G. Phillips, R. Picker, M.L. Pitt, B. Plaster, J.C. Ramsey, R. Rios, D.J. Salvat, A. Saunders, W. Sondheim, S. Sjue, S. Slutsky, C. Swank, G. Swift, E. Tatar, R.B. Vogelaar, B. VornDick, Z. Wang, W. Wei, J. Wexler, T. Womack, C. Wrede, A.R. Young, and B.A. Zeck, Phys. Rev. C **97**, 052501 (2018).

Sensitivity study of experimental measures for the nuclear liquid-gas phase transition in the statistical multifragmentation model, W. Lin, P. Ren, H. Zheng, X. Liu, M. Huang, R. Wada, G. Qu, Phys. Rev. C **97**, 054615 (2018).

Statistical analysis of experimental multifragmentation events in ^{64}Zn + ^{112}Sn at 40 MeV/nucleon, W. Lin, H. Zheng, P. Ren, X. Liu, M. Huang, R. Wada, Z. Chen, J. Wang, G.Q. Xiao, G. Qu, Phys. Rev. C **97**, 044603 (2018).

Study of excited states of 35Ar through β-decay of 35K for nucleosynthesis in novae and X-ray bursts, A. Saastamoinen, G.J. Lotay, A. Kankainen, B.T. Roeder, R. Chyzh, M. Dag, E. McCleskey, A. Spiridon, and R.E. Tribble, J. Phys. Conference Series **940**, 012004 (2018).

Sub-Coulomb ^{3}He transfer and its use to extract three-particle asymptotic normalization coefficients, M.L. Avila, L.T. Baby, J. Belarge, N. Keeley, K.W. Kemper, E. Koshchiy, A.N. Kuchera, G.V. Rogachev, K. Rusek, and D. Santiago-Gonzalez, Phys. Rev. C **97**, 014313 (2018).

Supplemental material for precision measurement of the β asymmetry in spin-polarized ^{37}K decay, B. Fenker, A. Gorelov, D. Melconian, J.A. Behr, M. Anholm, D. Ashery, R.S. Behling, I. Cohen, I. Craiciu, G. Gwinner, J. McNeil, M. Mehlman, K. Olchanski, P.D. Shidling, S. Smale, and C.L. Warner, Phys. Rev. Lett. **120**, 062502 (2018).

Searching for states analogous to the ^{12}C Hoyle state in heavier nuclei using the thick target inverse kinematics technique, M. Barbui, K. Hagel, J. Gauthier, S. Wuenschel, R. Wada, V.Z. Goldberg, R.T. deSouza, S. Hudan, D. Fang, X-G Cao and J. B. Natowitz, Phys. Rev. C **98**, 044601 (2018).

Dilepton radiation in heavy-ion collisions at small transverse momentum, M. Kłusek-Gawenda, R. Rapp, W. Schäfer, and A. Szczurek, Physics Letters B **790**, 339 (2019).

From in-medium color forces to transport properties of QGP, S.Y.F. Liu and R. Rapp, Nucl. Phys. **A982**, 215 (2019).

Hot and dense homogeneous nucleonic matter constrained by observations, experiment, and theory, X. Du, A.W. Steiner, and J.W. Holt, Phys. Rev. C **99**, 025803 (2019).

In-medium charmonium production in proton-nucleus collisions, X. Du and R. Rapp, J. High Energy Phys. **03**, 015 (2019).

Proton-beam stopping in hydrogen, J.J. Bailey, I.B. Abdurakhmanov, A.S. Kadyrov, I. Bray, and A.M. Mukhamedzhanov, Phys. Rev. A **99**, 042701 (2019).

Strongly resonating bosons in hot nuclei, S. Zhang, A. Bonasera, M. Huang, H. Zheng, D.X. Wang, J.C. Wang, L. Lu, G. Zhang, Z. Kohley, Y.G. Ma, and S.J. Yennello, Phys. Rev. C **99**, 044605 (2019).

Theory of surrogate nuclear and atomic reactions with three charged particles in the final state proceeding through a resonance in the intermediate subsystem, A.M. Mukhamedzhanov, and A.S. Kadyrov, Few-Body Systems **60**, 9 (2019).

T -matrix approach to quark-gluon plasma, S.Y.F. Liu and R. Rapp, Phys. Rev. C **97**, 034918 (2018).

Analysis of pairing correlations in neutron transfer reactions and comparison to the constrained molecular dynamics model, C. Agodi, G. Giuliani, F. Cappuzzello, A. Bonasera, D. Carbone, M. Cavallaro, A. Foti, R. Linares, and G. Santagati, Phys. Rev. C **97**, 034616 (2018).

Cluster correlation and fragment emission in ^{12}C + ^{12}C at 95 MeV/nucleon, G. Tian, Z. Chen, R. Han, F. Shi, F. Luo, Q. Sun, L. Song, X. Zhang, G.Q. Xiao, R. Wada, A. Ono, Phys. Rev. C **97**, 034610 (2018).

Decay modes of the Hoyle state in ^{12}C, H. Zheng, A. Bonasera, M. Huang, S. Zhang, Phys. Lett. B **779**, 460 (2018).

Effect of short-range correlations on the single proton $3s_{1/2}$ wave function in ^{206}Pb, S. Shlomo, I. Talmi, M.R. Anders, G. Bonasera, J. Phys. Conference Series **966**, 012013 (2018).

Extraction of heavy-flavor transport coefficients in QCD matter, R. Rapp, P.B. Gossiaux, A. Andronic, R. Averbeck, S. Masciocchi, A. Beraudo, E. Bratkovskaya, P. Braun-Munzinger, S. Cao, A. Dainese, S.K. Das, M. Djordjevic, V. Greco, M. He, H. Hees, G. Inghirami, O. Kaczmarek, Y.-. Lee, J. Liao, S.Y.F. Liu, G. Moore, M. Nahrgang, J. Pawlowski, P. Petreczky, S. Plumari, F. Prino, S. Shi, T. Song, J. Stachel, I. Vitev, X. Wang, Nucl. Phys. **A97**9, 21 (2018).

Extrapolation of scattering data to the negative-energy region. III. Application to the p $-^{16}$O system, L.D. Blokhintsev, A.S. Kadyrov, A.M. Mukhamedzhanov, D.A. Savin, Phys. Rev.C **98**, 064610 (2018).

Extrapolation of scattering data to the negative-energy region. II. Applicability of effective range functions within an exactly solvable model, L.D. Blokhintsev, A.S. Kadyrov, A.M. Mukhamedzhanov, D.A. Savin, Phys. Rev. C **97**, 024602 (2018).

Impact of the ^{7}Be(α, γ)^{11}C reaction on the primordial abundance of ^{7}Li, M. Hartos, C.A. Bertulani, Shubhchintak, A.M. Mukhamedzhanov, and S. Hou, Astrophysical J. **862**, 62 (2018).

Neutron star tidal deformabilities constrained by nuclear theory and experiment, Y. Lim and J.W. Holt, Phys. Rev. Lett. **121**, 062701 (2018).

Neutron enhancement from laser interaction with a critical fluid, H.J. Quevedo, G. Zhang, A. Bonasera, M. Donovan, G. Dyer, E. Gaul, G.L. Guardo, M. Gulino, M.L. Cognata, D. Lattuada, S. Palmerini, R.G.

Pizzone, S. Romano, H. Smith, O. Trippella, Anzalone, C. Spitaleri, and T. Ditmire, Phys. Lett. A **382**, 94 (2018).

Non-perturbative approach to equation of state and collective modes of the QGP, S.Y.F. Liu and R. Rapp, Eur. Phys. J. Web of Conferences **172**, 05001 (2018).

Nuclear dipole polarizability from mean-field modeling constrained by chiral effective field theory, Z. Zhang, Y. Lim, J.W. Holt, and C.M. Ko, Phys. Lett. B **777**, 73 (2018).

On unitarity of the particle–hole dispersive optical model, M.L. Gorelik, S. Shlomo, B.A. Tulupov, and M.H. Urin, Nucl. Phys. **A970**, 353 (2018).

Self-consistent mean-field approach to the statistical level density in spherical nuclei, V.M. Kolomietz, A.I. Sanzhur, and S. Shlomo, Phys. Rev. C **97**, 064302 (2018).

Tensor Fermi liquid parameters in nuclear matter from chiral effective field theory, J.W. Holt, N. Kaiser, T.R. Whitehead, Phys. Rev. C **97**, 054325 (2018).

Thermal dileptons as QCD matter probes at SIS, F. Seck, T. Galatyuk, R. Rapp, J. Stroth, J. Phys. Conference Series **1024**, 012011 (2018).

Three-body Faddeev equations in two-particle Alt-Grassberger- Sandhas form with distorted-wave-Born-approximation amplitudes as effective potentials, A.M. Mukhamedzhanov, Phys. Rev. C **98**, 044626 (2018).

Trojan Horse cross section measurements and their impact on primordial nucleosynthesis, R.G. Pizzone, R. Spartá, C. Bertulani, C. Spitaleri, M.L. Cognata, L. Lamia, A. Mukhamedzhanov, A. Tumino, J. Phys. Conference Series **940**, 012017 (2018).

Universal correlations in the nuclear symmetry energy, slope parameter, and curvature, J.W. Holt and Y. Lim, Phys. Lett. B **784**, 77 (2018).

Tidal deformability of neutron stars with realistic nuclear energy density functionals, Young-Min Kim, Yeunhwan Lim, Kyujin Kwak, Chang Ho Hyun, Chang-Hwan Lee, Phys. Rev. C **98**, 065805 (2018).

Light nuclei production in Pb+Pb collisions at $\sqrt{s_{NN}}$ = 2.76 TeV, L.L. Zhu, H. Zheng, C.M. Ko, and Y. Sun, Euro. J. Phys. A 54, **175** (2018).

Light nuclei production as a probe of the QCD phase diagram, K.J. Sun, L.W. Chen, C.M. Ko, J. Pu, and Z. Xu, Phys. Lett. B **781**, 499 (2018).

Chiral kinetic approach to chiral magnetic effect in isobaric collisions, Y. Sun and C.M. Ko, Phys. Rev. C **98**, 014911 (2018).

Spectra and flow of light Nuclei in relativistic heavy ion collisions at RHIC and the LHC, W. Zhao, L. Zhu, H. Zheng, C.M. Ko, and H. Song, Phys. Rev. C **98**, 054905 (2018).

Pion production in a transport model based on mean fields from chiral effective theory, Z. Zhang and C.M. Ko, Phys. Rev. C **98**, 054614 (2018).

Probing the topological charge in QCD matter via multiplicity up-down Asymmetry, Y. Sun and C.M. Ko, Phys. Lett. B **789**, 228-232 (2019).

Azimuthal angle dependence of the longitudinal spin polarization in relativistic heavy ion collisions, Y. Sun and C.M. Ko, Phys. Rev. C **99**, 011903(R) (2019).

Suppression of light nuclei production in collisions of small systems at the Large Hadron Collider, K. J. Sun, C.M. Ko, and B. Donigus, Phys. Lett. B **792**, 132 (2019).

Initial angular momentum and flow in high energy nuclear collisions, Rainer J. Fries, Guangyao Chen, and Sidharth Somanathan, Phys. Rev. C **97**, 034903 (2018)

Hybrid hadronization, Rainer J Fries and Michael Kordell. Proceedings of Science, Hard Probes 2018, 046 (2019).

Jet substructure modification in a QGP from a multi-scale description of jet evolution with JETSCAPE, Yasuki Tachibana *et al.*, Proceedings of Science, Hard Probes 2018, 099 (2019)

Centrality and transverse momentum dependence of D^0-meson production at mid-rapidity in Au + Au collisions at $\sqrt{s_{NN}}$ = 200 GeV, J. Adam, D.M. Anderson, C.A. Gagliardi, A. Hamed, L. He, T. Lin, Y. Liu, S. Mioduszewski, N.R. Sahoo, P.K. Sahu, R.E. Tribble, Phys. Rev. C **99**, 034908 (2019).

Constraining the initial conditions and temperature dependent viscosity with three-particle correlations in Au+Au collisions, L. Adamczyk, D.M. Anderson, Z. Chang, C.A. Gagliardi, A. Hamed, T. Lin, Y. Liu, S. Mioduszewski, N.R. Sahoo, R.E. Tribble, Physics Letters B **790**, 81 (2019).

Measurement of the longitudinal spin asymmetries for weak boson production in proton-proton collisions at $\sqrt{s}$ = 510 GeV, J. Adam, D.M. Anderson, C.A. Gagliardi, A. Hamed, L. He, T. Lin, Y. Liu, S. Mioduszewski, N.R. Sahoo, P.K. Sahu, R.E. Tribble, Phys. Rev. D **99**, 051102 (2019).

The proton−Ω correlation function in Au+Au collisions at $\sqrt{s_{NN}}$ = 200 GeV, J. Adam, D.M. Anderson, C.A. Gagliardi, A. Hamed, T. Lin, Y. Liu, S. Mioduszewski, N.R. Sahoo, P.K. Sahu, R.E. Tribble, Phys. Lett. B **790**, 490 (2019).

J/ψ production cross section and its dependence on charged-particle multiplicity in p + p collisions at s =200 GeV, J. Adam, C.A. Gagliardi, A. Hamed, L. He, S. Mioduszewski, N.R. Sahoo, P.K. Sahu, and R.E. Tribble, Phys. Lett. B **786**, 87 (2018).

Azimuthal anisotropy in Cu + Au collisions at $\sqrt{s_{NN}}$ =200 GeV, L. Adamczyk, STAR Collaboration, C.A. Gagliardi, A. Hamed, S. Mioduszewski, N.R. Sahoo, P.K. Sahu, and R.E. Tribble, Phys. Rev. C **98**, 014915 (2018).

Azimuthal transverse single-spin asymmetries of inclusive jets and charged pions within jets from polarized-proton collisions at $\sqrt{s}$ =500 GeV, L. Adamczyk, STAR Collaboration, C.A. Gagliardi, A. Hamed, S. Mioduszewski, N.R. Sahoo, P.K. Sahu, R.E. Tribble, Phys. Rev. D **97**, 032004 (2018).

Beam Energy Dependence of Jet-Quenching Effects in Au + Au Collisions at $\sqrt{s_{NN}}$ = 7.7, 11.5, 14.5, 19.6, 27,39, and 62.4 GeV, L. Adamczyk, STAR Collaboration, C.A. Gagliardi, A. Hamed, S. Mioduszewski, N.R. Sahoo, P.K. Sahu, R.E. Tribble, Phys. Rev. Lett. **121**, 032301 (2018).

Beam energy dependence of rapidity-even dipolar flow in Au + Au collisions, J. Adam, STAR Collaboration, C.A. Gagliardi, A. Hamed, S. Mioduszewski, N.R. Sahoo, P.K. Sahu, R.E. Tribble, Phys. Lett. B **784**, 26 (2018).

Beam-energy dependence of directed flow of Λ, $\bar{\Lambda}$, $K^{\pm}$, K_S^0 and φ in Au + Au collisions, L. Adamczyk, STAR Collaboration, C.A. Gagliardi, A. Hamed, S. Mioduszewski, N.R. Sahoo, P.K. Sahu, R.E. Tribble, Phys. Rev. Lett. **120**, 062301 (2018).

Collision energy dependence of moments of net-kaon multiplicity distributions at RHIC, L. Adamczyk, C.A. Gagliardi, A. Hamed, L. He, S. Mioduszewski, N.R. Sahoo, P.K. Sahu, R.E. Tribble, Phys. Lett. B **785**, 551 (2018).

Correlation measurements between flow harmonics in Au + Au collisions at RHIC, J. Adam, STAR Collaboration, C.A. Gagliardi, A. Hamed, S. Mioduszewski, N.R. Sahoo, P.K. Sahu, R.E. Tribble, Phys. Lett. B **783**, 459 (2018).

Global polarization of Λ hyperons in Au + Au collisions at $\sqrt{s_{NN}}$ =200 GeV, J. Adam, STAR Collaboration, C.A. Gagliardi, A. Hamed, S. Mioduszewski, N.R. Sahoo, P.K. Sahu, R.E. Tribble, Phys. Rev. C **98**, 014910 (2018).

Harmonic decomposition of three-particle azimuthal correlations at energies available at the BNL Relativistic Heavy Ion Collider, L. Adamczyk, C.A. Gagliardi, A. Hamed, L. He, S. Mioduszewski, N.R. Sahoo, P.K. Sahu, R.E. Tribble, Phys. Rev. C **98**, 034918 (2018).

Improved measurement of the longitudinal spin transfer to Λ and $\bar{\Lambda}$ hyperons in polarized proton-proton collisions at s=200 GeV, J. Adam, C.A. Gagliardi, A. Hamed, L. He, S. Mioduszewski, N.R. Sahoo, P.K. Sahu, R.E. Tribble, Phys. Rev. D **98**, 112009 (2018).

Longitudinal double-spin asymmetries for π^0s in the forward direction for 510 GeV polarized pp collisions, J. Adam, STAR Collaboration, C.A. Gagliardi, A. Hamed, S. Mioduszewski, N.R. Sahoo, P.K. Sahu, R.E. Tribble, Phys. Rev. D **98**, 032013 (2018).

Longitudinal double-spin asymmetries for dijet production at intermediate pseudorapidity in polarized pp collisions at $\sqrt{s}$ = 200 GeV, J. Adam, STAR Collaboration, C.A. Gagliardi, A. Hamed, S. Mioduszewski, N.R. Sahoo, P.K. Sahu, R.E. Tribble, Phys. Rev. D **98**, 032011 (2018).

Low-p_T e^+e^- Pair Production in Au + Au Collisions at $\sqrt{s_{NN}}$ =200 GeV and U + U Collisions at $\sqrt{s_{NN}}$ =193 GeV at STAR, J. Adam, C.A. Gagliardi, A. Hamed, L. He, S. Mioduszewski, N.R. Sahoo, P.K. Sahu, and R.E. Tribble, Phys. Rev. Lett. **121**, 132301 (2018).

Measurement of the $^3_\Lambda$He lifetime in Au + Au collisions at the BNL Relativistic Heavy Ion Collider, L. Adamczyk, STAR Collaboration, C.A. Gagliardi, A. Hamed, S. Mioduszewski, N.R. Sahoo, P.K. Sahu, R.E. Tribble, Phys. Rev. C **97**, 054909 (2018).

Transverse spin transfer to Λ and $\bar{\Lambda}$ hyperons in polarized proton-proton collisions at s=200 GeV, J. Adam, C.A. Gagliardi, A. Hamed, L. He, S. Mioduszewski, N.R. Sahoo, P.K. Sahu, R.E. Tribble, Phys. Rev. D **98**, 091103 (2018).

Transverse spin-dependent azimuthal correlations of charged pion pairs measured in $p^\uparrow$ + p collisions at $\sqrt{s}$ = 500 GeV, L. Adamczyk, STAR Collaboration, C.A. Gagliardi, A. Hamed, S. Mioduszewski, N.R. Sahoo, P.K. Sahu, and R.E. Tribble, Phys. Lett. B **780**, 332 (2018).

SECTION VI

APPENDIX

TALKS PRESENTED
April 1, 2018 – March 31, 2019

Using beta decay to extract $|V_{ud}|$ and test CKM unitarity, **J.C. Hardy**, **Invited talk**, Mainz Institute for Theoretical Physics Scientific Program, "Bridging the Standard Model to New Physics with the Parity Violation Program at MESA," Johannes Gutenberg University, Mainz, Germany (April 2018).

Nuclear beta decays and CKM unitarity, **J.C. Hardy**, **Invited talk**, 13th Conference on the Intersections of Particle and Nuclear Physics, CIPANP 2018, Palm Springs, Calfornia (May 2018).

Semi-leptonic weak interactions, **J.C. Hardy**, **Invited talk**, the Fundamental Neutron Summer School, hosted by North Carolina State University, Raleigh, North Carolina (July 2018).

Measuring $|V_{ud}|$ and testing CKM unitarity: Past presnt & future, **J.C. Hardy**, **Invited talk**, Top-Row CKM Unitarity Workshop, Texas A&M University, College Station, Texas (January 2019).

How weird is the weak force? **J.C. Hardy**, **Invited talk**, Saturday Morning Physics, Texas A&M University, College Station, Texas (February 2019).

Precise half-life measurement of the superallowed beta emitter S-30, **V. E. Iacob**, **Invited talk**, 6th Joint Carpathian Summer School of Physics 2018 (CSSP18), Sinaia, Romania (July 2018).

Precise half-life measurement of ^{30}S, **V. E. Iacob**, **Invited talk**, 5th Joint Meeting of the APS Division of Nuclear Physics and the Physical Society of Japan, Waikoloa, Hawaii (October 2018).

What do we learn from our giant resonances experiment? **Y.-W. Lui**, **Invited talk**, 6th International Conference on Collective Motion in Nuclei under Extreme Conditions (COMEX6), Cape Town, South Africa (October 2018).

Stellar explosions in the lab: Measurements of key nuclear reactions driving nucleosynthesis, **G. Christian**, **Invited talk**, Thirteenth Conference on the Intersections of Particle and Nuclear Physics (CIPANP), Palm Springs, California (May 2018).

Neutron spectroscopy at TAMU, **G. Christian**, CENTAUR Neutron Detector Workshop, College Station, Texas (May 2018).

Experiments with radioactive beams at the Texas A&M University Cyclotron Institute, **G. Christian**, **Invited talk**, 25th Conference on Application of Accelerators in Research and Industry, Grapevine, Texas (August, 2018).

Neutron detector development at Texas A&M, **G. Christian**, **Invited talk**, Low Energy Nuclear Physics Community Meeting, East Lansing, Michigan (August, 2018).

Reactions at the Texas A&M University Cyclotron Institute and Beyond, **G. Christian**, **Invited talk**, Nuclear Physics for the Next Generation, London, United Kingdom (September, 2018).

Neutron economy in stars: What can we learn from nuclear astrophysics? **S. Ota**, **Invited seminar**, Department of Physics, John D. Fox Accelerator Laboratory, Florida State University, Florida (March 2019).

Neutron production and capture for nucleosynthesis in stars: $^{22}Ne(\alpha, n)^{25}Mg$ reaction and radiative neutron captures of radioactive nuclei, **S. Ota**, **Invited seminar**, Physics Division, Brookhaven National Laboratory, Upton, New York (September 2018).

Constraining the astrophysical $^{23}Mg(p,)^{24}Al$ reaction rate using direct and indirect measurements, **E. Bennett**, 5th Joint Meeting of the APS Division of Nuclear Physics and the Physical Society of Japan, Waikoloa Village, Hawaii (October, 2018).

Precise α_K and α_T internal conversion coefficients measurements of 39.752(6)-keV E3 transition in ^{103m}Rh: Test of internal conversion theory, **N. Nica**, 5th Joint Meeting of the APS Division of Nuclear Physics and the Physical Society of Japan, Waikoloa, Hawaii (October 2018).

Internal conversion coefficients precision measurements, **N. Nica**, the US National Nuclear Data Week 2018, Brookhaven National Laboratory, Upton, New York (November 2018).

Texas A&M University US nuclear data program TAMU ENSDF report FY2018, **N. Nica**, the US National Nuclear Data Week 2018, Brookhaven National Laboratory, Upton, New York (November 2018).

Fundamentally cool physics with trapped atoms and ions, **D. Melconian**, Texas A&M University, College Station, Texas (September 2018).

Nuclear β decay: using the atomic nucleus to probe symmetries of the weak interaction, **D. Melconian**, **Invited talk**, Joint APS/AAPT/SPS meeting, Tarleton University, Stephenville, Texas (March 2018).

β-decay asymmetry measurements with trapped atoms, **D. Melconian**, **Invited talk**, 13th Conference on the Intersections of Particle and Nuclear Physics (CIPANP 2018), Palm Springs, California (May 2018).

A precision measurement of the β asymmetry parameter using laser-cooled ^{37}K, **D. Melconian**, **Invited talk**, 7th Symposium on Symmetries in Subatomic Physics (SSP 2018), Aachen, Germany (June 2018).

Trapped atoms and ions for tests of the charged electroweak interaction, **D. Melconian**, Center for Nuclear Physics and Astrophysics Seminar, University of Washington, Seattle, Washington (July 2018).

Fundamental symmetry tests using atoms and ions, **D. Melconian**, Physics Division Seminar, Argonne National Laboratory, Lemont, Illinois (February 2019).

Outlook for the determination of V_{ud}, **D. Melconian**, **Invited talk**, Workshop on Precise beta decay calculations for searches for new physics, ECT*, Trento, Italy (April 2019).

Outlook for the determination of V_{ud}, **D. Melconian**, **Invited talk**, Workshop on Atomic nuclei as laboratories for BSM physics, ECT*, Trento, Italy (Apr 2019).

Ion trap application: Fundamental weak interaction studies using ion traps, **P.D. Shidling**, **Invited talk**, 25th Conference on Application of Accelerators in Research and Industry (CAARI), Grapevine, Texas (August 2018).

TAMUTRAP facility update, **V. Kolhinen**, 2018 Low-Energy Community Meeting, East Lansing, Michigan (October 2018).

TAMUTRAP facility: Penning trap facility for weak interaction studies, **P.D. Shidling**, 7th International Conference on Trapped Charged Particles and Fundamental Physics (TCP2018), Traverse City, Michigan (October 2018).

In situ characterization of β scattering at TRINAT, **D. Melconian**, 5th Joint Meeting of the APS Division of Nuclear Physics and the Physical Society of Japan, Waikoloa Village, Hawaii (October, 2018).

TAMUTRAP facility: Penning trap facility for weak interaction studies, **P.D. Shidling**, 5th Joint Meeting of the APS Division of Nuclear Physics and the Physical Society of Japan, Waikoloa Village, Hawaii (October, 2018).

Beta-delayed proton decays for explosive hydrogen burning, **A. Saastamoinen**, **Invited talk**, Nuclear Physics for Next Generation, London, United Kingdom (September 2018).

MicroMegas based detectors at TAMU, **A. Saastamoinen**, **Invited talk**, GET Workshop: General Electronics for Physics, Bordeaux, France (October 2018).

The two biggest problems in heavy element science (and what the Cyclotron Institute is doing about them), **C.M. Folden III**, College of Science External Advisory and Development Council Meeting, College Station, Texas (March).

The evolving periodic table and its incredible elements! **C.M. Folden III** , One of two featured experts for the American Chemical Society's Program-in-a-Box webinar (February 2019).

Immigration, U.S. scientific innovation, and the discovery of new elements: At the intersection of science, politics, and policy, **C.M. Folden III**, **Invited talk**, Texas A&M University Department of International Affairs, College Station, Texas (October 2018).

Separated plutonium discrimination forensics at Texas A&M, **K.J. Glennon**, Nuclear Science and Security Consortium 2018 Fall Workshop and Advisory Board Meeting, Livermore, California (October 2018).

Measuring key isotope ratios in two irradiated UO_2 fuel samples, **K.J. Glennon**, J.M. Osborn, J.D. Burns, E.D. Kitcher, Sunil Chirayath, and C.M. Folden III, American Chemical Society Fall 2018 National Meeting, Boston, Massachusetts (August 2018).

Heavy element research at Texas A&M University, **C.M. Folden III**, **Invited talk**, Czech Technical University in Prague, Czech Republic (June 25, 2018).

Chemistry at the bottom of the periodic table, **C.M. Folden III**, **Invited talk**, Institut Pluridisciplinaire Hubert Curien, Strasbourg, France (June 2018).

A forensic investigation of two irradiated UO_2 fuel samples to further develop the discrimination forensics of separated Pu, **K.J. Glennon** and C.M. Folden III, Office of Defense Nuclear Nonproliferation Research and Development (DNN R&D) University Program Review, Ann Arbor, Michigan (June 2018).

Studying the stars here on earth: How the equation of state of nuclear matter impacts the formation of The elements, **S.J. Yennello**, **Invited talk**, San Jose State University, ACS-DNCT summer school, San Jose, California (June 2018).

Experimental constraints on the nuclear equation-of-state from heavy-ion collisions, **S.J. Yennello**, **Invited talk**, 1st Symposium on Intermediate-energy Heavy Ion Collisions (iHIC2018), Tsinghua University, Beijing, China (April 2018).

Isospin effects in nuclear reactions, **S.J. Yennello**, **Invited talk**, International Workshop on Multi facets of Eos and Clustering (IWM-EC2018), Catania, Italy (May 2018).

Experimental investigations of the nuclear equation-of-state, **S.J. Yennello**, **Invited talk**, EUroRib2018, Giens, France (June 2018).

Proton-proton correlation functions measured using position-sensitive FAUST, **S.J. Yennello, Invited talk**, LECM, East Lansing, Michigan (August 2018).

Increasing equity, inclusion and excellence in nuclear science, **S.J. Yennello, Invited talk**, LECM, East Lansing, Michigan (August 2018).

The Texas A&M ADVANCE Scholar Program, **S.J. Yennello, Invited talk**, 256th ACS National Meeting, Boston, Massachusetts (August 2018).

Remarkable, delightful, awesome: It will change your life, not over night but over time, **S.J. Yennello, Invited talk**, 256th ACS National Meeting, Boston, Massachusetts (August 2018).

An orbital of her own: Improving the environment to decrease the crystal-field splitting energy so no one is forced into alignment, **S.J. Yennello, Invited talk**, University of Virginia, Charlottesville, Virginia (October 2018).

Alpha decaying heavy elements produced in multi-nucleon transfer reactions of heavy nuclei, **K. Hagel**, **Invited talk**, State of the Art of Nuclear Cluster Physics, Galveston, Texas (May 2018).

Evidence for resonances in the 7α disassembly of ^{28}Si, **K. Hagel**, **Invited talk**, State of the Art of Nuclear Cluster Physics, Galveston, Texas (May 2018).

Evidence for resonances in the 7α disassembly of ^{28}Si, **K. Hagel**, **Invited talk**, XIII Workshop on Particle Correlations and Femtoscopy, Krakow, Poland (May 2018).

Tests of the supernova equation of state using heavy ion collisions, **K. Hagel**, **Invited talk**, XIII Workshop on Particle Correlations and Femtoscopy, Krakow, Poland (May 2018).

The symmetry energy of low density nuclear matter, **K. Hagel**, **Invited talk**, 8th International Symposium on Nuclear Symmetry Energy, Busan, South Korea (September 2018).

Use of a Nucleation Based Ternary Fission Model to Reproduce Neck Emission in Heavy-Ion Reactions, **J. Gauthier**, 4th international workshop on State of the Art in Nuclear Cluster Physics, Galveston, Texas (May 2018).

Benchmarking the active catcher array to study multi nucleon transfer reactions, **A. Wakhle**, 5th Joint Meeting of the APS Division of Nuclear Physics and the Physical Society of Japan, Waikoloa, Hawaii (October 2018).

Proton-proton correlation functions measured using position-sensitive FAUST, **L. Heilborn**, 5th joint meeting of DNP & JPS, Waikoloa, Hawaii (October 2018).

Equilibration chronometry and reaction dynamics, **A. Rodriguez Manso**, International Workshop on Multi facets of Eos and Clustering (IWM-EC2018), Catania, Italy (May 2018).

Neutron-proton equilibration in two and three bodies dynamically deformed nuclear systems (^{70}Zn+ ^{70}Zn @ 35 MeV/nucleon), **A. Rodriguez Manso**, APS Division of Nuclear Physics (HAWAII2018) Kona, Hawaii (October 2018).

Implementing PIXE and PIGE at the Texas A&M University Cyclotron Institute, **A. Rodriguez Manso**, **Invited talk**, Conference on Application of Accelerators in Research and Industry (CAARI2018), Dallas, Texas (August 2018).

Neutron-proton equilibration in heavy-ion dynamically deformed nuclear systems and Particle Induced γ-ray and X-ray Emission experiments for contamination and elemental composition studies, **A. Rodriguez Manso**, **Invited seminar**, San Diego State University (SDSU), San Diego, California (February 2019).

Searching for states analogous to the Hoyle state in heavier nuclei using the thick target inverse kinematics technique, **M. Barbui**, 4th International Workshop on "State of the Art in Nuclear Cluster Physics" Galveston, Texas (May 2018).

Sub- and Near- Coulomb alpha transfer reactions for nuclear astrophysics, **G. Rogachev**, **Invited talk**, Science with the Super-Enge Split-pole spectrograph and workshop on transfer reactions, Tallahassee, Florida (March 2019).

Insights into nuclear continuum though resonance scattering, **G. Rogachev**, **Invited Plenary talk**, XLI Brazilian Meeting on Nuclear PhysicsMaresias, São Sebastião, Brazil (September 2018).

Texas Active Target (TexAT) - design, commissioning and first results, **G. Rogachev**, 5th Joint Meeting of the APS Division of Nuclear Physics and the Physical Society of Japan, Waikoloa, Hawaii (October 2018).

Resonance scattering with exotic beams - past, present, and future, **G. Rogachev**, **Invited talk**, Direct Reactions with Exotic Beams conference (DREB2018), Matsue, Japan (June 2018).

State of the art measurements with TexAT - an active-target time projection chamber, **J. Bishop**, **Invited talk**, 42nd Symposium on Nuclear Physics, Cocoyoc Mexico (January 2019).

The first experimental (α, xn) compound reaction in inverse kinematics study using neutron-rich nuclei, **S. Ahn**, 6th International Workshop on Compound-Nuclear Reactions and Related Topics, Berkeley, California (September 2018).

Si detector array with Generic Electronics for TPC (GET), **S. Ahn**, Silicon Array Working Group, Low Energy Community Meeting 2018, Michigan State University, East Lansing, Michigan (August 2018).

The first (α,xn) reaction study for a neutron-rich nuclei with the HabaNERO neutron detector, **S. Ahn**, Nuclear Structure 2018, National Superconducting Cyclotron Laboratory, Michigan State University, East Lansing, Michigan (August 2018).

Probing the effect of the ^{22}Ne(alpha,n) reaction rate on the s-process isotope abundances using sub-Coulomb alpha-transfer, **H. Jayatissa**, Carpathian Summer School of Physics 2018 (Exotic Nuclei and Nuclear / Particle Astrophysics (VII). Physics with small accelerators), Sinaia, Romania (July, 2018).

Probing the cluster structure in ^{10}Be using resonant ^{6}He + α scattering, **S. Upadhayula**, SOTANCP4, Galveston, Texas (May 2018).

Low-lying negative parity T = 5 states in ^{48}Ca, **S. Upadhayula**, Direct Reactions with Exotic Beams conference (DREB2018), Matsue, Japan (June 2018).

Study of the A=9 T=3/2 isobaric quartet through R-Matrix analysis of resonance scattering of analogue states, **C. Hunt**, Direct Reactions with Exotic Beams conference (DREB2018), Matsue, Japan (June 2018).

Structure of ^{9}C via proton elastic scattering, **J. Hooker**, Direct Reactions with Exotic Beams conference (DREB2018), Matsue, Japan (June 2018).

Measuring the neutron background for MINER, **J. Hooker**, Summer School on Neutron Detectors, Trento, Italy (July 2018).

Structure of ^{9}C via proton elastic scattering, **J. Hooker**, Nuclear Structure 2018, East Lansing, Michigan (August 2018).

Structure of ^{9}C and ^{10}N with active target time project chambers, **J. Hooker**, **Invited talk**, Commerce, Texas (September 2018).

Structure of ^{9}C and ^{10}N with active target time project chambers, **J. Hooker**, **Invited talk**, Oak Ridge, Tennessee (October 2018).

Three body interaction and heavy ion collisions in intermediate energy regime, **R. Wada**, International workshop of nuclear dynamics (IWND 2018), Huzhou, China (June 2018).

Recent transverse spin measurements in pp collisions with STAR, **C.A. Gagliardi**, **Invited talk** (for the STAR Collaboration), XXVI International Workshop on Deep Inelastic Scattering and Related Subjects (DIS2018), Kobe, Japan (April 2018).

Development of in-flight and re-accelerated rare iIsotope beams with the MARS spectrometer at Texas A&M University, **B. T. Roeder**, **Invited talk**, National Superconducting Cyclotron Laboratory, NSCL, East Lansing, Michigan (July 2018).

Cyclotrons: Beam production and applications, **B. T. Roeder**, **Invited talk**, 25th International Conference on the Application of Accelerators in Research and Industry, CAARI 2018, Grapevine, Texas (August 2018).

Secondary heavy ion beams as a tool for investigation of fusion mechanism, **G. Chubaryan**, **Invited talk**, International Conference on Spontaneous and induced fission of very heavy and super-heavy nuclei, ECT, Villa Tambosi, Trento, Italy (April 2018).

Recent transverse spin measurements in pp collisions with STAR, **C.A. Gagliardi**, **Invited talk** (for the STAR Collaboration), 23rd International Spin Symposium (SPIN 2018), Ferrara, Italy (September 2018).

What makes the proton spin? **C.A. Gagliardi**, **Invited talk**, Fall Meeting of the Texas Section of the APS, Houston, Texas (October, 2018).

Longitudinal double-spin asymmetries for di-jet production at intermediate pseudorapidity in polarized proton proton collisions at √s=200 GeV, **T. Lin**, **Plenary talk**, RHIC and AGS Annual Users Meeting, Brookhaven National Laboratory, Upton, New York (June, 2018).

Recent progress of gluon helicity measurements at RHIC, **T. Lin**, **Invited talk**, RHIC and AGS Annual Users Meeting, Brookhaven National Laboratory, Upton, New York (June 2018).

Longitudinal double-spin asymmetries for dijet production at intermediate pseudorapidity in polarized proton proton collisions at √s=200 GeV, **T. Lin** (for the STAR Collaboration), 23rd International Spin Symposium (SPIN 2018), Ferrara, Italy (September, 2018).

Gamma-jet measurements in heavy-ion collisions, **S. Mioduszewski**, Conference on the Intersections of Particle and Nuclear Physics, Palm Springs, California (June 2018).

Neutral-triggered full jet reconstruction with STAR, **D. Anderson**, Jets Workshop at the RHIC & AGS Annual Users Meeting, Upton, New York (June 2018).

Measurement of the semi-inclusive distribution of jets recoiling from direct photon- and neutral pion-triggers in central Au+Au collisions at sqrt(s_{NN}) = 200 GeV in the STAR experiment, **N. Sahoo**, Conference on Hard and Electromagnetic Probes in High Energy Nuclear Collisions, Aix-Les-Bains, France (October 2018).

Recent direct-photon+jet and neutral pion+jet measurement in the STAR experiment, **N. Sahoo**, JETSCAPE Workshop, College Station, Texas (January 2019).

Constraints on the nuclear equation of state from neutron star observations, **J.W. Holt**, **Invited talk**, ECT* workshop: New Ideas in Constraining Nuclear Forces, Trento, Italy (June 2018).

Universal correlations in the nuclear symmetry energy, slope parameter, and curvature, **J.W. Holt**, **Invited talk**, 8th International Symposium on Nuclear Symmetry Energy, Busan, South Korea (September 2018).

Hot and dense neutron-rich matter in supernovae and neutron star mergers, **J.W. Holt**, **Invited talk**, 1st APCTP-TRIUMF Joint Workshop: Understanding Nuclei from Different Theoretical Approaches, Pohang, South Korea (September 2018).

Neutron star tidal deformabilities constrained by nuclear theory and experiment, **J.W. Holt**, **Invited talk**, 5th Joint Meeting of the APS Division of Nuclear Physics and the Physical Society of Japan, Waikoloa, Hawaii (October 2018).

Hot and dense neutron-rich matter in supernovae and neutron-star mergers, **J.W. Holt**, University of Maryland nuclear physics seminar, College Park, Maryland (November 2018).

Constraints on the nuclear equation of state from microscopic many-body theory, **J.W. Holt**, **Invited talk**, CUSTIPEN workshop: EOS of dense neutron-rich matter in the era of gravitational wave astronomy, Xiamen, Fujian, China (January 2019).

Hot and dense matter in supernovae and neutron star mergers, **J.W. Holt**, University of Houston Physics Colloquium, Houston, Texas (February 2019).

Nuclear physics using lasers, **A. Bonasera**, University of Prague Seminar, Prague, Czech Republic (February 2019).

Nuclear astrophysics with lasers, **A. Bonasera**, **Invited talk**, ECT* workshop on Indirect Methods in Nuclear Astrophysics Trento, Italy (October 2018).

Nuclear physics using lasers, **A. Bonasera**, **Invited talk**, Carpathian Summer School of Physics 2018 (CSSP18), Sinaia, Romania (July 2018).

Nuclear (astro) physics using lasers, **A. Bonasera**, Department of Chemistry Seminar, University of Athens, Athens, Greece (June 2018).

Bose Einsten condensation, fermionic quenching and Efimov states from heavy-ion collisions, **A. Bonasera**, 27th annual Symposium Hellenic Nuclear Physics Society (HNPS2018), Athens Greece (June 2018).

Nuclear symmetry energy from finite nuclei to neutron stars, **Y. Lim**, 8th International Symposium on Nuclear Symmetry Energy, Busan, South Korea (September 2018).

Heavy nuclei in neutron star crust, **Y. Lim**, 1st APCTP-TRIUMF Joint Workshop: Understanding Nuclei from Different Theoretical Approaches, Pohang, South Korea (September 2018).

Pion transport in heavy ion collisions, **C.M. Ko**, **Invited talk**, International Symposium on Intermediate-Energy Heavy Ion Collisions, Beijing, China (April 7-11, 2018).

What have we learnt from quarkonia production in relativistic heavy ion collisions?, **C.M. Ko**, **Invited talk**, Thirteen Conference on the Intersections of Particle and Nuclear Physics, Palm Springs, California (May 2018).

Symmetry potential effect on pion transport in asymmetric nuclear matter, **C.M. Ko**, **Invited talk**, International Workshop on Nuclear Dynamics in Heavy-Ion Reactions, Huzhou, China (June 2018).

Status of transport models, **C.M. Ko**, **Invited talk**, Workshop on Experimental Studies of Neutron-Rich Matter, Detroit, Michigan (June 2018).

Pion production in heavy ion collisions, **C.M. Ko**, **Invited talk**, 8th International Symposium on Nuclear Symmetry Energy, Busan, Korea (September 2018).

Hadronization: From dilute to dense systems, **R.J. Fries**, **Invited talk**, Opportunities and Challenges with Jets at LHC and beyond, Institute of Particle Physics, CCNU, Wuhan, China (June 2018).

Shear Viscosity in Hot Hadron Gas, **R.J. Fries**, **Invited talk**, Berkeley Jet Physics Jubilee, Lawrence Berkeley National Laboratory, Berkeley, California (July 2018).

Hybrid hadronization, **R.J. Fries**, Hard Probes 2018: International Conference on Hard & Electromagnetic Probes of High-Energy Nuclear Collisions, Aix-les-Bains, France (October 2018).

Shear viscosity in hot hadron gas estimated from data, **R.J. Fries**, **Invited talk**, New Developments in Thermal Field Theory, CERN, Geneva, Switzerland (October 2018).

Shear viscosity in hot hadron gas estimated from data, **R.J. Fries**, Bose Institute, Kolkata, India (December 2018).

Quarkonia in TAMU transport model, **X. Du**, remote video presentation, at Quarkonium Run 3-4 LHC Meeting, CERN, Geneva, Switzerland (April 2018).

T-matrix approach to QGP, **S.Y.F. Liu,** XXVII International Conference on Ultra-relativistic Nucleus-Nucleus Collisions (Quark Matter 2018), Venice, Italy (May 2018).

Future of electromagnetic probes, **R. Rapp**, **Invited talk**, at Retreat on Opportunities in High-Energy Nuclear Collisions, Terzolas, Italy (May 2018).

Thermal dileptons and hadrons in medium, **R. Rapp**, **Plenary talk**, 15th Int. Workshop on Meson Physics, Krakow, Poland (June 2018).

Probing in-medium QCD force with quarkonium **X. Du**, **Invited talk**, Heavy-Flavor workshop at annual RHIC & AGS Users Meeting, Brookhaven National Laboratory, Upton, New York (June 2018).

Quarkonia at high-luminosity LHC: Can we determine the in-medium QCD force?, **R. Rapp**, **Invited talk**, General WG-5 Heavy-Ion Meeting, CERN, Geneva, Switzerland (June 2018).

Heavy-flavor transport and microscopic properties of the QGP, **R. Rapp**, **Invited talk**, MIAPP Program on "Probing the QGP with Collective Phenomena and Heavy Quarks", TU Munich, Garching, Germany (September 2018).

Heavy-flavor theory at hard + EM probes '18, **R. Rapp**, **Invited plenary summary talk**, Int. Conference on Hard & Electromagnetic Probes of High-Energy Nuclear Collisions, Aix-Les-bains, France (October 2018).

Dileptons at low mass and low momentum, **R. Rapp**, **Invited talk**, ECT* Workshop on Electromagnetic Probes of Hot and Dense Matter, ECT* Trento, Italy (November 2018).

Heavy-quark radiative energy loss with a quantum many-body approach, **S.Y.F. Liu**, 2nd Jetscape Winter School and Workshop, Texas A&M University, College Station, Texas (January 2019).

In-medium charmonium production in proton/deuteron-nucleus collisions, **X. Du**, 2nd Jetscape Winter School and Workshop, Texas A&M University, College Station, Texas (January 2019).

Extracting the in-medium color force from heavy-ion collisions, **X. Du,** Santa Fe Jets and Heavy-Flavor Workshop, UCLA, Los Angeles, California (February 2019).

Heavy-quark radiative energy loss within a quantum many-body approach, **S.Y.F. Liu**, Santa Fe Jets and Heavy-Flavor Workshop, UCLA, Los Angeles, California (February 2019).

Heavy flavor in nuclear collisions, **R. Rapp**, **Invited opening talk**, Heavy-Flavor/sPHENIX MVTX Mini Workshop, Lawrence Berkeley National Laboratory, Berkeley, California (February 2019).

From heavy-flavor transport ot bulk and spectral properties of the QGP, **R. Rapp**, HIC for FAIR Nuclear Physics Colloquium, Frankfurt University, Frankfurt, Germany (June 2018).

Which properties of the quark-gluon plasma can heavy-flavor particles probe? **R. Rapp**, **Invited seminar**, ExtreMe Matter Institute (EMMI), GSI Darmstadt, Germany (June 2018).

Where does the mass in the universe come from?, **R. Rapp**, Lecture, Cyclotron REU Program, College Station, Texas (June 2018).

Mass generation in the big bang, **R. Rapp**, Physics Colloquium, Texas A&M University Commerce, Commerce Texas (November 2018).

Mass generation in the early universe, **R. Rapp**, Graduiertenkolleg Kolloquium, Münster, Germany (December 2018).

Indirect measurements of radiative capture reactions on lanthanides, **C. Reingold**, 5th Joint Meeting of the APS Division of Nuclear Physics and the Physical Society of Japan, October 23-27, 2018, Waikoloa, Hawaii (October 2018).

Photon-strength functions and experimental measurement techniques, **A. Simon**, **Invited talk**, Nuclear Structure 2018 (NS2018) East Lansing, Michigan (August 2018).

Stewardship science at the University of Notre Dame, **A. Simon**, 2018 Stewardship Science Academic Programs (SSAP) Symposium, North Bethesda, Maryland (February 2019).

RESEARCH PERSONNEL AND ENGINEERING STAFF

April 1, 2018 - March 31, 2019

Faculty and Research Group Leaders

Bonasera, Aldo - Senior Scientist
Christian, Gregory - Assist. Prof. of Physics
Fries, Rainer - Assoc. Professor of Physics
Folden, Charles M., III - Assoc. Prof. of Chemistry
Gagliardi, Carl A. - Professor of Physics
Hardy, John C. - Professor Emeritus
Holt, Jeremy - Assist. Professor of Physics
Ko, Che Ming - Professor of Physics
Melconian, Dan - Assoc. Professor of Physics
Mioduszewski, Saskia - Professor of Physics
Natowitz, J. B. - Professor of Chemistry, Retired
Rapp, Ralf - Professor of Physics
Rogachev, Grigory - Professor of Physics
Shlomo, Shalom - Senior Scientist
Tribble, Robert E. - Professor of Physics (20%)
Yennello, Sherry J. - Professor of Chemistry, Bright Chair, Director
Youngblood, Dave H. - Professor Emeritus Zhanov, Akram M. - Senior Scientist

Research Staff

Ahn, Sunghoon – Assist. Research Scientist
Ärje, Juha – Research Scientist
Barbui, Marina - Assist. Research Scientist
Chubaryan, Grigor - Research Scientist
Clark, Henry - Accelerator Physicist (50%)
Gauthier, Jerome - From 9/1/18
Goldberg, Vladilen - Research Scientist, Retired
Hagel, John C. - Research Scientist (50%) Heilborn, Lauren –Assist. Research Scientist - From 9/1/18
Horvat, Vladimir - Research Scientist (50%)
Iacob, Victor - Research Scientist
Koshchiy, Yevgen - Assist. Research Scientist
Lui, Yiu-Wing - Research Scientist
McIntosh, Alan - Assist. Res. Scientist
Nica, Ninel - Associate Research Scientist
Rodrigues, Marcia Dias - Assist. Res. Scientist
Saastamoinen, Antti (50%)
Shidling, Praveen - Assist. Research Scientist
Tereshatov, Evgeny - Assist. Research Scientist
Wada, Roichi (40%)

Accelerator Physics and Radiation Line Staff

Brinkley, Joseph - Research Associate (28%)
Chen, Lixin - Research Associate - To 2/20/19
Clark, Henry - Accelerator Physicist (50%)
Horvat, Vladimir - Research Scientist (50%)
Hyman, Bruce - Research Associate
Kim, George - Accelerator Physicist
May, Don – Senior Accelerator Physicist
Roeder, Brian - Accelerator Physicist
Park, Hyo-In - Accelerator Physicist – From 1/9/18
Saastamoinen, Antti (50%)
Tabacaru, Gabriel - Accelerator Physicist

Computer Systems Staff

Burch, Jr. Robert Lead Microcomputer/LAN Administrator
Hagel, John C. Research Scientist (50%)

Engineering Staff

Olsen, Robert Senior Mechanical Engineer

Postdoctoral Research Associates

Bishop, Jack – From 9/1/18
Gauthier, Jerome - To 8/31/18
Kirakosyan, Vahan
Holhinen, Veli Sakari
Kordell, Michael – From 8/6/18
Lim, Yeunhwan
Lin, Ting
Liu, Shuai – From 5/13/18
Ota, Shuya
Park, Hyo-In – To 1/8/18
Parker, Cody – From 11/19/18
Rodriguez Manos, Alis
Sahoo, Nihar – To 3/8/19
Sun KaiJia – From 9/24/18
Sun, Yifeng – To 8/30/18
Wakhle, Aditya
Zhang, Zhen – To 6/1/18

STUDENTS

April 1, 2018 - March 31, 2019

Graduate Students

Abbott, Austin – From 9/1/18
Aboona, Bassam – From 9/1/18
Aboud, Eric
Anderson, Derek
Atchison, Joseph
Balhoff, Mary Catherine – From 9/1/18
Bencomo, Miguel
Bennett, Eames
Bonasera, Giacomo
Bosh, Alexandra – From 9/1/18
Chyzh, Roman
Dede, Stefania
Du, Xiaojian
Edgecomb, Joseph – From 1/7/19
Fleming, Alex – To 1/1/19
Garza, Fabian – From 6/1/18
Glennon, Kevin
Hannaman, Andy – From 9/1/18
Henderson, Lawrence
Hooker, Josh
Hunt, Curtis
Jayatissa, Heshani
Jedele, Andrea
Kim, Byunggyu – From 9/1/18
Liu, Shuai – To 5/12/18
Liu, Yanfang
McCain, David – From 9/1/18
Nasser, Morgan
Onyango, Thomas – From 8/13/18
Ozmetin, Asim
Ramiriez, Mariah – From 9/1/18
Robicheaux, Stephen – From 9/1/18
Doosa, Michael – From 9/1/18
Rose, Steven
Sarver, Issac
Schroeder, Benjamin – From 5/30/17
Scriven, Dustin – From 9/17/17
Sengupta, Arjun – From 12/1/18
Shin, Eunkyoung –From 1/20/18
Sorensen, Maxwell – From 9/1/18
Tang, Zhanduo – From 1/1/19
Tobin, Zachary – From 9/1/18
Upadhyayula, Sriteja
Volia, Merinda
Wang, Kang – From 11/1/17
Wang, Shanshan – From 9/17/18
Whitehead, Taylor – From 5/1/17
Xu, Zhaojie
Yang, Zidong
Zarrella, Andrew – To 8/31/18

Undergraduates and Student Technicians

Baley, Colton
Bellesio, Andrew
Forbes, Haley
Jeanis, Ian – From 5/14/18
Jeffery, Logan – From 9/1/18
Jeske, Colby – From 5/29/18
Kircher, Philip
Muzak, Mateo
O'Dwyer, Rory
Pybus, Jackson – To 4/30/18
Salas, Elysia
Tamez, Celeste
Thomas, John – From 7/6/18
Tepe,Victoria

ORGANIZATIONAL CHART - CYCLOTRON INSTITUTE

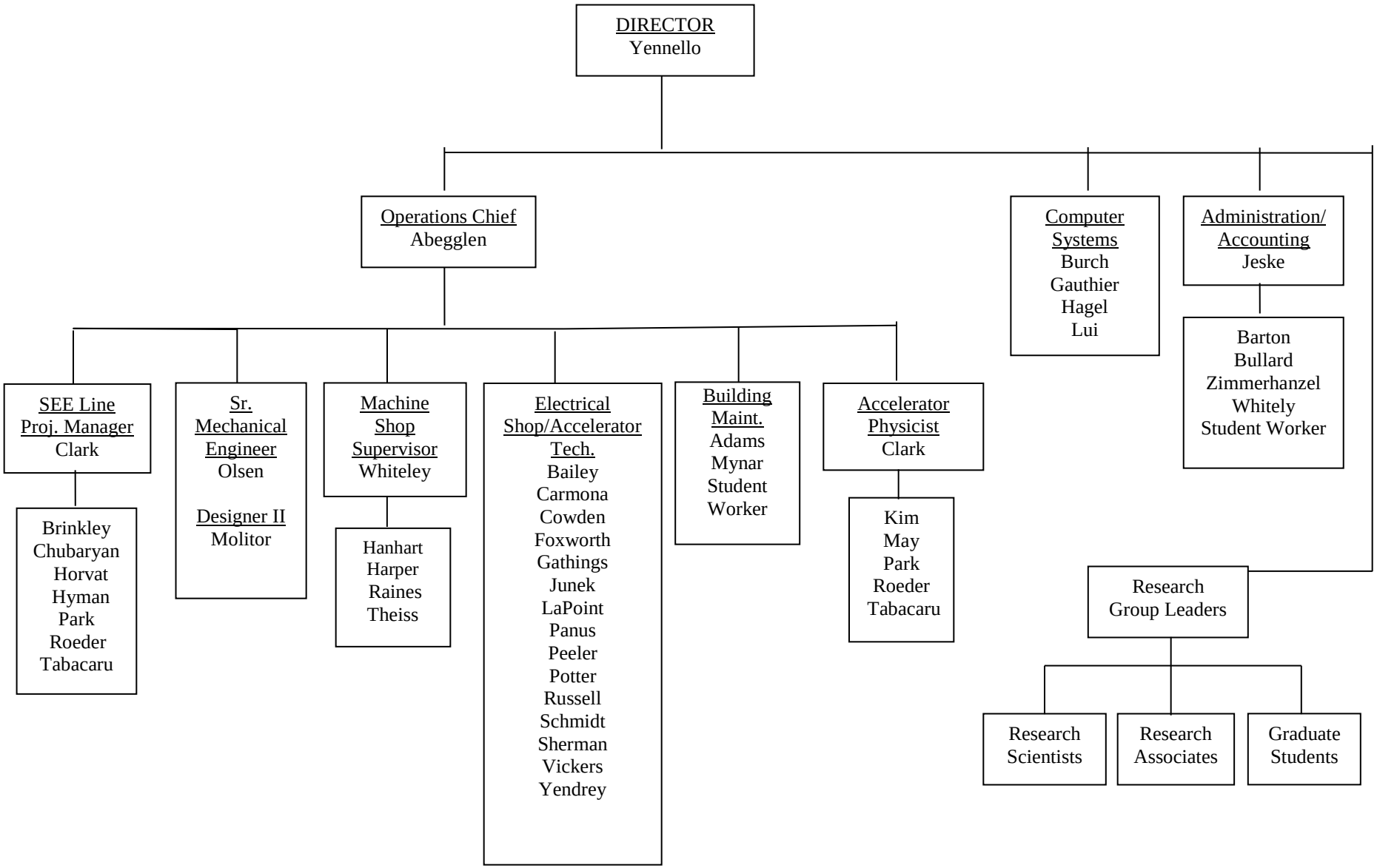

STUDENTS WHO RECEIVED GRADUATE DEGREES
FROM THESIS WORK CONDUCTED
AT
THE CYCLOTRON INSTITUTE

April 1, 2018 – March 31, 2019

Name	Year	Thesis Title	Advisor	Present Position
Miguel Bencomo	2018	*Branching ratio measurement for the superallowed β decay of 26Si*	J.C. Hardy	Postdoctoral Researcher, Lawrence Livermore National Laboratory, Livermore, California
Shuai Liu	2018	*A unified T-matrix approach to quark-gluon plasma*	Ralf Rapp	Post Doc. Cyclotron Institute, Texas A&M University, College Station, Texas
Lauren Ann Heilborn	2018	*Proton-proton correlation functions measured using position-sensitive FAUST*	S.J. Yennello	Assistant Research Scientist,Cyclotron Institute, Texas A&M University, College Station, Texas
Andrew James Zarrella	2018	*Pionic fusion of $^{4}He + ^{12}C$*	S.J. Yennello	Process Engineer, Intel Corporation, Hillsboro, Oregon

INSTITUTE COLLOQUIA AND SEMINARS
April 1, 2018- March 31, 2019

2018

April 3	Dr. Anna Simon, Assistant Professor, Department of Physics, University of Notre Dame, South Bend, Indiana	*Constraining the Hauser-Feshbach Models for Nucleosynthesis Processes*
April 10	Dr. R. Gianluca Pizzone, Laboratori Nazionali del Sud, Istituto Nazionale di Fisica Nucleare, Italy	*Trojan Horse Measurements with RIBs: The Case of the ^{18}F(p,alpha)^{15}O Reaction and Its Astrophysical Relevance*
April 17	Dr. Heather Crawford, Staff Scientist, Nuclear Science Division, Lawrence Berkeley National Laboratory, Berkeley, California	*Gamma-Ray Spectroscopy at the Limits*
May 1	Dr. Akram Zhanov, Senior Scientist, Cyclotron Institute, Texas A&M University, College Station, Texas	*Connection between ANCs and Resonance Widths for Mirror Nuclei*
May 10	Dr. Gerd Röpke, Professor, Institut für Physik, Universität Rostock, Rostock, Germany	*Correlations and Clustering in Dilute Matter*
September 18	Dr. Cody Parker, Postdoctoral Associate, Massachusetts Institute of Technology, Cambridge, Massachusetts	*From the ^{3}H(d,gamma)^{5}He reaction to ICF diagnostics: a fusion of nuclear and plasma science*
September 28	Dr. Lee Sabotka, Professor, Department of Chemistry, Washington University and Mr. Cole Pruitt, Department of Chemistry, Washington University, St. Louis, Missouri	*Two Projects at WU: A) Total (N) Cross sections : ^{16,18}O, ^{58,64}Ni, ^{112,124}Sn B) Two New Near p-Threshold Resonances Explained by a Continuum Cognizant SM*
October 16	Dr. Dr. Kyle Leach, Assistant Professor, Department of Physics, Colorado School of Mines, Golden, Colorado	*The Quest for the New Standard Model: Searching for BSM Physics with Rare-Isotopes*
October 30	Dr. Jinfeng Liao, Assistant Professor, Department of Physics, Indian University, Bloomington, Indiana	*Correlations and Clustering in Dilute Matter*
November 27	Dr. Or Hen, Assistant Professor, Department of Physics, Massachusetts Institute of Technology, Cambridge, Massachusetts	*Neutron Star Droplets and the Quarks Within*

2019

January 10	Dr. Henry Lamm, University of Maryland, College Park, Maryland	*Emerging Methods for Dense and Nonequilibrium Matter*
March 5	Ashley Hood, Research Assistant, Department of Physics and Astronomy, Louisiana State University, Baton Rouge, Louisiana	*Measurements of Fusion Reactions with ^{16}C for Understanding X-ray Superbursts*
March 12	Dr. Morgan White, Project Leader for Fission and Criticality Experimental Research, Los Alamos National Laboratory New Mexico	*No Really, Los Alamos is a Great Place to Work*
March 26	Dr. Michelle P. Kuchera, Assistant Professor, Physics Department, Davidson College, Davidson, North Carolina	*Machine Learning for Event Simulation and Classification in the Active-Target Time Projection Chamber*